



**HAL**  
open science

# Direct Mass Measurements and Global Evaluation of Atomic Masses

Wenjia Huang

► **To cite this version:**

Wenjia Huang. Direct Mass Measurements and Global Evaluation of Atomic Masses. Nuclear Experiment [nucl-ex]. Université Paris Saclay (COMUE), 2018. English. NNT : 2018SACLS151 . tel-01941720

**HAL Id: tel-01941720**

**<https://theses.hal.science/tel-01941720v1>**

Submitted on 2 Dec 2018

**HAL** is a multi-disciplinary open access archive for the deposit and dissemination of scientific research documents, whether they are published or not. The documents may come from teaching and research institutions in France or abroad, or from public or private research centers.

L'archive ouverte pluridisciplinaire **HAL**, est destinée au dépôt et à la diffusion de documents scientifiques de niveau recherche, publiés ou non, émanant des établissements d'enseignement et de recherche français ou étrangers, des laboratoires publics ou privés.

# Direct Mass Measurements and Global Evaluation of Atomic Masses

Thèse de doctorat de l'Université Paris-Saclay  
préparée à l'Université Paris-Sud

École doctorale n°576 particules hadrons énergie et noyau : instrumentation, image,  
cosmos et simulation (PHENIICS)  
Spécialité de doctorat : Structure et réactions nucléaires

Thèse présentée et soutenue à Orsay, le 6 juin 2018, par

**M. WENJIA HUANG**

## Après avis des rapporteurs :

M. YANLIN YE

Professeur des Universités, Peking University

M. STEPHANE GORIELY

Chercheur Qualifié FRS-FNRS, Université Libre de Bruxelles

## Composition du Jury :

M. DAVID LUNNEY

Directeur de Recherches, CSNSM (UMR8609)

Président

M. STEPHANE GORIELY

Chercheur Qualifié FRS-FNRS, Université Libre de Bruxelles

Rapporteur

Mme HAO FANG

Principal physicist, BIPM, France

Examinatrice

M. YURI LITVINOV

Directeur de Recherches, GSI, Germany

Examineur

M. GEORGES AUDI

Directeur de Recherches, CSNSM (UMR8609)

Directeur de thèse



# Acknowledgements

Foremost, I would like to thank my supervisor Georges Audi for his continuous support of my Ph.D. study. His patience, caution, and immense knowledge in experimental physics inspired me the first day I came to the lab. Sitting next to him within 1-m distance allowed us to immerse in fruitful discussions for the whole day, from which I could learn almost every detail in mass evaluation. Thanks for his encouragement and confidence in me, which pushed me to try something new and took on challenges, which I had never been imagining I could have done. I also appreciate his assistance in my daily life in France. I would also like to express my gratitude to David Lunney, a man who stood at the forefront of physics and always informed me of the latest news in mass measurements. He offered me the opportunity to work at ISOLTRAP/CERN, one of the greatest groups of mass measurements in the world, a place in which I had ever dreamt of going when I came across mass measurements for the first time.

I want to thank all the members of the local group at ISOLTRAP, who provided me a warm welcome when I was there. Vladimir Manea, the backbone of ISOLTRAP, who directed me and taught me everything he knew about Penning traps. I was always impressed by his knowledge and enthusiasm, and he was the man from whom I acquired the very first image of the ISOLTRAP setups. Frank Wienholtz, another backbone of ISOLTRAP and an expert at MR-TOF devices, who had always novel ideas and good suggestions. Dinko Atanasov and Maxime Mougeot, two “pythonic” guys, who provided help and suggestions for programming. I would also like to thank Andree Welker and Jonas Karthein for providing help and convenience when I was at CERN. I was so glad to work with these wonderful guys. Also many thanks to Vladimir and Frank, for their continuous support for data analysis and guidance after I finished my lovely stay at CERN.

In addition, I would like to thank all my CSNSM colleagues, who help me overcome the difficulties I met in France. Staying with them also allowed me to know more about the French culture and broaden my horizon.

I also thank the people from Lanzhou. Yuhu Zhang, my master supervisor, for his basic training in how to initiate research and support for my decision to work on AME. Meng Wang, the coordinator of AME, for his corrections and comments on my manuscript and his financial support for me to attend international conference meeting in Beijing.

I would like to thank our collaborators in AME : Georges Audi, Meng Wang, Filip Kondev, and Sarah Naimi, for their encouragement and insightful comments.

I would like to thank my jury members : Stephan Goriely from ULB, Yuri Litvinov from GIS, Hao Fang from BIPM, Georges and David from our local group, for their careful reading and enlightening comments on my manuscript. Thanks Stephan Goriely and Yanlin Ye (Peking University) for their reports of the thesis. A special thanks goes to Stephan, for his pointing out the defeat in my manuscript and hard questions.

I would like to thank China Scholarship Council for supporting my Ph.D. study ; and the ENSAR program for its financial support for my stay at CERN.

Last but not least, I would like to express my sincere gratitude to my beloved wife, who showed confidence, faith in me and never complained if I had to work at weekends. Thanks my parents for raising me up and their spiritual support, without which I could not have finished my thesis. I am also grateful to my wife’s family for their support.



# Preface

At the time I am writing this dissertation, I have spent more than three years and a half working on the Atomic Mass Evaluation (AME). AME is the most trustworthy, exclusive resource related to the atomic masses. And the mass tables, the main product of AME, are widely used in the physics community. Aaldert Hendrik Wapstra, the founder and grand inquisitor of AME, first noticed that the masses derived from different techniques can be best deduced by a least-squares method. A. H. Wapstra, together with F. Everling, L. A. Konig, and J. H. E. Mattauch, provided such an evaluation process at the first International Conference on Nuclidic Masses (AMCO-1) in 1960. His philosophy still serves as a main dish for the daily life of AME. Georges Audi, the Guardian of AME and also my Ph.D. supervisor, has been working in AME since 1981. He is the reason why AME can continue in a healthy way until now. His passion for AME also inspires me to take AME as my Ph.D. subject. Nowadays, when we speak of the masses tables, one often refers to Audi-Wapstra's mass tables.

Ten mass tables have been published up to now, starting from the first version in 1961 to the latest one in 2016. The only dissertation dedicated to AME was accomplished by K. Bos in his Ph.D. thesis in 1977 entitled "Determination of Atomic Masses from Experimental Data", under the supervision of A. H. Wapstra. Since then, not only the experimental techniques but also AME itself evolved.

The intention of this dissertation is not to cover every aspect in AME (it is also impossible to do so). The omissions are due to the limited length of the dissertation and my lack of special knowledge in some domains. One could have followed a series of mass tables in which one could give emphasis at that time. The aim is instead to show to the readers the most important features of AME. I think it could be an opportunity for the public to grasp the basic concept of AME and get acquainted with the way in which AME treat the data. In Chapter 1, a brief introduction to AME and the related concepts will be given. In Chapter 2, the indirect and the direct methods of mass measurements will be discussed, and two of the most important concepts of mass spectrometry, i.e., the resolving power and mass resolution, will be introduced. In Chapter 3, the philosophy of AME will be illustrated in detail, together with a detailed example to show how AME works. In Chapter 4, the most recent developments resulting from my Ph.D. work on the mass table, AME2016, will be presented, such as the calculation of molecular binding energy, the energy correction of the implantation experiments, and the relativistic formula for the alpha-decay process. In Chapter 5, the accuracy and the predictive power of different mass models will be discussed. In Chapter 6, the mass extrapolation of AME will be introduced. In Chapter 7, the results from the Penning-trap mass spectrometry (ISOLTRAP) will be presented. In Chapter 8, the study of the systematic error at the ISOLTRAP multi-reflection time-of-flight mass spectrometer will be discussed.

In order to finish this thesis, I consulted many AME publications, from which I know how AME evolves. I think it is an essential process for each evaluator to know what AME was in the past so that we could have some hints of how to improve it for the future.

---

# Contents

<b>Acknowledgements</b>	<b>3</b>
<b>Preface</b>	<b>5</b>
<b>1 Introduction</b>	<b>15</b>
<b>2 Experimental Techniques</b>	<b>23</b>
2.1 Energy Conversion . . . . .	23
2.2 Indirect Method . . . . .	24
2.2.1 Nuclear reaction . . . . .	24
2.2.2 Decay measurement . . . . .	25
2.3 Direct Methods . . . . .	27
2.3.1 Mass Resolution and Resolving Power . . . . .	28
2.3.2 Mass Spectrometry . . . . .	29
<b>3 The Evaluation Procedures</b>	<b>35</b>
3.1 General remark . . . . .	35
3.2 Introduction to least-squares method . . . . .	36
3.3 Reduction of the problem . . . . .	38
3.4 $\chi^2$ test and consistency factor . . . . .	42
3.5 Flow-of-information matrix . . . . .	44
3.6 Local adjustment in the lightest mass region . . . . .	44
3.7 Removal of certain input data . . . . .	48
<b>4 Developments for AME2016</b>	<b>51</b>
4.1 Molecular binding energy . . . . .	51
4.2 $\alpha$ - and proton-decay energies . . . . .	55
4.3 High precision $\alpha$ -decay energies . . . . .	61
4.4 Correlation . . . . .	62
<b>5 Mass Models</b>	<b>65</b>
5.1 Semi-empirical approaches . . . . .	65
5.2 Accuracy . . . . .	66
5.3 Predictive power . . . . .	71

---

<b>6</b>	<b>Mass Extrapolation</b>	<b>81</b>
6.1	Regularity of the Mass Surface . . . . .	81
6.2	Scrutinizing the Mass Surface . . . . .	82
6.3	Subtracting a mass model from the experimental mass surface	83
<b>7</b>	<b>Experiments</b>	<b>91</b>
7.1	Principle of Ion Traps . . . . .	91
7.2	Experimental setup at ISOLTRAP . . . . .	95
7.3	Data analysis and discussions . . . . .	96
<b>8</b>	<b>MR-TOF MS</b>	<b>107</b>
8.1	Principle of MR-TOF MS . . . . .	107
8.2	Systematic error study . . . . .	108
	<b>Conclusions and Outlook</b>	<b>125</b>
	<b>Appendix A Relativistic formula of alpha decay</b>	<b>129</b>
	<b>Appendix B TOF-ICR Spectra</b>	<b>133</b>
	<b>Synthèse</b>	<b>155</b>

# List of Figures

1.1	Nuclear binding energy per nucleon for all known ground-state masses from AME2016. . . . .	17
1.2	Schematic representation of all the available nuclear data [Aud01].	19
1.3	Number of publications included in AME each year starting from 1951 to the cut-off date in AME2016. The maximum number appears in the year of 1995, where over 180 publications are included. It was due to the conference on Exotic Nuclei and Atomic Masses (ENAM-95), where mass measurements were a central topic. . . . .	20
1.4	Flow diagram of the four-phase computing process in AME. . .	22
2.1	Valley of stability formed by black boxes (192 stable nuclides).	24
2.2	Diagram of all the common types of decay and reactions which connect to a mass represented by a square, in which $A$ is the mass number, $E$ the element symbol, $N$ the neutron number, and $Z$ is the atomic number. Letters from a to m in circles represent different types of connection defined in Table 2.1. . .	27
2.3	Illustration of a) two barely separate spectral peaks of two masses $m_1$ and $m_2$ with equal height and width, where two horizontal dash lines denote the height at 50% and 100%; b) two spectral peaks of the same masses as in a) but with unequal height are mixed and cannot be separated. . . . .	28
3.1	Connection plot with <i>primary</i> , <i>secondary</i> and unconnected items.	40
3.2	Connection plot in the $^{163}\text{Ho}$ region. Each symbol (square and circle) represents a nuclide: the large ones denote nuclides that would be used in the least-squares procedure; the small ones denote <i>secondary</i> nuclides that would not be used in the least-squares procedure. The upper red square symbol indicates $^{163}\text{Dy}$ and the lower one indicates $^{163}\text{Ho}$ . . . . .	40
3.3	Birge Ratio of all the <i>parallel</i> data . . . . .	42
3.4	Connection plot of the lightest nuclides. Each line represents an experimental datum. The corresponding reference papers are also indicated. . . . .	46

4.1	Illustration of $\alpha$ -decay spectra where line-1 and line-2 are calibrants and line-3 is unknown at an equal distance from line-2. (a) Case for which the detector detects only the $\alpha$ -particle energy. (b) Case where the detector detects also the recoiling nuclide. . . . .	57
4.2	Detection efficiency $K$ for different species at different recoiling energy $E_R$ in Si-detector. The range of $E_R$ selected here covers most of the decay experiment cases. . . . .	58
5.1	Masses of different Sn isotopes calculated from different models with respect to the mass model DUZU. . . . .	67
5.2	Root-mean-square deviations of eight mass models for nuclides $Z, N \geq 8$ with respect to mass tables AME2003, AME2012, and AME2016. The number in the parenthesis indicates the number of parameters in the corresponding mass model. Same illustrations will be applied to the successive figures. . . . .	69
5.3	Root-mean-square deviations of eight mass models in four regions: Light ( $8 \leq Z < 28, N \geq 8$ ), Medium-I ( $28 \leq Z < 50$ ) Medium-II ( $50 \leq Z < 82$ ) and Heavy ( $Z \geq 82$ ). . . . .	71
5.4	Root-mean-square deviations from AME2016 in four regions (represented by lines in green): (a) Light, (b) Medium-I, (c) Medium-II, and (d) Heavy. The Global rms deviation is also displayed (represented by black lines). . . . .	72
5.5	$\delta_{\text{rms}}(2012)$ and $\delta_{\text{rms}}(\text{new})$ in (a) Global (b) Light (c) Medium-I (d) Medium-II and (e) Heavy regions. . . . .	76
5.6	Display of deviations between masses from models and that from AME2016 in color plots. . . . .	80
6.1	Screen shot of the “Interactive Graphical” tool displaying four <i>derivative</i> of the mass <i>surface</i> : two-neutron separation energy $S_{2n}$ , two-proton separation energy $S_{2p}$ , $\alpha$ -decay energy $Q_\alpha$ and double-beta-decay energy $Q_{\beta\beta}$ from upper left to bottom right. The lines between two points have the same iso-properties $Z, N, Z$ and $Z$ , respectively. A universal smoothness is identified in each quadrant, except when it comes across a shell closure: in the $S_{2p}$ plot at $Z = 50$ (a sudden drop of slope). . . . .	84
6.2	Two-neutron separation energies of Sn isotopes for all models discussed in Chapter 5. Two vertical dash lines signify magic numbers $N = 50$ and $N = 82$ . . . . .	85
6.3	Display of the differences between experimental masses and the DUZU model as a function of $N$ and $Z$ , of the experimental two-neutron separation energies, and of the experimental two-proton separation energies in four quadrants. . . . .	86

## LIST OF FIGURES

---

6.4	Four <i>derivatives</i> the same as Fig. 6.3 but zooming around $^{79}\text{Cu}$ . New extrapolation (in blue) based on the results from [WAA <sup>+</sup> 17].	88
7.1	Hyperbolic electrode geometry of Paul trap (a) and Penning trap (b). Trapping of charged ions can be realized by applying a voltage difference between the ring electrode and the end electrodes. Penning traps can also have cylindrical electrodes (c). Figure from [Bla06].	92
7.2	Sketch of ion motion in a Penning trap.	93
7.3	Illustration of the TOF-ICR technique	95
7.4	Schematic view of the ISOLTRAP setup [KAB <sup>+</sup> 13]. See text for details.	96
7.5	Time-of-flight spectrum of $^{57}\text{Cr}$ .	100
7.6	TOF-ICR spectra for $^{168}\text{Lu}$ . Two excitation times are taken: $T_{rf} = 1.2$ s (a) and $T_{rf} = 3$ s (b). The arrows indicate the position of the expected ground state.	102
7.7	Two-neutron separation energy in the ytterbium region between (Ho ( $Z = 67$ ) and W ( $Z = 74$ )). The experimental data are denoted by black circles, estimated masses are denoted by empty diamonds, and the red circle represents the new $^{178}\text{Yb}$ mass.	103
7.8	Flow of information diagram for the chromium masses from $A = 52$ to $A = 55$ . Each box represents a nuclide, with the mass uncertainty (in keV) in the lower right corner. The numbers in black represent the old evaluation in AME2012, and numbers in blue represent the new evaluation including the new chromium results. The numbers in blue in the lower parts indicate the influences the current data on the corresponding nuclides. The dash arrows indicate the contribution from other experiments.	106
8.1	Time of flight of five reference species fitted as a function of the number of reflection.	109
8.2	Illustration of the relative residuals as a function of reflection number.	110
8.3	Relation between the square root of mass and the TOF at $N = 0$ (a). Residuals of TOF at $N = 0$ (b).	111
8.4	Mass of $^{87}\text{Rb}$ determined by using $^{39}\text{K}$ and $^{133}\text{Cs}$ as reference masses.	112
8.5	Standard deviation of 100 TOF spectra for each species at different number of reflection.	114
8.6	Relative residuals for three reference ions. The data was averaged by 100 spectra.	114
8.7	Mass determination of $^{87}\text{Rb}$ from 100 spectra using $^{85}\text{Rb}$ and $^{133}\text{Cs}$ as reference ions.	115

8.8	Mass of $^{87}\text{Rb}$ determined by varying the number of the accumulated spectra at different reflection number. . . . .	115
8.9	Scan of $U_{lift}$ voltages of $^{85}\text{Rb}$ at $N = 900$ from 1000 V to 1080 V in steps of 4 V (lower figure). Beam intensity as a function of $U_{lift}$ . . . . .	117
8.10	Optimized cavity voltage as a function of reflection number $N$ of $^{85}\text{Rb}$ . . . . .	117
8.11	Mass determination of $^{87}\text{Rb}$ at the optimum cavity voltage for two different data set. . . . .	118
8.12	(a) Mass of $^{87}\text{Rb}$ determined at reflection number 1000. The x-axis indicates when the measurement was performed. (b) Distribution of deviations of (a). The red curve represents a Gaussian fit. . . . .	120
8.13	Time-of-flight spectrum of $A = 46$ nuclides. . . . .	121
8.14	Mass deviations from AME2016 for 47 measurements. The insert figure displays the distribution of the deviation divided by the uncertainty for each measurement. . . . .	122
8.15	Parameter $\beta$ in Eq. 8.2 for on-line measurements. . . . .	123
8.16	Difference of mass of the same nuclide determined by using one and two reference ions. The red curve is the linear fit to the data point. . . . .	124
B.-2	TOF-ICR spectra. . . . .	136

# List of Tables

2.1	Calculations of common types of decay and reaction energies. . .	26
3.1	Typical input in Eq. 3.2 and corresponding mass equation. . .	37
3.2	Related information for the local adjustment in the lightest mass region. . . . .	45
3.3	Adjusted $Q$ -values in the lightest mass region. $v/s$ indicate the difference between the input $Q$ -value and the adjusted $Q$ -value divided by the uncertainty of the input $Q$ -value. . . . .	48
4.1	Frequency ratios and mass differences. . . . .	54
4.2	Accurate $\alpha$ -decay calculations. Col. 1 is the decay incident , Col. 2 is the $\alpha$ energy, Col. 3 and Col. 4 are the calculated decay energies using classical (Eq. 4.12) and relativistic (Eq. 4.21) formulae, respectively, and col. 5 is difference between the values from two formulae. . . . .	62
5.1	Information of eight mass models: the year of publication, the number of parameters in the model, and the mass table that was used to fit parameters. . . . .	66
5.2	Root-mean-square deviation $\delta_{\text{rms}}$ , mean deviation $\bar{\delta}$ , and maximum deviation $\delta_{\text{max}}$ for nuclides with $Z, N \geq 8$ with respect to three mass tables AME2003, AME2012, and AME2016. The results for the eight mass models are listed. . . . .	68
5.3	Root-mean-square deviation $\delta_{\text{rms}}$ , mean deviation $\bar{\delta}$ , and maximum deviation $\delta_{\text{rms}}$ from AME2016 in four regions: Light ( $8 \leq Z < 28, N \geq 8$ ), Medium-I ( $28 \leq Z < 50$ ), Medium-II ( $50 \leq Z < 82$ ), and Heavy ( $Z \geq 82$ ). . . . .	70
5.4	Root-mean-square deviations in the Global ( $Z, N \geq 8$ ), Light ( $8 \leq Z < 28, N \geq 8$ ), Medium-I ( $28 \leq Z < 50$ ) Medium-II ( $50 \leq Z < 82$ ) and Heavy ( $Z \geq 82$ ) regions. The rms deviations are calculated separately for the masses that were known in AME2012 $\delta_{\text{rms}}(2012)$ and for the new ones in AME2016 $\delta_{\text{rms}}(\text{new})$ . . . . .	73

7.1	Experimental details in the production of the ions of interest. Listed are the experiment date, the target, the ionization technique, the ion energy from ISOLDE, and the mass separator used. . . . .	97
7.2	Frequency ratios between the ions of interest and reference ions.	99
7.3	Influences of the ISOLTRAP results and the adjusted chromium masses. . . . .	104
8.1	Fitting parameters $a$ and $b$ in Eq. 8.7 . . . . .	110

# Chapter 1

## Introduction

When we speak of mass, one would immediately think of the mass of the Sun, our body, a coin, and the like. However, mass, no matter how small it is, is a quantity that every existing object possesses. We can: weigh our body by scales; weigh the mass of a coin by counterpoise balance; we can even weigh the mass of the Sun by Newton's law of universal gravitation through observing the period of the Earth moving around the Sun. But how to weigh the mass of an atom, whose mass and size are extremely smaller than those of the Sun since no one can really see it?

The history of atomic-mass measurements is as old as nuclear physics (one can refer to [Aud06] for the history of early atomic-mass measurements). In 1897, J. J. Thomson found that the cathode rays containing electrical charges had a very large value for the charge-to-mass ratio. He measured this ratio by using electric and magnetic fields and tracking their trajectories. This historic event marks the discovery of what we call "electron" today. In 1912, with the development of Thomson's instrument, F. W. Aston first showed evidence for the presence of two different isotopes of neon, having mass numbers of 20 and 22, respectively. During his career, Aston discovered more than 200 naturally-occurring isotopes, which were the first systematic studies of atomic masses. Aston found that the hypothesis: "*the mass of all isotopes were integer multiples of that of hydrogen*" was *very nearly true* (He replaced the original word "atom" by isotope). This hypothesis was what we call the *whole-number hypothesis*, put forward by J. Dalton and W. Prout. But *very nearly true* means something is missing. Actually, Aston found that the masses he measured for all stable isotopes were less massive than that from the *whole-number hypothesis*. This famous "mass defect" is henceforth explained as the "binding energy" effect, based on Einstein's famous mass-energy equation  $E = mc^2$ .

Nowadays, we known that the basic building blocks of a nucleus are protons and neutrons\* (they are two types of nucleon). The "mass excess", at the origin called "mass defect", is defined as the difference between the atomic

---

\*. Neutron was discovered by J. Chadwick in 1932.

---

mass of a nucleus and its mass number:

$$ME = M - A \cdot u, \quad (1.1)$$

where  $u$  stands for the Unified Atomic Mass Unit (defined below). The “mass excess” is a more convenient way to tabulate atomic masses, since it carries less digits.

## Nuclear Binding Energy

The mass of an atom  $M(N, Z)$  is the sum of the masses of its constituents (protons, neutrons, and electrons) minus its electronic binding energy and nuclear binding energy:

$$M(N, Z) = Nm_n + Zm_p + Zm_e c^2 - \sum_{i=1}^Z B_i - B_{nuc}(N, Z), \quad (1.2)$$

where  $m_n$  is the neutron mass,  $m_p$  the proton mass,  $m_e$  the electron mass,  $B_i$  the  $i$ -th electron binding energy, and  $B_{nuc}$  the nuclear binding energy. The total electronic binding energy of a hydrogen atom is 13.6 eV and can reach  $10 \sim 100$  keV for heavy nuclides. Considering that the atomic mass is of the order of  $A \times 1000$  MeV, a precision better than 1 part in  $10^{10}$  is required to study the atomic effects [BNW10]. For the nuclear binding energy  $B_{nuc}(N, Z)$ , or more interestingly the nuclear binding energy per nucleon which is of the order of 8 MeV, a precision of 1 part in  $10^6$  is needed to study nuclear shell effects [LPT03]. In this chapter, we concentrate only on the nuclear binding energy and without making a confusion,  $B_{nuc}(N, Z)$  is replaced by  $B(N, Z)$ .

The nuclear binding energy of a nucleus is traditionally expressed as:

$$B(N, Z) = Nm_n + ZM(^1\text{H}) - M(N, Z), \quad (1.3)$$

where  $M(^1\text{H})$  is the mass of hydrogen. The mass, or equivalently, the nuclear binding energy, includes all the interactions (strong, weak, and electromagnetic) at work in the nucleus. The systematic studies of the binding energy provide valuable clues for nuclear structure.

Fig. 1.1 shows the nuclear binding energy per nucleon for 2498 known masses in their ground states [WAK<sup>+</sup>17]. Several phenomena can be seen in the first place. The curve is relatively constant at  $B/A \sim 8$  MeV, except for light nuclides. This leads to the idea of saturation of nuclear forces, i.e., each nucleon interacts only with its neighboring nucleons (otherwise  $B$  would increase as a function of  $A^2$  instead of  $A$ ). Secondly, the curve reaches its maximum at  $A \approx 60$  ( $^{62}\text{Ni}$  is the mostly bound nucleus with  $B/A = 8.794$  MeV and is followed by the second mostly bound nucleus  $^{56}\text{Fe}$  which has 8.790 MeV), meaning that there are two ways to gain energy: either below  $A = 60$  by

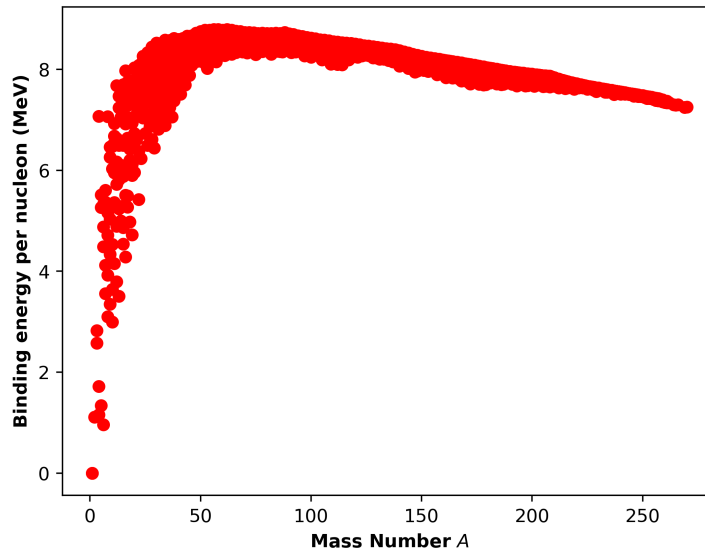


Figure 1.1: Nuclear binding energy per nucleon for all known ground-state masses from AME2016.

assembling light nuclides into a heavier one, or above  $A = 60$  by breaking a heavy nuclide into light parts. The first one is called *nuclear fusion* and the second one is called *nuclear fission*.

In trying to describe the curve in Fig. 1.1 a *semiempirical* mass formula can be derived:

$$B = a_v A - a_s A^{2/3} - a_c Z(Z-1)A^{-1/3} - a_{sym} \frac{(N-Z)^2}{A} + \delta, \quad (1.4)$$

where  $a_v$ ,  $a_s$ ,  $a_c$ ,  $a_{sym}$ , and  $\delta$  are five coefficients to be determined. This formula was first devised by Weizsäcker [Wei35] and Bethe [BB36], which serves also as a basic ingredient in some modern mass models. The first term is called the volume term and comes from the fact that the binding energy per nucleon is linear to the mass number  $A$ . The second term is called the surface term and stems from the fact that the nucleons on the surface interact only with the internal nucleons. The third term is the Coulomb term which accounts for the Coulomb repulsion between protons. The fourth term is based on the fact that nuclei with  $N \approx Z$  are more stable than their neighbors. The last term comes from the pairing force, which has the tendency to couple nucleons of the same type to stable configurations (zero total angular momentum). This pairing energy  $\delta$  can be expressed [KH88] as  $+a_p A^{-3/4}$  for even  $Z$  and  $N$ ,  $-a_p A^{-3/4}$  for odd  $Z$  and  $N$ , and zero for odd  $A$  nuclides.

The five terms of the Bethe-Weizsäcker formula in Eq. 1.4 describes a nucleus “macroscopically”, which mimic a charged droplet. The Bethe-Weizsäcker

---

mass formula is the mostly used nuclear mass model, which lies in its simplicity and relatively good predictive power for most of the nuclei. However, it fails to describe the nuclei with “magic” numbers ( $N$  and  $Z$  equal 2, 8, 20, 28, 50, and 82), meaning that extra components (such as shell effect) should be also considered in the formula.

## Unified Atomic Mass Unit

Nowadays, the standard mass unit  $u$  is defined as one-twelfth of the mass of a carbon-12 atom in its nuclear and atomic ground state, namely  $1u^\dagger = \frac{M(^{12}\text{C})}{12}$ . The unit “ $u$ ” stands for “Unified Atomic Mass Unit”, which has its historical reason. There existed, before 1960, two scales on atomic masses: taking the mass of one atom  $^{16}\text{O}$  as 16 units (physics scale) or taking the mass of natural-mixture oxygen sample as 16 units (chemical scale or atomic weight). The proposals for unifying the mass unit were widely discussed, e.g., J. H. E. Mattauch was one of the physicists who had been studying the scale problem at that time. In 1956, A. Nier and A. Ölander suggested that atomic weight scale be based on a  $^{12}\text{C}$  atom to the International Commission on Atomic Weights. It had been concluded that  $^{12}\text{C}$  was not only an acceptable substitute but also had operational advantages for physical comparisons of nuclidic masses. However, the proposal for unifying the mass unit did not please chemists. As demonstrated by T. P. Kohman, J. H. E. Mattauch, and A. H. Wapstra [KMW58], accepting the new definition of the mass standard would cause a change of 275 ppm instead of using the oxygen atomic weight. It meant chemists would lose millions of dollars selling their products. A revision of innumerable tabulations of data would also need to be initiated. Despite all the difficulties in unification, the candidate  $^{12}\text{C}$  is advantageous for several reasons. First, the mass of a nuclide can be expressed very nearly to its mass number  $A$  (maximum deviation of 0.1  $u$ ). Secondly,  $^{12}\text{C}$  was the most important substance in the mass-spectroscopic determination of nuclidic masses and it will allow direct comparisons with standard mass. Moreover, carbon forms many hydrides at almost every mass number (up to  $A = 120$ ). The atomic mass unit based on  $^{12}\text{C}$  was approved by the International Union of Pure and Applied Physics (1960) and is still used worldwide.

## Nuclear Data

Nuclear data, such as atomic mass, excitation energy, half-life, magnetic moment, spin and parity, etc., finds its application from basic research such as nuclear structure studies, astrophysics, and fundamental physics studies, to nuclear engineering, medicine, environment, and the like. All these domains

---

†.  $1 u = 1.660539040(20) \times 10^{-27} \text{ kg}$

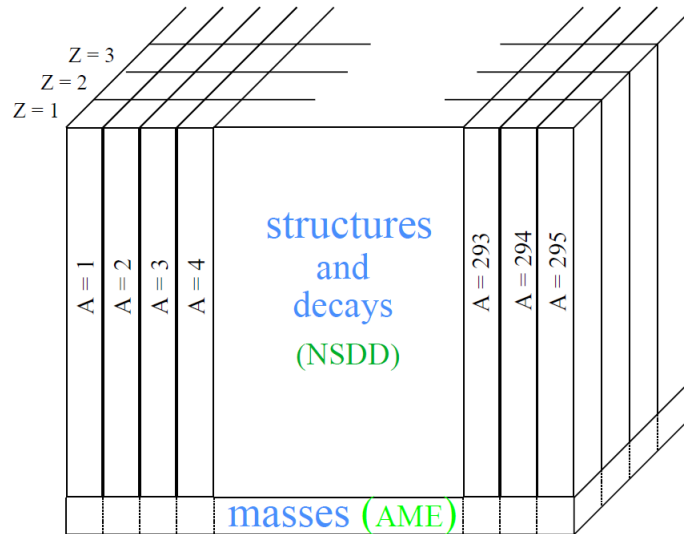


Figure 1.2: Schematic representation of all the available nuclear data [Aud01].

require a canonical data bank which stores all the information and provides recommended values for users.

We can imagine that all the nuclear data are stored in a building, as illustrated in Fig. 1.2. Each vertical bar represents a nuclide, whose ground-state properties are stored on the ground floor and the properties of excited states are stored above the ground floor.

The Evaluated Nuclear Structure Data File (ENSDF) contains the evaluated nuclear properties of all known nuclides derived from nuclear reaction and decay measurements [Tul96]. The ENSDF files are organised by mass number  $A$  and this  $A$ -chain evaluations are undertaken by the members of the International Nuclear Structure and Decay Data (NSDD) network. Such evaluation is *vertical*, since all nuclides within the same mass chain are evaluated at once when new experimental information becomes available [NBD<sup>+</sup>17].

AME is a bit different from ENSDF, in that it connects a quantity which maps across the whole nuclear chart: the mass. Thus the evaluation of atomic mass is *horizontal*. All the *indirect* and *direct* methods (discussed in Chapter 2) yield the mass difference between two or more nuclides, which result in an overdetermined system for mass.

## The AME process

AME shares many similarities with other nuclear-data evaluation projects [Aud01]. The first step in the evaluation is to make a compilation, i.e., collect all available data. Up to the publication of AME2016 [WAK<sup>+</sup>17], we scanned 24 different kinds of physics journals and conference proceedings. Each year, around 100 publications are included in AME. Fig. 1.3 shows the number of

publications included in AME yearly until the cut-off date of AME2016.

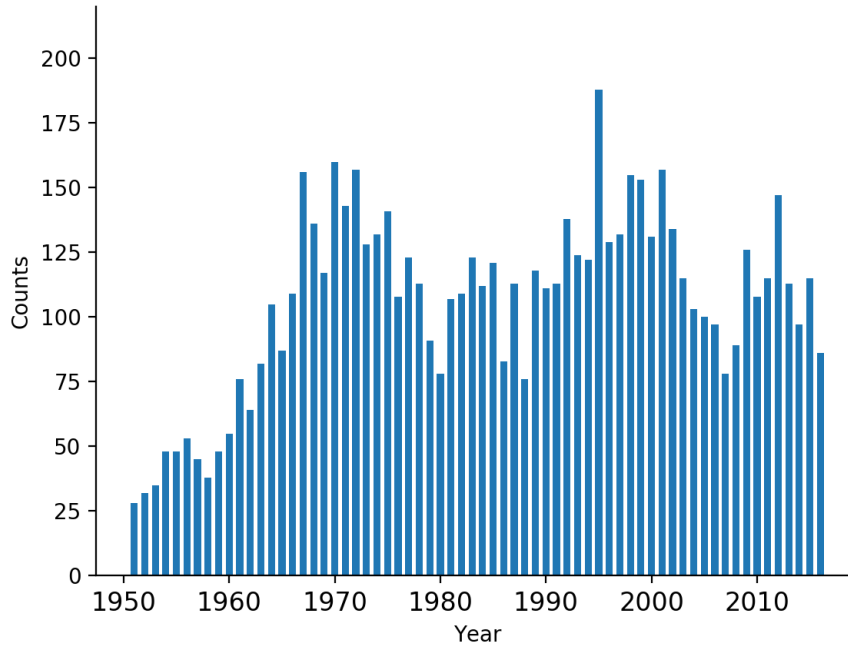


Figure 1.3: Number of publications included in AME each year starting from 1951 to the cut-off date in AME2016. The maximum number appears in the year of 1995, where over 180 publications are included. It was due to the conference on Exotic Nuclei and Atomic Masses (ENAM-95), where mass measurements were a central topic.

The second step is the critical reading process. Decay spectroscopy, reactions, and mass spectrometry determine masses using different techniques and give very diverse uncertainties. During critical reading, we should make a judgment on several parts [Aud01]:

- calibration procedure: the use of calibrants, calibration function;
- spectra examination: peak position, shape, intensity, the goodness of fit;
- the primary data: keep only the original data and not use other values that are deduced by the combination with other experiments and evaluated values.

After examining a paper, we will compare the new results with the previous ones, if any, and their quality will be judged (see Section 3.7 in Chapter 3).

The last step is to enter the new data in the AME database. Here is an entry associated with the  $\alpha$ -decay energy of  $^{236}\text{Cm}$  in AME:

```
236 850963000a1 UHGsa 10Kh06 7074.1 20.  $^{236}\text{Cm}(\alpha)^{232}\text{Pu}$  6954 20 A,
```

where the first 14 digits is the unique ID-number for each input datum, followed by a label U (means no weight for this entry), a reference for the laboratory "GSa", and its Nuclear Science References (NSR) [PBK<sup>+</sup>11] key-number "10Kh06", the  $\alpha$ -decay energy with its associated uncertainty in keV, the input equation, the  $\alpha$ -particle energy with its uncertainty in keV, and a label "A" which denotes that the decaying level and the final level are well established. If they were not, we should have given the label "O", causing the program to increase the uncertainty to 50 keV.

### The AME computer program

The AME evaluators work primarily on three files: *Q*-file, *M*-file, and the *R*-file. The *Q*-file contains a wealth of data which has the same format as the example discussed above. The *M*-file contains the fundamental properties of nucleus, such as atomic mass, excitation energy, half-life, spin and parity, decay mode, etc. The *R*-file includes all the references related to the input data.

After data compilation, the AME computer program will perform a four-phase task [Aud01]:

1. Decoding and Checking. The data will be decoded and the correctness of the ID assignment for each datum will be checked.
2. Building Connection. The connection between the masses will be built, thus allowing the separation between *primary* and *secondary* (see definitions in Section 3.3) nuclides.
3. Applying the least-squares method. See Chapter 3 for details.
4. Calculating outputs. Different sorts of outputs will be represented, including the adjusted masses, adjusted input values, flow-of-information matrix, etc (see Chapter 3 for details).

Once finishing the four-phase program, one can compare the input data with the adjusted one, from which we can recognize if there exists inconsistency or not, or the labels for some data should be reassigned. For example, the values of some input data can be obtained by the combination of other data with higher precision. In this case, the less precise data will be labeled "U". This is the very essential part of evaluation. After such fine tuning, which would not affect the adjusted results, the figures for separation energy and decay energy can be provided. The computing process is displayed in a flow diagram in Fig. 1.4.

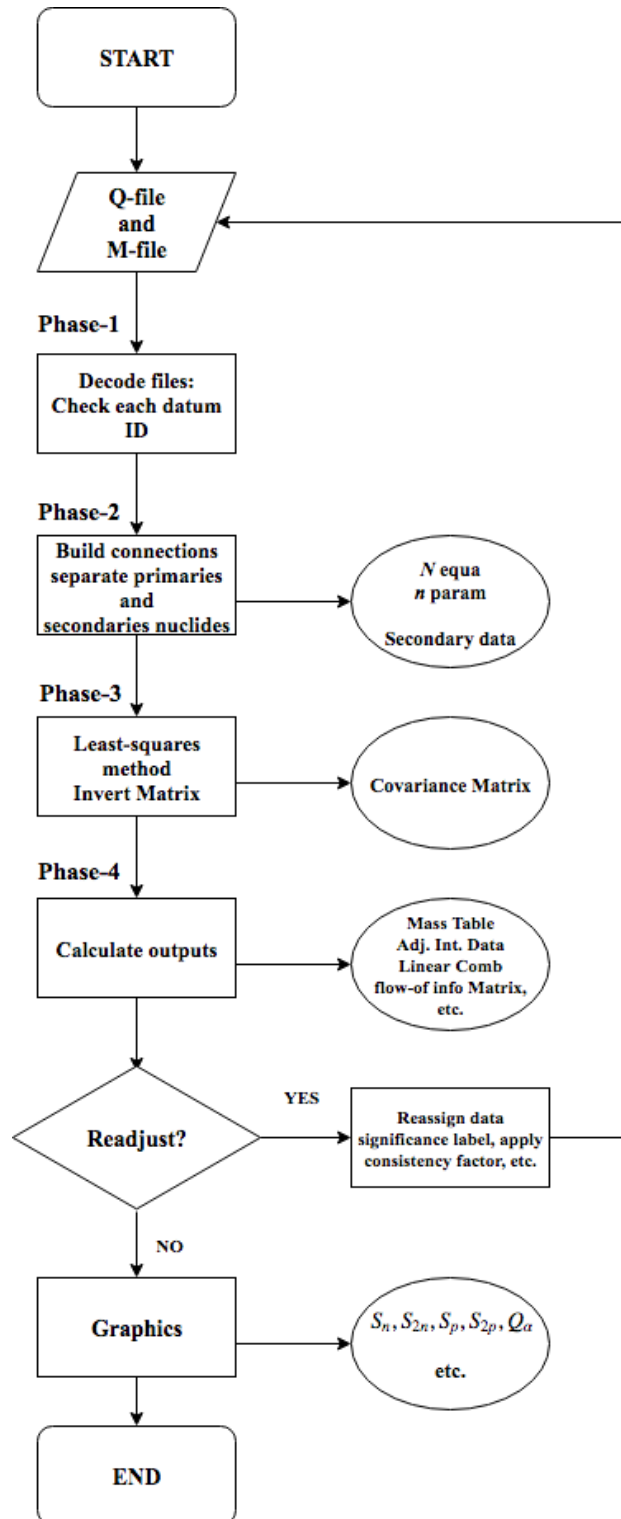


Figure 1.4: Flow diagram of the four-phase computing process in AME.

# Chapter 2

## Experimental Techniques

### 2.1 Energy Conversion

Mass measurements can be carried out by two different methods: the *indirect* method, which establishes an energy relation between two or more nuclides through reactions or decays, and the *direct* method, which “observes” the inertial mass from its movement in an electromagnetic field. The energy relation established in the *indirect* method is expressed in electron-volt (eV), while the masses determined by the *direct* method is expressed in “unified atomic mass” unit (u).

The choice of the volt in the energy unit is not evident: it can be expressed in volt ( $V_{\text{SI}}$ ), which is based on the internationally accepted definition (SI), or the one as *maintained* ( $V_{90}$ ) by the Bureau International de Poids et Mesures (BIPM) using the Josephson effect [Jos62]. It was demonstrated [CW83] that the energy would be expressed more precisely in the *maintained* volt than in the standard volt. The relation between the two defined volts and their relations with the atomic mass unit can be expressed as [MNT16a]:

$$\begin{aligned}V_{90} &= 1 + 9.83(61) \times 10^{-8} V_{\text{SI}} \\1 \text{ u} &= 931494.0954 \pm 0.0057 \text{ keV}_{\text{SI}} \\1 \text{ u} &= 931494.0038 \pm 0.0004 \text{ keV}_{90}.\end{aligned}$$

When combining the inertial mass from mass spectrometry and the energy relation from reactions and decays, one has to apply the conversion factor. The last equation, due to its higher precision, was used in AME2016 for all the energy conversion. For simplicity, the label “V” denotes the *maintained* volt in the following text.

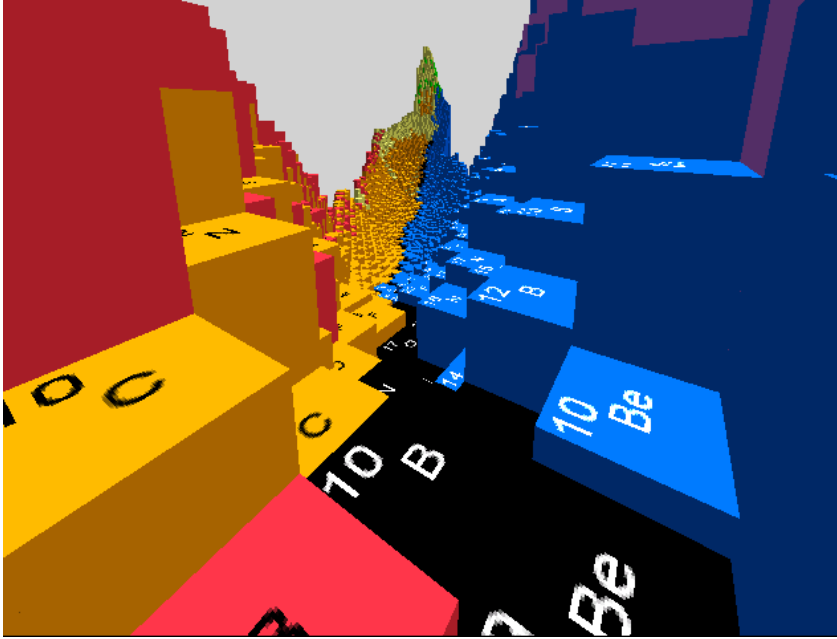


Figure 2.1: Valley of stability formed by black boxes (192 stable nuclides).

## 2.2 Indirect Method

### 2.2.1 Nuclear reaction

From Einstein's Mass-Energy equation  $E = mc^2$ , we know that the released energy in a reaction is directly related to the involved masses. For a nuclear reaction type  $A(a, b)B$ , the released (absorbed) energy is defined as:

$$Q = M_A + M_a - M_b - M_B. \quad (2.1)$$

The reaction is exothermic if  $Q > 0$  and endothermic if  $Q < 0$ . In most cases the masses of the target A, the projectile a, and the ejectile b are well known. Hence the mass of the fragment B can be derived by the measured  $Q$ -value, based on reaction kinematics. Generally, the target, the projectile, and the ejectile are stable or very close to stability, and the fragment will not be very exotic. In the nuclear chart, 192 nuclides are stable, meaning that no decay mode is observed in experiments. These nuclides form the valley of stability, see Fig. 2.1, which is the destiny of all the unstable nuclides.

In the 1970s, the advent of radioactive ion beams allowed to explore the properties of nuclides with extreme proton-to-neutron ratio [BND13]. The best way to study the properties of these exotic nuclides in reaction is the missing mass method [Pen01]. For a binary-product system, the property, here the mass, of a nuclide can be determined by measuring the spectrum of its well-known partner from the laws of energy and momentum conservation. This method can be applied even if the nuclide under investigation has no bound

state. For example, the mass of  ${}^7\text{He}$  (with half-life  $2.51 \text{ zs}^*$ ) was determined by the  ${}^9\text{Be}({}^{15}\text{N}, {}^{17}\text{F})$  reaction [BBG<sup>+</sup>99]. However, the missing-mass method would meet difficulty when it goes further from stability due to the necessity of finding a stable complementary nuclide.

An alternative to the missing mass method is to measure unbound nuclides using invariant-mass spectrometry. For example, if we want to know the mass of an unbound nuclide  $B = x + C$  (where  $x$  and  $C$  are two decaying products), we can measure the four-momentum of the subsystem  $x + C$ . The decay energy, which is a quantity that is measured directly, of the unbound nuclide  $B$  is related to other masses through:

$$Q = M(B) - M(x) - M(C), \quad (2.2)$$

where  $M(x)$  and  $M(C)$  are the masses of the decaying particles. The advantage of this method is that the energy of the incident beam does not need to be known in advance. However, this method may suffer from low efficiency for the registration of light particles, such as neutron, which is the most common decaying particle for neutron-rich nuclides, and the difficulty in assigning ground-state. Some of the light exotic nuclides approaching the neutron drip line were measured this way, such as  ${}^{10}\text{He}$  [JAA<sup>+</sup>10, KSB<sup>+</sup>12],  ${}^{13}\text{Li}$  [KLD<sup>+</sup>13],  ${}^{16}\text{Be}$  [SKB<sup>+</sup>12], and  ${}^{26}\text{O}$  [KNT<sup>+</sup>16].

Neutron-induced  $\gamma$ -ray measurements  ${}^A\text{X}(n, \gamma){}^{A+1}\text{X}$  give directly information on the one-neutron separation energy through:

$$S_n = M({}^A\text{X}) + M_n - M({}^{A+1}\text{X}). \quad (2.3)$$

Since the  $\gamma$ -ray energies are usually measured with high precision, the  $(n, \gamma)$  reactions, along with proton capture reactions, serve as backbone<sup>†</sup> in AME. For example, the  $\gamma$ -ray energy for the reaction  ${}^{185}\text{Re}(n, \gamma){}^{186}\text{Re}$  was measured with a precision of  $0.05 \text{ keV}$  ( $\sigma(m)/m = 3 \times 10^{-10}$ ) [MLH<sup>+</sup>16] at the Budapest Research Reactor [Ros02].

## 2.2.2 Decay measurement

In nuclear-decay experiments, the decay energy is often measured to determine an unknown mass if the mass of its decay-companion is known. Beta decay is the universal phenomenon for all particle-bound nuclides far from stability. Since the beta-decay spectrum has continuous distribution, the decay energy is obtained from the maximum energy so-called the *endpoint* energy. For neutron-rich nuclei, beta decay occurs by emitting an electron ( $\beta^-$ ), where the  $\beta^-$ -decay  $Q$ -value is associated with the mass difference  $Q_{\beta^-} = M_A - M_B$ .

---

\*.  $1 \text{ zs} = 1 \times 10^{-21} \text{ s}$

†. Another contribution to the backbone comes from Penning-trap mass spectrometry.

Table 2.1: Calculations of common types of decay and reaction energies.

$$\begin{aligned}
 Q(\beta^-) &= M(A, Z) - M(A, Z + 1) & (a) \\
 Q(2\beta^-) &= M(A, Z) - M(A, Z + 2) & (b) \\
 Q(4\beta^-) &= M(A, Z) - M(A, Z + 4) & (c) \\
 Q(\beta^-n) &= M(A, Z) - M(A - 1, Z + 1) - n & (d) \\
 S(n) &= -M(A, Z) + M(A - 1, Z) + n & (e) \\
 S(p) &= -M(A, Z) + M(A - 1, Z - 1) + {}^1\text{H} & (f) \\
 Q(\epsilon p) &= M(A, Z) - M(A - 1, Z - 2) - {}^1\text{H} & (g) \\
 S(2n) &= -M(A, Z) + M(A - 2, Z) + 2n & (h) \\
 Q(d, \alpha) &= M(A, Z) - M(A - 2, Z - 1) - {}^2\text{H} - {}^4\text{He} & (i) \\
 S(2p) &= -M(A, Z) + M(A - 2, Z - 2) + 2{}^1\text{H} & (j) \\
 Q(p, \alpha) &= M(A, Z) - M(A - 3, Z - 1) - {}^4\text{He} + p & (k) \\
 Q(n, \alpha) &= M(A, Z) - M(A - 3, Z - 2) - {}^4\text{He} + n & (l) \\
 Q(\alpha) &= M(A, Z) - M(A - 4, Z - 2) - {}^4\text{He} & (m)
 \end{aligned}$$

Proton-rich nuclei decay via the emission of a positron ( $\beta^+$ ), where the decay energy  $Q_{\beta^+} = M_A - M_B - 2m_e c^2$ , or via electron capture (EC) process, where  $Q_{EC} = M_A - M_B$ .

Beta-decay spectrometry has long been used as a powerful tool to study the properties of nuclei not too far from stability. When further out of stability, due to high energy available, such experiments could suffer from the *Pandemonium* effect [HCJH77], where the decaying daughter nuclide is populated through a large number of excited levels from which the energy of the emitted  $\gamma$  is not observed.

For the  $\beta^+$  decay, it would also suffer from the summing effect where a positron annihilates into two photons. For the EC process, the  $Q$ -value is not a quantity that can be measured directly. One has to rely on the measurement of the X-ray intensities, the correct assignment of the decay-level schemes and theoretical calculations.

The measurement of the  $\alpha$ -decay energy  $Q_\alpha$  yields the mass of a heavy nuclide through:  $Q_\alpha = M(N, Z) - M(N - 2, Z - 2) - M({}^4\text{He})$ . If the  $\alpha$ -decay chain ends up with a nuclide with known mass then we can deduce all the masses along the chain from the succession of  $\alpha$  lines. For even-even nuclei, ground state to ground state transitions dominate and the assignment is usually reliable. For odd-odd nuclei, on the contrary, their  $\alpha$  decay does not go directly to the ground state for most of the cases.

The most accurate  $\alpha$ -decay energy came from magnetic spectrograph of the Bureau International des Poids et Mesures [GR71] and such high-precision  $\alpha$  energies serve as standards for other  $\alpha$ -decay experiments. Nowadays, the implantation method has been applied widely to measure  $\alpha$ -particle energies of heavy nuclides using semiconductor (e.g. silicon) detector. In such case, the

partial deposited energy from the heavy recoil should be considered (see Section 4.2 for detailed discussions).

The masses of nuclides close to the proton-drip line between  $Z = 50$  and  $Z = 80$  have been obtained mainly from proton radioactivity [BB08]. This special decay mode allows to investigate the properties of proton-rich nuclei which is of interest to nuclear and astrophysics models [TBH<sup>+</sup>12].

Table 2.1 lists, for a specific nuclide ( $A, Z$ ), the derived values for different types of decay, separation, and reaction energy as the combinations of atomic masses (the letters correspond to the connection diagram in Fig. 2.2).

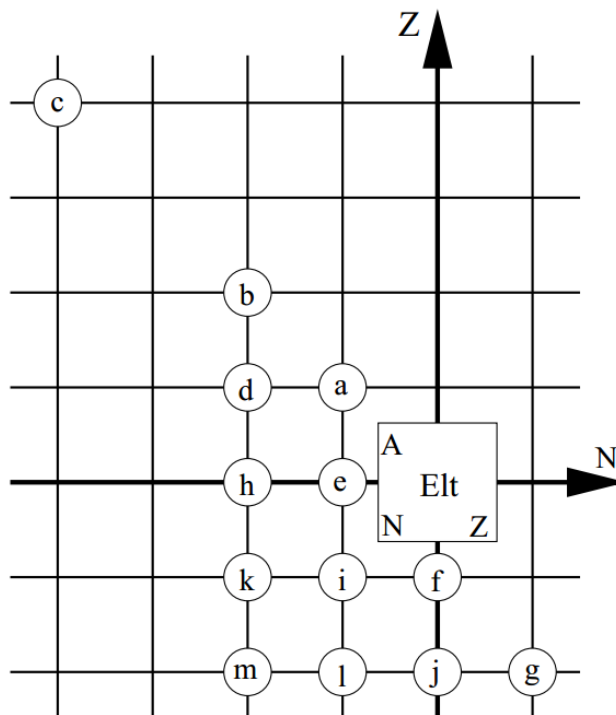


Figure 2.2: Diagram of all the common types of decay and reactions which connect to a mass represented by a square, in which  $A$  is the mass number,  $Elt$  the element symbol,  $N$  the neutron number, and  $Z$  is the atomic number. Letters from  $a$  to  $m$  in circles represent different types of connection defined in Table 2.1.

## 2.3 Direct Methods

Instead of measuring the released energy in reactions or decays, which could involve the identification of complex level schemes, the mass can be

measured directly by mass spectrometry. Mass spectrometry is an analytical method that determines the mass-to-charge ratio of ions. Before discussing different types of mass spectrometers, two important concepts, i.e., mass resolution and resolving power, should be introduced. They will allow a better understanding of the performance of the different setups.

### 2.3.1 Mass Resolution and Resolving Power

The relation between mass resolution and resolving power is symbiotic: resolution is the experimental observable of the resolving power of an instrument and resolving power is the ability of an instrument to separate two spectral peaks which are similar in mass-to-charge ratio.

The mass resolution<sup>‡</sup> is conventionally defined by the Bureau International des Poids et Mesures (BIPM) as the minimum distinguishable distance between two peaks of equal height and width. Marshall *et al.* [MBC<sup>+</sup>13] defines the resolution in the same way that there exists a detectable “valley” between the two close peaks. Fig. 2.3 (a) shows two peaks that are barely separated by a detectable valley. If the distance between the two peaks is smaller than the full width at half-maximum (FWHM) of the peak height  $\Delta m_{50\%}$ , they would not be separated. Generally, *unit* resolution can separate mass 50 from mass 51, or 100 from 101; resolution of 0.01 u is needed to distinguish mass number 100 from 100.01, etc. In order to separate two spectral peaks with different intensity, as illustrated in Fig. 2.3 (b), the resolution should be improved. As demonstrated in [MBC<sup>+</sup>13], the required mass resolution should be  $\sim 10$  times smaller for two peaks with equal width but with height ratio of 100:1.

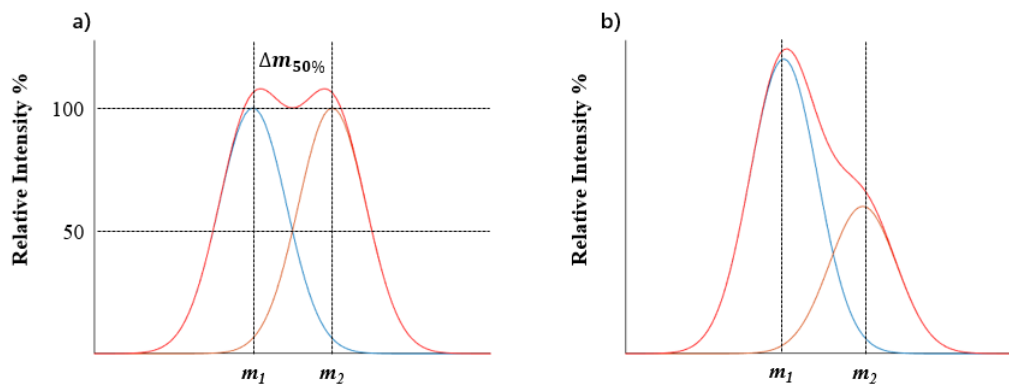


Figure 2.3: Illustration of a) two barely separate spectral peaks of two masses  $m_1$  and  $m_2$  with equal height and width, where two horizontal dash lines denote the height at 50% and 100%; b) two spectral peaks of the same masses as in a) but with unequal height are mixed and cannot be separated.

<sup>‡</sup>. If presented without unit, it means relative resolution.

Conventionally, the mass resolving power is defined as:

$$R = \frac{m_1}{m_1 - m_2},$$

where  $m_1$  and  $m_2$  denote the heavier and lighter mass, respectively. In a spectrum where exists only one single peak, such definition is still applicable. In this case, the mass resolving power is  $m/\Delta m_{50\%}$ . Higher resolving power indicates a better ability to distinguish two peaks with smaller mass difference. In the example given above, to separate two peaks at mass 100 and 100.01 of equal height, a spectrometer with a resolving power of 10,000 is required at least.

One would notice that the BIPM definitions of mass resolution and mass resolving power are in contradiction to the definition given by the International Union of Pure and Applied Chemistry (IUPAC) [IUP14], where both are defined as mass ratios in mass spectrometry. In this thesis, the definition by BIPM is adopted.

### 2.3.2 Mass Spectrometry

All direct methods (except the MR-TOF mass spectrometry) described below measure the motion of a charged ion in a magnetic field [LS01]:

$$\frac{B\rho}{v} = \gamma \frac{m}{q}, \quad \text{or} \quad \gamma \frac{m}{q} = \frac{B}{\omega_c}, \quad (2.4)$$

where  $B\rho$  is the magnetic rigidity of the charged ion,  $v$  the velocity,  $\gamma$  the Lorentz factor,  $m$  the rest mass,  $q$  the charge state,  $B$  is the strength of the magnetic field, and  $\omega_c$  is the cyclotron angular frequency. In principle, one can measure two or three parameters in absolute values to obtain the mass. However, such absolute measurements are limited by the precision of the devices and are usually not practical. To avoid the direct measurements of the absolute values of the apparatus, a delicate calibration is imperative.

#### TOF- $B\rho$ mass spectrometry

The time-of-flight-magnetic-rigidity (TOF- $B\rho$ ) technique offers a good opportunity to map a wide range of exotic and short-lived nuclides. The atomic mass of an ion can be deduced from Eq. 2.4 by measuring the time of flight (TOF) in a magnetic field [MG13]:

$$B\rho = \frac{\gamma m}{q} \left( \frac{L}{TOF} \right), \quad (2.5)$$

where  $L$  is the flight length. Usually, the time of flight can be measured precisely while the magnetic rigidity and flight length are unknown. The mass of

an ion of interest can be determined by using well-known masses as calibrants, from which the relation between the time of flight, magnetic rigidity and the mass can be deduced.

The TOF- $B\rho$  technique has been used mainly at three facilities: the energy loss spectrometer (SPEG) [BFG<sup>+</sup>89] at the National Heavy Ion Laboratory (GANIL), the time-of-flight isochronous spectrometer (TOFI) [WVW<sup>+</sup>85] at Los Alamos National Laboratory (LANL), and the most recent one at the National Superconducting Cyclotron Laboratory (NSCL) [MES<sup>+</sup>12].

The SPEG spectrometer measured the time of flights in a typical range 1000-1500 ns over a 116-m flight path [BFG<sup>+</sup>89]. The time of flight is measured using a radio-frequency signal of the accelerator as the start signal and the stop signal was provided by a plastic detector with resolution of 350 ps (FWHM). To account for the velocity dispersion, which introduced the deviation in the flight path, the position was measured by two drift chambers for vertical position, and a position-sensitive parallel plates counter, for horizontal position. The position measurement provided a resolution of  $10^{-4}$  in the determination of  $B\rho$ . Combining with the resolution of  $2.9 \times 10^{-4}$  in the TOF measurement at a given time of flight 1200 ns, the final mass resolution was  $3.2 \times 10^{-4}$ . The experimental masses were obtained using a fit function up to second order in mass number and atomic number [GMO<sup>+</sup>12].

TOFI employed an isochronous design [WVW<sup>+</sup>85], i.e., an ion with a given mass-to-charge ratio travels along a longer path with higher velocity but a shorter path with lower velocity, which resulted in a time of flight depending only on the mass-to-charge ratio. TOFI measured a typical time of flight of 600 ns with a flight path of about 14 m. A time resolution of 230 ps (FWHM) [VWV<sup>+</sup>86] was obtained by using microchannel plate (MCP) detectors, which resulted in a mass resolution of  $3.8 \times 10^{-4}$ . The mass of ions of interest were obtained by fitting a quadratic function to the measured time of flight of the known masses.

The NSCL spectrometer shares many similarities with the SPEG spectrometer. The flight path is about 60.6 m with a typical time of flight of about 500 ns [MGA<sup>+</sup>15]. The time of flight is measured by two plastic scintillators and the magnetic rigidity is measured with position-sensitive microchannel plate detectors. The time resolution is 80 ps, which includes the position resolution of the MCP detector, based on which a mass resolution of about  $1.6 \times 10^{-4}$  [MES<sup>+</sup>12] is obtained.

The TOF- $B\rho$  technique can access the most exotic nuclides with half-life down to 1  $\mu$ s due to its short flight path and hence short measuring time. The simultaneous production of the less exotic nuclides at the same experiments can also provide reliable masses for calibration. These two features enable the TOF- $B\rho$  technique to be suitable for short-lived, exotic nuclides.

However, this technique cannot in most cases separate a ground state from an eventual (long-lived) isomeric state of a nuclide due to its limited resolving power. For example, a resolving power of  $1 \times 10^4$  is needed to separate the

ground state and its isomeric state at excitation energy of 3 MeV for a nuclide at  $A = 30$ , which is beyond the capability of all the TOF- $B\rho$  spectrometers discussed above. Moreover, neither the magnetic rigidity nor the flight length can be measured with sufficient precision, which means that an unknown mass is usually deduced from a complex calibration function using as many reference nuclides as possible. This could lead to erroneous results if some of the low-lying excited states have not been identified.

## Storage Ring Mass Spectrometry

The idea of increasing of the flight path and thus the resolving power opens a new era for TOF mass measurements. The circulating ions are confined in a well-defined orbit by a magnetic field and their revolution times or frequencies can be determined with various methods. There exists only two facilities which perform mass measurements using storage rings: the experimental storage ring ESR [Fra87] at GSI and the experimental cooler storage ring CSRe [XZW<sup>+</sup>02] at the Institute of Modern Physics (IMP), Lanzhou. Both facilities can store and measure ions at relativistic energy.

The difference in revolution frequency of two ions is related to the difference in mass-over-charge ratio through [FGM08]:

$$\frac{\Delta f}{f} = -\frac{1}{\gamma_t^2} \frac{\Delta(m/q)}{m/q} + \left(1 - \frac{\gamma}{\gamma_t^2}\right) \frac{\Delta v}{v}, \quad (2.6)$$

where  $\gamma$  is the Lorentz factor,  $\gamma_t^2$  the transition point energy of the storage ring, and  $v$  is the velocity of the ion.

In order to minimize the dependence on the velocity term in Eq. 2.6 and obtain a direct expression of mass in terms of revolution frequency, two complementary methods can be used [FGM08]. One is called the Schottky Mass Spectrometry (SMS) and the other is the Isochronous Mass Spectrometry (IMS). In the SMS mode, the velocity dispersion is reduced to a level of well below  $\frac{\Delta v}{v} \sim 10^{-6}$  by using electron cooling [FGM08]. The cooling process lasts for several seconds and hence SMS is only applicable for long-lived nuclides. The beam noise is picked up by two opposite metallic plates and the time signals are Fourier transformed to frequencies. Most of the frequency spectra are measured around the 30th harmonic [FGM08] in order to have a better signal-to-noise ratio.

In the IMS mode, no electron cooling is needed, and instead, by tuning the optical setting  $\gamma_t = \gamma$ , ions with different velocities will have different orbit lengths resulting in the same revolution time. Without cooling, IMS can measure ions with half-lives down to tens of  $\mu s$ , which is equivalent to tens of revolution. In IMS, a thin carbon foil is placed inside the storage ring and the secondary electrons induced by the passing ions are recorded by a MCP detector.

Both methods are employed in ESR and the resolving power of  $7.5 \times 10^5$  was achieved by SMS [GAB<sup>+</sup>01] and  $2 \times 10^5$  by IMS [SKL<sup>+</sup>08]. CSRe uses presently the IMS technique and a resolving power of  $2.2 \times 10^5$  has been obtained in a recent measurement [ZXS<sup>+</sup>17].

Similarly to the TOF- $B\rho$  measurements, the ion trajectory in a storage ring cannot be measured precisely and hence the mass accuracy is limited by the velocity dispersion. To overcome this difficulty, a double-TOF-detector system has been constructed at CSRe to correct the momentum dispersion of the stored ions [SXZ<sup>+</sup>16]. The idea is that by using two TOF detectors installed in a straight section of the storage ring, the velocity of ions can be determined and thus the information of the actual orbit length can be obtained. In this way, the deviation of the revolution orbit from the central orbit can be corrected.

## Multi-Reflection Time-of-Flight Mass Spectrometry

The newly developed multi-reflection time-of-flight (MR-TOF) technique [WP90] has been widely used to determine the mass of very short-lived nuclides. The principle is that, by using two symmetric electrostatic mirror electrodes facing each other, the ions can be reflected hundreds or thousands of times and hence the resolving power can be largely increased. A large number of ions can be trapped simultaneously and the number of reflection of an ion can be adjusted easily according to the half-lives of the ions of interest. The reflection number is usually chosen to be 1000 at ISOLTRAP, and larger than  $\sim 150$  at RIKEN.

The mass resolving power for the MR-TOF mass spectrometry can be defined as:

$$R = \frac{m}{\Delta m} = \frac{t}{2\Delta t}, \quad (2.7)$$

where  $t$  is the time of flight and  $\Delta t$  is the peak width (FWHM). From the definition, we know that the resolving power  $R$  scales with the time of flight and hence the number of reflection, given the time resolution is constant.

A resolving power of 200,000 (for  $A = 40$  at  $t = 30$  ms) has been reached at ISOLTRAP [WWA<sup>+</sup>13], 600,000 (for  $A = 133$  at  $t = 49$  ms) at GSI [DPB<sup>+</sup>15] and 203,000 (for  $A = 12$  at  $t \approx 10$  ms) at RIKEN [ISW<sup>+</sup>13]. More details about the MR-TOF mass spectrometry will be given in Chapter 8.

## Penning-trap mass spectrometry

Nowadays, Penning-trap mass spectrometry provides the most accurate and precise data in atomic mass measurements. Almost all radioactive beam facilities around the world use (or plan to use) Penning-trap mass measurement systems [BDN13]. For stable nuclides, a mass precision of an unprecedented

level ( $7 \times 10^{-12}$ ) [RTP04] has been reached, and for short-lived nuclides, precisions better than  $10^{-7}$  are routinely obtained. Such high precision allow to perform studies in different fields of physics [BDN13], e.g., in astrophysical physics (the study of the composition of neutron-star crusts [WBB<sup>+</sup>13b] and waiting points in rapid proton capture process [RKA<sup>+</sup>04, TXW<sup>+</sup>11, CSS<sup>+</sup>04]) and neutrino physics [EBB<sup>+</sup>15].

The principle of Penning-trap mass spectrometry is to measure the cyclotron frequency  $\omega_c$  of an ion in the magnetic field  $B$ , which is related to its mass-to-charge ratio:

$$\omega_c = \frac{q}{m} B. \quad (2.8)$$

Since the strength of  $B$  cannot be known precisely, the measurement of a well-known mass is essential to make a reliable calibration.

From the derivative of Eq. 2.8 with respect to  $m$ :

$$\frac{d\omega_c}{dm} = -\frac{qB}{m^2} = -\frac{\omega_c}{m}, \quad (2.9)$$

the resolving power of Penning traps can be defined:

$$R = \frac{m}{\Delta m} = \frac{\omega_c}{\Delta \omega_c} = \frac{\nu_c}{\Delta \nu_c} \quad (2.10)$$

where  $\omega_c = 2\pi\nu_c$ . The line width  $\Delta\nu_c$  with which the cyclotron frequency is determined is given by [Bol01]:

$$\Delta\nu_c \approx 0.8/T_{obs}, \quad (2.11)$$

where  $T_{obs}$  is the observation time of the ion motion in seconds.

Thus, the resolving power can be written:

$$R \approx 1.25 \cdot \nu_c \cdot T_{obs}. \quad (2.12)$$

In order to have a high resolving power, high cyclotron frequency caused by highly charged state or strong magnetic field, and long observation time are desirable. The cyclotron frequency of a singly charged ion with mass 100 u in an 8-T field is around 1.2 MHz. A resolving power of  $1.5 \times 10^6$  can be obtained if the observation time  $T_{obs} = 1$  s.

In this chapter, the basic concept of different types of methods in atomic-mass measurements is introduced. The Penning-trap mass spectrometry will be detailed in Chapter 7 and the MR-TOF technique will be discussed in depth in Chapter 8.



# Chapter 3

## The Evaluation Procedures

### 3.1 General remark

The evaluation of atomic masses is subject to a special way of treating data. The present knowledge of atomic masses, as discussed in Chapter 2, can be categorized into four classes: a) beta-decay energies, b) disintegration energies from light-particle emissions, such as  $\alpha$  and proton decays, c) energy released in nuclear reactions, and d) mass-spectrometric data (calorimeters can also yield energy information by detecting heat). All mass measurements are relative measurements, meaning that every single experimental datum basically establishes a relation between two, or sometimes more, masses, even the “absolute” mass measurements compare an ion of interest with carbon clusters [BBH<sup>+</sup>02]. Obtaining the best value for masses from numerous data, which are sometimes conflicting, is not an easy task. The ideal situation would be that the whole dataset forms a homogeneous system, meaning that all the data is subjected to the same analysis procedure and errors are given in a unique way. It is however far from realistic. Not all the experimentalists use the same methods to treat data and even the assigned errors have different interpretations. There thus exists no unique way of treating such an inhomogeneous set of data. One may try to scrutinize, select, correct, or even reject data according to some rules to make it as homogeneous as possible. But it depends strongly on evaluators’ experience.

Another characteristic in mass measurements lies in the fact that a nuclide can be involved in both nuclear reaction and mass-spectrometric measurements, meaning that the number of measurements is inevitably larger than that of the involved masses. How to handle such interconnected links is another challenge.

We should also pay attention that input data are not always independent. For example, the decay energy for a ground-state nuclide can be derived more accurately by combining transition to some excited states, while the ground-state transition assignment can be based on mass-spectrometric data.

The evaluation strategy is to consider all the input data as independent. Such treatment is of course not perfect but we notice that the correlation between input data affects only some of the ultra-precise measurements.

There are two fundamental hypotheses on which the mass evaluation are based [Bos77]: a) the mass of an atom is constant and b) masses are additive. The first statement is the key in the least-squares adjustment. The second one means that if the mass difference between A and B is  $q_1$  and between B and C is  $q_2$ , then the mass difference between A and C is  $q_1 + q_2$ . These two hypotheses are so fundamental that everyone takes them for granted.

## 3.2 Introduction to least-squares method

Suppose that we have  $N$  measurements connecting  $n$  masses ( $N > n$ ). Each experiment establishes a relation between several nuclides:

$$q_i = \sum_{\mu} k_{i\mu} m_{\mu}, \quad (3.1)$$

where  $q_i$  denotes the result of the  $i$ -th experiment and  $m_{\mu}$  is the  $\mu$ -th related mass.  $\mathbf{K} = (k_{i\mu})$  indicates the coefficient matrix and the index  $i$  ranges from 1 to  $N$  and index  $\mu$  ranges from 1 to  $n$ . As mentioned above, the number of observations  $N$  is usually much larger than that of masses  $n$ . It is inadmissible to discard  $N - n$  data and calculate the unknown quantities through  $m_{\mu} = \sum_i \kappa_{\mu i} q_i$  (with  $\sum_i \kappa_{\mu i} k_{i\gamma} = \delta_{\mu\gamma}$ ), which would results in

$$\binom{N}{n}$$

different values for each mass. This predicament can be solved by using least-squares method [Wap60].

First, we can rewrite Eq. 3.1 using matrix notation:

$$\mathbf{q} = \mathbf{K}\mathbf{m}, \quad (3.2)$$

where  $\mathbf{q} = \{q_i\}$  and  $\mathbf{m} = \{m_{\mu}\}$  are both column vectors.  $\mathbf{K}$  is an  $(N \times n)$  dimensional matrix. The variance  $\sigma_i$  of the  $i$ -th measurement  $q_i$  is used to build a weight matrix  $\mathbf{W}$ . If the input data is independent, which is always the case, then  $\mathbf{W}$  is a diagonal matrix and can be written:

$$\mathbf{W} = \text{diag}\{\mathbf{1}/\sigma_i^2\}. \quad (3.3)$$

The normal matrix  $\mathbf{A}$  can be constructed [rB96]:

$$\mathbf{A} = \mathbf{K}^t \mathbf{W} \mathbf{K}, \quad (3.4)$$

where  $\mathbf{K}^t$  is the transpose matrix of  $\mathbf{K}$ .  $\mathbf{A}$  is an  $(n \times n)$  square positive definite matrix and its inverse matrix  $\mathbf{A}^{-1}$  has the same properties. The whole system can be solved by the so-called normal equation:

$$\mathbf{A}\bar{\mathbf{m}} = \mathbf{K}^t\mathbf{W}\mathbf{q}, \quad (3.5)$$

where  $\bar{\mathbf{m}}$  is a column vector which contains the adjusted values for the masses. Since  $\mathbf{A}$  is invertible, the best values for the masses can be obtained by solving:

$$\bar{\mathbf{m}} = \mathbf{A}^{-1}\mathbf{K}^t\mathbf{W}\mathbf{q}, \quad \text{or} \quad \bar{\mathbf{m}} = \mathbf{R}\mathbf{q}. \quad (3.6)$$

The  $(n \times N)$  matrix  $\mathbf{R}$  is called the response matrix. The inverse matrix  $\mathbf{A}^{-1}$  is none other than the covariance matrix, with its diagonal element  $(A^{-1})_{\mu\mu}$  standing for the variance of the  $\mu$ -th mass and its off-diagonal element  $(A^{-1})_{\mu\nu}$  signifying the covariance between two masses  $m_\mu$  and  $m_\nu$ .

We can replace the unknown quantity  $\mathbf{m}$  in Eq. 3.2 by the best value  $\bar{\mathbf{m}}$  then we obtain the adjusted values for each input datum:

$$\bar{\mathbf{q}} = \mathbf{K}\bar{\mathbf{m}}, \quad (3.7)$$

with its variance:

$$\sigma^2(\bar{\mathbf{q}}) = \mathbf{K}\mathbf{A}^{-1}\mathbf{K}^t. \quad (3.8)$$

The root of the variance represents the uncertainty of each adjusted input datum.

To be general, any linear combination of the adjusted values can be written as:

$$q^* = \mathbf{g}^t\bar{\mathbf{m}}, \quad (3.9)$$

where  $\mathbf{g}^t$  denotes a row vector of coefficients. With the help of the covariance matrix, one can calculate the variance of any linear combination of masses:

$$\sigma^2(q^*) = \mathbf{g}^t\mathbf{A}^{-1}\mathbf{g}. \quad (3.10)$$

Table 3.1: Typical input in Eq. 3.2 and corresponding mass equation.

i-th datum	Types	$\sum_{\mu} k_{i\mu}m_{\mu}$
1	$^{33}\text{P}(\beta^-)^{33}\text{S}$	$^{33}\text{P} - ^{33}\text{S}$
2	$^{214}\text{Th}(\alpha)^{210}\text{Ra}$	$^{214}\text{Th} - ^4\text{He} - ^{210}\text{Ra}$
3	$^{19}\text{Na}(\text{p})^{18}\text{Ne}$	$^{19}\text{Na} - ^1\text{H} - ^{18}\text{Ne}$
4	$^{27}\text{Al}(\text{p,n})^{27}\text{Si}$	$^{27}\text{Al} + ^1\text{H} - ^1\text{n} - ^{27}\text{Si}$
5	$\text{C}_7\text{H}_{14} - ^{98}\text{Ru}$	$7 \cdot ^{12}\text{C} + 14 \cdot ^1\text{H} - ^{98}\text{Ru}$
6	Penning Trap	$M - k \cdot M_{\text{ref}}$

Table 3.1 lists some typical input data. One may already see that the coefficient matrix  $\mathbf{K}$  in Eq. 3.2 is a sparse matrix: only a few nuclides are

involved in each measurement, making most of the elements null in  $\mathbf{K}$ . For decay and reaction measurements,  $k = 1$  for entrance channel and  $k = -1$  for exit channel. For mass-spectrometric measurements  $k$  is not always an integer number (see Section 4.1 for discussions).

## Why least-squares?

One may ask why use the least-squares method to extract the best values from a wealth of observations. I think there are mainly two reasons for that. First, the mass itself is usually not the quantity of interest\* and what matters most of the time is a certain linear combination of masses such as separation energy, beta-decay energy, etc. However, the precision of any combination in mass could not be obtained without considering the *error matrix*, which appears automatically in the least-squares method. Secondly, when the least-squares method is carried through over the whole data set, one can judge the correctness of an input datum by comparing with the adjusted one. Such treatment could reveal undiscovered systematic errors among some measurements. The adjustment is justified only if the consistency of the input data is satisfied.

## 3.3 Reduction of the problem

### PRIMARY AND SECONDARY

Before performing the least-squares adjustment, all the data is separated into two groups. Suppose we have a series of measurements like in the first column below:

$$\left. \begin{array}{l} A - B = q_1 \\ A - C = q_2 \\ B - C = q_3 \\ B - D = q_4 \\ C - D = q_5 \\ D - E = q_6 \\ E - F = q_7 \\ E - G = q_8 \\ H - I = q_9 \end{array} \right\} \implies \left. \begin{array}{l} A - B = q_1 \\ A - C = q_2 \\ B - C = q_3 \\ B - D = q_4 \\ C - D = q_5 \\ D - E = q_6 \end{array} \right\} \implies \left. \begin{array}{l} A - B = q_1 \\ A - C = q_2 \\ B - C = q_3 \\ B - D = q_4 \\ C - D = q_5 \end{array} \right\}$$

Each capital letter represents the mass of a nuclide and  $q_i$  represents the corresponding  $i$ -th  $Q$ -value. As the nuclides  $H$ ,  $I$ ,  $G$ , and  $F$  appear only once in

\*. One exception would be the Avogadro Project of redefining the kilogram, where the atomic mass of  $^{28}\text{Si}$  would be used as an input parameter.

the system, they can be removed temporarily with their corresponding input data. What remained are listed in the middle column.  $E$  should be also removed since  $E - F$  and  $E - G$  were removed in the first round. Finally, only five equations which connect four unknown masses are left in the last column and they will be entered into the least-squares evaluation.

The nuclides that are left are *primary* and their related equations are *primary* data, while the nuclides that are removed are *secondary* nuclides and the related equations are called *secondary* data. This classification does not mean that one is more important than the other: the *primary* data are subject to the least-squares process to obtain the masses of *primary* nuclides while *secondary* data give information for a specific nuclide and will never improve the precision of other nuclides (*secondary* data has no contribution to the  $\chi^2$  (detailed next)). Figure 3.1 illustrates this example. The masses of  $A, B, C, D$  form an overdetermined system and they are subject to the least-squares adjustment. The masses of *secondary* nuclides can be derived, without any loss of information, in a straightforward way once the masses of the *primary* nuclides are fixed. Nuclides,  $H$  and  $I$ , which have no connection to neither *primary* nuclides nor *secondary* nuclides are called unconnected nuclides. Their masses can be obtained only if a link is built which connects them to an experimentally known nuclide (see Chapter 6). The link is *estimated* and AME assigns a special symbol “#” for those *estimated* masses.

In AME, we assign a *degree* to each nuclide: all *primary* nuclides have *degree* 1 while *secondary* nuclides have their *degree* increasing from two to higher values depending on how far they are from the *primary* nuclides. The division of the input data into two groups was adopted for two reasons: a) in the old times, the computation ability was strongly limited by the dimension of the normal matrix in Eq. 3.4. The time necessary for the inversion of a matrix is the cube of the number of the *primary* nuclides (in 1960, the inversion of a matrix with 670 rows needed a CPU machine time of some 20 days [Kön60]); b) the separation of *secondaries* allows to localize abnormalities more easily. And also allows to check the dependencies faster. Even though the calculation time nowadays is no longer a problem for AME (it takes only 30 s to complete the inversion), we still keep such a policy in our evaluation process, since it is much more pleasant to get a result almost 30 times faster (assuming the numbers of *primary* and *secondary* nuclides are 1000 and 2000, respectively).

Fig. 3.2 displays the connection plot in the  $^{163}\text{Ho}$  region. Each symbol represents a nuclide and each line represent an experimental datum. The direct measurement of the mass difference between  $^{163}\text{Ho}$  and  $^{163}\text{Dy}$  is essential to address the neutrino mass [EBB<sup>+</sup>15]. The two nuclides of interest  $^{163}\text{Ho}$  and  $^{163}\text{Dy}$ , which are colored in red, are connected directly by mass spectrometry (double line) and EC-decay spectrometry (single line). They also connect indirectly through the neighboring nuclides through several different paths. Only the AME procedure can disentangle such a complex connection and obtain a reliable  $Q$ -value for the mass difference between  $^{163}\text{Ho}$  and  $^{163}\text{Dy}$ .

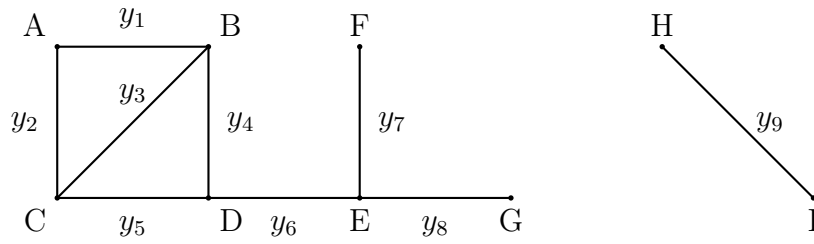


Figure 3.1: Connection plot with *primary*, *secondary* and unconnected items.

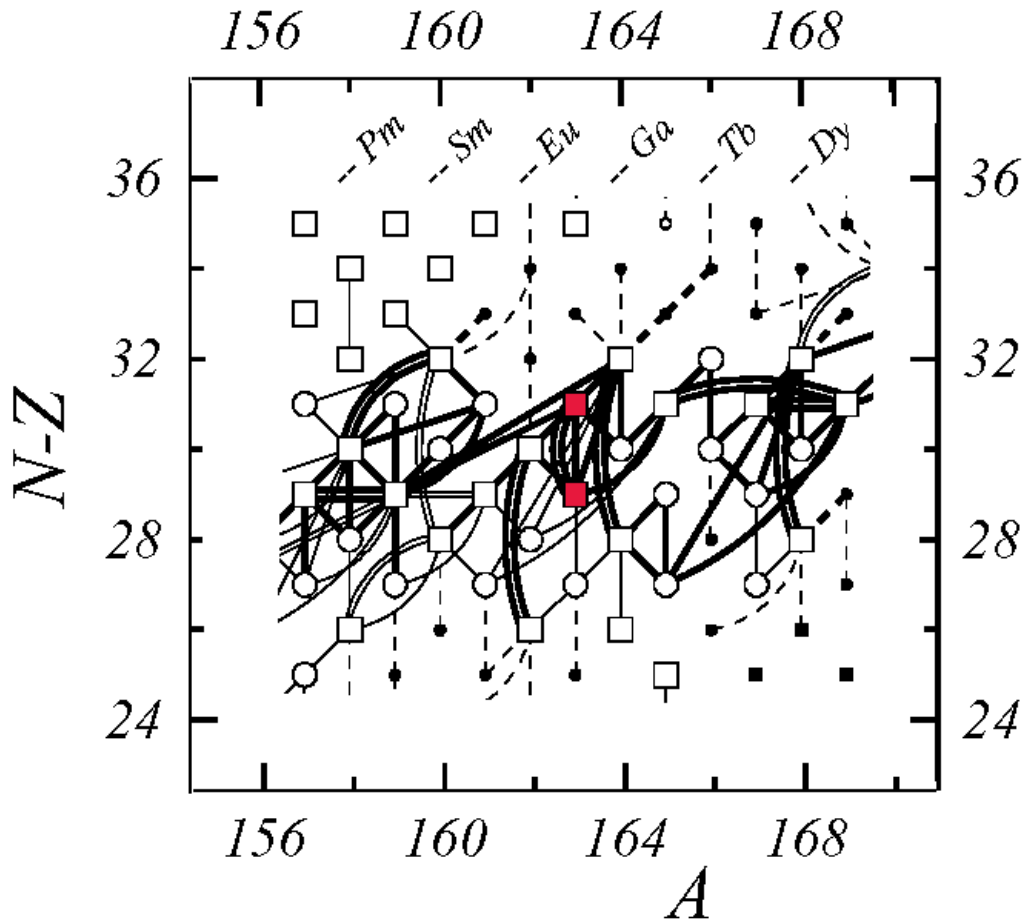


Figure 3.2: Connection plot in the  $^{163}\text{Ho}$  region. Each symbol (square and circle) represents a nuclide: the large ones denote nuclides that would be used in the least-squares procedure; the small ones denote *secondary* nuclides that would not be used in the least-squares procedure. The upper red square symbol indicates  $^{163}\text{Dy}$  and the lower one indicates  $^{163}\text{Ho}$ .

### Pre-averaging

Two or more experiments measuring the same quantity can be averaged without losing information. The adjusted mass values will not be affected whether such pre-averaging is applied or not, provided that the internal errors are assigned to the weighted means. Our policy is to give only one value for a specific reaction or decay  $Q$ -value. Such pre-averaged data are considered as *parallel* data and their weighted mean is calculated by:

$$\bar{q} = \frac{\sum_i q_i \sigma_i^{-2}}{\sum_i \sigma_i^{-2}}, \quad (3.11)$$

where  $\sigma_i$  is the uncertainty of the  $i$ -th  $Q$ -value and its associated internal error is:

$$\varepsilon_{int} = \left( \sum_i \sigma_i^{-2} \right)^{-1}. \quad (3.12)$$

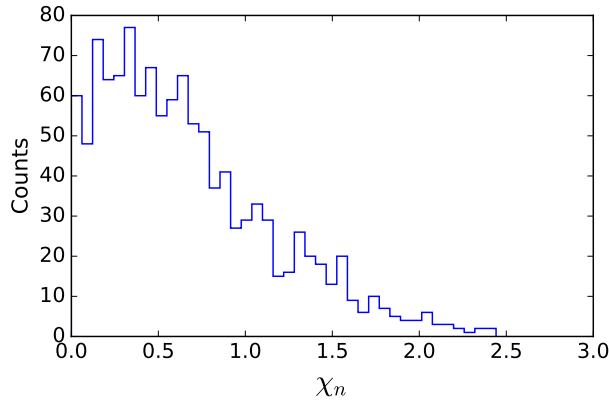
However, one cannot use blindly the internal error as the adjusted input error since it makes no sense to enter some data which conflicts with each other. Under such circumstance, besides the internal error, one also needs to calculate the external error:

$$\varepsilon_{ext} = \frac{\sum_i (\bar{q} - q_i)^2 \sigma_i^{-2}}{(N - 1) \sum_i \sigma_i^{-2}}, \quad (3.13)$$

where  $N$  is the number of the averaged items. If the ratio  $\chi_n = \varepsilon_{ext}/\varepsilon_{int}$ <sup>†</sup> is larger than 2.5, then the internal error will be replaced by the external error.

The pre-averaging procedure is also applied to parallel data, i.e., the data connecting the two of the same nuclides. The masses of some light particles involved in reactions can be regarded as constants because they are measured with very high precision by other experiments. That is to say that some reaction data that gives the mass difference between two identical nuclides can also be averaged. For example, two equations  $^{48}\text{Ca}(p,g)^{49}\text{Sc}=9628.7 \pm 3.6$  keV [VCB68] and  $^{48}\text{Ca}(d,n)^{49}\text{Sc}=7404 \pm 4$  keV [GMDN68] give the same information for the mass difference between  $^{48}\text{Ca}$  and  $^{49}\text{Sc}$  because the masses of proton, neutron, and deuteron are well known (zero mass for rest photon). Then the above two equations can be rewritten as  $q_1 = 9628.7 - M(^1\text{H}) \pm 3.6$  and  $q_2 = 7404 - M(^2\text{H}) - M(n) \pm 7$ , where both  $q_1$  and  $q_2$  represent the mass difference  $M(^{48}\text{Ca}) - M(^{49}\text{Sc})$ . Inserting the light masses, one obtains  $q_1 = 2339.7 \pm 3.6$  and  $q_2 = 2340 \pm 7$ . The average of the two data gives  $\bar{q} = 2339.7 \pm 3.2$  keV with external error 0.05 keV, which shows excellent consistency of the two data. In AME2016, 2977 data were replaced by 1186 averages. As can be seen from Fig. 3.3, 23% of the data have  $\chi_n$  beyond unity, 1.6% beyond two and none beyond 2.5, meaning a satisfactory treatment for the pre-averaging data was achieved.

<sup>†</sup>. This ratio is called Birge Ratio and has exactly the same definition as the consistency factor described below as  $n = 1$  in Eq. 3.15


 Figure 3.3: Birge Ratio of all the *parallel* data

### 3.4 $\chi^2$ test and consistency factor

The prerequisite for the least-square method described above is that each input datum should have a distribution function with a mean (expected value) and a variance (square of the standard deviation of the mean) such that the value of  $\chi^2$ :

$$\chi^2 = (\mathbf{q} - \mathbf{K}\bar{\mathbf{m}})^t \mathbf{W} (\mathbf{q} - \mathbf{K}\bar{\mathbf{m}}) = \mathbf{v}^t \mathbf{W} \mathbf{v} = \sum_i W_i v_i^2, \quad (3.14)$$

is minimum. Here we introduce a residual  $v_i$  which is defined as the difference between the input value and the adjusted one. The expectation value and the variance of  $\chi^2$  are:

$$\overline{\chi^2} = N - n = f \quad \text{and} \quad V(\chi^2) = 2(N - n) = 2f, \quad (3.15)$$

where  $f$  is the number of degrees of freedom.  $\chi^2$  serves as an indicator for the consistency of the input data. One can also define a more intuitive quantity called consistency factor:

$$\chi_n = \sqrt{\frac{\chi^2}{f}}, \quad (3.16)$$

where its expectation value and one standard deviation are:

$$\bar{\chi}_n = 1 \quad \text{and} \quad \sigma(\bar{\chi}_n) = 1/\sqrt{2f}. \quad (3.17)$$

One may expect that  $\chi_n$  would be very close to unity if the errors are assigned properly for each input datum. It may, however, be rather large. One would not be bothered too much if  $\chi_n$  is implausibly smaller than one, which would be due to the fact that the assigned errors are too large and the experiments were turned out to be more reliable than what we had expected. On the other hand, if the consistency factor is much too large ( $\chi_n \gg 1$ ) then

we might suspect correctness of the input data, which would suffer from an undiscovered systematic error.

In 1961, the first AME adjustments [EKMW61] were performed for mass doublets and reaction data separately. The evaluation for the mass-doublet data taken from the Brookhaven and Minnesota laboratories yielded consistency factors of 3.58 ( $N = 13, n = 3$ ) and 2.35 ( $N = 39, n = 8$ ) for the former one, and 2.65 ( $N = 36, n = 12$ ) for the later. The evaluation of the reaction data yielded a consistency factor of 0.60 ( $N = 73, n = 19$ ). Based on the pre-adjusted results, all the reported errors for the mass doublets from these two groups were multiplied by the corresponding consistency factor before they were combined with other nuclear and decay measurements in the final adjustment.

In principle, if the consistent factor defined in Eq. 3.16 is significantly larger than one, then all errors used should be multiplied by  $\sqrt{\chi^2/(N-n)}$  in order to achieve overall consistency. This is the last thing we want to do since a large  $\chi^2$  value could arise from a few number of data or a special group. Correcting, or sometimes discarding, all the inconsistent data which deviates largely from the least-squares result and re-evaluating the input data without those anomalies could greatly improve the consistency of the whole system.

Another quantity that is also of interest is the PARTIAL CONSISTENCY FACTOR (PCF), which is defined for a group of  $p$  data:

$$\chi_n^p = \sqrt{\frac{N}{N-n} \frac{1}{p} \sum_{i=1}^p W_i v_i^2}. \quad (3.18)$$

One can consider two groups of data: the reaction- and decay-energy measurements on one side, and the mass-spectrometric ones on the other side. One can also consider the PARTIAL CONSISTENCY FACTOR for the data from a given laboratory using a certain device. The advantage of using PARTIAL CONSISTENCY FACTOR is that we do not need to separate the system into several sub-systems<sup>‡</sup> which should have no correlation with each other. The PARTIAL CONSISTENCY FACTOR has a value one for all the reaction and decay data since they have been studied so thoroughly and there is very little doubt about the correctness of the ground-state assignment: the distance between the ground state and the first excited state is usually so large that a faulty assignment would result in a glaring inconsistency. The determination of the ground-state masses from mass-spectrometric experiment could mix other isomeric states due to the limited resolving power. At present, AME applies PARTIAL CONSISTENCY FACTORS of 1.0, 1.5, 2.5, and 4.0 to the mass-

---

<sup>‡</sup>. It is not always practical, I would say for most of the time impossible, to obtain a sub-group of data from the whole data set, since it requires that the data are treated in a homogeneous way; moreover, the condition  $N > n$  can hardly be met unless one disregards some other data.

spectrometric data, depending on the agreement between the experimental results and the adjusted ones.

One should keep in mind that the PARTIAL CONSISTENCY FACTOR cannot be derived from any statistical theory. It only indicates the degree of consistency for a set of data among the full adjusted system. Of course the definition is such that  $\chi_n^p$  reduces to  $\chi_n$  if the sum is taken over all the input data.

### 3.5 Flow-of-information matrix

Up to now we can calculate the best values for all masses and obtain the adjusted input values using the least-squares method. Besides, we are also interested in finding out the information an equation brings to each mass. The flow-of-information matrix, discovered by G. Audi in 1986 [ADLW86], allows us to trace back the contribution of each input datum on each mass. The flow-of-information matrix is defined as:

$$\mathbf{F} = \mathbf{R}^t \otimes \mathbf{K}, \quad (3.19)$$

where the symbol  $\otimes$  means the term-by-term product operation of the corresponding elements in transpose matrix  $\mathbf{R}^t$  and that of  $\mathbf{K}$ . It is very practical to define  $\mathbf{F}$  this way, since, as proved in [ADLW86], each matrix element  $(i, \mu)$  represents the contribution brought by the input datum  $i$  in the determination of the mass  $m_\mu$ . The contribution here is called *influence*. The sum of all the *influences* in a row of  $\mathbf{F}$  is the *significance* of the corresponding datum, which signifies the overall contribution brought by this input datum to all the related masses. The *significance* of each input datum is less or equal to one and would decrease as more data comes into the system. The *significance* defined in this way is exactly the quantity which can be obtained by squaring the ratio of the adjusted uncertainty over the input one. The sum of a column of  $\mathbf{F}$  is the total *influences* brought by all the input data to a specific mass, which is always 100 %. The flow-of-information matrix has its name because it sheds light on how the information of a particular datum “flow” into each mass. It can also help plan future experiments in order to achieve maximum precision.

### 3.6 Local adjustment in the lightest mass region

The  $\beta$ -decay  $Q$ -value of  ${}^3\text{H}(\beta^-){}^3\text{He}$  is very important in the determination of the neutrino mass. The accurate measurement of the mass difference between  ${}^3\text{H}$  and  ${}^3\text{He}$  is essential for understanding the shape of the tritium  $\beta$ -decay spectrum and for investigating the systematic effects in the endpoint region [ABB<sup>+</sup>11]. However, we noticed that the evaluation outcome in this mass region is not satisfactory. In this section, a detailed example will be

given to illustrate how to use the least-squares method to carry out a local evaluation. Fig. 3.4 shows all the related nuclides  $^1\text{H}$ ,  $^2\text{H}$ ,  $^3\text{H}$ , and  $^3\text{He}$  under

Table 3.2: Related information for the local adjustment in the lightest mass region.

Refs	Penning trap	Equation	input $Q$ -value ( $\mu\text{u}$ )
[SBN <sup>+</sup> 08]	SMILETRAP	$2\cdot^1\text{H} - ^2\text{H}$	1548.28649(0.00035)
[VDZS01]	Seattle	$12\cdot^1\text{H} - ^{12}\text{C}$	93900.3865(0.0017)
[ZJ15]	Seattle	$6\cdot^2\text{H} - ^{12}\text{C}$	84610.66834(0.00024)
[ZJ15]	Seattle	$4\cdot^3\text{He} - ^{12}\text{C}$	64117.28668(0.00017)
[MWKW15]	FSU	$^3\text{He} - ^1\text{H} - ^2\text{H}$	-5897.48771(0.00014)
[MWKW15]	FSU	$^3\text{H} - ^3\text{He}$	19.95934(0.00007)

consideration, and they are connected by lines which represent the experimental data with corresponding references. Since the number of experimental data is larger than that of nuclides, the least-square method is applicable. Since the mass of  $^{12}\text{C}$  is defined as mass standard, it is not included in the mass adjustment. Though  $^3\text{H}$  is a secondary nuclide, we also include it in the least-square procedure for convenience. In [MWKW15], three frequency ratios, i.e.  $^3\text{H}/\text{HD}$ ,  $^3\text{He}/\text{HD}$ , and  $^3\text{H}/^3\text{He}$ , were given while only two of them were considered as independent. The less precise datum which connects  $^3\text{H}$  with  $^1\text{H}$  and  $^2\text{H}$  was not used in AME2016. We will see that the inclusion of this *secondary* datum has no effect on other masses. What's more, the evaluation is "local", which means that they are isolated from the rest of the chart. The mass of  $^2\text{H}$  is also determined by other experiments. Here, we concentrate only on the most relevant data for simple illustration.

All input data for the evaluation is listed in Table 3.2. The first column lists the publication references, followed by the corresponding Penning-trap spectrometer in the second column, the third column lists the equations entered in the adjustment and the fourth column is the related  $Q$ -value in  $\mu\text{u}$ . Once we have all the equations, we can build the coefficient matrix  $\mathbf{K}$ :

$$\mathbf{K} = \begin{matrix} & \begin{matrix} ^1\text{H} & ^2\text{H} & ^3\text{H} & ^3\text{He} \end{matrix} \\ \begin{bmatrix} 2 & -1 & 0 & 0 \\ 12 & 0 & 0 & 0 \\ 0 & 6 & 0 & 0 \\ 0 & 0 & 0 & 4 \\ -1 & -1 & 0 & 1 \\ 0 & 0 & 1 & -1 \end{bmatrix} & \end{matrix} \quad (3.20)$$

and its transposed matrix  $\mathbf{K}^t$  :

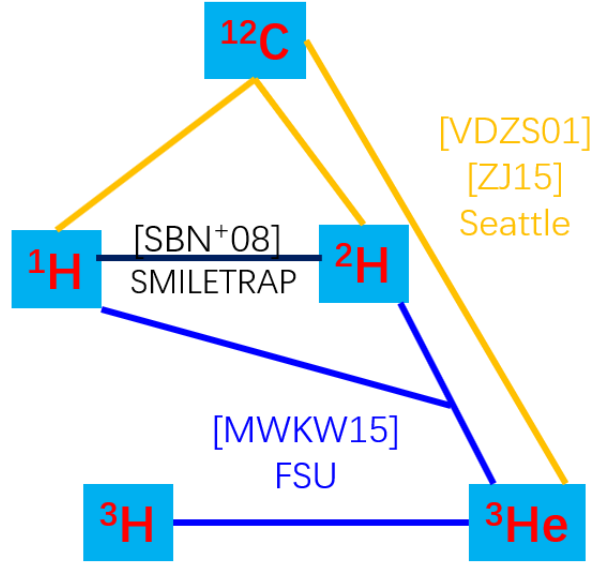


Figure 3.4: Connection plot of the lightest nuclides. Each line represents an experimental datum. The corresponding reference papers are also indicated.

$$\mathbf{K}^t = \begin{bmatrix} 2 & 12 & 0 & 0 & -1 & 0 \\ -1 & 0 & 6 & 0 & -1 & 0 \\ 0 & 0 & 0 & 0 & 0 & 1 \\ 0 & 0 & 0 & 4 & 1 & -1 \end{bmatrix} \quad (3.21)$$

The weight matrix  $\mathbf{W}$  can be constructed from Eq. 3.3 using the uncertainties listed in the third column in Table 3.2:

$$\mathbf{W} = \begin{bmatrix} 8163265.306 & 0 & 0 & 0 & 0 & 0 \\ 0 & 346020.7612 & 0 & 0 & 0 & 0 \\ 0 & 0 & 17361111.11 & 0 & 0 & 0 \\ 0 & 0 & 0 & 34602076.12 & 0 & 0 \\ 0 & 0 & 0 & 0 & 51020408.16 & 0 \\ 0 & 0 & 0 & 0 & 0 & 204081632.7 \end{bmatrix} \quad (3.22)$$

Hence, the normal matrix  $\mathbf{A}$  can be constructed:

$$\mathbf{A} = \mathbf{K}^t \mathbf{W} \mathbf{K} = \begin{bmatrix} 133500459 & 34693877.55 & 0 & -51020408.16 \\ 34693877.55 & 684183673.5 & 0 & -51020408.16 \\ 0 & 0 & 204081632.7 & -204081632.7 \\ -51020408.16 & -51020408.16 & -204081632.7 & 808735258.8 \end{bmatrix} \quad (3.23)$$

The inverted matrix  $\mathbf{A}^{-1}$  is:

$$\mathbf{A}^{-1} = \begin{bmatrix} 7.82246\text{E-}09 & -3.49643\text{E-}10 & 6.30553\text{E-}10 & 6.30553\text{E-}10 \\ -3.49643\text{E-}10 & 1.48648\text{E-}09 & 9.59257\text{E-}11 & 9.59257\text{E-}11 \\ 6.30553\text{E-}10 & 9.59257\text{E-}11 & 6.61514\text{E-}09 & 1.71514\text{E-}09 \\ 6.30553\text{E-}10 & 9.59257\text{E-}11 & 1.71514\text{E-}09 & 1.71514\text{E-}09 \end{bmatrix} \quad (3.24)$$

The response matrix  $\mathbf{R}$  is:

$$\mathbf{R} = \mathbf{A}^{-1}\mathbf{K}^t\mathbf{W} = \begin{bmatrix} 0.130567808 & 0.032480788 & -0.036421186 & 0.087273731 & -0.349094922 & 0 \\ -0.017842986 & -0.001451806 & 0.154841561 & 0.013276912 & -0.053107649 & 0 \\ 0.009511671 & 0.002618212 & 0.009992259 & 0.237389529 & 0.050441885 & 1 \\ 0.009511671 & 0.002618212 & 0.009992259 & 0.237389529 & 0.050441885 & 0 \end{bmatrix} \quad (3.25)$$

Combining with the vector  $\mathbf{q}$  which contains the experimental results:

$$\mathbf{q} = \begin{bmatrix} 1548.28649 \\ 93900.3865 \\ 84610.66834 \\ 64117.28668 \\ -5897.48771 \\ 19.95934 \end{bmatrix} \quad (3.26)$$

The evaluated values of all nuclides can be obtained:

$$\bar{\mathbf{m}} = \mathbf{R}\mathbf{q} = \begin{bmatrix} 7825.031916 \\ 14101.778007 \\ 16049.281056 \\ 16029.321716 \end{bmatrix} \quad (3.27)$$

and their uncertainty can be obtained from the root of the diagonal elements of  $\mathbf{A}^{-1}$ . Finally, the masses and uncertainties for each nuclide are :

$$\begin{aligned} M(^1\text{H}) &= 7825.031916 \pm 0.000088 \mu\text{u} \\ M(^2\text{H}) &= 14101.778007 \pm 0.000039 \mu\text{u} \\ M(^3\text{H}) &= 16049.281056 \pm 0.000081 \mu\text{u} \\ M(^3\text{He}) &= 16029.321716 \pm 0.000041 \mu\text{u} \end{aligned} \quad (3.28)$$

The flow-of-information matrix is:

$$\mathbf{F} = \mathbf{R}^t \otimes \mathbf{K} = \begin{bmatrix} 0.261135616 & 0.017842986 & 0 & 0 \\ 0.389769462 & 0 & 0 & 0 \\ 0 & 0.929049366 & 0 & 0 \\ 0 & 0 & 0 & 0.949558115 \\ 0.349094922 & 0.053107649 & 0 & 0.050441885 \\ 0 & 0 & 1 & 0 \end{bmatrix} \quad (3.29)$$

From the flow-of-information matrix in Eq. 3.29, we can acquire the information of the importance of each input in the evaluation. For example,

from the first row of  $\mathbf{F}$  we know that the *influences* of [SBN<sup>+</sup>08] are 26.11% and 1.78% in the determination of the masses of  $^1\text{H}$  and  $^2\text{H}$ , respectively, which result in the *significance* of 27.89%. From the last row of  $\mathbf{F}$ , we can see that the *influence* of [MWKW15] is 100% in the determination of the mass of  $^3\text{H}$  and 0% elsewhere, which guarantees that the *secondary* datum does not affect other PRIMARY nuclides.

Table 3.3 lists the results of the adjusted  $Q$ -values, and  $v/s$  indicates the difference between the input  $Q$ -value and adjusted  $Q$ -value divided by the uncertainty of the input  $Q$ -value. The largest deviation comes from the mass measurement of  $^3\text{He}/\text{HD}$  [MWKW15], which results in  $v/s$  of 3.6. The consistency factor  $\chi_n$  is 3.4 ( $N = 6, n = 4$ ) calculated from Eq. 3.16, which indicates that the measurement is subject to systematic errors which have not been found.

Table 3.3: Adjusted  $Q$ -values in the lightest mass region.  $v/s$  indicate the difference between the input  $Q$ -value and the adjusted  $Q$ -value divided by the uncertainty of the input  $Q$ -value.

Refs	Equation	input $Q$ -value ( $\mu\text{u}$ )	adjusted $Q$ -value ( $\mu\text{u}$ )	$v/s$
[SBN <sup>+</sup> 08]	$2\cdot^1\text{H} - ^2\text{H}$	1548.28649(0.00035)	1548.28583(0.00019)	1.9
[VDZS01]	$12\cdot^1\text{H} - ^{12}\text{C}$	93900.3865(0.0017)	93900.38300(0.00106)	2.1
[ZJ15]	$6\cdot^2\text{H} - ^{12}\text{C}$	84610.66834(0.00024)	84610.66804(0.00023)	1.2
[ZJ15]	$4\cdot^3\text{He} - ^{12}\text{C}$	64117.28668(0.00017)	64117.28686(0.00017)	-1.1
[MWKW15]	$^3\text{He} - ^1\text{H} - ^2\text{H}$	-5897.48771(0.00014)	-5897.48821(0.00009)	3.6
[MWKW15]	$^3\text{H} - ^3\text{He}$	19.95934(0.00007)	19.95934(0.00007)	0

If one uses the most recent result of the proton mass from [HKLR<sup>+</sup>17], which is over four times more precise than that of [VDZS01], the consistency factor will decrease to 3.0. However, the inconsistency still remains. In AME2016, the results from [ZJ15] were not used, since the mass difference between the ions of interest and reference ions (carbon) are relatively large. This case has been discussed in detail in section 7.1 in AME2016 [HAW<sup>+</sup>17]).

Recently, the authors in [MWKW15] remeasured the frequency ratio of  $^3\text{He}$  to  $\text{HD}^+$ , which yields the mass difference of  $-5897.48780(0.00007)$   $\mu\text{u}$  [HSFM17]. The new result is in good agreement with their previous result and thus validates our choice in AME2016.

### 3.7 Removal of certain input data

AME deals with all kinds of input data that are related to atomic masses. We apply a special label to each of them to signify its role in the mass evaluation. All cases discussed here are not used.

Some experiments would present the same input item with different precision. If one is three times less precise than the other, or if its value can be

deduced by the combination of other data, it is marked with label “U” (for unweighted).

In some cases, discrepancies exist between two experiments which give the same information, or a single input datum has a strong conflict with the previous adjustment compared with its reported precision. By looking into the original paper, one may find a reason to doubt their reported value and such data would be marked with “F”.

Sometimes, interesting results appear in the abstract of conference proceedings or annual reports but no more information could be obtained. Such results would be marked with “C” if they were not compatible with other experimental results.

The most worrisome cases would be those whose results have been published in regular journals in which no fault could be found. Including these results would cause a large contribution to  $\chi^2$ , which could give some impression that the evaluation is wrong. In this case, they would be marked with “B”.

An old result would be replaced by a new one from the same laboratory with higher precision. In this case, only the latest result would be adopted and the old one would be marked with “O”.

Including some experimental data could violate the continuity of the *mass surface* (see Chapter 6). Our policy is to replace them by the estimates from the trends of the *mass surface* if the deviation is larger than 200 keV. Such replaced data would be marked with “D”.

Some nuclides involved in the reaction or decay measurements could be also measured directly by mass spectrometry. Using both data would make these nuclides *primary*. We can, without loss of any information, replace one of them by an equivalent expressed like the other one. The two results will be then pre-averaged inside the adjustment program. We avoid using all these data since they would only effect in a local region. We would cut one of the original links and replace it with another input item with the same precision. Such replaced data would be marked with “R”.

In this chapter, the philosophy of AME in treating experimental data is described. The most important feature of AME is to consider the masses as parameters in the least-squares method. Since the masses enter linearly in each input equation, the parameters (masses) can be solved without approximation. Up to now, ten atomic-mass tables have been published based on this method: AME1955 [Wap54a, Wap54b, Hui54], AME1961 [EKMW60a, EKMW60b], AME1964 [MTW65], AME1971 [WG71], AME1977 [WKB77], AME1983 [WA85], AME1993 [AW93], AME2003 [AWT03], AME2012 [WAW<sup>+</sup>12], and AME2016 [WAK<sup>+</sup>17].

Next, the developments for the latest AME adjustment AME2016 will be illustrated.



# Chapter 4

## Developments for AME2016

### 4.1 Calculation of molecular binding energies for the most precise mass measurements

The most precise mass-spectrometric measurements use Penning-trap mass spectrometry (see Chapter 7). One can measure not only the mass of a single atomic ion, but also the mass of a molecular ion in experiments [DNB<sup>+</sup>95]. For most molecules, the binding energy represents typically a correction of a few parts in  $10^{10}$ , and its uncertainty only limits the accuracy of the neutral atomic mass to a few parts in  $10^{12}$  [RTP04]. For measurements with precision not better than  $10^{-9}$  (100 eV/100 u), the molecular binding energy could be neglected without losing too much accuracy. For precisions exceeding  $10^{-10}$  (10 eV/100 u), which are routinely attained at MIT [DNBP94] and FSU [MWKW15], the importance of the molecular binding energy should be taken into account so as to obtain accurate atomic masses.

#### Reducing frequencies to linear equations

The measured quantity in a Penning trap is a frequency ratio. As mentioned in Chapter 3, the input data should be linear in mass so that the least-squares method can treat such an input item without approximation. Ptrap (see Appendix C.1 in [AWW<sup>+</sup>12]) is a program of deriving the mass difference from Penning-trap mass measurements carried out with atoms. The relation between the ion of interest and the reference ion can be expressed as [AWW<sup>+</sup>12]:

$$\frac{\mathcal{M} - m_e q + B}{\mathcal{M}_r - m_e q_r + B_r} \frac{q_r}{q} = R, \quad (4.1)$$

where  $R$  is the frequency ratio between the ion of interest and the reference ion (in the following, quantities with subscript  $r$  represent the reference ion and without subscript represents the ion of interest),  $\mathcal{M}$  is the total atomic

mass (in atomic mass unit “u”),  $q$  is the number of electrons removed from the atom,  $m_e$  is the electron mass, and  $B$  is the ionization energy of the atom.

If molecules are involved in experiments, the molecular binding energy  $D$  should be included in the calculation. In this case, Eq. 4.1 should be rewritten:

$$\frac{\mathcal{M} - D - m_e q + B}{\mathcal{M}_r - D_r - m_e q_r + B_r} \frac{q_r}{q} = R. \quad (4.2)$$

The total atomic mass  $\mathcal{M}$  can be expressed as  $\mathcal{M} = M + A$ , where  $M$  is the mass excess and  $A$  is the mass number. Eq. 4.2 thus becomes:

$$\begin{aligned} A + M - D - m_e q + B &= R \frac{q}{q_r} (A_r + M_r - D_r - m_e q_r + B_r) \\ M - R \frac{q}{q_r} M_r &= m_e q (1 - R) + A_r \left( \frac{q}{q_r} R - \frac{A}{A_r} \right) + R \frac{q}{q_r} (B_r - D_r) - (B - D), \end{aligned} \quad (4.3)$$

which comprises all necessary components to calculate the mass  $M$ .

Since the experimental data should be entered as linear equations in mass, we define a constant  $C$  as a three-digit decimal approximation of  $A$  over  $A_r$  and want to find a quantity  $y$  such that:

$$y = M - C M_r. \quad (4.4)$$

The advantage of constructing such a quantity is that, once the precision of the reference mass  $M_r$  is improved, the mass  $M$  can be recalculated automatically. Combining Eq. 4.3 and Eq. 4.4, one finds the quantity  $y$  has the form:

$$\begin{aligned} y &= M_r \left( R \frac{q}{q_r} - C \right) + m_e q (1 - R) + A_r \left( \frac{q}{q_r} R - \frac{A}{A_r} \right) + R \frac{q}{q_r} (B_r - D_r) - (B - D) \\ &= \quad y_1 \quad + \quad y_2 \quad + \quad y_3 \quad + \quad y_4. \end{aligned} \quad (4.5)$$

$M_r$  is generally smaller than 0.1 u,  $m_e$  is of the order of 500  $\mu$ u,  $(R \frac{q}{q_r} - C)$  and  $(1 - R)$  are a few  $10^{-4}$ ,  $A_r = 100$  u for mass number 100,  $R - \frac{A}{A_r}$  varies from  $10^{-6}$  to  $10^{-4}$ ,  $B_r - D_r$  has order of tens of nu (see below). In this case, Eq. 4.4 can be entered directly into the AME least-squares adjustment.

The uncertainty on  $y$  can be expressed from the variation  $dy$ :

$$dy = dy_1 + dy_2 + dy_3 + dy_4, \quad (4.6)$$

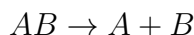
where

$$\begin{aligned}
dy_1 &= \frac{q}{q_r} M_r dR + \left(R \frac{q}{q_r} - C\right) dM_r \approx dR * 10^5 \mu\text{u} \\
dy_2 &= -m_e q dR \approx -dR * 5 * 10^2 \mu\text{u} \\
dy_3 &= A_r \frac{q}{q_r} dR \approx dR * 10^8 \mu\text{u} \\
dy_4 &= \frac{q}{q_r} (B_r - D_r) dR \approx dR * 10^{-2} \mu\text{u}.
\end{aligned} \tag{4.7}$$

$dy_1$ ,  $dy_2$  and  $dy_4$  are always negligible compared to the third term. Only the 3rd term  $dy_3$  contributes to the final uncertainty. Although the quantity  $y$  depends on the reference mass, as can be seen from  $y_1$  in Eq. 4.5, the multiplication of  $M_r$  by the factor  $(R \frac{q}{q_r} - c)$ , which has an magnitude of  $10^{-4}$ , practically removes any dependence of the measured mass on the reference mass.

## Bond Dissociation Energy

The bond dissociation energy (**BDE**) is a quantity which signifies the strength of a chemical bond and has its synonym of molecular binding energy ( $D$ ). The bond dissociation energy  $D^\circ$  for a bond A-B which is broken through a reaction:



is defined as the standard enthalpy change at a specified temperature [Dar70]:

$$D^\circ(AB) = \Delta H f_0^\circ(A) + \Delta H f_0^\circ(B) - \Delta H f_0^\circ(AB), \tag{4.8}$$

where  $\Delta H f_0^\circ$  is the standard heat of formation and its value for atoms and compounds is available on the NIST Chemistry Webbook [LM16a]. The superscript in  $D^\circ$  refer to the gaseous state at 0 K temperature.

Unlike diatomic molecules which involve only one bond, polyatomic molecules have several bonds and their **BDEs** are the sum of all the single bonds. For example, if one wants to know the **BDE** of  $\text{CH}_4$ , one needs to calculate the **BDE** of  $\text{CH}_3\text{-H}$ ,  $\text{CH}_2\text{-H}$ ,  $\text{CH-H}$  and  $\text{C-H}$ :

$$\begin{aligned}
D^\circ(\text{CH}_3 - \text{H}) &= \Delta H f_0^\circ(\text{CH}_3) + \Delta H f_0^\circ(\text{H}) - \Delta H f_0^\circ(\text{CH}_4) \\
D^\circ(\text{CH}_2 - \text{H}) &= \Delta H f_0^\circ(\text{CH}_2) + \Delta H f_0^\circ(\text{H}) - \Delta H f_0^\circ(\text{CH}_3) \\
D^\circ(\text{CH} - \text{H}) &= \Delta H f_0^\circ(\text{CH}) + \Delta H f_0^\circ(\text{H}) - \Delta H f_0^\circ(\text{CH}_2) \\
D^\circ(\text{C} - \text{H}) &= \Delta H f_0^\circ(\text{C}) + \Delta H f_0^\circ(\text{H}) - \Delta H f_0^\circ(\text{CH})
\end{aligned} \tag{4.9}$$

Summing over all four bonds above, we can obtain the **BDE** for  $\text{CH}_4$ :

$$\begin{aligned}
D^\circ(\text{CH}_4) &= D(\text{CH}_3 - \text{H}) + D(\text{CH}_2 - \text{H}) + D(\text{CH} - \text{H}) + D(\text{C} - \text{H}) \\
&= \Delta H f_0^\circ(\text{C}) + 4 \cdot \Delta H f_0^\circ(\text{H}) - \Delta H f_0^\circ(\text{CH}_4)
\end{aligned}$$

For a polyatomic molecule which has the form  $A_n B_k C_i$ , its **BDE** can be generalized:

$$D^o(A_n B_k C_i) = n \cdot \Delta H f_0^o(A) + k \cdot \Delta H f_0^o(B) + i \cdot \Delta H f_0^o(C) - \Delta H f_0^o(A_n B_k C_i) \quad (4.10)$$

Below two examples of the calculations of molecular binding energies will be given.

### Atomic Masses of Tritium and Helium-3

By measuring the cyclotron frequency ratios of  ${}^3\text{He}^+$  and  $\text{T}^+$  to  $\text{HD}^+$ , using  $\text{HD}^+$  as a mass reference, atomic masses for  ${}^3\text{He}$  and  $\text{T}$  were obtained [MWKW15]. The essential part here is to calculate the molecular binding energy  $D^o(\text{HD})$ . Applying Eq. 4.8, the molecular binding energy of  $\text{HD}$  can be obtained:

$$\begin{aligned} D^o(\text{HD}) &= \Delta H f_0^o(\text{H}) + \Delta H f_0^o(\text{D}) - \Delta H f_0^o(\text{HD}) \\ &= 218 + 221.72 - 0.32 \text{ kJ/mol} \\ &= 439.4 \text{ kJ/mol} \end{aligned} \quad (4.11)$$

or alternately,  $D^o(\text{HD}) = 4.55 \text{ eV}$  (using conversion factor  $1 \text{ eV} = 96.485 \text{ kJ/mol}$ ). Combining the ionization energies  $B(\text{HD})=15.44 \text{ eV}$ ,  $B({}^3\text{He})=24.59 \text{ eV}$  and  $B(\text{T})=13.60 \text{ eV}$  from [KRR16] and atomic masses of  $\text{H}$  and  $\text{D}$  from AME12, the mass differences and their uncertainties can be obtained in Table 4.1.

Table 4.1: Frequency ratios and mass differences.

Ion pair	Frequency ratio	Mass difference	Value ( $\mu\text{u}$ )
$\text{HD}^+ / {}^3\text{He}^+$	0.998048085153(48)	${}^3\text{He} - \text{H} - \text{D}$	-5897.48771(14)
$\text{HD}^+ / \text{T}^+$	0.998054687288(48)	$\text{T} - \text{H} - \text{D}$	-5877.52837(14)

The correction of the molecular binding energy  $D^o(\text{HD}) = 4.55 \text{ eV}$  is 30 times larger than the uncertainty of the mass differences, which is  $0.14 \text{ nu} \approx 0.14 \text{ eV}$  (Table 4.1).

### ${}^{13}\text{C}_2\text{H}_2^+$ and ${}^{14}\text{N}_2^+$ mass doublet

In the work of [RTP04] at MIT, a cyclotron frequency ratio  $R = 0.999421460888(7)$  of relative precision of  $7 \times 10^{-12}$  has been obtained for molecular ions  ${}^{13}\text{C}_2\text{H}_2^+$  and  ${}^{14}\text{N}_2^+$ . We first calculate  $D^o(\text{C}_2\text{H}_2)$  by applying Eq. 4.10:

$$\begin{aligned}D^{\circ}(C_2H_2) &= 2 \cdot \Delta H f_0^{\circ}(C) + 2 \cdot \Delta H f_0^{\circ}(H) - \Delta H f_0^{\circ}(C_2H_2) \\ &= 2 \cdot 716.7 + 2 \cdot 218.0 - 227.4 \\ &= 1642.0 \text{ kJ/mol} \\ &= 17.0 \text{ eV}\end{aligned}$$

$D^{\circ}(N_2) = 944.9 \text{ kJ/mol} = 9.793 \text{ eV}$  is imported from Ref [LK12], since the value  $\Delta H f_0^{\circ}(N_2)$  is not on the list of [LM16a]. Combining the ionization energy  $B(C_2H_2) = 11.4 \text{ eV}$  and  $B(N_2) = 15.6 \text{ eV}$ , we obtain the mass difference:

$$13C - H - 14N = 8105.86300(10) \mu u.$$

In the original paper [RTP04], this equation is given as:

$$13C - H - 14N = 8105.86288(10) \mu u,$$

which differs by 0.12(10) nu from the new calculation, because an updated tabulation of molecular binding energies [LM16a, LK12] is used.

From the two examples discussed here, we notice that the consideration of molecular binding energies is essential to obtain correct input values for precise mass-spectrometric data. Even using the updated stand heat of formation will change the original result significantly. In AME2016, all precise mass-spectrometric data has been recalculated, based on the latest standard heat of formation [LM16a].

## 4.2 Experimental $\alpha$ -decay and proton-decay energies

According to AME2016, more than 65% of the input data in the mass range  $A > 200$  results from  $\alpha$ -decay experiments. In lighter mass regions there are also a large number of proton-decay data, which shares many similarities with  $\alpha$ -decay data. Energies from  $\alpha$  and proton decay yield information of capital importance for deriving mass values of superheavy and exotic nuclides. But when we refer to  $\alpha$ -decay or proton-decay experiments, we often find some confusion: energy values referred to by one author as the particle kinetic energy  $E$  could sometimes be referred to as the decay energy  $Q$  by another.

The decay energy is the sum of kinetic energies of the emitted particle and the recoiling daughter nuclide. Typically, in an  $\alpha$ -decay measurement, the  $\alpha$  particle carries about 97-98% of its  $Q$  value and the recoiling nuclide carries the rest. In the literature one can find too many cases of confusion, especially in the case of proton-decay experiments where  $Q_p$  and  $E_p$  are numerically closer to each other. Sometimes, the confusion could be solved through a meticulous

inspection of the paper and a discussion with the authors. However, it remains unclear in a few other cases.

There are four major experimental approaches for  $\alpha$ -decay measurements: The first one uses a magnetic spectrograph [GR71], from which the  $\alpha$  kinetic energies are determined by direct measurements of the orbit diameters and the magnetic induction field. All  $\alpha$ -energy standards have been measured using this method. The second one uses the scintillating bolometer technique, which detects the total  $\alpha$ -decay energy at temperatures below 100 mK [DMCD<sup>+</sup>03]. In third method the nuclide of interest is implanted into a foil and the  $\alpha$  particle is detected by the surrounding Si detectors [AEH<sup>+</sup>10]. Last but not least, the radioactive species, which are produced in a nuclear reaction, are directly implanted into a Si detector (a double-sided silicon-strip detector (DSSD) or a resistive-strip detector [Kno12]). The first three methods measure either the pure  $\alpha$ -particle energy or the total  $\alpha$ -decay energy, while the last implantation method detects the  $\alpha$  (or a proton in proton decay) particle and the heavy recoil daughter nuclide in coincidence. This method has been widely used in recent years and will be discussed in detail.

In order to perform accurate decay experiments, detectors should be calibrated carefully. If the calibration is not applied correctly, then an erroneous published value could follow, sometimes with a deviation not negligible compared to the claimed precision.

## Particle energy vs. Decay energy

Magnetic spectrographs have been used for absolute  $\alpha$ -particle energy measurement [GR71, RWK86]. Since it is the measurement of a single  $\alpha$ -particle movement in spectrometer, one obtains  $\alpha$ -particle energy  $E_\alpha$ . For the radioactive source measurement, where the emitted particle has been detected in the Si detector while the recoiling nuclide remained in the sample, one obtains also purely the  $\alpha$ -particle energy (except for a small correction due to dead-layer absorption). These two types of experiments clearly establish a particle energy  $E_\alpha$  from which decay energy  $Q_\alpha$  can be kinematically derived from classical mechanics:

$$Q_\alpha = \frac{M}{M - M_{\text{He-4}}} E_\alpha, \quad (4.12)$$

where  $M$  and  $M_{\text{He-4}}$  are the atomic masses of the parent and of the helium-4 atoms, respectively (see Eq. 4.21 for cases requiring relativistic calculation). In order to obtain the proton-decay energy  $Q_p$  from proton-energy  $E_p$ , one should replace  $E_\alpha$  and  $M_{\text{He-4}}$  by  $E_p$  and  $M_{\text{H}}$  (hydrogen mass), respectively.

Cases would be less straightforward for measurements performed by implantation methods, where not only the emitted particle but also a partial energy of the recoil are measured at the same time.

## Energy calibration

The position-sensitive silicon strip detector (DSSD) is one of the most widely used detectors in decay-spectroscopy experiments not only for its high energy resolution, but also for its ability to record the position of implantation of the particle which is necessary to identify decay chains (thus the sensitivity can be enhanced significantly by reducing the background).

Suppose a simple case where there are three equidistant lines in an  $\alpha$ -decay spectrum in Fig. 4.1. Two well-known  $\alpha$ -energy activities line-1 (with  $E(\alpha_1) = 5000$  keV) and line-2 (with  $E(\alpha_2) = 5200$  keV) are used as calibrants and line-3 is assigned to the unknown nuclide. If the detector does not detect the recoiling nuclide in experiments as in Fig. 4.1 (a), then what is measured would be the  $\alpha$ -particle energy and  $E(\alpha_3) = 5400$  keV is easily obtained. In the the opposite case where the detector measures all the energy of the recoiling ion, then the energy scale will change to Fig. 4.1 (b). If line-1 and line-2 correspond to nuclides with mass number  $A = 150$ , the new scales will change to  $Q_\alpha(\text{line-1}) = 5137$  keV and  $Q_\alpha(\text{line-2}) = 5342$  keV based on Eq. 4.12. In this case we measure the  $\alpha$ -decay energy  $Q_\alpha$  and obtain  $Q_\alpha(\text{line-3}) = 5547$  keV.



Figure 4.1: Illustration of  $\alpha$ -decay spectra where line-1 and line-2 are calibrants and line-3 is unknown at an equal distance from line-2. (a) Case for which the detector detects only the  $\alpha$ -particle energy. (b) Case where the detector detects also the recoiling nuclide.

If line-3 corresponds to a nuclide with mass number  $A = 150$ , its energy  $E_\alpha$  is deduced to be 5399 keV according to the transformation of Eq. 4.12, which is 1 keV smaller than the value obtained from Fig. 4.1 (a). However, if line-3 corresponds to a nuclide with a different mass number, for example,  $A = 200$ ,  $E_\alpha$  will increase from 5400 keV to 5436 keV, which is off by 36 keV. The deviation would become bigger for super-heavy nuclide  $\alpha$ -decay measurements in case the mass of calibrants is much smaller than that of  $\alpha$ -decaying daughter.

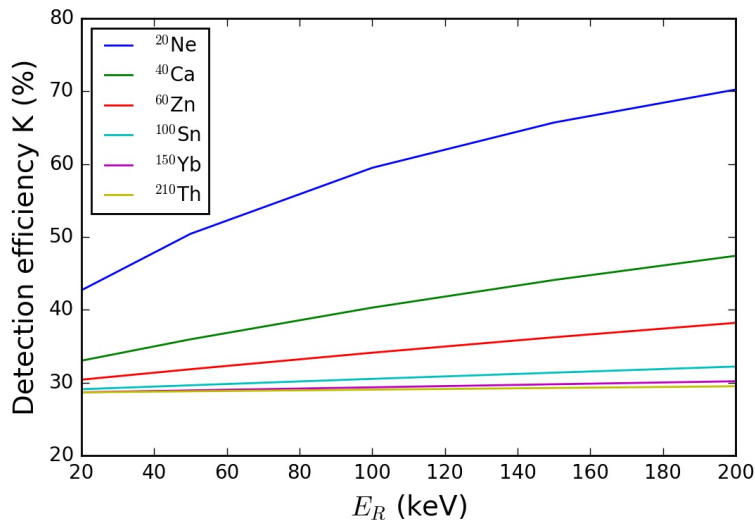


Figure 4.2: Detection efficiency  $K$  for different species at different recoiling energy  $E_R$  in Si-detector. The range of  $E_R$  selected here covers most of the decay experiment cases.

In real case, the detector is not 100% sensitive to the recoiling nuclide. In the next section, I will show how to take into account the efficiency of the detector.

### Detection efficiency for the heavy recoil

The recoiling ions lose their energies in the Si detector in two ways: excitation and ionization of the electrons of the atoms (electronic process), or collision with nuclei of the atoms (nuclear process). The electronic process produces a signal in the detector, while the nuclear process does not. Knowledge of both processes is important for implantation  $\alpha$ -decay and proton-decay experiments where the heavy recoil is detected simultaneously with the light particle. In 1963, Lindhard *et al.* [LNST63] derived a theory to describe these processes, from which the detection efficiency  $K$  was defined as:

$$K = \frac{\bar{\eta}_R}{E_R} = \frac{kg(\epsilon)}{1 + kg(\epsilon)}, \quad (4.13)$$

where  $\bar{\eta}_R$  is the part of the recoiling energy that is effectively detected in the detector,  $E_R$  is the total recoiling energy,  $\epsilon$  is called the “dimensionless reduced energy” which is related to  $E_R$ ,  $k$  is a coefficient related to the mass number and the atomic number of the recoil nuclide and the target nuclide,  $g(\epsilon)$  is a semi-empirical function (for more details refer to [LNST63]). This theory was derived to predict the detected energy of heavy atomic projectiles in matter and agrees well with experimental data [Rat75, HMV<sup>+</sup>82].

Fig. 4.2 shows the calculations of the detection efficiency  $K$  for different

nuclides [HA17] based on Lindhard's theory. For light nuclides (e.g.  $^{20}\text{Ne}$  and  $^{40}\text{Ca}$ ), the detection efficiencies increase rapidly as their energies increase. For intermediate mass (e.g.  $^{60}\text{Zn}$  and  $^{100}\text{Sn}$ ) and heavy nuclides (e.g.  $^{150}\text{Yb}$  and  $^{210}\text{Th}$ ), the detection efficiencies increase much more slowly than those of the light nuclides. For  $\alpha$  particles and protons with energies larger than 1 MeV, both detection efficiencies can be considered to be 100%. For the implantation method where both the energies of the emitted particles and a part of the heavy recoil are detected, one needs to consider properly the energy loss of the heavy recoil in the detector. Some experimentalists have already noticed this effect and made the correction for their results [BJP<sup>+</sup>91, BAB<sup>+</sup>96, HHM<sup>+</sup>12]. However, the partial deposited energy of the heavy recoil is not always considered by others.

In the following, a concept about how to treat the calibration line and make a correction to the published experimental results will be illustrated, in case the partial recoiling effect was not taken into account.

Here we take  $\alpha$  decay as an example. If we consider the recoiling energy, the new scale should be adjusted to:

$$E_d = E_\alpha + E_R \times K, \quad (4.14)$$

where  $E_d$  is the total detected energy,  $E_\alpha$  is the kinetic energy of the  $\alpha$  particle,  $E_R$  is the recoiling energy and  $K$  is the detection efficiency for the recoil nuclide at energy  $E_R$ . It is  $E_d$  that should be used in the energy calibration rather than  $E_\alpha$ . The recoiling energy can be expressed as:

$$E_R = \frac{4}{M-4} E_\alpha, \quad (4.15)$$

where  $M$  is the mass number of the mother nuclide. Combining Eq. 4.14 and Eq. 4.15, the pure  $\alpha$ -particle energy can be obtained:

$$E_\alpha = \frac{E_d}{1 + \frac{4K}{M-4}} \quad (4.16)$$

For proton-decay experiments where  $Q_p$  is often used in the calibration (as one considers erroneously that the energies of the proton and of the heavy recoil nuclide are fully detected at the same time), one can obtain a similar relation as Eq. 4.14:

$$E_d = E_p + E_R \times K \quad (4.17)$$

where  $E_p$  is the proton energy and has the expression:

$$E_p = \frac{M-1}{M} Q_p \quad (4.18)$$

with recoiling energy in proton decay:

$$E_R = \frac{1}{M} Q_p. \quad (4.19)$$

Combining Eq. 4.17, 4.18 and 4.19, one can obtain:

$$Q_p = \frac{M}{M - 1 + K} E_d \quad (4.20)$$

## Applications

Here I will illustrate how to make corrections for the decay data, when the partial recoiling energy was not considered in experiments.

### The case of $^{255}\text{Lr}^m(\alpha)$

In [HLMY<sup>+</sup>08], the detector was calibrated using a well-known  $\alpha$ -particle energy of 7923(4) keV in  $^{216}\text{Th}$  [LM16b]. The recoiling energy of the daughter nuclide  $^{212}\text{Ra}$  is calculated as  $7923 \times 4/212 \approx 150$  keV and at this energy the detection efficiency  $K$  is 29.12%. The calibration line of  $^{216}\text{Th}$  should be adjusted to  $E_d(^{216}\text{Th}) = 7923 + 150 \times 0.2912 = 7967$  keV. In the  $\alpha$ -decay spectrum, the  $\alpha$ -particle energy of  $^{255}\text{Lr}^m$  is 8371 keV, from which the detected energy of  $^{255}\text{Lr}^m$  can be deduced as  $E_d(^{255}\text{Lr}) = 7967 \times 8371/7923 = 8417$  keV. The recoiling energy of the  $\alpha$ -decay daughter nuclide  $^{251}\text{Md}$  can be calculated approximately as  $8417 * 4/255 \approx 131$  keV and at this energy, its detection efficiency is 29.08%. According to Eq. 4.16, the pure  $\alpha$ -particle energy of  $^{255}\text{Lr}^m$  is calculated to be 8378 keV. The difference between the published value and the corrected value is 7(10) keV. The same routine can be applied to the  $\alpha$ -decay energy of the  $^{255}\text{Lr}$  ground state.

### The case of $^{69}\text{Kr}(\beta^+ \text{p})$

In [SMB<sup>+</sup>14], the  $\beta$ -delayed proton-decay ( $\beta^+ \text{p}$ ) energy of  $^{69}\text{Kr}$  was determined to be 2939(22) keV using known  $\beta$ -delayed proton decay energies of 806, 1679, and 2692 keV for  $^{20}\text{Mg}$  and 1320, 2400, 2830, 3020, and 3650 keV for  $^{23}\text{Si}$ . The authors assumed (erroneously) that the recoil energy would be fully recorded at the same time [Mei15]. As one can see from Fig. 4.2 the detection efficiency for the intermediate nuclide, e.g.  $^{60}\text{Zn}$ , is between 30%~40% and its neighbouring nuclides show similar behaviour. The recoiling energy of the  $\beta$ -delayed proton-decay  $^{23}\text{Si}$  at 3020 keV is  $3020/23 \approx 131$  keV and the detection efficiency for the decay daughter nuclide  $^{22}\text{Mg}$  is 59.75%. The effectively detected energy of this calibration line is 2967 keV according to Eq. 4.17. The detected energy of  $\beta$ -delayed proton-decay nuclide  $^{69}\text{Kr}$  is deduced to be  $2967 \times 2939/3020 \approx 2887$  keV. The detection efficiency of the daughter nuclide  $^{68}\text{Se}$  is 30.79% at the corresponding recoiling energy. Applying Eq. 4.20,

the  $\beta$ -delayed proton decay energy of  $^{69}\text{Kr}$  is calculated to be 2916 keV. The difference between the corrected value and the published one is 23(22) keV, which exceeds  $1\sigma$ .

### The case of $^{53}\text{Co}^m(\text{p})$

In [SLS<sup>+</sup>15], the DSSD was calibrated using  $^{41}\text{Ti}$   $\beta$ -delayed proton energies  $E_p$  of 986(2), 1542(2), 3083(4), and 4735(3) keV from [CS01]. For the proton energy of  $E_p = 1542$  keV from  $^{41}\text{Sc}$ , the energy of the recoiling nuclide is  $1542/38 = 39$  keV and the detection efficiency at this energy is 34.87%. The effectively detected energy is therefore  $1542 + 39 \times 0.3487 = 1555.5$  keV. In the publication the proton-decay energy  $Q_p = 1558(8)$  keV of  $^{53}\text{Co}^m$  was obtained from an observed line lying 23 keV lower than the  $^{41}\text{Sc}(\text{p})$   $E_p = 1542$  keV line (supposed then to have deposited a total energy of  $Q_p = 1581$  keV). The deposited energy for the proton-decay of  $^{53}\text{Co}^m$  is  $E_d = 1558/1581 \times 1555.5 = 1532.9$  keV. The recoiling energy of  $^{52}\text{Fe}$  is approximately  $1558/52 = 30$  keV and the detection efficiency  $K$  at this energy is 31.76%. Thus, the proton-energy of  $^{53}\text{Co}^m$  was effectively  $E_p = 1532.9/(1 + 0.318/32) = 1523.7$  keV and  $Q_p = 1553.0$  keV, with uncertainty of 8 keV. We (M. Wang, G. Audi, and W. Huang) discussed this case with Shen *et al.* [SLS<sup>+</sup>15], and they agreed with us on the general idea of the detection efficiency. They have re-calibrated the detectors with the detection efficiencies and obtained the new value  $Q_p$  of  $^{53}\text{Co}^m$ , which is 1553.3 keV. Their result is in agreement with our corrected value, thus confirming the validity of our treatment.

From the three examples discussed above, we demonstrated that the recoiling effect should not be ignored. In [HHM<sup>+</sup>12], the detection efficiency  $K$  was assumed to be 28% and was applied to all the calibration lines and the nuclide of interest. It is reasonable to use  $K = 28\%$  universally in this case as one can see from Fig. 4.2 that  $K$  becomes almost constant for heavy nuclides. For light nuclides, where  $K$  differs quite a lot (59.75% for  $^{22}\text{Mg}$  and 30.79% for  $^{68}\text{Se}$ ), one should treat them differently.

The correction method for the recoiling energy has been published in [HA17].

## 4.3 High precision $\alpha$ -decay energies

From the direct  $\alpha$ -particle energy  $E_\alpha$  measurement, one could obtain the  $Q_\alpha$  value via Eq. 4.12. One should however recall that Eq. 4.12 was derived from non-relativistic conditions and without consideration of atomic effects. Eq. 4.12 is valid only in  $\alpha$ -spectroscopy measurements where a moderately accurate energy scale is needed.

The highest precision of  $\alpha$ -decay energies comes from magnetic spectrograph [GR71, RWK86, RW84] and they have been used for several reasons [RGG72]: a) they provide calibration points for all  $\alpha$  spectra observed with high resolving power; b) precise  $Q$ -value determinations of nuclear reactions are often based on  $\alpha$ -energy standards; c) atomic mass difference may be calculated accurately based on  $\alpha$  energies.

In  $\alpha$  decay, where the final atom is left in such a state but the emerging  $\alpha$  particle is a bare nucleus, the relation between the  $\alpha$ -particle energy  $E_\alpha$  and its  $\alpha$ -decay energy  $Q_\alpha$ , taking relativistic and atomic effects into account, can be written as:

$$Q_\alpha = (M - m_\alpha) \pm \sqrt{(M - m_\alpha)^2 - 2 \cdot M \cdot E_\alpha + B_{\text{He}}}, \quad (4.21)$$

where  $M$  is the mass of the decaying parent nuclide,  $m_\alpha$  is the mass of  $\alpha$  particle and  $B_{\text{He}}$  is the two-electron binding energy in helium which is 79 eV. The derivation of Eq. 4.21 can be found in Appendix A.

When the decay takes place between the ground state of the parent and excited state of the daughter nuclide, the decay- $Q$  value should be revised to:

$$Q_\alpha = Q_\alpha^* - E_x \quad (4.22)$$

where  $Q_\alpha^*$  represents the decay- $Q$  value to an excited state  $E_x$  in the daughter nuclide.

Table 4.2 lists some of the most precise  $\alpha$ -particle energy data and their deduced values of  $Q_\alpha$ , using the classical formula and the relativistic one (plus atomic binding energy). It shows that the relativistic and the atomic corrections are indispensable: the difference between the two formulae, which is listed in the last column, is larger than  $3\sigma$ .

Table 4.2: Accurate  $\alpha$ -decay calculations. Col. 1 is the decay incident, Col. 2 is the  $\alpha$  energy, Col. 3 and Col. 4 are the calculated decay energies using classical (Eq. 4.12) and relativistic (Eq. 4.21) formulae, respectively, and col. 5 is difference between the values from two formulae.

Item	$\alpha$ energy (keV)	$Q_\alpha(\text{cla})$ (keV)	$Q_\alpha(\text{rel})(3)$ (keV)	Diff (keV)
$^{148}\text{Gd}(\alpha)^{144}\text{Sm}$	3182.68(0.03)	3271.12(0.03)	3271.24(0.03)	0.12(0.03)
$^{252}\text{Cf}(\alpha)^{248}\text{Cm}$	6118.10(0.04)	6216.82(0.04)	6216.98(0.03)	0.16(0.04)
$^{253}\text{Es}(\alpha)^{249}\text{Bk}$	6632.51(0.05)	6739.10(0.05)	6739.28(0.05)	0.18(0.05)

## 4.4 Correlation

It is a basic assumption, as mentioned in Section 3.1, that all the input data is independent. Such a treatment is reasonable since correlations affect only very few masses with high precision. However, even though the input data

are considered independent, the parameters, here the masses, which need to be fitted, are correlated. This can be seen directly from the non-zero off-diagonal elements in the *error matrix*\*  $\mathbf{A}^{-1}$ .

The atomic masses have long been used as input data in the Committee on Data for Science and Technology (CODATA) adjustments [MNT16b]. The correlations among the input data, here the masses, will be considered by the CODATA evaluators. The discussion in this section was initiated by B. N. Taylor [Tay14].

### Correlation coefficients between $^{28}\text{Si}$ , $^{29}\text{Si}$ and $^{30}\text{Si}$

In this section, for simplicity, the atomic mass of a nuclide  $X$  is denoted by  $A(X)$ , the uncertainty is denoted by  $u(X)$ , and the covariance between two nuclides  $X$  and  $Y$  is denoted by  $u(X, Y)$ . The correlation coefficient between  $X$  and  $Y$  can be expressed as:

$$r(X, Y) = \frac{u(X, Y)}{u(X)u(Y)}. \quad (4.23)$$

Note that the covariance of a mass  $A(X)$  with itself is the variance of  $A(X)$ , which is the square of its uncertainty  $u(X)$ . Also note that, in general,  $u(X, Y) = u(Y, X)$ .

The calculations here concern three nuclides  $^{28}\text{Si}$ ,  $^{29}\text{Si}$ , and  $^{30}\text{Si}$ , which are labeled  $r(28, 29)$ ,  $r(28, 30)$  and  $r(29, 30)$ , respectively. From the covariance matrix, one reads  $u(28, 29) = 2.84 \times 10^{-19}$ . Combining  $u(28) = 5.24 \times 10^{-10}$  and  $u(29) = 6.00 \times 10^{-10}$ , one obtains immediately the correlation between  $^{28}\text{Si}$  and  $^{29}\text{Si}$ :

$$r(28, 29) = \frac{u(28, 29)}{u(28)u(29)} = \frac{2.84 \times 10^{-19}}{5.24 \times 10^{-10} \times 6.00 \times 10^{-10}} = 0.9033$$

However, the covariance matrix does not give the covariances involving  $A(30)$ , because  $A(30)$  is a *secondary* nuclide and was not included in the AME2016 least-squares adjustment.

To calculate the covariance  $u(29, 30)$ , one notes that the only common component of uncertainty to  $A(29)$  and  $A(30)$  is the uncertainty of  $A(29)$  itself<sup>†</sup>. Thus, their covariance is just the product  $u(29) \times u(29)$  or  $u^2(29)$ . Hence we have:

$$u(29, 30) = u(29, 29) = 3.60 \times 10^{-19},$$

which leads to a correlation coefficient of:

$$r(29, 30) = \frac{u(29, 29)}{u(29)u(30)} = \frac{u(29)}{u(30)} = 0.0803.$$

\*. The *error matrix* can be accessed easily through AMDC website "<http://amdc.in2p3.fr/masstabes/Ame2016/file1.html>" under the file name "a0p5gqfu.zip" for the all masses involved in the least-squares procedure in 2016.

†. The mass of  $^{30}\text{Si}$  is determined by  $^{29}\text{Si}$  through a  $(n, \gamma)$  reaction

In the calculation, we use  $u(30) = 7.47 \times 10^{-9}$ .

To calculate the covariance  $u(28, 30)$ , we note that the source of the covariance of  $A(28)$  and  $A(29)$  is present in  $A(30)$  because  $A(30)$  is derived directly from  $A(29)$  and there are no other common sources of uncertainty in  $A(28)$  and  $A(30)$  (otherwise  $A(30)$  would become *primary*). Hence we have:

$$u(28, 30) = u(28, 29) = 2.84 \times 10^{-19},$$

from which the correlation coefficient can be obtained:

$$r(28, 30) = \frac{u(28, 29)}{u(28)u(30)} = 0.073.$$

Correlations between adjusted masses are important for the CODATA group, because masses are entered directly as a part of input data in their adjustment for the fundamental constants. A covariance matrix which contains fourteen nuclides were provided to the CODATA group after the publication of AME2016.

# Chapter 5

## Mass Models

### 5.1 Semi-empirical approaches

An ideal theory of mass would be the one that reproduces the nuclear binding energies from “real” nucleonic interactions, meaning solving the Schrödinger equation [Pea01]:

$$H\Psi = E\Psi, \quad (5.1)$$

where

$$H = -\frac{\hbar}{2M} \sum_i \nabla_i^2 + \sum_{ij} V_{ij} + \sum_{ijk} V_{ijk}. \quad (5.2)$$

Here  $V_{ij}$  and  $V_{ijk}$  are two-body and three-body interactions, respectively. The total energy of a nucleus  $E$  is equivalent to the binding energy  $B$  but with opposite sign ( $E = -B$ ). The *ab initio methods* (*ab initio* is a Latin term meaning “from the beginning”) aim at finding the solution of the Schrödinger equation for the atomic nucleus from nucleon-nucleon interactions. So far, calculations can only reach the tin region [MSS<sup>+</sup>18]. At the same time, the calculation is not simple, since one has to deal with the strong short-range repulsion force between nucleons and the tensor coupling. Due to the difficulties in the calculation, one has to resort to a phenomenological method, e.g., based on phenomenological interactions, which can calculate the properties (here the mass) for a vast number of nuclei, especially for those that are related to the r-process nucleosynthesis [Arn96].

Since we can not obtain the exact wave function  $\Psi$  in Eq. 5.1 for such a many-body system (nucleus), we have to refer to the semi-empirical approaches: one can simplify the many-body problem, e.g., by replacing  $\Psi$  by a Slater determinant  $\Phi = \det\{\phi_i(x_i)\}$  by properly antisymmetrizing the single particle wave functions  $\phi_i(x_i)$  (Hartree Fock) using effective interactions, such as Skyrme forces [VB72] and Gogny forces [DG80]; or refine the Bethe-Weizsäcker formula by including shell corrections. The former method is *microscopic* and the later one is *macroscopic-microscopic*.

For the moment, the stellar nucleosynthesis models, in particular r-process, requires masses which cannot be produced by current facilities and one has to rely on mass models. The choice of a mass model is important since a slight change in mass (strictly speaking the mass difference between two adjacent nuclides) has a strong impact on energy generation and hence on astrophysical scenarios [Sch13]. Before using a model, its predictive power should be estimated carefully. The intention of this chapter is not to describe in detail every component in each mass model. It only serves as an illustration of the ability of the models in the description of experimental masses and their predictive power. A detailed discussion of different models and applications can be found in a review paper [LPT03].

Table 5.1: Information of eight mass models: the year of publication, the number of parameters in the model, and the mass table that was used to fit parameters.

Mass model	Year of publication	Number of parameters	Mass table
ETFSI-2	2000	9	AME1993
FRDM95	1995	38	AME1993
FRDM12	2012	41	AME2003
KTUY05	2003	115*	AME2003
HFB26	2013	30	AME2012
HFB27	2013	27	AME2012
WS4+RBF	2014	18 <sup>+</sup>	AME2012
DUZU	1995	33	AME1993

\* Based on the original formulation from [KUTY00].

<sup>+</sup> To construct the smooth function  $S(\mathbf{X})$  with the RBF approach, the masses of 2148 experimentally known nuclides are considered. More details can be found in [WL11].

## 5.2 Accuracy

In this section, eight mass models are examined: Extended Thomas-Fermi plus Strutinsky Integral method (ETFSI-2) [Gor00], Finite Range Droplet Model (FRDM95) [MNMS95] and its updated version with improved treatment of deformation (FRDM12) [MSIS16], a recent Weizsäcker-Skyrme plus Radial Basic Function (WS4+RBF) model [WLWM14], two recent Hartree-Fock-Bogoliubov mass models HFB26 [GCP13a] and HFB27 [GCP13b], the Duflo and Zuker (DUZU) model [DZ95], and the KTUY05 [KTUY05] model. Four models are macroscopic-microscopic (ETFSI-2, FRDM1995, FRDM2012, WS4+RBF), two are microscopic (HFB26, HFB27), and two are phenomenological (DUZU, KTUY05). All mass models discussed here are semi empirical in that some (or all) parameters are fitted to experimental masses. Table 5.1

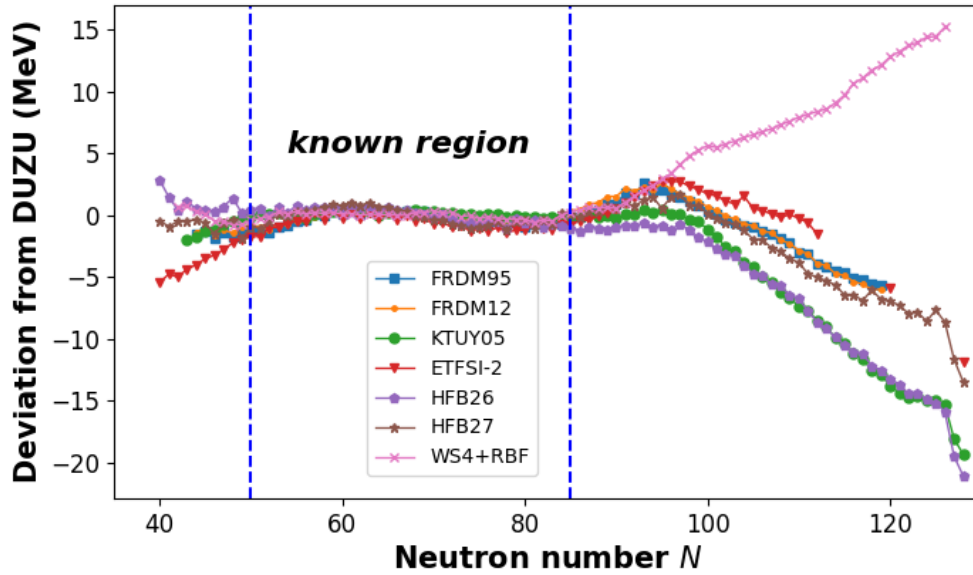


Figure 5.1: Masses of different Sn isotopes calculated from different models with respect to the mass model DUZU.

details the information related to each mass model.

A good mass model should on one hand reproduce the binding energies as seen in Fig. 1.1, and on the other hand have a good predictive power (see next section) when it extrapolates towards the unknown region. Fig. 5.1 represents the deviations of different mass models with respect to the DUZU model for the masses of Sn isotopes. Within the known region (between blue-dash lines), all models give similar results, since all models were fitted to the experimental masses. But when they go further away from the known region, they diverge: especially the neutron drip-line, different mass models predict different trends. Two mass models HFB26 and KTUY05 follow almost the same trend and four mass models ETFSI-2, FRDM95, FRDM12 and HFB27 seem to group together. The mass model WS4+RBF goes in the opposite direction with respect to all the other mass models. We should notice that all models were published before AME2016, giving a good opportunity to check their predictive power.

We will first study the model accuracy. The accuracy is the degree of agreement between the masses calculated by a mass model and those from experiments. In order to study the model accuracy, we can define a root-mean-square deviation (rms) for a mass model:

$$\delta_{\text{rms}} = \sqrt{\frac{\sum_{i=1}^{N_{\text{nuc}}} (m_{\text{cal}}^i - m_{\text{exp}}^i)^2}{N_{\text{nuc}}}}, \quad (5.3)$$

where  $m_{\text{cal}}^i$  and  $m_{\text{exp}}^i$  are the masses from a model and from an experiment, respectively, with the number of nuclides  $N_{\text{nuc}}$  included in the calculation. The rms deviation is an indicator of the accuracy for a mass model, and will be used in the following discussion\*. Other quantities such a mean error  $\bar{\delta}$  which is defined:

$$\bar{\delta} = \frac{\sum_{i=1}^{N_{\text{nuc}}} (m_{\text{cal}}^i - m_{\text{exp}}^i)}{N_{\text{nuc}}}, \quad (5.4)$$

and the maximum deviation  $\delta_{\text{max}}$ , which calculates the largest deviation from experimental masses, is also used.

Table 5.2 lists the rms deviation  $\delta_{\text{rms}}$ , mean deviation  $\bar{\delta}$ , and the maximum deviation  $\delta_{\text{max}}$  for eight mass models for all nuclides with  $Z, N \geq 8$  with respect to three mass tables AME2003, AME2012, and AME2016. It is intriguing to include AME2003 and AME2012 for comparison: some models are relatively old (dating back in 1995 as seen in Table 5.1) and their intrinsic robustness can be checked with time. To have a better vision of the accuracy for various

Table 5.2: Root-mean-square deviation  $\delta_{\text{rms}}$ , mean deviation  $\bar{\delta}$ , and maximum deviation  $\delta_{\text{max}}$  for nuclides with  $Z, N \geq 8$  with respect to three mass tables AME2003, AME2012, and AME2016. The results for the eight mass models are listed.

AME2003								
Models	FRDM95	FRDM12	KTUY05	ETFSI-2	HFB26	HFB27	WS4+RBF	DUZU
count	2149	2149	2149	2048	2149	2148	2149	2149
$\delta_{\text{rms}}$	0.656	0.581	0.653	0.695	0.571	0.533	0.206	0.360
$\bar{\delta}$	-0.058	-0.004	-0.018	0.085	0.022	-0.021	-0.002	-0.009
$\delta_{\text{max}}$	-3.783	-3.012	-3.052	-3.236	-2.698	-2.560	-1.441	-2.706
AME2012								
count	2353	2353	2353	2249	2353	2352	2353	2353
$\delta_{\text{rms}}$	0.654	0.579	0.701	0.679	0.564	0.512	0.170	0.394
$\bar{\delta}$	-0.059	-0.010	-0.058	-0.086	-0.006	0.005	0.000	-0.032
$\delta_{\text{max}}$	3.640	3.263	-2.932	-2.150	-2.715	-2.564	0.897	-3.060
AME2016								
count	2408	2408	2408	2300	2408	2407	2408	2408
$\delta_{\text{rms}}$	0.677	0.599	0.723	0.676	0.580	0.517	0.187	0.422
$\bar{\delta}$	-0.060	-0.009	-0.068	-0.087	-0.011	0.000	0.001	-0.032
$\delta_{\text{max}}$	3.998	4.568	-2.930	-2.150	-3.540	-2.554	1.485	3.458

mass models, the rms deviations are also plotted in Fig. 5.2. One can see from

\*. P. Möller introduced a “model error” [MN88]. But since it is not commonly used in the literature, we omit it here.

Fig. 5.2 that the rms deviation is very similar for each mass model with respect to three mass tables. The mass model ETFSI-2 gives a  $\delta_{\text{rms}}$  value of around 0.7 MeV and DUZU gives a  $\delta_{\text{rms}}$  around 0.4 MeV, which increases slowly with successive mass tables. FRDM95, which was proposed before the publication of AME2003, gives a  $\delta_{\text{rms}}$  value of  $\sim 0.7$  MeV with respect to three mass tables. FRDM12, which used the same droplet model but with an improved treatment of deformation and fewer approximations, gives a  $\delta_{\text{rms}}$  value of around 0.6 MeV. The two *microscopic* mass models HFB27 (with the standard 10-parameter Skyrme force) and HFB26 (with two extra unconventional terms  $t_4$  and  $t_5$  in the Skyrme force) give rms deviations lower than 0.6 MeV. WS4+RBF gives the lowest-ever rms deviation, which is below 0.2 MeV. KTUY05 gives a  $\delta_{\text{rms}}$  of 650 keV compared to AME2003 and a slightly larger value of 720 keV compared to AME2016. The very similar rms deviations for each mass model compared to different mass tables are due to the fact that, in AME2016, only 17 masses have changed more than 500 keV compared to AME2003.

The average error  $\bar{\delta}$  is between several keV and tens of keV for all mass models. The maximum deviation  $\delta_{\text{max}}$  is for most of the mass models larger than 2 MeV, except for WS4+RBF, which reaches only 1.4 MeV.

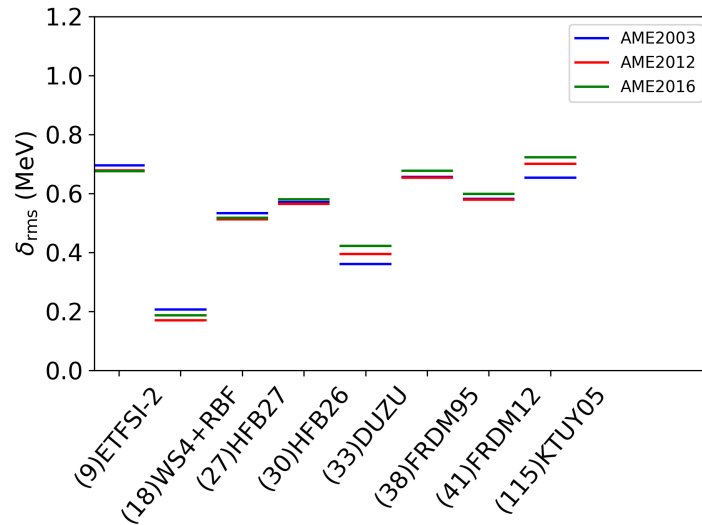


Figure 5.2: Root-mean-square deviations of eight mass models for nuclides  $Z, N \geq 8$  with respect to mass tables AME2003, AME2012, and AME2016. The number in the parenthesis indicates the number of parameters in the corresponding mass model. Same illustrations will be applied to the successive figures.

The global ( $Z, N \geq 8$ ) rms deviation displayed in Fig. 5.2 reflects the average accuracy of a model for the whole nuclear chart. It would however induce a bias: a model with a good accuracy does not necessarily have the same

quality for a specific region. It is demonstrated in [SLP18] that the accuracy of a mass model strongly depends on the region of nuclei to which it is applied. Following the same routine as in [SLP18], the global region is divided into four subregions: Light ( $8 \leq Z < 28, N \geq 8$ ), Medium-I ( $28 \leq Z < 50$ ), Medium-II ( $50 \leq Z < 82$ ), and Heavy ( $Z \geq 82$ ). The calculations of  $\delta_{\text{rms}}$ ,  $\bar{\delta}$  and  $\delta_{\text{max}}$  with respect to the experimentally known masses in AME2016 are listed in Table 5.3. Also listed are the number of nuclides in different regions.

Table 5.3: Root-mean-square deviation  $\delta_{\text{rms}}$ , mean deviation  $\bar{\delta}$ , and maximum deviation  $\delta_{\text{max}}$  from AME2016 in four regions: Light ( $8 \leq Z < 28, N \geq 8$ ), Medium-I ( $28 \leq Z < 50$ ), Medium-II ( $50 \leq Z < 82$ ), and Heavy ( $Z \geq 82$ ).

Light								
Models	FRDM95	FRDM12	KTUY05	ETFSI-2	HFB26	HFB27	WS4+RBF	DUZU
count	350	350	350	242	350	350	350	350
$\delta_{\text{rms}}$	1.196	1.119	0.733	0.939	0.967	0.820	0.302	0.637
$\bar{\delta}$	-0.122	-0.017	-0.013	-0.603	0.033	-0.089	0.022	0.104
$\delta_{\text{max}}$	4.000	4.568	2.608	-2.150	-3.540	-2.554	1.485	3.458
Medium-I								
count	591	591	591	591	591	591	591	591
$\delta_{\text{rms}}$	0.687	0.620	0.824	0.582	0.520	0.579	0.194	0.428
$\bar{\delta}$	0.051	-0.007	-0.346	0.002	0.030	0.143	-0.006	-0.019
$\delta_{\text{max}}$	2.441	2.301	-2.930	-1.752	1.648	2.016	1.105	-1.811
Medium-II								
count	977	977	977	977	977	977	976	977
$\delta_{\text{rms}}$	0.478	0.370	0.550	0.641	0.455	0.390	0.148	0.330
$\bar{\delta}$	-0.136	-0.045	0.208	-0.065	-0.048	-0.045	0.003	-0.031
$\delta_{\text{max}}$	-1.496	-1.330	-1.760	2.004	-1.730	1.523	0.494	-1.386
Heavy								
count	490	490	490	490	490	490	490	490
$\delta_{\text{rms}}$	0.451	0.367	0.874	0.693	0.495	0.353	0.133	0.379
$\bar{\delta}$	0.003	0.064	-0.209	0.017	-0.020	-0.017	-0.010	-0.026
$\delta_{\text{max}}$	-1.999	-1.889	-2.587	-1.788	-1.764	-1.564	-0.412	-3.058

From Table 5.3 one can see that the rms deviation changes from region to region. In the light region,  $\delta_{\text{rms}}$  ranges from the lowest value of 0.302 MeV (WS4+RBF) to the highest one of 1.196 MeV (FRDM95). For a specific model, a strong variation of  $\delta_{\text{rms}}$  can also be identified in different regions: HFB27 gives its lowest  $\delta_{\text{rms}}$  of 0.353 MeV in the heavy region while the  $\delta_{\text{rms}}$  increases to 0.816 MeV in the light region. Fig. 5.3 displays the dependence of  $\delta_{\text{rms}}$  on different regions of eight models. As seen from Fig. 5.3, the rms deviations for the mass models FRDM95, FRDM12, HFB26, HFB27, WS4+RBF, and DUZU have a tendency to decrease towards the heavy mass region. A ‘‘saturation’’ of  $\delta_{\text{rms}}$  is also spotted in these models: their  $\delta_{\text{rms}}$  remains almost unchanged when they pass from Medium-II to Heavy. However, a totally different trend is noted in two mass models KTUY05 and ETFSI-2. KTUY05 presents the largest rms deviation of 874 keV in the heavy region, and its smallest  $\delta_{\text{rms}}$  value of 550 keV

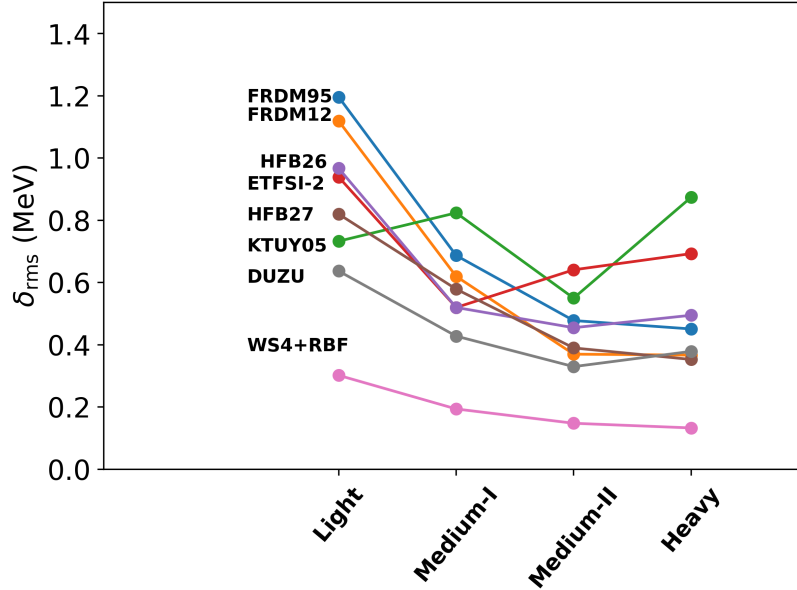


Figure 5.3: Root-mean-square deviations of eight mass models in four regions: Light ( $8 \leq Z < 28, N \geq 8$ ), Medium-I ( $28 \leq Z < 50$ ) Medium-II ( $50 \leq Z < 82$ ) and Heavy ( $Z \geq 82$ ).

in the meadium-II region. The minimum  $\delta_{\text{rms}}$  value for ETFSI-2 is found in the medium-I region, which is 582 keV.

The rms deviations are also displayed separately in different regions for all models in Fig. 5.4 (represented by green lines), together with the lines in black displaying the Global accuracy. In the light region, FRDM95 gives the largest  $\delta_{\text{rms}}$  value of 1.196 MeV and WS4+RBF gives the smallest value of 0.302 MeV. But all mass models have larger  $\delta_{\text{rms}}$  than their global ( $Z, N \geq 8$ ) values. It is probably due to the fact that the mean field on which all models depend is not sufficient to describe the light nuclides. When going to the medium-I region,  $\delta_{\text{rms}}$  becomes smaller for all models, except for KTUY05, whose rms deviation increases to 0.824 MeV compared to 0.733 MeV in the light region. And in this region, the  $\delta_{\text{rms}}$  overlaps with the Global  $\delta_{\text{rms}}$ . Going further into the medium-II region, the largest rms deviation is found for ETFSI-2 and the smallest one for WS4+RBF. And the  $\delta_{\text{rms}}$  values are smaller than the Global  $\delta_{\text{rms}}$  for all models. In the heavy region, the largest rms deviation is found for KTUY05 and the smallest one for WS4+RBF.

### 5.3 Predictive power

The predictive power is the ability of a mass model to predict the unknown masses. To some extent, the predictive power could be more important than the

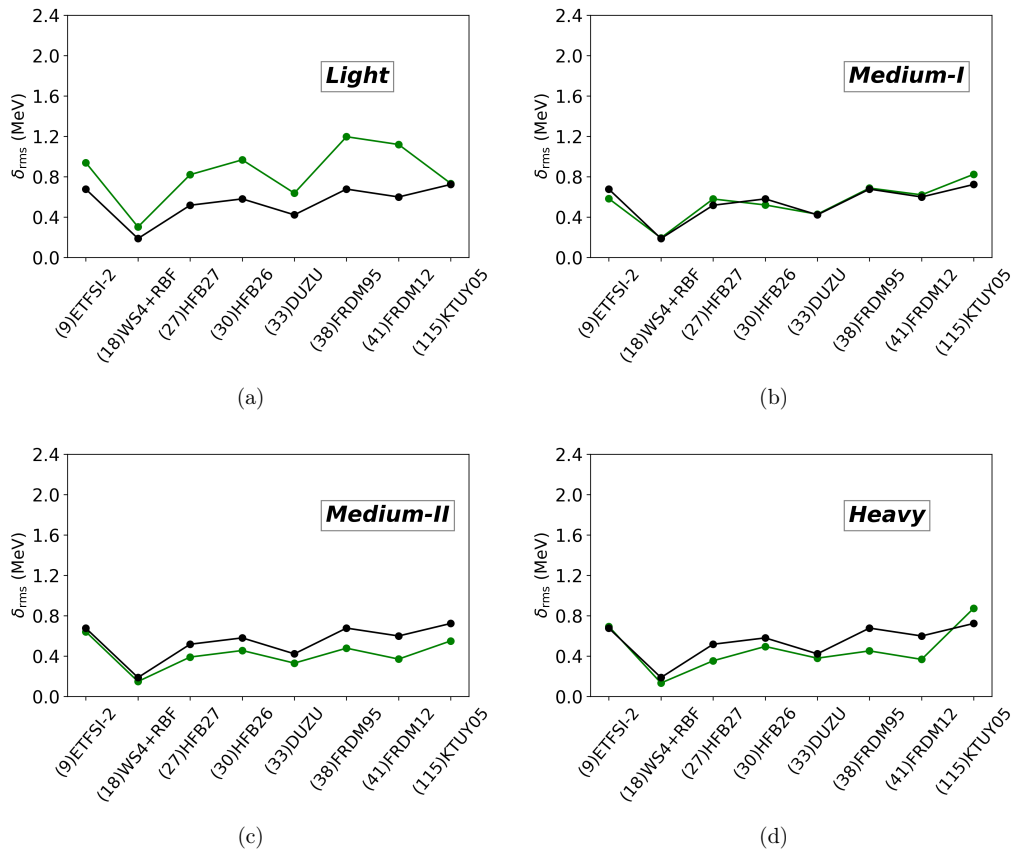


Figure 5.4: Root-mean-square deviations from AME2016 in four regions (represented by lines in green): (a) Light, (b) Medium-I, (c) Medium-II, and (d) Heavy. The Global rms deviation is also displayed (represented by black lines).

accuracy, since it can provide masses that cannot be produced at the current facilities, but are crucial in astrophysical calculations. To examine the relation between the accuracy and the predictive power, we can calculate the rms deviation separately: one is based on the experimental masses in AME2012 ( $\delta_{\text{rms}}(2012)$ ), the other is based on the new measured masses in AME2016 ( $\delta_{\text{rms}}(\text{new})$ ) which were unknown in AME2012.

Table 5.4: Root-mean-square deviations in the Global ( $Z, N \geq 8$ ), Light ( $8 \leq Z < 28, N \geq 8$ ), Medium-I ( $28 \leq Z < 50$ ) Medium-II ( $50 \leq Z < 82$ ) and Heavy ( $Z \geq 82$ ) regions. The rms deviations are calculated separately for the masses that were known in AME2012  $\delta_{\text{rms}}(2012)$  and for the new ones in AME2016  $\delta_{\text{rms}}(\text{new})$ .

Global								
Models	FRDM95	FRDM12	KTUY05	ETFSI-2	HFB26	HFB27	WS4+RBF	DUZU
count(2012)	2353	2353	2353	2249	2353	2352	2353	2353
count(new)	61	61	61	57	61	61	61	61
$\delta_{\text{rms}}(2012)$	0.654	0.579	0.701	0.679	0.564	0.512	0.170	0.394
$\delta_{\text{rms}}(\text{new})$	1.231	1.096	1.279	0.731	0.986	0.779	0.489	1.009
Light								
count(2012)	335	335	335	216	335	335	335	335
count(new)	17	17	17	13	17	17	17	17
$\delta_{\text{rms}}(2012)$	1.144	1.056	0.692	0.959	0.926	0.791	0.247	0.546
$\delta_{\text{rms}}(\text{new})$	1.851	1.879	1.310	0.700	1.489	1.157	0.790	1.528
Medium-I								
count(2012)	575	575	575	575	575	575	575	575
count(new)	18	18	18	18	18	18	18	18
$\delta_{\text{rms}}(2012)$	0.664	0.618	0.783	0.583	0.516	0.593	0.175	0.406
$\delta_{\text{rms}}(\text{new})$	1.210	0.729	1.571	0.859	0.662	0.726	0.430	0.892
Medium-II								
count(2012)	970	970	970	970	970	969	970	970
count(new)	7	7	7	7	7	7	7	7
$\delta_{\text{rms}}(2012)$	0.475	0.368	0.542	0.643	0.449	0.389	0.148	0.328
$\delta_{\text{rms}}(\text{new})$	0.660	0.513	1.054	0.469	0.904	0.525	0.194	0.678
Heavy								
count(2012)	473	473	473	473	473	473	473	473
count(new)	19	19	19	19	19	19	19	19
$\delta_{\text{rms}}(2012)$	0.448	0.367	0.870	0.694	0.489	0.352	0.133	0.376
$\delta_{\text{rms}}(\text{new})$	0.530	0.360	0.992	0.703	0.655	0.403	0.161	0.525

The calculation of  $\delta_{\text{rms}}$  based on two different sets is listed in Table 5.4. The dependence of  $\delta_{\text{rms}}(2012)$  and  $\delta_{\text{rms}}(\text{new})$  for different mass models in different regions are illustrated in Fig. 5.5. One can see from Fig. 5.5a that in the global region, the condition of good predictive power defined by [SLP18]:

$$\text{rms}(\text{new}) \approx \text{rms}(2012), \quad (5.5)$$

is only roughly achieved by ETFSI-2 (but with a large value of  $\sim 700$  keV), while other models present a much larger  $\delta_{\text{rms}}(\text{new})$  value than that of their  $\delta_{\text{rms}}(2012)$ . For example, FRDM12 gives a  $\delta_{\text{rms}}(2012)$  value of 0.579 MeV but

gives 1.096 MeV for  $\delta_{\text{rms}}(\text{new})$ . In the light region, ETFSI-2 shows the best predictive power (0.7 MeV) compared to other mass models. In the medium-I region, the predictive power of the mass models is becoming better and the difference between  $\delta_{\text{rms}}(2012)$  and  $\delta_{\text{rms}}(\text{new})$  is becoming smaller, except for KTUY05. In the medium-II region, the difference between  $\delta_{\text{rms}}(2012)$  and  $\delta_{\text{rms}}(\text{new})$  is strongly compressed for all models except for KTUY05, DUZU and HFB26. In the heavy region, two curves are almost overlapped, meaning that the predictive power of all the mass models are compatible with their accuracy. One can refer to [SLP18] for the discussions of the predictive power of other models.

In this chapter, the accuracy and predictive power of eight mass models are studied. The mass models, regardless of their intrinsic characters, could reproduce the experimentally known masses but predict different behavior when they extrapolate towards unknown regions.

The rms deviations for all the mass models are well below 0.8 MeV compared to three mass tables AME2003, AME2012, and AME2016. To check the accuracy in different mass regions, we divide the global region into four subregions. We observe that going from the light region to the heavy region, the rms deviation for most of the mass models is becoming smaller, meaning that their accuracy is becoming better. But it is not the case for the mass model KTUY05, which presents the largest rms deviation in the heavy region. To estimate the predictive power, we use two sets of data for comparison, the mass table AME2012 and the newly measured masses in AME2016. We find that the predictive power of mass models depends strongly on the considered regions. In the global region, the condition  $\text{rms}(\text{new}) \approx \text{rms}(2012)$  is only roughly fulfilled by the mass model ETFSI-2, while other mass models present a much large  $\text{rms}(\text{new})$  value than that of their  $\text{rms}(2012)$ . We also observe that ETFSI-2 has the best predictive power in the light region, while in other regions, the mass model WS4+RBF has the best predictive power. In the heavy region, all the mass models find their lowest  $\text{rms}(\text{new})$  value, and the predictive power is compatible with the accuracy.

In general, phenomenological models could well reproduce known masses, but extrapolate badly; microscopic models have slightly larger rms deviations but show better extrapolation ability. The more fundamental basis that a model relies on, the better chance it would have in reproducing actual masses. Fig. 5.6 displays the deviations of calculated masses and the experimental ones in AME2016. With Fig. 5.6, we can examine the discrepancies in subtle regions. For example, FRDM95, FRDM12, and DUZU have worse predictive power ( $\delta_{\text{rms}} > 2$  MeV) in the neutron-rich calcium ( $Z = 20$ ) region, while ETFSI-2 presents  $\delta_{\text{rms}} \approx 0.5$  MeV. The shell and deformation effects are also recognized. For example, in the  $A \sim 100$  ( $Z \sim 38$ ) deformation region, FRDM95, FRDM12, ETFSI-2, HFB26, and HFB27 over-predict the masses.

To qualify a mass model, the rms deviation should not be the only concern. Other nuclear ingredients such as  $Q$ -values, half-lives, spin and parity, fission

barriers, ect., should be also provided by mass models. The application of a modern mass model can also be found in astrophysics, such as the elucidation of the r-process nucleosynthesis [GCP16].

Next, a more reliable way to estimate the masses in AME, by observing the smoothness of mass surface, will be discussed.

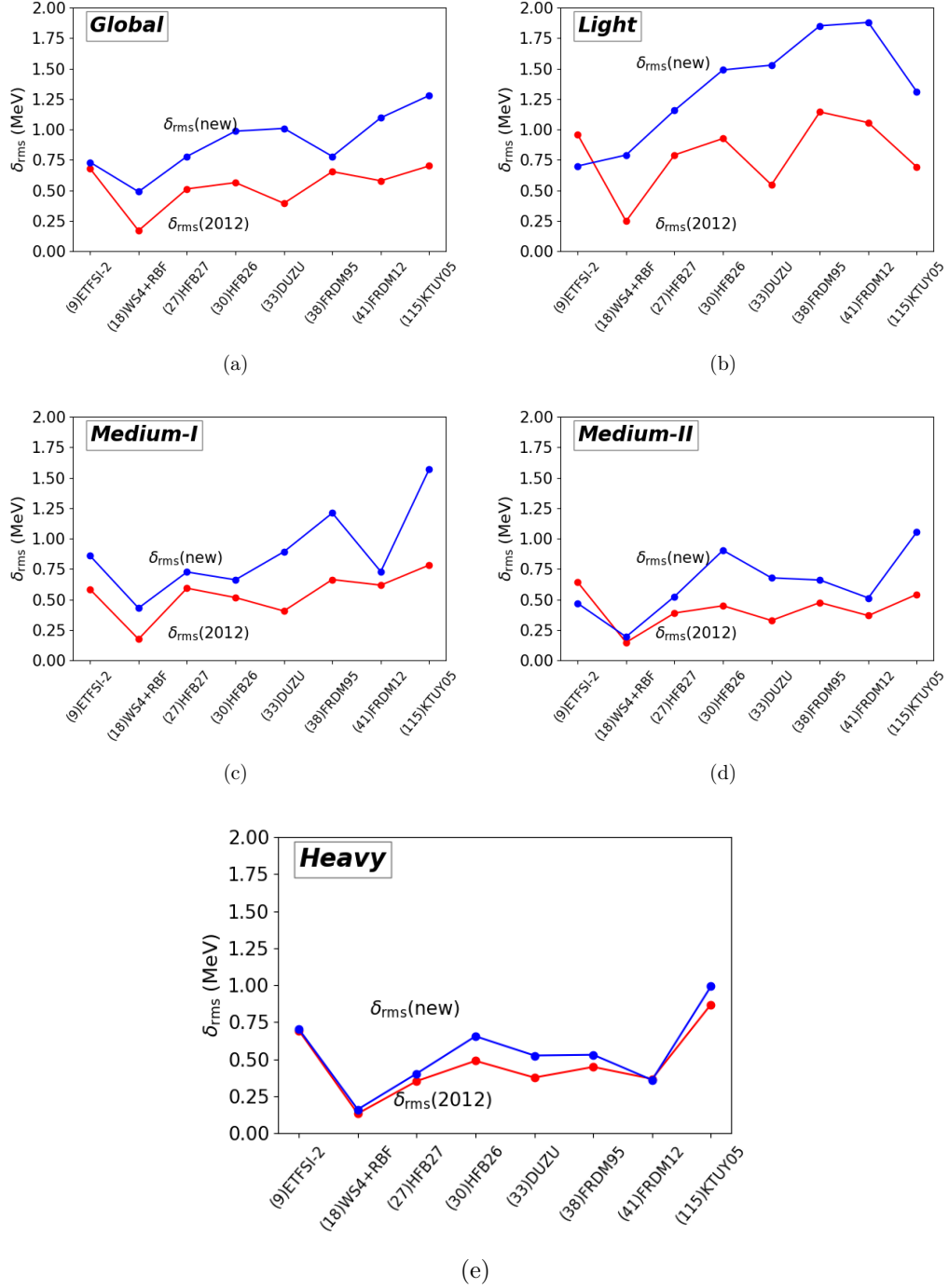
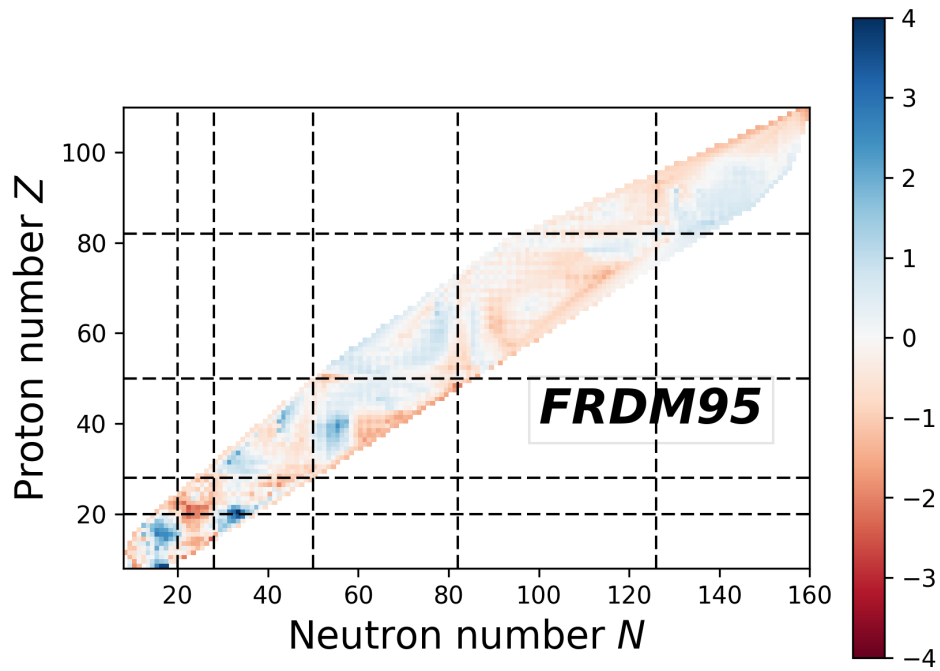
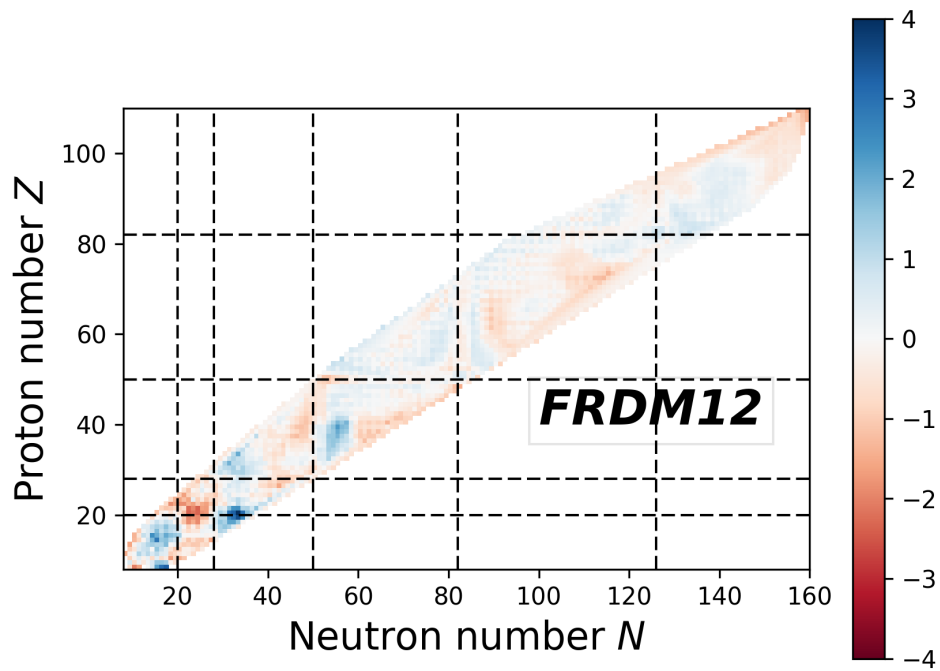


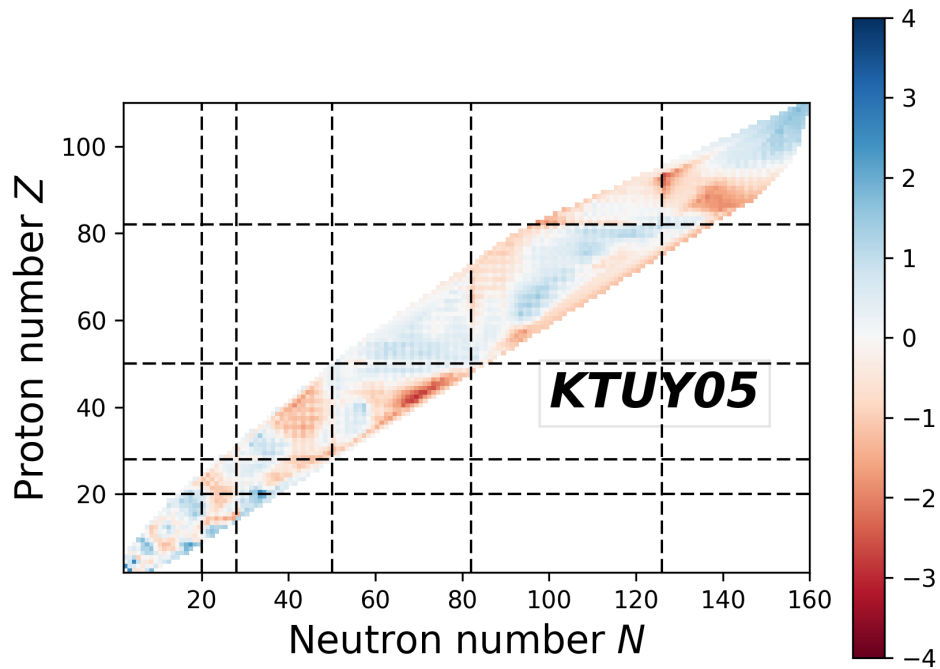
Figure 5.5:  $\delta_{\text{rms}}(2012)$  and  $\delta_{\text{rms}}(\text{new})$  in (a) Global (b) Light (c) Medium-I (d) Medium-II and (e) Heavy regions.



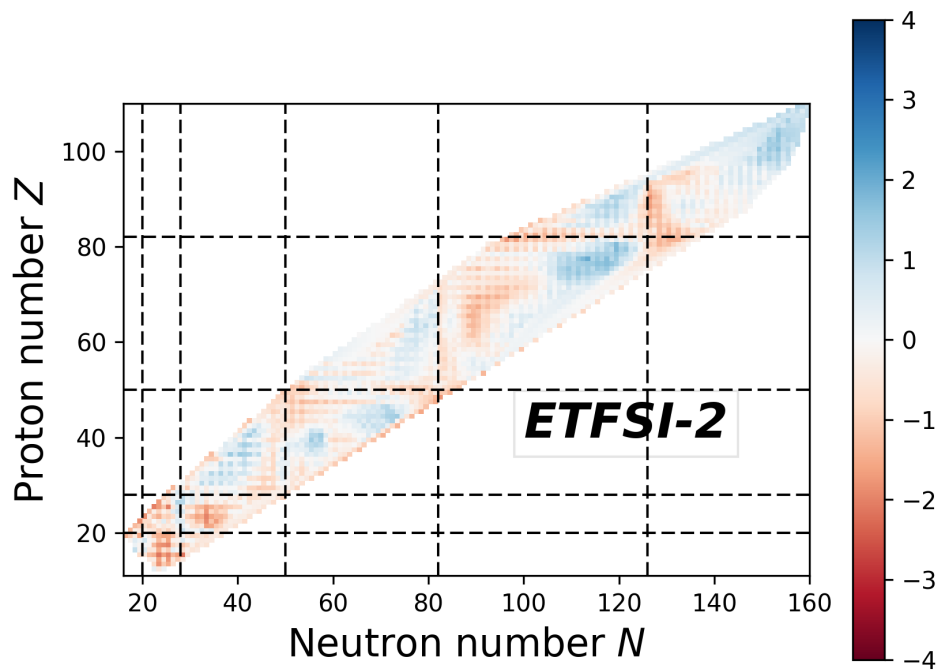
(a) Display of the deviations between the calculated masses and experimental ones in AME2016 in a color plot for the mass model FRDM95.



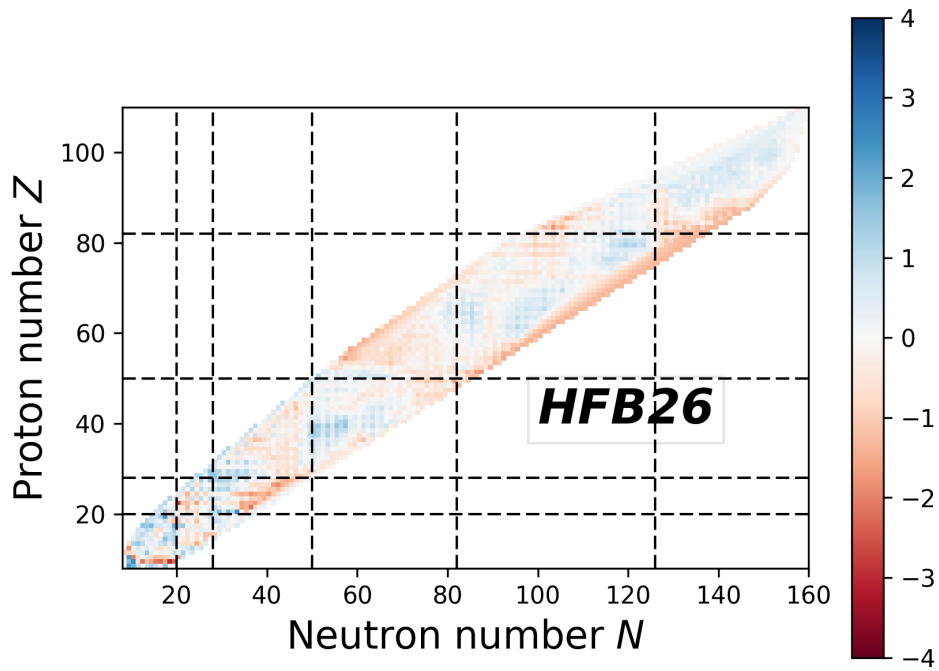
(b) Same as Fig. 5.6a but for the mass model FRDM12.



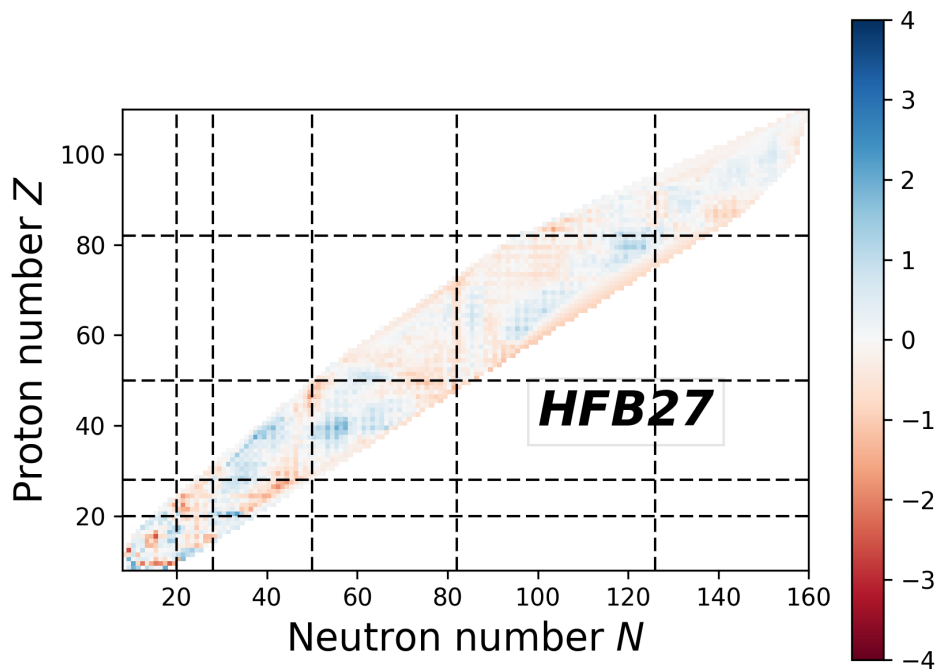
(c) Same as Fig. 5.6a but for the mass model KTUY05.



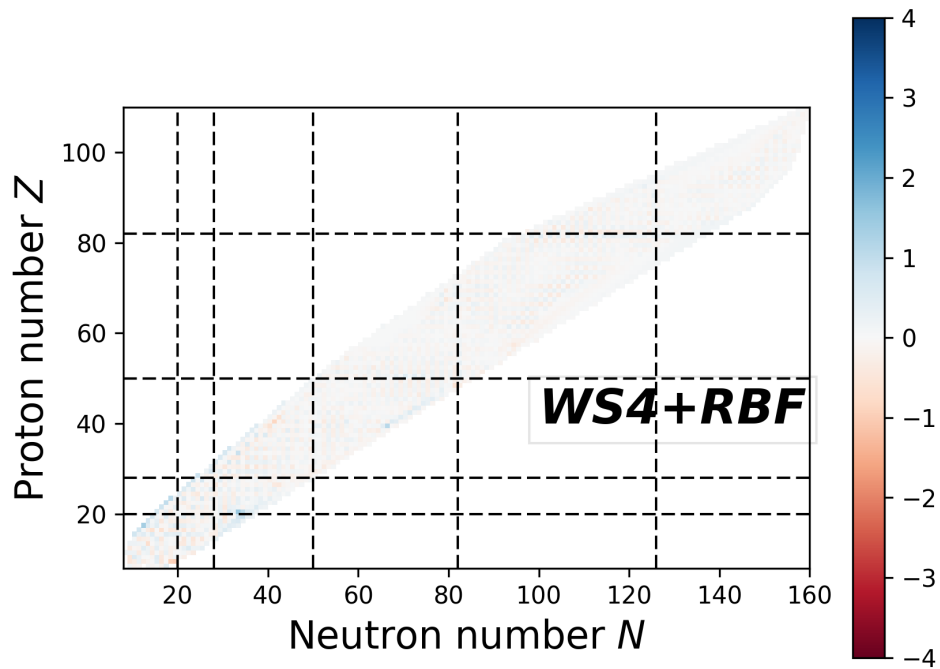
(d) Same as Fig. 5.6a but for the mass model ETFSI-2.



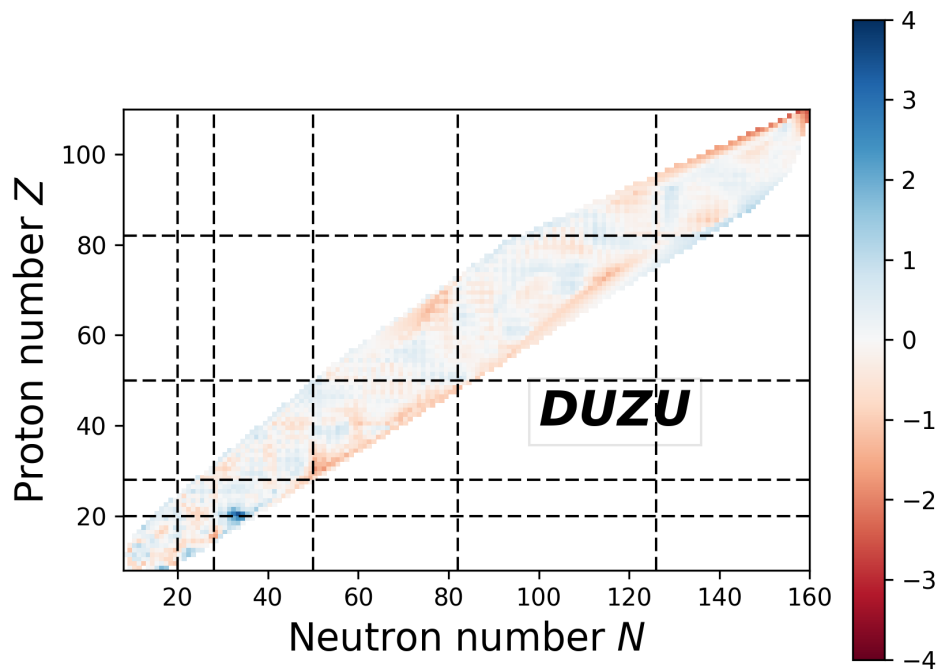
(e) Same as Fig. 5.6a but for the mass model HFB26.



(f) Same as Fig. 5.6a but for the mass model HFB27.



(g) Same as Fig. 5.6a but for the mass model WS4+RBF.



(h) Same as Fig. 5.6a but for the mass model DUZU.

# Chapter 6

## Mass Extrapolation

### 6.1 Regularity of the Mass Surface

When atomic masses are displayed as a function of  $N$  and  $Z$ , we obtain a *surface* in a 3-dimensional space. However, the *surface*, which is subject to odd-even staggering effect caused by pairing, is rather uneven. If one divides the *surface* into four sheets (e-e, e-o, o-e and o-o, e-o means even in  $N$  and odd in  $Z$ ), one would immediately note that the e-e sheet lies in the lowest, the o-o lies in the highest and the e-o and o-e sheets lie nearly half way between the e-e and o-o sheets. The separation of four sheets, where each of which has a smooth behavior, minimizes the pairing effects. Therefore, the smoothness (regularity) is observed to be a basic property of the *mass surface* and can help deriving unknown masses from measured ones. Thus, dependable short-range estimates of unknown or poorly known masses can be obtained by extrapolating well from well-known masses on the same sheet. However, the smoothness could also be interrupted by a sudden change of physical quantities (shell closure, deformation, etc.).

The extrapolation is used for several purposes:

a) A coherent deviation from regularity indicates a change of physical properties in a region. If only a single mass violates the trends from the mass *surface* (TMS) while its neighbouring nuclides show a regular character, its correctness would be questioned.

b) For two measurements using different methods which conflict with each other and no conclusion can be drawn, the one that agrees with TMS would help decide which one to be accepted or rejected.

c) For some extremely exotic nuclides whose masses were measured only once, their values should be checked against the estimate from the TMS.

d) We want to include a number of nuclides occurring in reactions and decays with precise energy values but having no connection to any known mass.

e) Drawings of the mass *surface* allows to derive estimates for still-unknown

masses, which serves as a guide for future experiments.

In addition, the masses of all nuclides having the same iso-parameters of  $N, Z, A = N + Z$  and  $N - Z$  lying between known nuclides would also be obtained in the same way.

## 6.2 Scrutinizing the Mass Surface

Direct representations of masses in a 3-dimensional space is not convenient, since the mass surface has a very large expansion along the mass axis (mass number ranging from 1 u to about 300 u). In the work of [WAH88], the extrapolation was done by scrutinizing the mass surface in four sheets. Wapstra *et al.* [WAH88] analyzed the differences between the differences between experimental masses and an expression obtained by a proper consideration of pairing effects [JHJ84] with a suitable smooth function  $f(Z, N)$ . Such a treatment allowed to examine the mass surface on almost the same scale (around several MeV) and remedy some oscillations caused by pairing. However, the procedure was rather complicated (see Fig. 1 in [WAH88]). And the separate sheets might diverge, which makes such extrapolation unpredictable.

An alternative to bypass these difficulties is to look at the *derivatives* of the mass *surface*. By *derivative*, we mean a specific difference between the masses of two nearby nuclides. The *derivatives* preserve the smooth behavior which extends from the known masses to the unknown ones on one hand, and magnify the local structure on the other hand. The pioneering work of [Wap65] aimed at estimating unknown masses based on the studies of five *derivatives*: two-neutron and two-proton separation energies,  $\alpha$ -decay energies, beta-decay and double-beta decay energies. The primary intention was to retain reaction and decay results with known energies but having no connection to the known masses. A suspect mass which ruins the *derivative* plots can also be spotted easily.

An “Interactive Graphical” (I-G) tool was devised [BA93] in the 1990s for observing different *derivatives* of mass *surface*. It can display four *derivatives* simultaneously in the same graph, which allows to study constraints superimposed by different *derivatives*, i.e. the smooth property should be fulfilled at each quadrant at the same time. Fig. 6.1 is a screen shot from the (I-G) tool for four *derivatives*: two-proton separation energy  $S_{2p}$ , two-neutron separation energy  $S_{2n}$ ,  $\alpha$ -decay energy  $Q_\alpha$ , and double-beta-decay energy  $Q_{\beta\beta}$ . Each point represents a nuclide and is connected by iso-parameters  $Z, N, Z$  and  $Z$ , respectively. Vertical lines at each point represent the corresponding uncertainty. As mentioned before, the extrapolation is based on the assumption that the mass *surface* is smooth and it is indeed true: in the  $S_{2n}$  quadrant (upper left in Fig. 6.1), their values decrease smoothly with  $N$  from  $N = 62$  to  $N = 72$ . The change of a physical property can also be noted: a sudden change of the values of  $S_{2p}$  (upper right in Fig. 6.1) at  $Z = 50$  depicts a shell

closure. Based on the regular smoothness of the mass *surface*, an experimental mass which ruins the smoothness of the mass *surface* should be checked with caution and, if necessary, should be replaced by an estimated value (with label #). In AME2016, 31 cases which violates the smoothness of the mass *surface* have been replaced by values from the trends from the mass surface (TMS) (see Table C in [HAW<sup>+</sup>17]).

Since we are dealing with *derivatives* which involve two nuclides, i.e. each point is the difference between two masses, a deviation from the regular *surface* could be either due to the related mass itself or its connected partner. Other constraints, apart from the requirement that all *derivatives* should be compatible with each other, should be also imposed. Two algebraic constraints are mainly considered here. First, if the masses of two nuclides  $(Z, N)$  and  $(Z, N + 4)$  are known but not the mass  $(Z, N + 2)$  then the choice of  $S_{2n}(Z, N + 2)$  and  $S_{2n}(Z, N + 4)$  is not random, since the sum of the two is known. Secondly, two  $\alpha$ -decay energies  $Q_\alpha(A + 4i, Z + 2i)$  and  $Q_\alpha(A - 2 + 4i, Z + 2i)$  ( $i$  is an integer number) may be known and thus the difference between the two is the two-neutron separation energy of a nuclide with  $(A + 4i, Z + 2i)$ .

Other *derivatives* such as one-proton and one-neutron separation energies could also be used in the mass extrapolation. In this case, *derivatives* should be plotted separately according to different parities.

### 6.3 Subtracting a mass model from the experimental mass surface

If we consider the difference between two nearby masses from a mass model instead of absolute masses, one would immediately find that the difference between any two models becomes much smaller. Fig. 6.2 illustrates the calculation of two-neutron separation for Sn isotopic chains based on the mass models discussed above. The calculation shows a similar trend for all mass models, even when they extend to the unknown region. It is probably due to the fact the different nature of models are to some extent smeared out when one expresses mass difference of adjacent nuclides instead of absolute masses. Moreover, all models predict well the shell closures at  $N = 50$  and  $N = 82$ , shown with black-dash lines in Fig. 6.2.

It was first noticed by Wapstra [BW72] that, for practical use, a mass formula should not (actually cannot) reproduce absolute masses as well as possible, but rather the mass differences (separation energies,  $\alpha$ -decay energies, etc.). A better solution for introducing a mass formula in the mass extrapolation is to subtract the actual masses from a “good” mass model. The study of these differences is another way to perform extrapolation. However, choosing such a model is not straightforward: a mass model should have a good



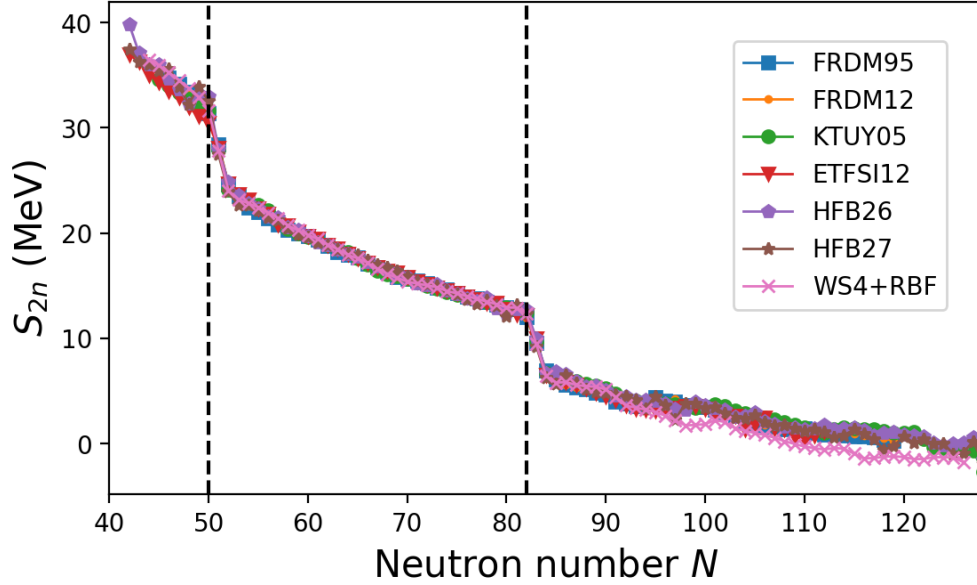


Figure 6.2: Two-neutron separation energies of Sn isotopes for all models discussed in Chapter 5. Two vertical dash lines signify magic numbers  $N = 50$  and  $N = 82$ .

treatment of all phenomena in a nucleus (deformation, Wigner effect, pairing, etc.) as complete as possible by adjusting its model parameters to the actual masses, which gives an overall satisfactory prediction. Thirteen mass models were studied using the I-G tool [BA93] and the DUZU model with spherical basis (DZ10sph) [DZ96] was chosen to be such a preferred model, because the *mass surface* can be displayed much more smoothly with this mass model.

The combination of *derivatives* and the use of difference between actual masses and the masses from a model enables practical extrapolation. As mentioned above, every point in the *derivative* plots involve two masses and one has to find out which one is the “culprit” that is responsible for the derailed point in any *derivative* plot. If one works on the mass difference plot, one can manipulate every single mass more easily.

The modification of any single point in one of the quadrant of the I-G plot will automatically update the other plots. Fig. 6.3 displays the experimental masses subtracted by the spherical DUZU model (DZ10sph) as a function of  $N$  and  $Z$ , the experimental two-neutron separation energies, and the experimental two-proton separation energies in four quadrants. It is rather remarkable to see that in the upper two quadrants the trends are very flat: the shell closure has been well considered by DZ10sph and no sudden drop in the plot is seen. As DZ10sph used the same shell strength for all nuclides at  $N = 50$ , a continuous increasing trend is noticed in the upper-left quadrant in Fig. 6.3 for

### 6.3. SUBTRACTING A MASS MODEL FROM THE EXPERIMENTAL MASS SURFACE

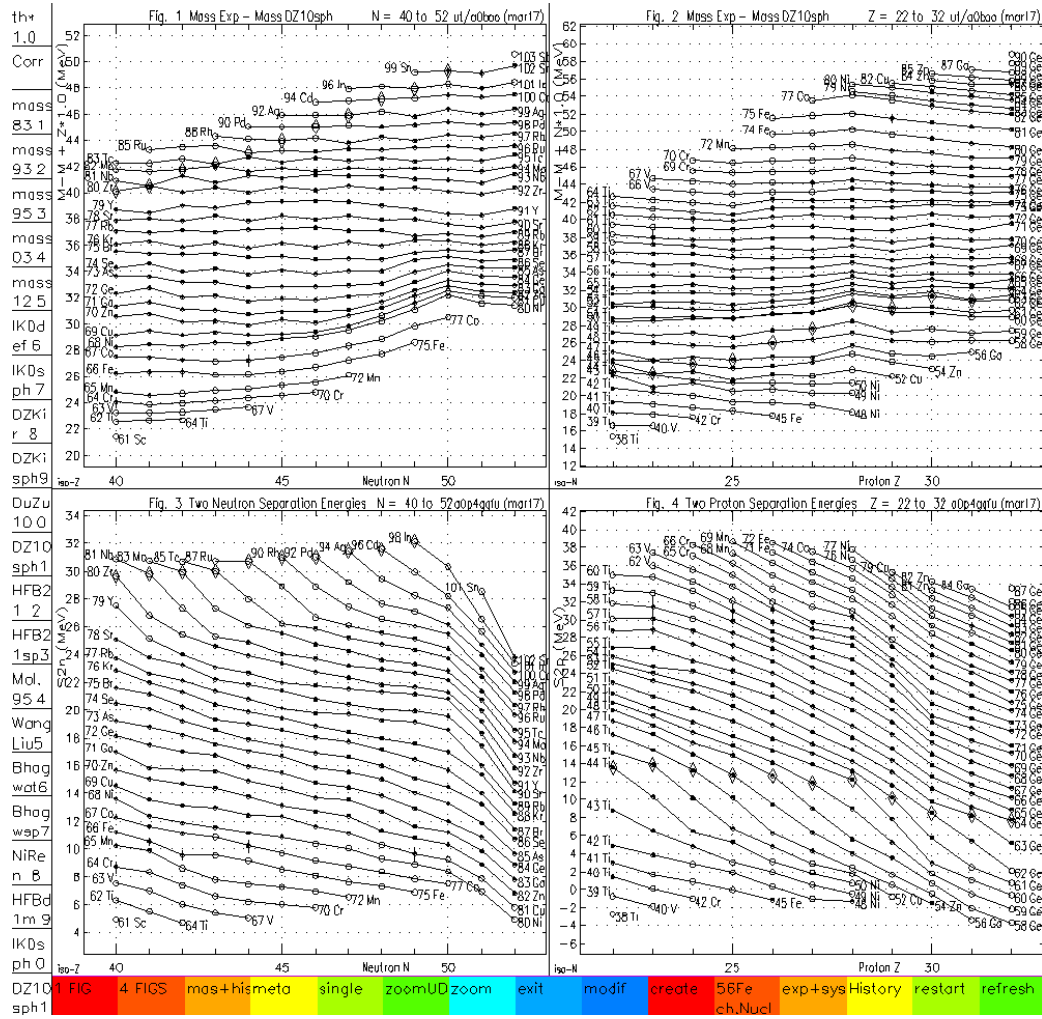


Figure 6.3: Display of the differences between experimental masses and the DUZU model as a function of  $N$  and  $Z$ , of the experimental two-neutron separation energies, and of the experimental two-proton separation energies in four quadrants.

decreasing  $Z$  due to shell quenching. However, such trends, as long as regular and smooth, would instead help extrapolation.

The extrapolation, which is based on the observation of different *derivatives* and the difference between actual masses and a formula, has been proven to be the most powerful tool to obtain still-unknown masses that are not too far (two or three mass unit) away from the last known mass. The root-mean-square deviation for all estimated masses in AME2012 that are known in AME2016 is 0.396 MeV (55 cases in total), which is smaller than any of the the mass model discussed in the previous chapter (see Table 5.4). However, such extrapolation, which strongly depends on the knowledge of the last known masses, has obvious shortcoming: if the mass value of the last known nuclide is wrong, and based on which the extrapolation is performed, erroneous extrapolation would propagate towards the unknown region.

For example, the masses of  $^{77-79}\text{Cu}$  were measured previously with precisions of 500 keV [HBGU+06]. However, the TMS suggested that  $^{77}\text{Cu}$  and  $^{79}\text{Cu}$  should be 320 keV and 1760 keV more bound, respectively. In AME2016, their results of  $^{77}\text{Cu}$  and  $^{79}\text{Cu}$  were replaced by estimated values (see Table C in [HAW+17]). Only the result of  $^{78}\text{Cu}$  was used.

Recently, the masses of copper isotopes  $^{75-79}\text{Cu}$  have been remeasured by the ISOLTRAP mass spectrometer [WAA+17]. Their resulting masses show that  $^{77}\text{Cu}$  and  $^{79}\text{Cu}$  are more bound by 240 keV and 670 keV, respectively, compared with the estimated values in AME2016. The extrapolation in AME2016 for the Copper isotopic chain was based on the mass values of  $^{76}\text{Cu}$  [GAB+07] and a poorly known mass of  $^{78}\text{Cu}$  [HBGU+06]. The results from [WAA+17] confirms the  $^{76}\text{Cu}$  mass in [GAB+07], while disagreeing with  $^{78}\text{Cu}$  in [HBGU+06] by  $\sim 300$  keV. For extrapolation, we first replace the poorly known mass ( $^{78}\text{Cu}$ ) and estimated masses ( $^{77}\text{Cu}$  and  $^{79}\text{Cu}$ ) by the new ISOLTRAP results [WAA+17]. And then extend the trend of the copper chain following that of the zinc isotopic chain. Since the masses of  $^{80-82}\text{Zn}$  were well known, we known roughly the position of successive copper masses after crossing the  $N = 50$  shell closure. The new mass surface is illustrated in Fig. 6.4, where the blue curve represents the new extrapolation. Based on the new results from [WAA+17], the estimated masses of  $^{80}\text{Cu}$ ,  $^{81}\text{Cu}$ , and  $^{80}\text{Cu}$  have been reduced by 480 keV, 490 keV, and 410 keV, respectively, compared with the AME2016 extrapolation. The isotopic chains of nickel, cobalt, iron, manganese, chromium and vanadium are also affected).

In this chapter, the extrapolation method in AME is described. Based on the smooth and regular observation of the *mass surface*, we can assign a mass to an unknown nuclide, given the regular behavior extends to the unknown regions. Such extrapolation routine strongly depends on the knowledge of the last known nuclide based on which the extrapolation is performed. In principle, AME make an estimate for the nuclide which has been observed or proven to exist. We notice that the predictive power of the AME extrapolation was studied previously in the literature (see Table I in [LPT03]) and the authors

### 6.3. SUBTRACTING A MASS MODEL FROM THE EXPERIMENTAL MASS SURFACE

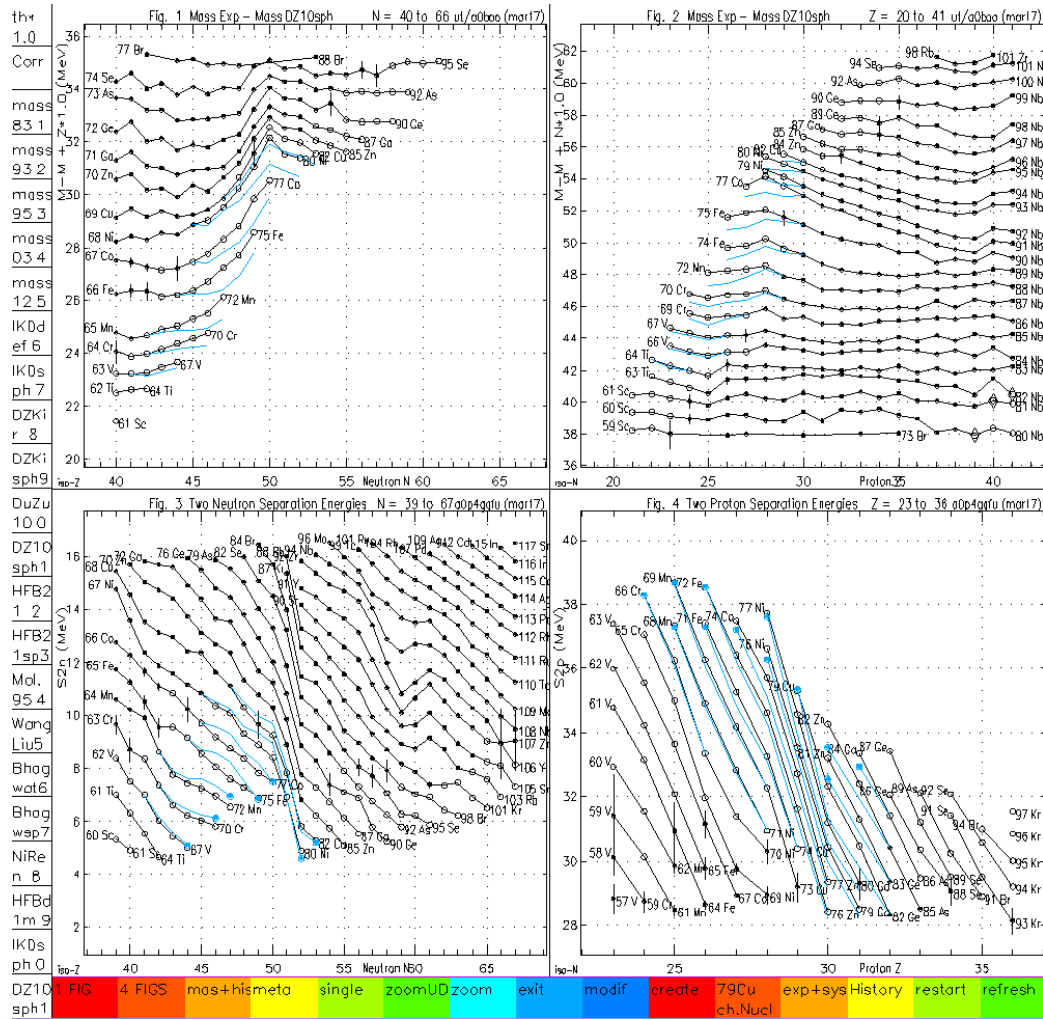


Figure 6.4: Four *derivatives* the same as Fig. 6.3 but zooming around  $^{79}\text{Cu}$ . New extrapolation (in blue) based on the results from [WAA<sup>+</sup>17].

demonstrated that the systematics-based predictions in AME are particularly accurate.



# Chapter 7

## Experiments

### 7.1 Principle of Ion Traps

The advantages of trapping ions are threefold. First, this allows observing the ion motion for an extended period of time until they decay. In this case, we can make the best use of the ions, especially for those that are produced in minute quantity. Secondly, the ions are confined in a small volume thus the inhomogeneity of the magnetic field has less effect on the stored-ion frequency. Thirdly, one can manipulate the stored ions using an external circuit for various purposes, such as cooling and excitation.

To achieve the confinement of ions in space, a potential minimum is required in three dimensions. A desirable confining force is the one which linearly depends on the distance between the stored ions and the center of the trap. This results in a harmonic potential for the confined ions. Fig. 7.1(b) displays the trapping configuration of a Penning trap, where a DC potential (providing axial confinement) is applied between a ring electrode and two end electrodes of hyperbolic shape. The direction of the homogeneous magnetic field (providing radial confinement) is aligned with the rotational symmetry. Ions can also be trapped without magnetic field. In this case, a radio-frequency (RF) voltage is applied between the ring electrode and the end caps (Fig. 7.1 (a)). Such a trap is called Paul trap or radio-frequency quadrupole (RFQ) trap. Besides the hyperbolic geometry, cylindrical Penning traps (Fig. 7.1 (c)) can also provide a quadrupole potential by applying appropriate voltages between ring segments.

### Ion Motion in a Penning trap

The ions in a magnetic field and a quadrupole electric potential perform three independent eigenmotions [BG86]: the harmonic oscillation along the trap axis at the axial oscillation frequency  $\omega_z$ , the modified cyclotron motion at frequency  $\omega_+$  and the magnetron motion at frequency  $\omega_-$ . The latter two

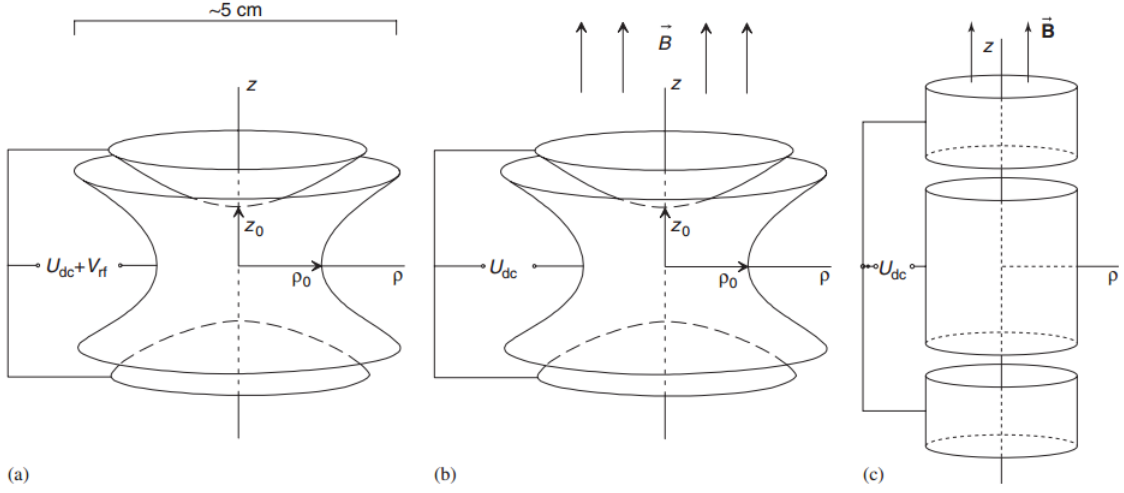


Figure 7.1: Hyperbolic electrode geometry of Paul trap (a) and Penning trap (b). Trapping of charged ions can be realized by applying a voltage difference between the ring electrode and the end electrodes. Penning traps can also have cylindrical electrodes (c). Figure from [Bla06].

motions are radial motions and perpendicular to the trap axis. Fig. 7.2 displays the ion motion in a Penning trap.

The three eigenfrequencies can be written as [BG86]:

$$\omega_z = \sqrt{\frac{qU_{dc}}{md^2}}, \quad (7.1)$$

$$\omega_+ = \frac{\omega_c}{2} + \sqrt{\frac{\omega_c^2}{4} - \frac{\omega_z^2}{2}}, \quad (7.2)$$

$$\omega_- = \frac{\omega_c}{2} - \sqrt{\frac{\omega_c^2}{4} - \frac{\omega_z^2}{2}}, \quad (7.3)$$

where  $U_{dc}$  is the voltage applied between the ring electrode and the two end caps, and  $d$  is the dimension of the trap  $d = \sqrt{(z_0^2) + \frac{\rho_0^2}{2}}$  ( $2\rho_0$  and  $2z_0$  are the inner ring diameter and the closest distance between the end caps, respectively, see Fig. 7.1 (b)).

By comparing the three eigenfrequencies, one can obtain the relations between the cyclotron frequency and the eigenfrequencies in a perfect quadrupole field:

$$\omega_c = \omega_+ + \omega_-, \quad (7.4)$$

and

$$\omega_c^2 = \omega_+^2 + \omega_-^2 + \omega_z^2. \quad (7.5)$$

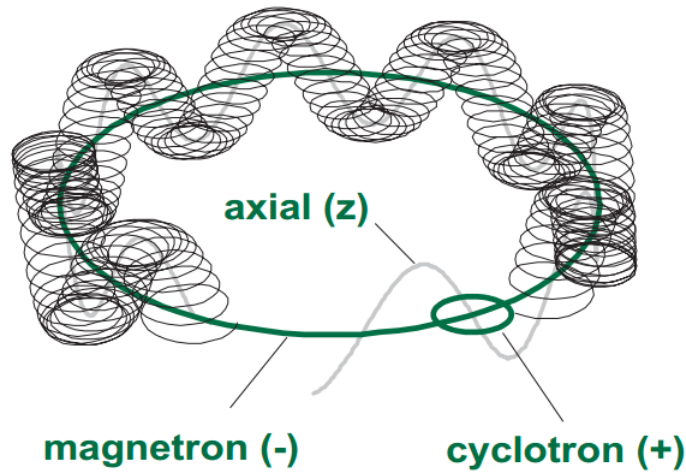


Figure 7.2: Sketch of ion motion in a Penning trap.

Thus, the mass of an ion can be determined either by measuring the sum of the two radial frequencies or by measuring the three independent eigenfrequencies. In this thesis, the relation in Eq. 7.4 is used to determine the masses.

## Cooling

Due to the imperfections of the real Penning trap, such as the opening holes for ion injection and ejection, or electrodes not extending infinitely, which would induce a higher-order multipole electric field, which renders Eq. 7.4 invalid, cooling is essential. Various ion cooling techniques such as resistive cooling, buffer gas cooling, laser cooling, etc., can reduce the amplitude of the ion motion and thus confine ions in a smaller volume. This is important for performing high-accuracy measurements, since ions probe less the imperfections of the electric and magnetic fields. For radioactive nuclides, buffer gas cooling is generally used. Since noble gases have high excitation potential, they are ideal choice to cool ions. By collisions with noble gas, such as helium, the hot ions lose energy and their motion can be damped. However, the situation in Penning traps becomes more complex. During cooling, the amplitudes of the axial and modified cyclotron motions will decrease while the amplitude of the magnetron motion\* will increase. Finally, the ions will hit the ring electrode and be lost. To counteract the outward radial diffusion caused by the buffer gas, one can use the side-band cooling technique [SBB<sup>+</sup>91]. By applying an RF voltage to the segmented ring electrode at the cyclotron frequency  $\omega_c = \omega_+ + \omega_-$ , the radial motions will couple with each other, i.e. the conversion between the modified cyclotron motion and the magnetron motion

\*. The maximum energy of the magnetron motion is at the center of the trap.

will take place periodically [BMSS90]. Since the modified cyclotron motion is damped faster than the magnetron motion, the ions can be recentered after a certain cooling time. Side-band cooling is mass selective and can be used to recenter the ions of interest and eliminate isobaric contaminations.

### Time-of-flight detection of the cyclotron resonance

There are various types of techniques to determine the cyclotron frequency. The one that is widely used for the radioactive nuclides is the time-of-flight detection of the ejected ion cyclotron resonance (TOF-ICR), which was first applied to the measurement of the mass ratio between proton and electron [GKT80]. The idea of TOF-ICR is to measure the cyclotron energy by measuring the time of flight of the ions through an inhomogeneous magnetic field. This technique, though destructive, is suitable for short-lived nuclides.

After being captured in the Penning trap, a dipole excitation is applied to the magnetron motion of the stored ions. After a certain period of time, the ions are first driven to a magnetron radius  $\rho_-$ . An azimuthal quadrupole rf-excitation is then applied for a time period  $T_{rf}$  at the sum of the radial frequencies  $\omega_c = \omega_+ + \omega_-$ , which converts the magnetron motion to the modified cyclotron motion [KBK<sup>+</sup>95]. After full conversion, the initial magnetron radius  $\rho_-$  is transferred completely to the modified cyclotron radius  $\rho_+$ . As the frequency of the modified cyclotron motion is generally much higher than that of the magnetron motion, the radial energy of the ion can be expressed as  $E_r(\omega_{rf}) \approx E_+(\omega_{rf}) = m/2\omega_+^2\rho_+^2(\omega_{rf})$ . At resonance, the ions gain maximum energy (maximum  $\rho_+$ ) while in the case of off-resonance, the ions gain less energy. After excitation, the ions are released axially from the center of the trap to a MCP detector, which is placed 1.2 m above. In the Penning trap, the magnetic moment of the ions  $\vec{\mu}(\omega_{rf}) = (E_r/B)\hat{z}$  is proportional to the radial energy and is conserved after ejection if the magnetic field in the drift path changes slowly. When ions pass through the magnetic field gradient outside the Penning trap, the interaction between the magnetic moment and the magnetic field gives rise to an accelerating force  $\vec{F} = -\vec{\mu}(\omega_{rf})(\vec{\nabla}\vec{B})$  on the ions. The detection technique is illustrated in Fig. 7.3

Therefore, if the rf field is at resonance with the ion cyclotron frequency, the ion will gain more energy and reach the detector faster than the off-resonance ions. This can be seen (see Fig. 7.4) from the minimum of the time of flight as a function of the excitation frequency.

A theoretical description of the line shape of the TOF from the trap center  $z_0$  to the detector position  $z_1$  for a given radial energy  $E_r$  as a function of the applied rf frequency is given in [KBK<sup>+</sup>95]:

$$T(\omega_{rf}) = \int_{z_0}^{z_1} \sqrt{\frac{m}{2(E_0 - q \cdot V(z) - \mu(\omega_{rf}) \cdot B(z))}} dz, \quad (7.6)$$

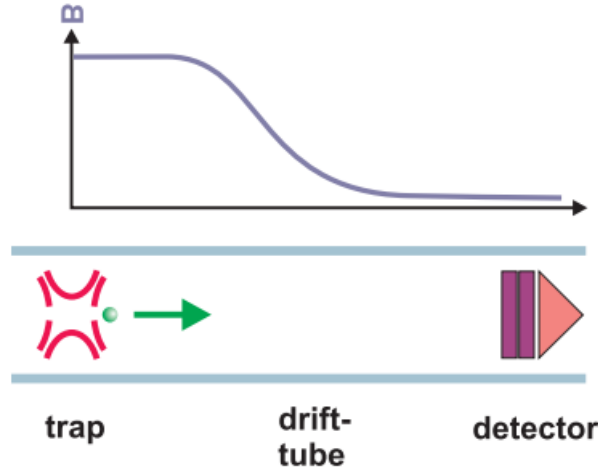


Figure 7.3: Illustration of the TOF-ICR technique

where  $E_0$  denotes the initial axial energy,  $V_z$  and  $B_z$  the electric and magnetic potential along the drift path, respectively.

## 7.2 Experimental setup at ISOLTRAP

The Penning trap mass spectrometer ISOLTRAP is located at the Isotope mass Separator On-Line facility ISOLDE at CERN. Radioactive nuclides are produced by the bombardment of a thick, heated target with 1.4-GeV proton beam from the CERN proton synchrotron (PS) booster. The resulting nuclides then pass through a transfer line and are ionized using different ionization techniques such as surface ionization, laser ionization (Resonance Ionization Laser Ion Source RILIS), or plasma ionization, depending on the chemical properties of the nuclides under investigation. After ionization, the ions are accelerated and mass-separated either by the High Resolution Separator (HRS) or General Purpose Separator (GPS), with mass resolving power of 5000 and 1000, respectively. The ion beam is then transported to the ISOLTRAP setup, see Fig 7.4

The ISOLTRAP setup consists of four traps [KAB<sup>+</sup>13]: a linear radio-frequency quadrupole cooler and buncher (RFQ), a multi-reflection time-of-flight mass separator/spectrometer (MR-TOF MS), a cylindrical preparation Penning trap and a hyperbolic precision Penning trap. The RFQ is placed at a voltage-flotable platform and used for stopping, cooling, and bunching the continuous ion beam with energy between 30 ~ 50 keV from ISOLDE. After a few milliseconds of accumulation, an ion bunch is ejected from the RFQ with a typical kinetic energy of  $E_{trans} \approx 3$  keV and transferred to the MR-TOF MS. In MR-TOF MS, the ions can be trapped by using the in-trap lift

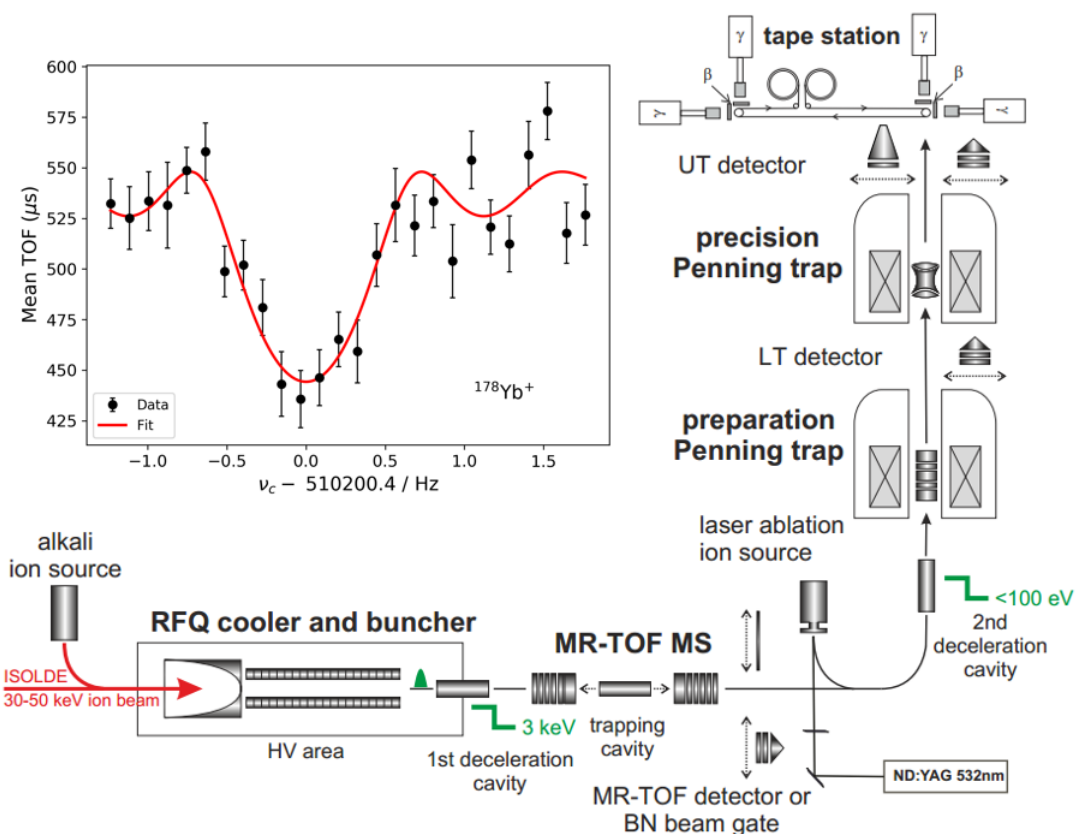


Figure 7.4: Schematic view of the ISOLTRAP setup [KAB<sup>+</sup>13]. See text for details.

technique [WMRS12], which reduces the kinetic energy of the ions to  $E_{\text{trap}} \approx 2$  keV. The contaminants can be separated after several hundred reflections between two electrostatic mirrors, based on the different mass-to-charge ratio. The ion beam is then ejected from the MR-TOF MS. If the ion beam is strongly contaminated by isobars, one can use a Bradbury-Nielsen gate to further suppress the contaminants. Subsequently, the ion beam is transferred upwards to the preparation Penning trap. Here the isobaric contaminants are removed by the mass-selective buffer gas cooling technique discussed above. Finally, the purified ion beam is transferred to the precision Penning trap for high-precision mass measurements.

### 7.3 Data analysis and discussions

The determination of the mass is carried out by measuring the cyclotron frequency of the stored ions:

$$\nu_c = \frac{1}{2\pi} \cdot \frac{qB}{m}. \quad (7.7)$$

In the precision Penning trap, a dipole excitation is first applied to the ion at its magnetron frequency, which brings the ions to a radius of about 0.7 mm. And then a quadrupole rf excitation at  $\nu_c = \nu_+ + \nu_-$  is applied for an excitation time  $T_{rf}$  to the ion, which converts the magnetron motion to the reduced cyclotron motion. The cyclotron frequency of the ions of interest is extracted by fitting the data by the theoretical line shape in Eq. 7.6. To obtain the time-of-flight spectrum, the frequency of the rf field has to be scanned around the ion's cyclotron frequency. The time of flight of the ions from the center of the precision Penning trap to the MCP detector is recorded.

A TOF-ICR spectrum of  $^{178}\text{Yb}$  is displayed in the insert figure in Fig. 7.4, where the excitation time was set to  $T_{rf} = 1.2$  s. The x-axis denotes the quadrupole rf-excitation frequency and y-axis represents the mean time of flight. The black points represent the experimental data and the red curve is the theoretical line shape in Eq. 7.6. To calibrate the magnetic field, the cyclotron frequency  $\nu_{c,ref}$  of an ion with well-known mass, either from an alkali ion source or a laser ablation ion source, is measured before and after the measurement of the ion of interest. To compensate the slow drift of the magnetic field, the cyclotron frequency of the reference ion is interpolated to the time when the ion of interest is measured.

Table 7.1: Experimental details in the production of the ions of interest. Listed are the experiment date, the target, the ionization technique, the ion energy from ISOLDE, and the mass separator used.

Species	Date	Target	Ion source	Energy	Separator
$^{168}\text{Lu}$	Jun 2011	Ta	W surface	50 keV	GPS
$^{178}\text{Yb}$	Oct 2011	Ta	RILIS	30 keV	HRS
$^{160}\text{Yb}$ , $^{140}\text{CeO}$ , $^{140}\text{NdO}$ , $^{156}\text{Dy}$	Aug 2014	Ta	W surface	30 keV	GPS
$^{52,55-57}\text{Cr}$ , $^{55}\text{Mn}$	Oct-Nov 2014	UCx	Ta surface	30 keV	HRS
$^{75,77-79}\text{Ga}$	Jun 2015	UCx-n	Ta surface	30 keV	HRS
$^{52}\text{Cr}$	Apr 2016	UCx	Ta surface	30 keV	HRS
$^{53}\text{Cr}$			RILIS		
$^{54}\text{Cr}$					
$^{55}\text{Mn}$			Ta surface		

The atomic mass of the nuclide of interest  $m$  can be derived by:

$$m = r \cdot (m_{ref} - m_e) + m_e, \quad \text{with} \quad r = \frac{\nu_{c,ref}}{\nu_c}, \quad (7.8)$$

where  $m_{ref}$  is the mass of the reference nuclide and  $m_e$  is the electron mass. The electron binding energy can be neglected in the current analysis. Apart from the statistical uncertainty, the known error and uncertainty have to be taken into account. The two main contributions are the mass-dependent shift and

the short-term fluctuation of the magnetic field [KBB<sup>+</sup>03]. The imperfection of the electric quadrupole field and the misalignment of the precision trap axis with respect to the the magnetic field axis can bring about a frequency shift, if the masses of the ion of interest and the reference ion are not the same. The magnitude of the mass-dependent shift was determined to be [KBB<sup>+</sup>03]:

$$\frac{\varepsilon_m(r)}{r} = -1.6(4) \times 10^{-10}/u \times (m - m_{ref}). \quad (7.9)$$

This correction should be applied to the frequency ratio  $r$ . In the current analysis, the absolute value of  $\frac{\varepsilon_m(r)}{r}$  is also added quadratically to the statistical uncertainty of the frequency ratio  $r$ .

Another source of uncertainties comes from the magnetic-field drift. Due to the change of temperature, pressure, and the ferromagnetic materials near the magnet, the strength of the magnetic field can change over time. This effect can be minimized by shortening the time interval between the measurements of the frequencies of the ions of interest and the reference ion. However, it would only eliminate the long-term, slow decay of the magnetic field. The magnitude of the short-term fluctuation was determined to be [KBB<sup>+</sup>03]:

$$\frac{u_B(\nu_{ref})}{\nu_{ref}} = 6.35(45) \times 10^{-11}/\text{min} \times \Delta T, \quad (7.10)$$

where  $\Delta T$  is the time interval between the two frequency measurements of the reference ions. After considering all the known uncertainties, the systematic uncertainty was determined from the cross-reference carbon cluster measurements to be [KBB<sup>+</sup>03]:

$$\frac{u_{ref}(r)}{r} = 8 \times 10^{-9}. \quad (7.11)$$

This is the current precision that ISOLTRAP can reach for the TOF-ICR technique.

Besides the traditional TOF-ICR technique, Ramsey's method of separated oscillatory fields [GBB<sup>+</sup>07] were employed to excite the ion's cyclotron motion. The idea of the Ramsey-type excitation is to use two rf pulses separated by a waiting time. Such excitation scheme allows reducing the line width by around 60% and the statistical uncertainty of the cyclotron frequency by a factor of three, given the excitation time and the number of the recorded ions are the same [GBB<sup>+</sup>07]. Fig 7.5a displays the TOF spectrum of <sup>57</sup>Cr using the Ramsey-type excitation, where the excitation time is 100 ms for both rf pulses and the waiting time is 1 s. Prior to performing the Ramsey-type excitation, the cyclotron frequency should be known. In this case, a traditional TOF-ICR spectrum was taken (see Fig. 7.5b). As we can see from the Fig. 7.5a, the TOF spectrum is symmetric with respect to the central frequency. Moreover, the Ramsey fringes are more prominent than the sidebands in Fig. 7.5b, which permits to determine the cyclotron frequency more precisely. The red curve represents the theoretical line shape for the Ramsey scheme [Kre07].

The newly developed Phase-Imaging Ion-Cyclotron-Resonance technique [EBB<sup>+</sup>13] has been tested recently at ISOLTRAP [Kar17].

The mass measurements in this thesis stem from several experimental campaigns between 2011 and 2016. The related information is listed in Table 7.1. The cyclotron frequency ratios of the ions of interest and the related reference ion are listed in Table 7.2, together with the derived masses of the nuclides. Since some of the data were already included in AME2016, values from the mass table of AME2012 are given instead for comparison. The half-lives of all the nuclides, extracted from [AKM<sup>+</sup>17], are also listed.

In the following, all the masses and their discrepancies will be discussed in detail. The TOF-ICR spectra for all the nuclides are listed in Appendix B.

Table 7.2: Frequency ratios between the ions of interest and reference ions.

Nuclide	$T_{1/2}$	Ref	$r = \frac{\nu_{c.ref}}{\nu}$	ME (keV)		$\Delta$ ME (keV)
				ISOLTRAP	AME2012	
<sup>140</sup> CeO <sup>*</sup>	Stable	<sup>133</sup> Cs	1.173017796(19)	-92809.0(2.3)	-92816.2(2.2)	7.2(3.2)
<sup>140</sup> NdO <sup>*</sup>	3.34 d	<sup>133</sup> Cs	1.173048610(26)	-88994.3(3.2)	-88991(26)	-3(26)
<sup>156</sup> Dy <sup>*</sup>	Stable	<sup>133</sup> Cs	1.173197811(34)	-70523.1(4.2)	-70528.3(1.6)	5.2(4.5)
<sup>160</sup> Yb <sup>*</sup>	4.8 m	<sup>133</sup> Cs	1.203394356(44)	-58163.2(5.5)	-58165(16)	2(17)
<sup>168</sup> Lu <sup>m</sup>	6.7 m	<sup>133</sup> Cs	1.263597908(46)	-56908.2(5.8)	-56870(39)	-38(40)
<sup>178</sup> Yb	74 m	<sup>85</sup> Rb	2.095672299(110)	-49663.1(8.7)	-49694(10)	31(13)
<sup>52</sup> Cr <sup>*</sup>	Stable	<sup>39</sup> K	1.333053034(12)	-55419.7(0.4)	-55418.1(0.6)	-1.6(0.8)
<sup>52</sup> Cr		<sup>85</sup> Rb	0.6116970566(67)	-55419.4(0.5)		-1.2(0.8)
<sup>53</sup> Cr	Stable	<sup>85</sup> Rb	0.6234757106(68)	-55288.8(0.5)	-55285.9(0.6)	-2.9(0.6)
<sup>54</sup> Cr	Stable	<sup>85</sup> Rb	0.6352318839(81)	-56936.4(0.6)	-56933.7(0.6)	-2.7(0.7)
<sup>55</sup> Cr <sup>b,*</sup>	3.497 m	<sup>85</sup> Rb	0.6470319500(225)	-55112.3(1.8)	-55108.6(0.6)	-3.6(1.9)
<sup>56</sup> Cr <sup>*</sup>	5.94 m	<sup>56</sup> Fe	1.000102145(9)	-55284.4(0.7)	-55281.2(1.9)	-3.2(2.0)
<sup>57</sup> Cr <sup>b,*</sup>	21.1 s	<sup>85</sup> Rb	0.6706186690(233)	-52525.0(1.8)	-52524.1(1.9)	-0.8(2.6)
<sup>55</sup> Mn	Stable	<sup>85</sup> Rb	0.646999088(9)	-57711.5(0.7)	-57711.7(0.4)	0.2(0.9)
<sup>55</sup> Mn <sup>b,*</sup>		<sup>85</sup> Rb	0.6469990510(225)	-57714.4(1.8)		-2.7(1.8)
<sup>59</sup> Fe <sup>*</sup>	44.495 d	<sup>85</sup> Rb	0.694069772(13)	-60664.1(1.0)	-60664.2(0.5)	0.1(1.1)
<sup>75</sup> Ga <sup>R</sup>	126 s	<sup>85</sup> Rb	0.882403259(9)	-68460.6(0.7)	-68464.6(2.4)	4.0(2.5)
<sup>77</sup> Ga	13.2 s	<sup>85</sup> Rb	0.905988440(53)	-65995.0(4.2)	-65992.3(2.4)	-2.6(4.9)
<sup>78</sup> Ga	5.09 s	<sup>85</sup> Rb	0.917794409(14)	-63704.0(1.1)	-63706.0(1.9)	2.0(2.2)
<sup>79</sup> Ga	2.848 s	<sup>85</sup> Rb	0.929586018(20)	-62548.8(1.6)	-62547.7(1.9)	-1.1(2.5)

<sup>m</sup> Assigned to the  $J^\pi = 3^+$  isomeric state.

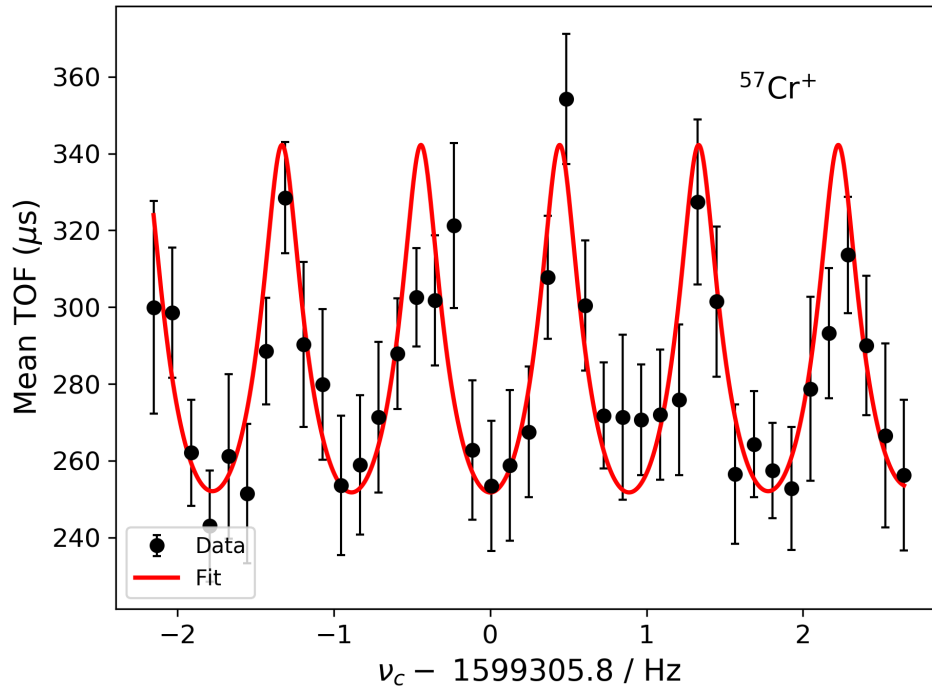
<sup>R</sup> Measured by Ramsey's method.

<sup>b</sup> Extra systematic error was added to account for helium-filling.

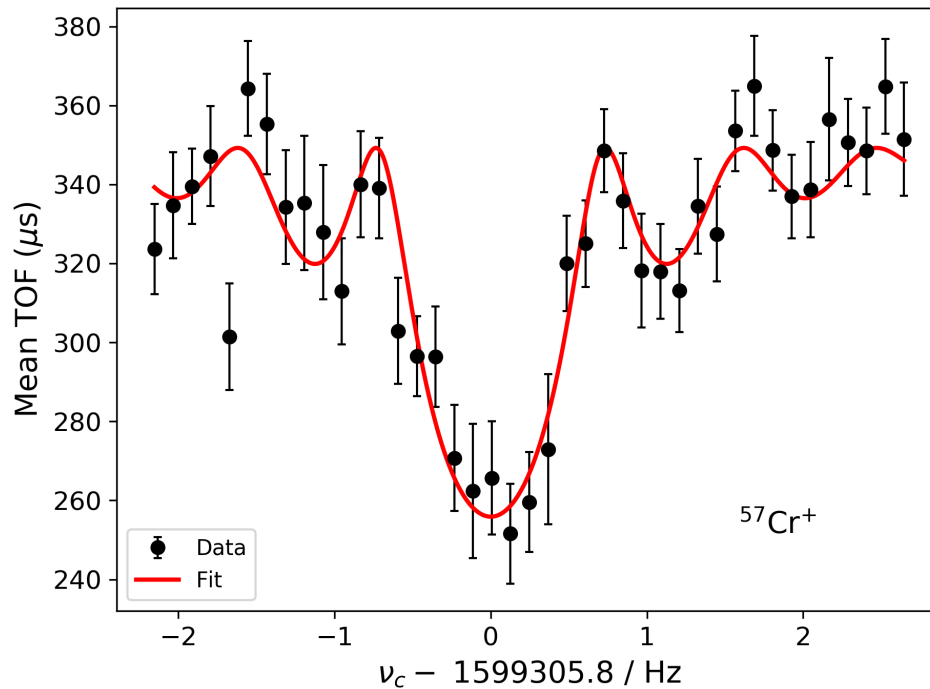
\* Already included in AME2016.

## <sup>168</sup>Lu

Two isomers were reported in <sup>168</sup>Lu [CCP<sup>+</sup>72] with half-lives of 5.5 min ( $J^\pi = 6^-$ ) and 6.7 min ( $J^\pi = 3^+$ ). In that experiment, the authors obtained two distinct  $\beta^+$  spectra. The excitation energy for the higher isomeric state



(a) TOF-ICR spectrum using a two-pulse Ramsey scheme with two 100 ms duration times and 1 s waiting time.



(b) TOF-ICR spectrum with excitation time  $T_{rf} = 1.2$  s.

Figure 7.5: Time-of-flight spectrum of  $^{57}\text{Cr}$ .

( $J^\pi = 3^+$ ) was determined to be 220(130) keV from two endpoint energies. In 1997, the level scheme of  $^{168}\text{Lu}$  was re-investigated [BATH97]. The intensity of a  $\gamma$  transition of 202.8 keV was determined to be 0.86(0.21) per 100 decays, which is much lower than the prediction [CCP<sup>+</sup>72]. The authors in [BATH97] concluded that: “*This transition is very weak in the  $\gamma$  channel: it was only observed in the total sum spectrum of all irradiations, so it was considered doubtful ...*” No other transition from a low-spin state in the neighborhood of 220(130) keV was reported. This  $\gamma$ -ray might be interpreted as the transition between the two isomeric state.

The production yields of the rare-earth nuclides were studied at ISOLTRAP [BAA<sup>+</sup>00]. By the measurements of the  $\gamma$ -line intensities, the relative production ratio between the isomeric state and the ground state for  $^{168}\text{Lu}$  was determined to be  $\sim 20 : 1$  (see Table 7 in [BAA<sup>+</sup>00]). However, no mass information concerning  $^{168}\text{Lu}$  was given. The only direct mass measurement of  $^{168}\text{Lu}$  was performed using Schottky mass spectrometry [LGR<sup>+</sup>05] at GSI with precision of 28 keV, while no excited isomeric state was reported.

In the current study, we tried to produce two states in  $^{168}\text{Lu}$  using the bombardment of proton beams on a tantalum target, the same production mechanism as in [BAA<sup>+</sup>00], and measure the masses of the two states directly at ISOLTRAP. Fig. 7.6a shows the TOF-ICR spectrum of  $^{168}\text{Lu}$  with excitation time  $T_{rf} = 1.2$  s. We notice that there exists only one resonance. To separate two states which differ by  $\sim 200$  keV, the minimum resolving power  $R_{min} = 168 \times 931.494 \times 1000 / 200 \sim 7.8 \times 10^5$  is required. The resolving power of the precision Penning trap at  $T_{rf} = 1.2$  s is  $R = 1.25 \times 540607 \times 1.2 \approx 8.1 \times 10^5$ . Since the resolving power of the current setting is merely larger than  $R_{min}$ , the two states could be mixed together.

To avoid the possibility of mixing two resonances, we increased the excitation time to  $T_{rf} = 3$  s, which would increase as a consequence the resolving power by a factor of 2.5. The TOF-ICR spectra at  $T_{rf} = 3$  s is shown in Fig. 7.6b. One notices that the width of the resonance at  $T_{rf} = 3$  s did not reduce significantly. It was due to the collisions between the ions and the rest gas atoms, as the ions were stored for a longer time. It is clear that, even though the rest gas might play a role, only one resonance was found and no trace of a second minimum TOF was seen.

Based on the previous study [BAA<sup>+</sup>00], where the isomeric state of  $^{168}\text{Lu}$  was populated a factor of 20 higher than the ground state, the resonance peak in Fig. 7.6 is assigned to the isomeric state. The arrows in Fig. 7.6 indicate the position of the expected ground state, if produced. Based on the fact that no second resonance is visible, we are convinced that only the isomeric state was produced in the experiments. If the ground state were produced, as the excitation time was increased to  $T_{rf} = 3$  s, a second peak would have appeared at the corresponding position indicated by the arrows in Fig. 7.6.

The mass for the  $^{168}\text{Lu}$   $J^\pi = 3^+$  isomeric state is determined to be  $-56908.2(5.8)$  keV, which is in agreement with the result of  $-56922(28)$  keV

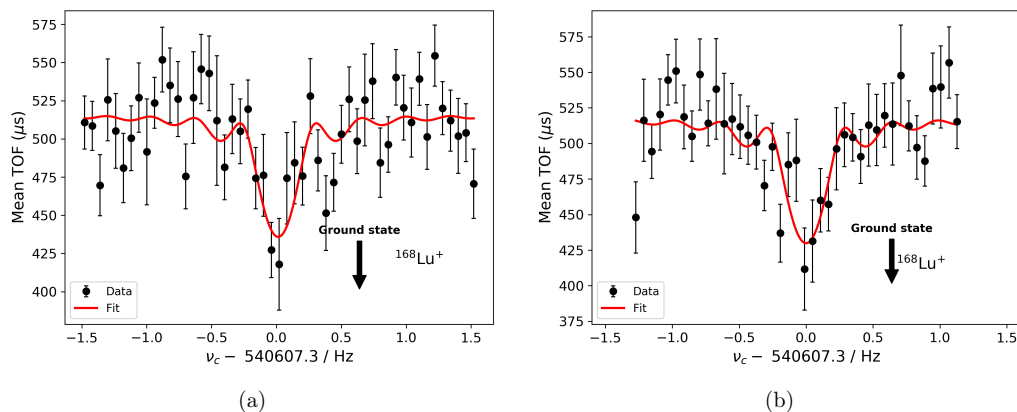


Figure 7.6: TOF-ICR spectra for  $^{168}\text{Lu}$ . Two excitation times are taken:  $T_{rf} = 1.2$  s (a) and  $T_{rf} = 3$  s (b). The arrows indicate the position of the expected ground state.

from the Schottky measurement [LGR<sup>+</sup>05], where  $^{168}\text{Lu}$  was produced by the fragmentation of a bismuth target and its mass was assigned to the ground state. In AME2012, it was assumed that the result from the Schottky measurement could suffer from the mixture of two isomeric states that its value was corrected by evaluators to  $-57023(65)$  keV for the ground state. Combining the isomeric-state mass of  $^{168}\text{Lu}$  in the current analysis with the mass value for the ground state in AME2012 yields the excitation energy of the isomeric state of  $160(40)$  keV, which is compatible with the excitation energy deduced from the two *endpoint* energies [CCP<sup>+</sup>72]

### $^{178}\text{Yb}$

$^{178}\text{Yb}$  is the last known nuclide in the ytterbium isotopic chain. Its mass was determined from a  $^{176}\text{Yb}(t,p)$  reaction [ZBM<sup>+</sup>82] with a precision of 10 keV. The new ISOLTRAP value shows a difference of  $31(13)$  keV from the reaction value. As mentioned before, the mass derived from a reaction depends also on the other masses. Sometimes, the recalibration could change a mass by around 20 keV (the reaction  $Q$ -value will not change) if new masses are used for the nuclides involved in the reaction. In [ZBM<sup>+</sup>82], the reaction was calibrated using two reference reactions  $^{12}\text{C}(t,p)^{14}\text{C}$  and  $^{16}\text{O}(t,p)^{18}\text{O}$ . Since the masses of all the involved nuclides were well known at that time, such a difference cannot be due to recalibration.

Fig. 7.7 displays the two-neutron separation energy in the ytterbium region. For isotopic chains with high  $Z$  number Hf ( $Z = 72$ ), Ta ( $Z = 73$ ), and W ( $Z = 74$ ), the regular behavior of  $S_{2n}$  breaks down at  $N = 108$ , which was interpreted in terms of an energy gap above the Nilsson single-particle level  $\frac{9}{2}^+$  [624] [BMS<sup>+</sup>73]. Above  $N = 107$ , the  $S_{2n}$  value at  $^{178}\text{Yb}$  ( $Z = 70$ ) remains

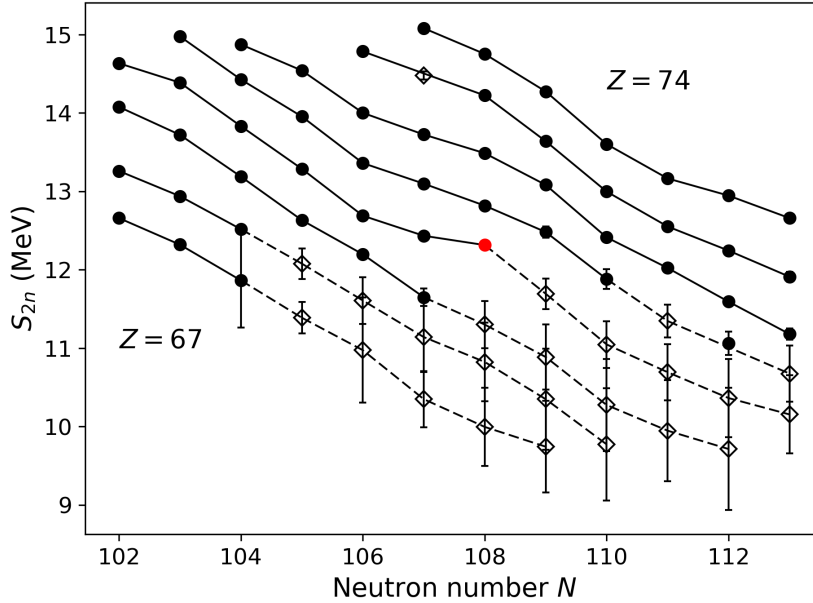


Figure 7.7: Two-neutron separation energy in the ytterbium region between (Ho ( $Z = 67$ ) and W ( $Z = 74$ )). The experimental data are denoted by black circles, estimated masses are denoted by empty diamonds, and the red circle represents the new  $^{178}\text{Yb}$  mass.

almost unchanged, which means extra binding is gained in  $^{178}\text{Yb}$ . Even though the new ISOLTRAP result for  $^{178}\text{Yb}$  differs from the reaction value [ZBM<sup>+</sup>82] by 31(13) keV, the extra binding energy of  $\sim 440$  keV is confirmed. A sudden flattening of  $S_{2n}$  could be explained as Quantum Phase Transition (QPT) in atomic nuclei [Cas09]. For example, the discontinuity of  $S_{2n}$  at  $N \sim 90$  in  $^{60}\text{Nd}$ ,  $^{62}\text{Sm}$ , and  $^{64}\text{Gd}$  [DSI80] signals the spherical-deformed transition region. And the transition phenomenon can also be seen as a striking change of  $R_{4/2} \equiv E(4_1^+)/E(2_1^+)$  for the  $^{60}\text{Nd}$ ,  $^{62}\text{Sm}$ , and  $^{64}\text{Gd}$  isotopic chains (see Fig. 3 of [CWBG81]), where  $E(4_1^+)$  and  $E(2_1^+)$  are the excitation energies of the first  $4^+$  and  $2^+$  states, respectively. In the current mass region,  $^{176}\text{Tm}$  ( $Z = 69$ ) is the last known nuclide of thulium. Its mass came from a  $\beta^-$  decay [67Gu11] with poor precision of 100 keV. The  $S_{2n}$  at  $^{176}\text{Tm}$  decreases significantly compared to other nuclides at  $N = 107$ . This nuclide is poorly known, it could be an excited isomeric state. In lower  $Z$  region, neither mass information nor spectroscopic data is available after  $N = 105$ . To clarify if there exists also a phase transition in the ytterbium region at  $N = 108$ , more experiments are called for in this mass region.

### Other rare-earth masses

In AME2012, the mass of  $^{140}\text{Ce}$  was determined by several methods. The ISOLTRAP result of  $^{140}\text{Ce}$  (cerium oxide) differs from the value in AME2012 by 7.2(3.2) keV. However, this mass was included in AME2016, and the global adjustment shows that it agrees with the adjusted value within  $1.2\sigma$ .

The mass of  $^{140}\text{Nd}$  (neodymium oxide) agrees well with the previous Schottky measurement [LGR<sup>+</sup>05]. And the precision is improved by a factor of 8.

In AME2012, the mass of  $^{156}\text{Dy}$  was mainly determined by Penning trap spectrometry at SHIPTRAP [EGB<sup>+</sup>11]. The ISOLTRAP result agrees with their value within  $1.2\sigma$ .

The mass of  $^{160}\text{Yb}$  was previously measured by ISOLTRAP [BAA<sup>+</sup>01]. The new result agrees with the previous one perfectly and the precision is improved by a factor of almost three.

### Chromium masses

Table 7.3: Influences of the ISOLTRAP results and the adjusted chromium masses.

Nuclide	ISOLTRAP	Influence %	Adjusted Mass	$v/s$
$^{52}\text{Cr}$	-55419.7(0.4)	27	-55419.82(0.23)	0.3
	-55419.4(0.5)	21		-0.8
$^{53}\text{Cr}$	-55288.8(0.5)	24	-55287.68(0.23)	2.5
$^{54}\text{Cr}$	-56936.4(0.6)	18	-56935.44(0.24)	1.6
$^{55}\text{Cr}$	-55112.3(1.8)	0	-55110.39(0.30)	1.1

The masses of  $^{52-57}\text{Cr}$  were measured in two experimental campaigns in 2014 and 2016. The results show that the determined masses of the chromium isotopes are systematically smaller than the values in AME2012 (see Table 7.2). In AME2012, the masses from  $^{52}\text{Cr}$  to  $^{55}\text{Cr}$  were mainly determined by a series of  $(n,\gamma)$  reactions with precision better than 0.3 keV. A  $(p,\gamma)$  reaction also plays a role in the determination of the mass of  $^{54}\text{Cr}$ . Other reactions contribute much less to the chromium mass region under discussion. As both the Penning trap measurements and the reaction measurements have comparable precision, the origin of these differences remains unclear. In this case, to quantify the influences of the new measurements on the existing chromium masses, all the chromium results were included in the global adjustment. The influences of the ISOLTRAP results and the adjusted masses of  $^{52-55}\text{Cr}$  are listed in the third and the fourth column of Table 7.3, followed by  $v/s$  in the fifth column. The results from the global adjustment shows that the masses

of  $^{52}\text{Cr}$ ,  $^{54}\text{Cr}$ , and  $^{55}\text{Cr}$  in the current analysis agree with the adjusted masses within  $1.6\sigma$ , while the mass of  $^{53}\text{Cr}$  differs from the adjusted one by  $2.5\sigma$ .

Fig. 7.8 displays the flow of information diagram in the chromium region, where the numbers in black represents the evaluation outcome in AME2012, while the numbers in blue represent the new evaluation results. We can see from Fig. 7.8 that the mass of  $^{53}\text{Cr}$  is now determined by  $^{52}\text{Cr}(n,\gamma)$  (42.9%),  $^{53}\text{Cr}(n,\gamma)$  (32.6%) and the ISOLTRAP result (24.5%). The discrepancy originates from the mass difference between  $^{52}\text{Cr}$  and  $^{53}\text{Cr}$ . The  $Q$  value for  $^{52}\text{Cr}(n,\gamma)^{53}\text{Cr}$  is determined to be 7940.5(0.6) keV based on the ISOLTRAP results. However, this value is not consistent with the three input values 7939.5(0.3) keV [IKKP80], 7939.0(0.2) keV [KCL80] and 7939.1(0.3) keV [INT07], which give the average value 7939.15(0.14) keV. The difference between the ISOLTRAP result and the average input value is 1.6(0.6) keV.

Using the masses of  $^{53}\text{Cr}$  and  $^{54}\text{Cr}$ , the  $Q$  value for the reaction  $^{53}\text{Cr}(n,\gamma)^{54}\text{Cr}$  can be derived to be 9718.9(0.7) keV. In AME2012, this reaction  $Q$  value was the average of four results<sup>†</sup> 9719.3(0.2) keV [WGB68], 9718.3(0.4) keV [LT72], 9718.9(0.3) keV [IKKP80], and 9719.7(0.5) keV [Hof89], which gives the average value of 9719.14(0.13) keV. The ISOLTRAP result for the reaction  $Q$  value of  $^{53}\text{Cr}(n,\gamma)^{54}\text{Cr}$  is in agreement with the four average values.

The mass of  $^{53}\text{Cr}$  was measured in the same run as  $^{52}\text{Cr}$ ,  $^{54}\text{Cr}$ , and  $^{55}\text{Mn}$ . The  $v/s$  values for the later three nuclides are within  $1.5\sigma$  with respect to the new adjustment. We found no reason for the discrepancy of  $^{53}\text{Cr}$ . For the moment, the Penning-trap mass of  $^{53}\text{Cr}$  and the three  $^{52}\text{Cr}(n,\gamma)$  reaction  $Q$  values are used to determine the mass of  $^{53}\text{Cr}$ . Remeasurements of the mass of  $^{53}\text{Cr}$  is highly desired to clarify this discrepancy.

Including all the ISOLTRAP results for the chromium masses in the global adjustment, the precision of all the masses of  $^{52-55}\text{Cr}$  has been improved by a factor of two, which is indicated in the lower-right corner of each box in Fig. 7.8.

The masses of  $^{56}\text{Cr}$  and  $^{57}\text{Cr}$  were measured previously by ISOLTRAP [GAB<sup>+</sup>05]. The new ISOLTRAP results differ from the previous ones by  $-3.2(2.0)$  keV and  $-0.8(2.6)$  keV, respectively. The results obtained from the current analysis agree well with the old results but the uncertainty of the mass of  $^{56}\text{Cr}$  is improved by a factor of three.

## Gallium masses

The masses of  $^{75,77-79}\text{Ga}$  were measured previously by ISOLTRAP [07Gu09]. The new measurements for these gallium isotopes agree with the previous results within  $1.6\sigma$ . The precision for  $^{75}\text{Ga}$  is three times higher than the previous result.

<sup>†</sup>. The original values were recalibrated by Wapstra.

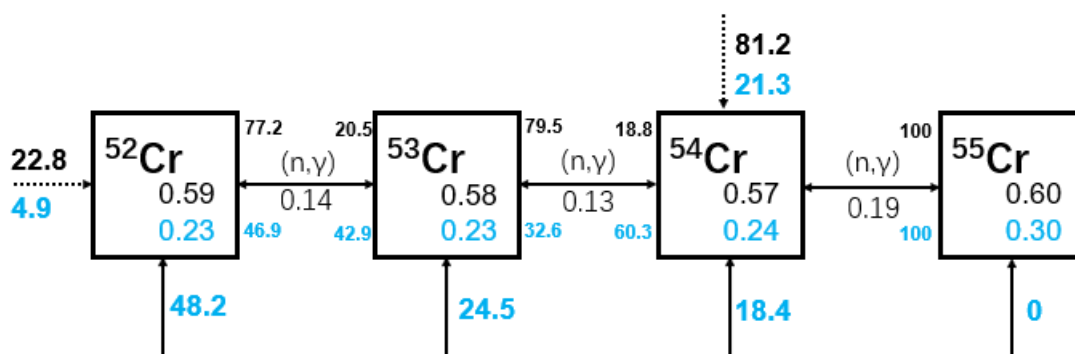


Figure 7.8: Flow of information diagram for the chromium masses from  $A = 52$  to  $A = 55$ . Each box represents a nuclide, with the mass uncertainty (in keV) in the lower right corner. The numbers in black represent the old evaluation in AME2012, and numbers in blue represent the new evaluation including the new chromium results. The numbers in blue in the lower parts indicate the influences the current data on the corresponding nuclides. The dash arrows indicate the contribution from other experiments.

### $^{55}\text{Mn}$ and $^{59}\text{Fe}$

The mass of  $^{55}\text{Mn}$  was well-known in AME2012 with a precision of 0.4 keV. The two measurements of  $^{55}\text{Mn}$  in 2014 and 2016 differ from the AME2012 value by  $-2.7(1.8)$  keV and  $0.2(0.9)$  keV, respectively, within  $1.5\sigma$ .

The mass of  $^{59}\text{Fe}$  was determined to be  $-60664.2(0.5)$  keV in AME2012 by  $(n,\gamma)$  reactions. Our value of  $-60664.1(1.0)$  agrees perfectly with the recommended values.

All the results in this thesis have been included in the AME adjustment. We can obtain the  $v/s$  values for 16 out of 20 cases: eight cases smaller than one, seven cases between one and two, and one case between two and three. The reduced chi-square is determined to be 1.2, to which the discrepancy of  $^{53}\text{Cr}$  contributes the most.

# Chapter 8

## Systematic error studies of the MR-TOF MS at ISOLTRAP

### 8.1 Principle of MR-TOF MS

The MR-TOF device serves as a versatile tool for mass determination. It can be used as a mass separator before the preparation Penning trap, and most importantly, it can be used as a mass spectrometer. For nuclides with half-lives below 100 ms, the MR-TOF MS is superior to the Penning trap spectrometry with its higher resolving power [WWA<sup>+</sup>13].

Ions with different mass-to-charge ratio ( $m/q$ ) can be separated from each other longitudinally if they are accelerated by the same potential  $U$ , from which the ions acquire kinetic energy:

$$E_k = qU = mv^2/2. \quad (8.1)$$

The MR-TOF MS can be tuned in such a way that the time of flights are independent of the energies of the ions and depend only on their mass-over-charge ratios (isochronicity). The time of flights, after passing through the same length, are mass dependent:  $t \propto 1/v \propto \sqrt{m}$ , assuming  $q = 1$ .

The relation between the mass-to-charge ratio and the TOF can be determined as follows:

$$t = \alpha(m/q)^{1/2} + \beta, \quad (8.2)$$

where  $\alpha$  and  $\beta$  are two parameters related to the MR-TOF device. The TOF spectrum can be transformed into a mass spectrum by measuring the TOFs of two reference ions with well-known masses:

$$t_1 = \alpha(m_1/q)^{1/2} + \beta, \quad t_2 = \alpha(m_2/q)^{1/2} + \beta, \quad (8.3)$$

from which  $\alpha$  and  $\beta$  can be determined.

We introduce a parameter [WBB<sup>+</sup>13a]:

$$C_{TOF} = (2t - t_1 - t_2)/2(t_1 - t_2), \quad (8.4)$$

where  $t$ ,  $t_1$  and  $t_2$  are the TOFs of the ion of interest and the two reference ions, respectively. Then the unknown mass is:

$$m^{1/2} = C_{TOF}\Delta_{ref} + \Sigma_{ref}/2, \quad (8.5)$$

where  $\Delta_{ref} = m_1^{1/2} - m_2^{1/2}$  and  $\Sigma_{ref} = m_1^{1/2} + m_2^{1/2}$ . The uncertainty of  $C_{TOF}$  is:

$$\Delta C_{TOF} = \sqrt{\Delta t^2/(t_2 - t_1)^2 + (t - t_2)^2/(t_2 - t_1)^4 \Delta t_1^2 + (t - t_1)^2/(t_2 - t_1)^4 \Delta t_2^2}. \quad (8.6)$$

## 8.2 Systematic error study

Systematic errors exist in all experimental devices and can be significant or not. Unlike random errors, which can be reduced by repeating the measurements, the systematic bias can not be eliminated by simple repetition and can affect the accuracy of a measurement.

In this thesis, an off-line ion source was used to study the systematic errors in MR-TOF MS. The off-line reference ions are first decelerated, accumulated, and bunched in the RFQ buncher, and then re-accelerated to  $E_k \approx 3$  keV (Fig. 7.4). Since the energy of the ions is larger than the maximum potential of the entrance mirror electrode, they will pass this electrode and enter into drift tube. At this time, an in-trap lift [WMRS12] voltage  $U_{lift}$  of 1 kV is applied to the drift tube, which reduces the energy of the ions to  $E_{trap} = E_k - eU_{lift}$ . When the ions pass through the center of the lifted electrode, this electrode is switched to ground. Since the energy of the ions is no longer larger than the maxima of the two mirror electrode potentials, the ions are trapped and bounce back and forth between the two mirror electrodes. After a few hundred reflections, the in-trap potential is lifted again. The ions regain the energy and pass the exit mirror electrode, and are detected by the MCP. The signals from the MCP are registered by a multiple-event time digitizer (MSC6A).

In the following, different settings of the MR-TOF MS will be discussed.

### Off-line Study

#### Setting 1: Measurement of $^{39,41}\text{K}$ , $^{85,87}\text{Rb}$ , $^{133}\text{Cs}$ starting from reflection number 100 to 1000.

In this setting, five reference ion species  $^{39,41}\text{K}$ ,  $^{85,87}\text{Rb}$ ,  $^{133}\text{Cs}$  were used and their TOFs were measured sequentially from reflection 100 to 1000 with

steps of 100 reflection. For each species, the TOFs were fitted as a function of the number of reflection using a linear model:

$$T = aN + b, \quad (8.7)$$

where  $a$  and  $b$  are two mass-dependent parameters.

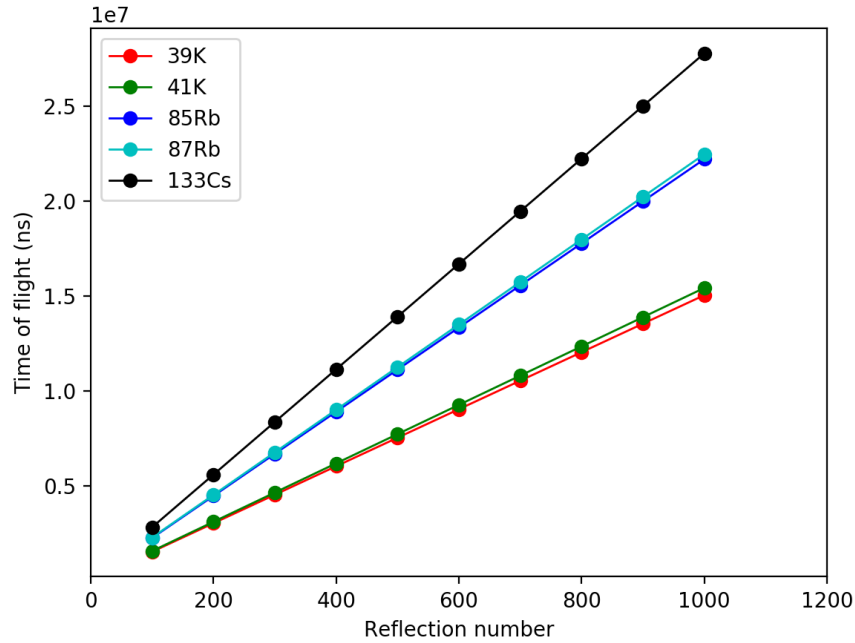


Figure 8.1: Time of flight of five reference species fitted as a function of the number of reflection.

Figure 8.1 shows that the TOFs are proportional to the number of reflection for each species. Table 8.1 lists the fitting parameters  $a$  and  $b$ . Obtaining these two parameters, we can calculate the TOF at any number of reflection. In order to see how the TOF differs from the linear trend, the relative residual, which is defined as the difference between “Raw TOF” (obtained from experiments) and the TOF extracted from Eq. 8.7 (“Fit” TOF) divided by the Raw TOF, is also plotted in Fig. 8.2. As one can see, for relatively small reflection number, the relative residuals are around  $5 \times 10^{-6}$ , which was probably due to the imperfect injection and the saturation of the detector. While as the number of reflection increases, the unstable effects can be averaged out and the relative residuals can be reduced below  $1 \times 10^{-6}$ .

The TOFs at  $N = 0$  (ions shooting through the MR-TOF MS without trapping) for five species can be also fitted by a linear function:

$$T(N = 0) = b = a_0\sqrt{m} + b_0, \quad (8.8)$$

ion	a (ns)	a error (ns)	b (ns)	b error (ns)
$^{39}\text{K}$	15016.044	0.010	23165.548	6.475
$^{41}\text{K}$	15396.275	0.005	23720.824	3.303
$^{85}\text{Rb}$	22167.192	0.019	33969.901	13.459
$^{87}\text{Rb}$	22426.429	0.012	34340.019	8.384
$^{133}\text{Cs}$	27733.159	0.017	42332.383	11.773

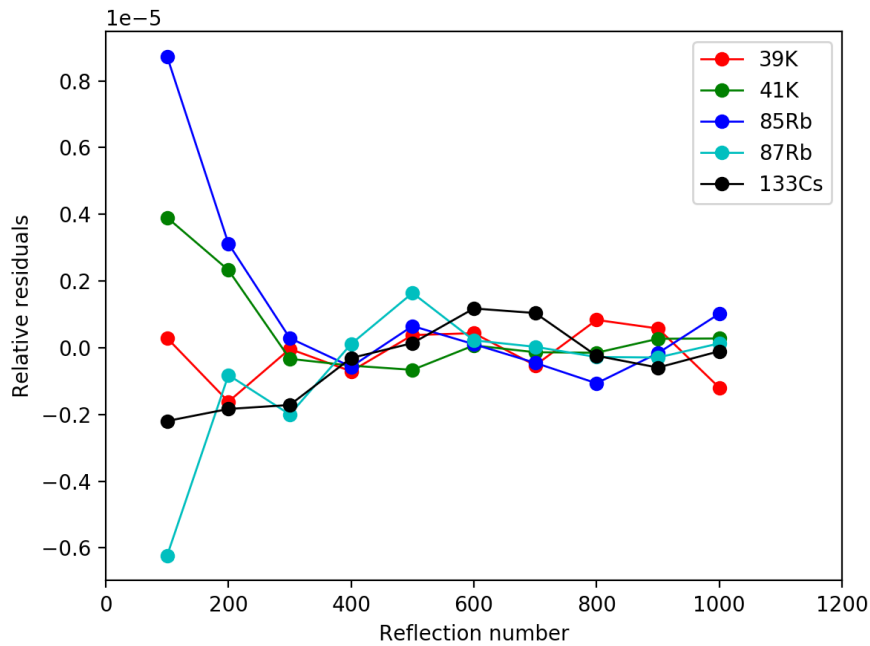
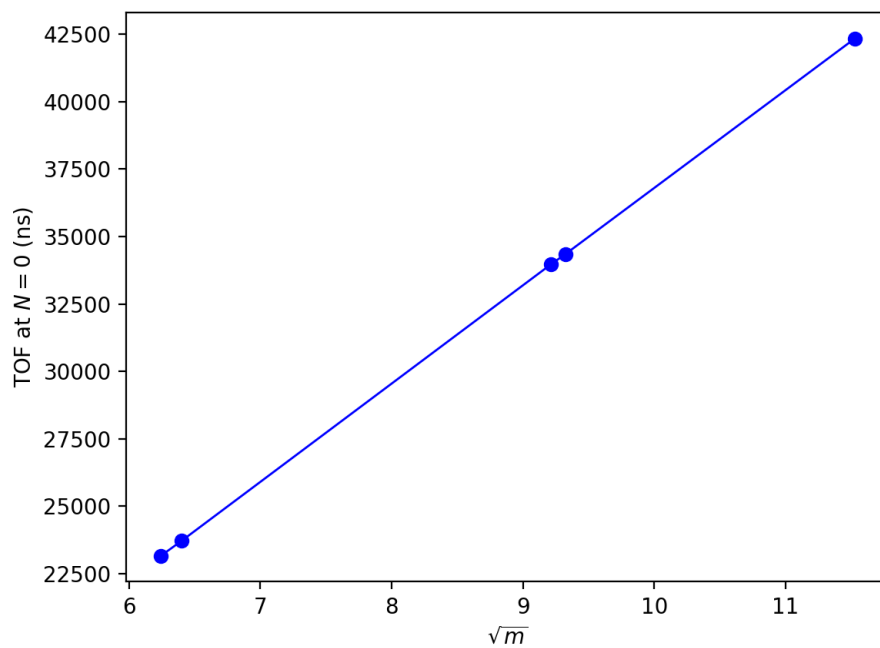
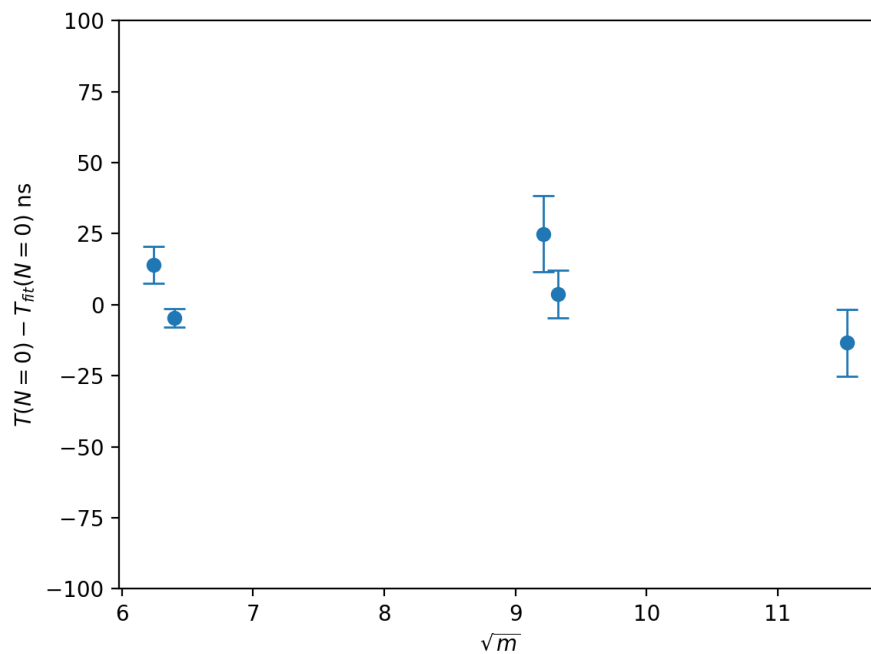
Table 8.1: Fitting parameters  $a$  and  $b$  in Eq. 8.7

Figure 8.2: Illustration of the relative residuals as a function of reflection number.



(a)



(b)

Figure 8.3: Relation between the square root of mass and the TOF at  $N = 0$  (a). Residuals of TOF at  $N = 0$  (b).

where  $a_0$  and  $b_0$  are two mass-independent parameters in this case.

Fig. 8.3a shows the TOF at  $N = 0$  as a function of square-root of mass. We observe that the data points are well described by the linear function in Eq. 8.8. The two fitting parameters are deduced to be  $a_0 = 3630.8(3.6)$  and  $b_0 = 487.7(25.8)$  ns. The parameter  $b_0$  is probably due to the unsynchronized time signal sent to the RFQ for injection and to the MCP for data acquisition. It confirms the necessity of the use of the offset parameter  $\beta$  in mass determination in Eq. 8.2.

The mass of  $^{87}\text{Rb}$  was used as the ion of interest and its mass was derived for each number of reflection using  $^{39}\text{K}$  and  $^{133}\text{Cs}$  as two reference ions. The mass was determined using two sets of TOFs: the ‘‘Raw’’ TOF from the experiment data and the ‘‘Fit’’ TOF (see above) from the linear fit function. The results are displayed in Fig. 8.4. We can see that the ‘‘Fit’’ masses follows a smooth trend and have a large uncertainty. It is because the fluctuation was averaged in the linear fit function. And the masses from ‘‘Raw’’ TOF scatter around the ‘‘Fit’’ masses. The largest deviation of ‘‘Raw’’ TOF from AME2016 is 1147(277) keV at  $N = 100$ , while the ‘‘Fit’’ TOF gives a deviation of 381(689) keV. At  $N = 1000$ , which was the normal setting in MR-TOF MS, the ‘‘Raw’’ TOF deviated by  $-75(12)$  keV and the ‘‘Fit’’ TOF by  $12(48)$  keV.

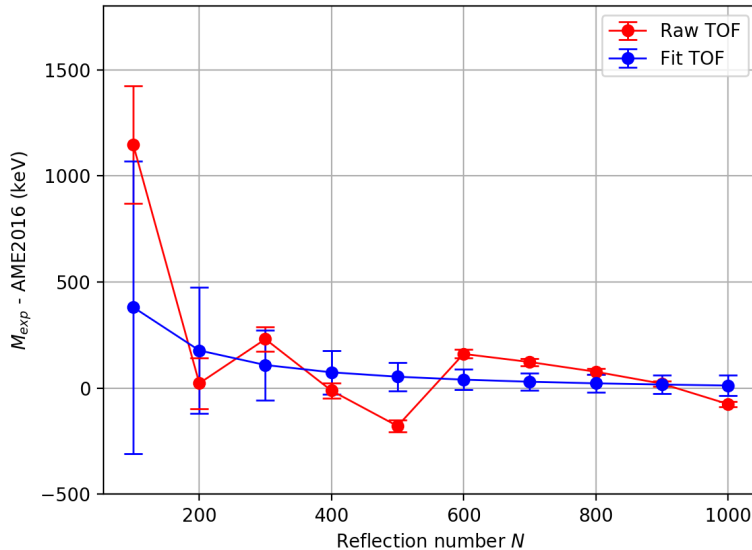


Figure 8.4: Mass of  $^{87}\text{Rb}$  determined by using  $^{39}\text{K}$  and  $^{133}\text{Cs}$  as reference masses.

## Setting 2: Many measurements of $^{85}\text{Rb}$ , $^{87}\text{Rb}$ and $^{133}\text{Cs}$ from reflection number of 50 to 750.

In this setting, the TOF spectra were obtained from the accumulation of 100 single spectrum for each species from reflection number 50 to 750, by steps of 50 reflections.

We define here the standard deviation for each reflection number:

$$std = \sqrt{\frac{\sum_{i=1}^K (t_i - \bar{t})^2}{K - 1}}, \quad (8.9)$$

where  $t_i$  is the TOF for the  $i$ -th spectrum,  $\bar{t}$  is the weighted mean of TOF and  $K$  is the number of the spectrum ( $K = 100$  for all reflection number except  $K = 86$  for  $N = 750$ ). The calculated standard deviation for each reflection number is shown in Fig. 8.5. We can see that the  $std$  generally increases with the reflection number, it is probably due to the fact that the cavity voltage was not optimal and the deviations were somehow accumulating. The rising of the standard deviation at low reflection is again due to the imperfect injection and saturation.

The relative residuals (see Fig. 8.6) defined in Setting 1 was also calculated for this setting. Fig. 8.6 shows that the relative residual of TOFs of three species are strongly related to each other. It is because the time of flights of three species were measured continuously that they suffered from the same electric field drift.

The mass determination of  $^{87}\text{Rb}$  is shown in Fig. 8.7. We can see that the deviation is largely suppressed when we used the TOF from the average of 100 spectra. The deviations at  $N = 100$  are 259(25) keV and 164(385) keV for the “Raw” TOF and the “Fit” TOF, respectively. Above reflection number  $N = 500$ , the deviation is less than 25 keV.

In order to see how the deviation changes as a function of the number of the accumulated spectra, the mass of  $^{87}\text{Rb}$  was calculated for different number of accumulated spectra. We started with 10 spectra and increased by 10 each time, and finally the total number of 100 spectra for each reflection number was used. The results are displayed in Fig. 8.8. In this setting, the mass deviation for  $N = 100$  increases continuously as a function of the number of measurement, while the deviations for other reflection numbers slowly converge at larger number of spectra. Fig. 8.8 gives us the first impression of how the deviation changes as a function of the number of the accumulated spectra. If we examine carefully Fig. 8.8, we can notice complex structure for different reflection numbers, i.e., the position of the minimum deviation is not the same. For example, for  $N = 300$  (the green curve), its minimum deviation appears at the number of spectra of 60; for  $N = 600$  (the brown curve), its

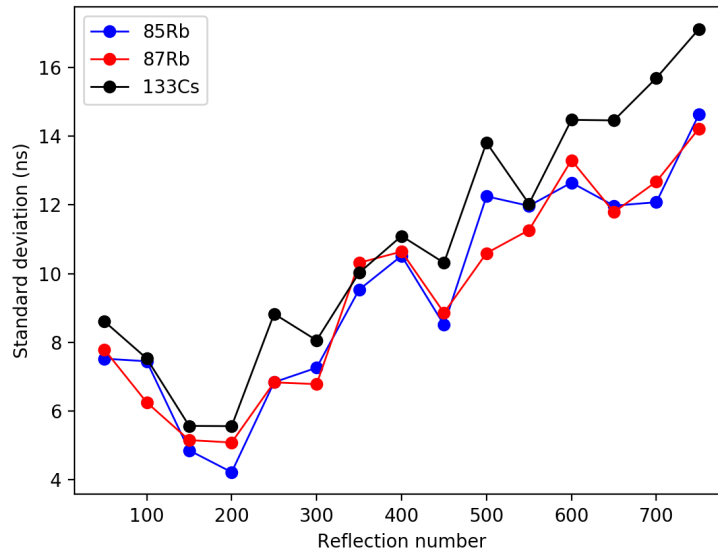


Figure 8.5: Standard deviation of 100 TOF spectra for each species at different number of reflection.

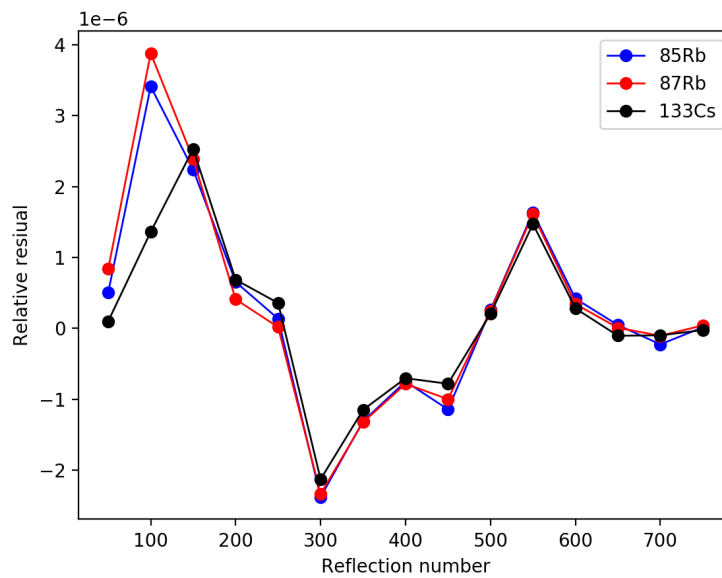


Figure 8.6: Relative residuals for three reference ions. The data was averaged by 100 spectra.

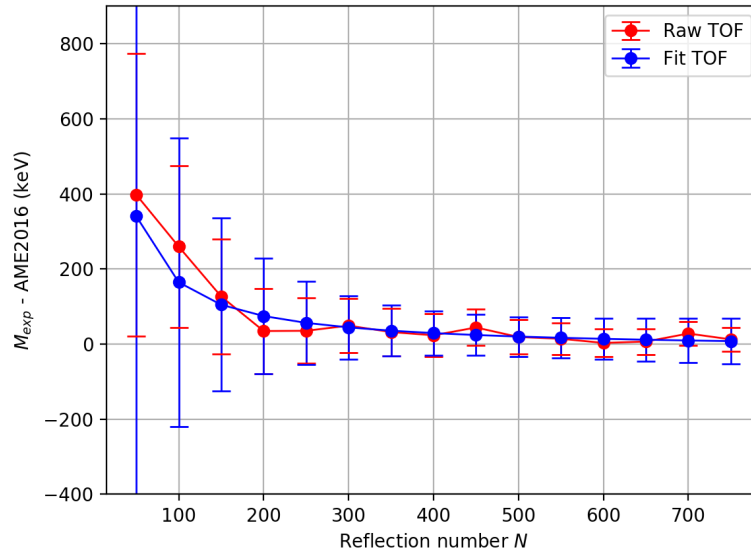


Figure 8.7: Mass determination of  $^{87}\text{Rb}$  from 100 spectra using  $^{85}\text{Rb}$  and  $^{133}\text{Cs}$  as reference ions.

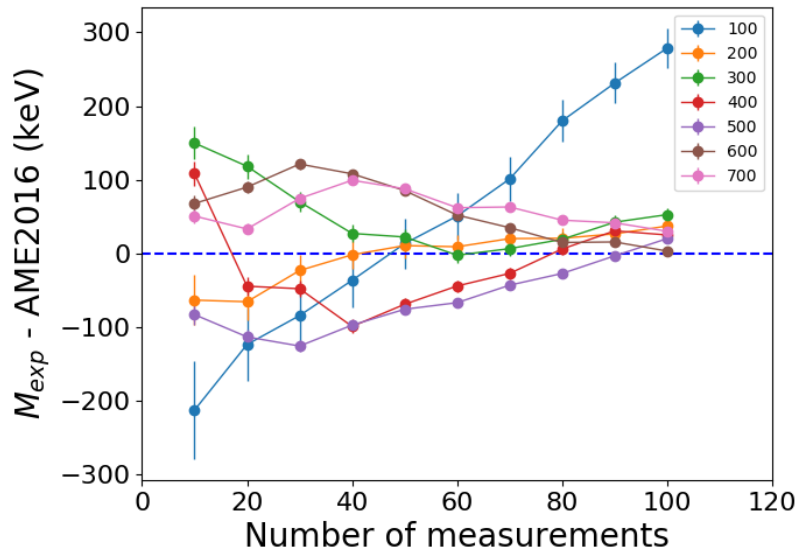


Figure 8.8: Mass of  $^{87}\text{Rb}$  determined by varying the number of the accumulated spectra at different reflection number.

minimum deviation is found at the number of spectra of 100. We can conclude from Fig. 8.8 that the measurements performed at reflection number  $N = 100$  is not reliable, and the minimum deviation is found at reflection numbers of  $N = 600$  and  $N = 700$  (in this setting) for the largest number of measurements.

The mass-independent parameter  $b_0$  in this setting is determined to be 683.2(9.7) ns, which is not too far away from the value determined from Setting 1.

### Setting 3: Adjustment of the cavity voltage for each reflection number.

As mentioned in the *principle* at the beginning of this chapter, the velocity of ions in the MR-TOF are modulated by the in-trap voltage  $U_{lift}$ . One can modify the kinetic energy of the ions, i.e., by changing the value of  $U_{lift}$ , as illustrated in Fig. 3 of [WWA<sup>+</sup>13], to focus the time-of-flight plane of the ions on the detector. With such adjustment, the dispersion of the time-of-flight spectrum can reach minimum. Fig. 8.9 shows a typical  $U_{lift}$  voltage scan of  $^{85}\text{Rb}$  at reflection number  $N = 900$  from 1000 V to 1080 V in steps of 4 V. As one can see the TOFs, in the lower part of Fig. 8.9, varies at different  $U_{lift}$  values (represented as steps in y-axis). The minimum width of TOF locates at  $U_{lift} = 1056\text{V}$ . The beam intensity, shown in the upper part of Fig. 8.9, remains almost unchanged.

In this setting, the cavity voltage was scanned for each number of reflection to make sure that the dispersion of TOF is minimum. The corresponding cavity voltage is displayed in Fig. 8.10.

The measurements were performed at the corresponding optimum voltages. Two data sets for each species were acquired: one resulted from 10 spectra for each number of reflection while the other from 40 spectra.

Fig. 8.11 shows the mass of  $^{87}\text{Rb}$ . We can see that the deviation, after adjusting the cavity voltage, is strongly compressed, especially at the lower reflection number, comparing with the red points in Fig. 8.7. Remember that in the current setting, only 10 and 40 spectra were taken while in the Setting 3 a hundred spectra were accumulated. By only adjusting the cavity voltage, the deviation for both measurements can be greatly reduced. The deviation of these two settings at reflection number of  $N = 1000$  is 43(6) keV for 10 accumulated spectra and 0.1(3.0) keV for 40 accumulated spectra.

### Setting 4: Delayed measurements at $N = 1000$ .

In this setting, the reflection number was fixed at  $N = 1000$  for three reference species  $^{85}\text{Rb}$ ,  $^{87}\text{Rb}$  and  $^{133}\text{Cs}$ . We also introduced a delayed time in data acquisition: after each five measurements, an increment of 30 s was added to each measurement. See below a sequence example:

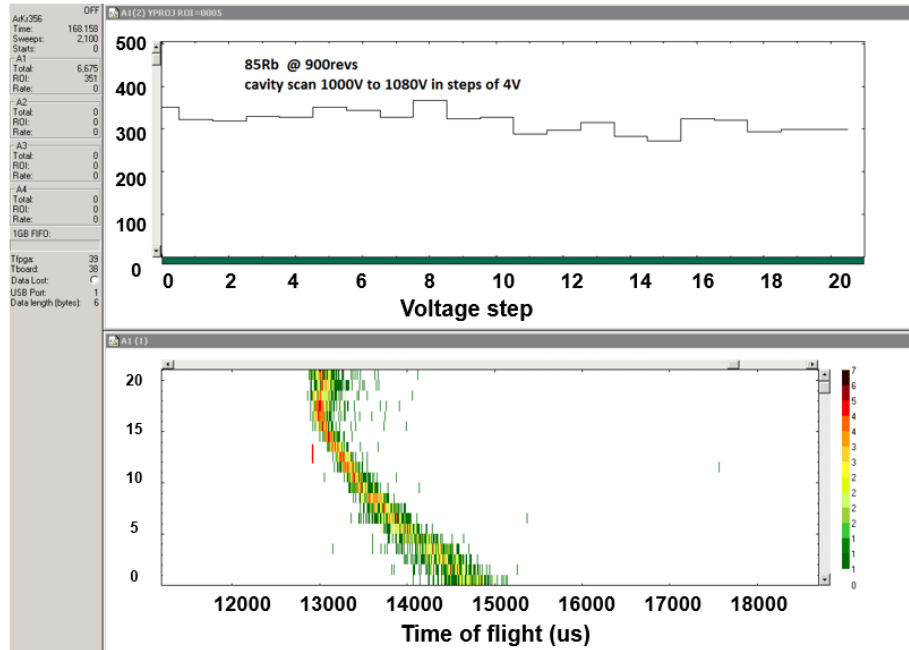


Figure 8.9: Scan of  $U_{lift}$  voltages of  $^{85}\text{Rb}$  at  $N = 900$  from 1000 V to 1080 V in steps of 4 V (lower figure). Beam intensity as a function of  $U_{lift}$ .

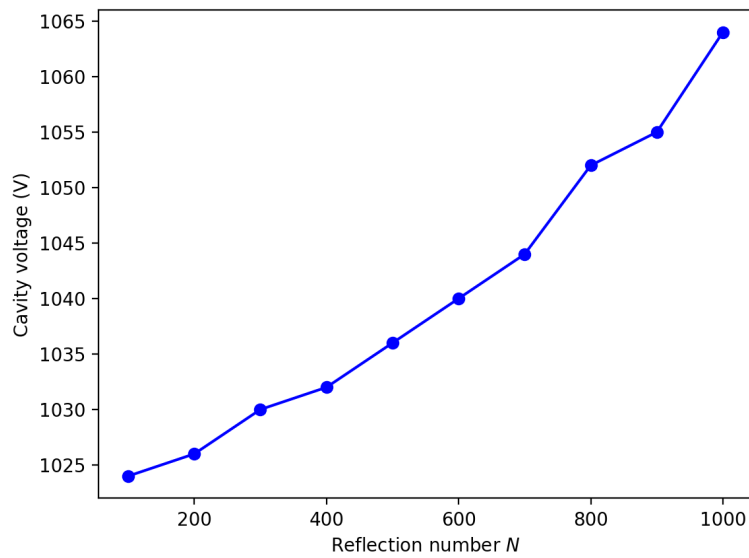


Figure 8.10: Optimized cavity voltage as a function of reflection number  $N$  of  $^{85}\text{Rb}$

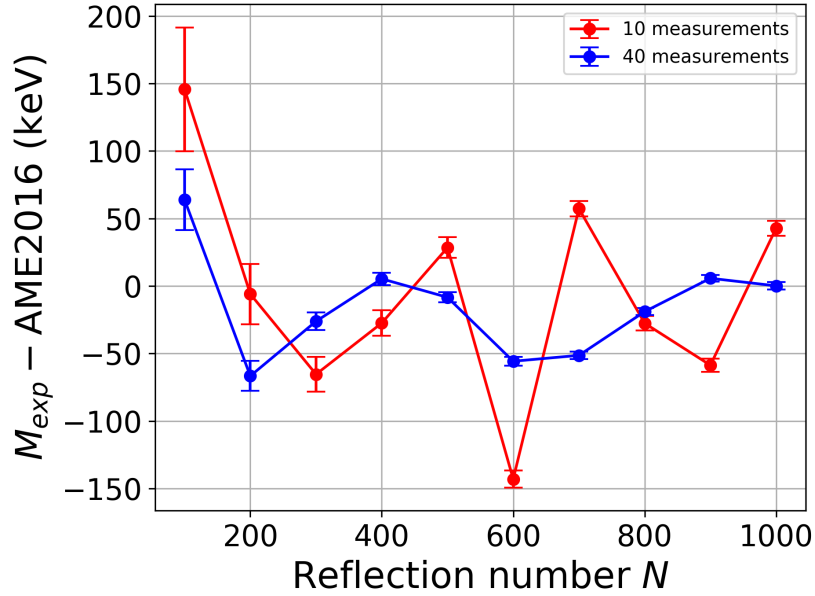


Figure 8.11: Mass determination of  $^{87}\text{Rb}$  at the optimum cavity voltage for two different data set.

85Rb – 30s – 87Rb – 30s – 133Cs – 30s  
 85Rb – 30s – 87Rb – 30s – 133Cs – 30s  
 85Rb – 30s – 87Rb – 30s – 133Cs – 30s  
 85Rb – 30s – 87Rb – 30s – 133Cs – 30s  
 85Rb – 30s – 87Rb – 30s – 133Cs – 30s  
 85Rb – 60s – 87Rb – 60s – 133Cs – 60s

...

It means that the spectra were not taken at the same time (at least not in a relatively short time). The intention of this setting is to examine how deviation changes along with the time difference between two measurements increases. In this setting, we obtained 72 spectra from 20:00 p.m. to 09:30 a.m. the next day, the biggest time difference between two spectra was about 7 minutes. The results are listed in Fig. 8.12a. From Fig. 8.12, we can see that the deviations does not depend on whether the spectra were taken in a fast mode between two ions or not: for the very first spectra, they were measured promptly; for the last spectrum, the time difference between the measurements of two ions was seven minutes. It could imply that deviation can not be accounted for the drift of the electrode voltage: an undiscovered source should be responsible for this deviation. For a single spectrum, a deviation around 500 keV can be reached. This is not a surprising result since each ion was measured at different time (They would never appear at the same spectrum for off-line ions). It thus posed an upper limit of 500 keV for the mass accuracy.

As the deviation is much larger than the uncertainty, the calculation of  $v/s$  does not make sense in this case. Thus all the measurements can be considered independent. The dispersion of the deviations is displayed in Fig. 8.12b. A Gaussian fit is applied to the distribution of deviation, which gives a mean value of 17 keV and a standard deviation of 170 keV. If we use off-line beams as reference ions, a systematic error of 170 keV should be added quadratically to the statistical uncertainties.

### Conclusion (off-line ion source)

- The parameter  $\beta$  in Eq. 8.2 is mass independent and has a value around 500 ns. It is probably due to the time difference between the ion injection into the RFQ trap and the trigger sent to the acquisition card. The delay of the ion injection could minimize this quantity.
- The mass calculated from the “Fit” TOF agrees better than that from the “Raw” TOF. It is due to the fact the fluctuation was averaged for each reflection number.
- Measurements performed at reflection number  $N = 100$  is not reliable, and the minimum deviation is found at reflection numbers of  $N = 600$  and  $N = 700$  (in Setting 2) for the largest number of measurements.
- The deviation is probably not due to the drift of the electrode voltage, see Fig. 8.12. A yet undiscovered reason should be responsible for this deviation.
- In one single measurement (spectrum), a maximum deviation of 500 keV can be observed. It thus set the upper limit for the mass precision. The dispersion for one single measurement is 170 keV.

### On-line Study

Up to now, the discussion is based on the off-line ion sources. Recently, measurements have been performed to check the yield of exotic species using proton beams in various target. This provides a good opportunity to study the systematic errors of MR-TOF during on-line runs.

The yield check measurements were carried out for nuclides with mass number varying from  $A = 46$  to  $A = 175$ . However, not all the data were used in the systematic analysis since the measurements were not optimized for mass measurements. Below lists all the criteria in the data selection:

- the beam gate was set properly so that no saturation was seen in the peak.
- a spectrum contained at least two peaks.
- a peak was identified without contaminants.
- the uncertainty of the time of flight for each peak should be smaller than 12 ns both for ions of interest and reference ions.

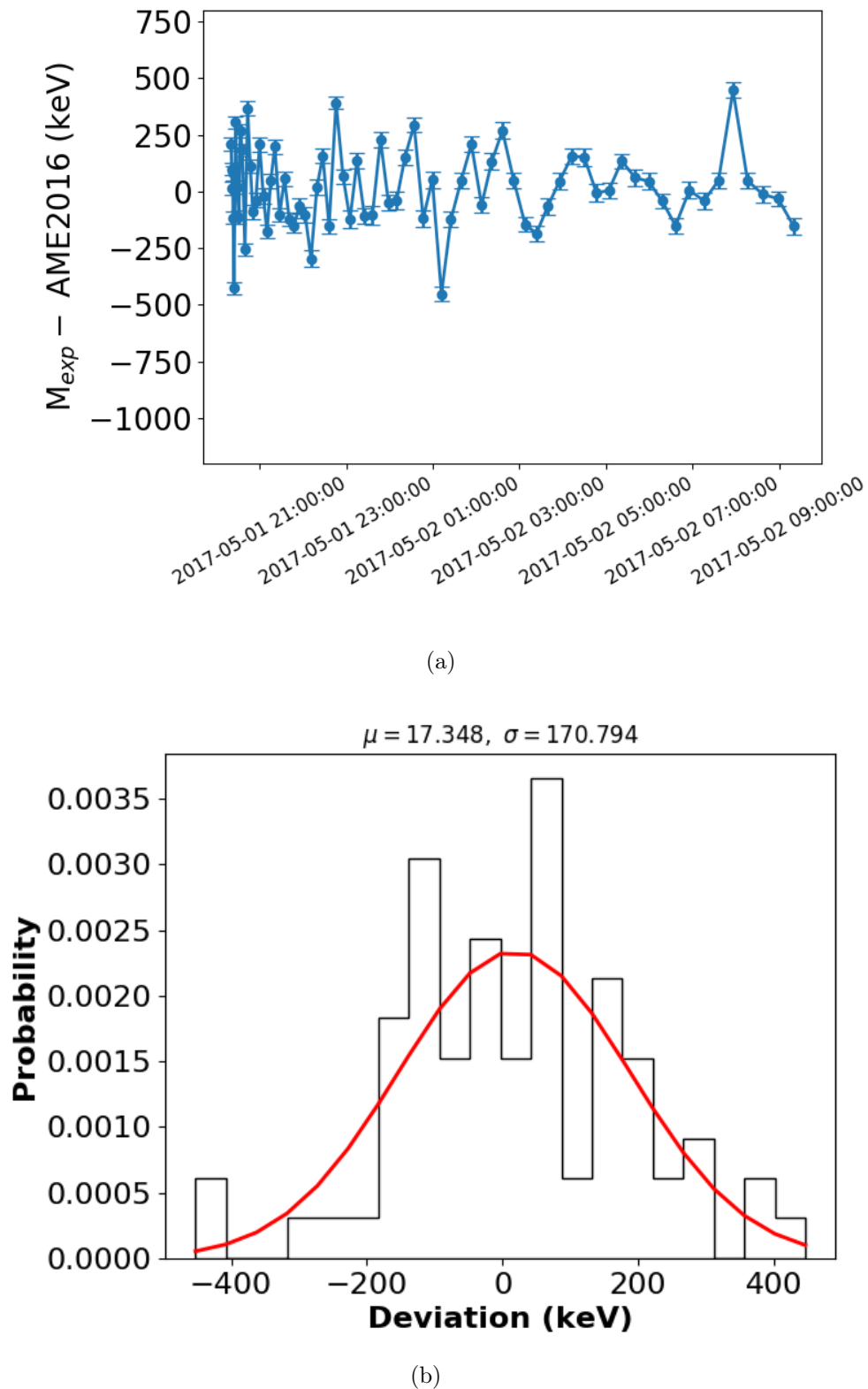


Figure 8.12: (a) Mass of  $^{87}\text{Rb}$  determined at reflection number 1000. The x-axis indicates when the measurement was performed. (b) Distribution of deviations of (a). The red curve represents a Gaussian fit.

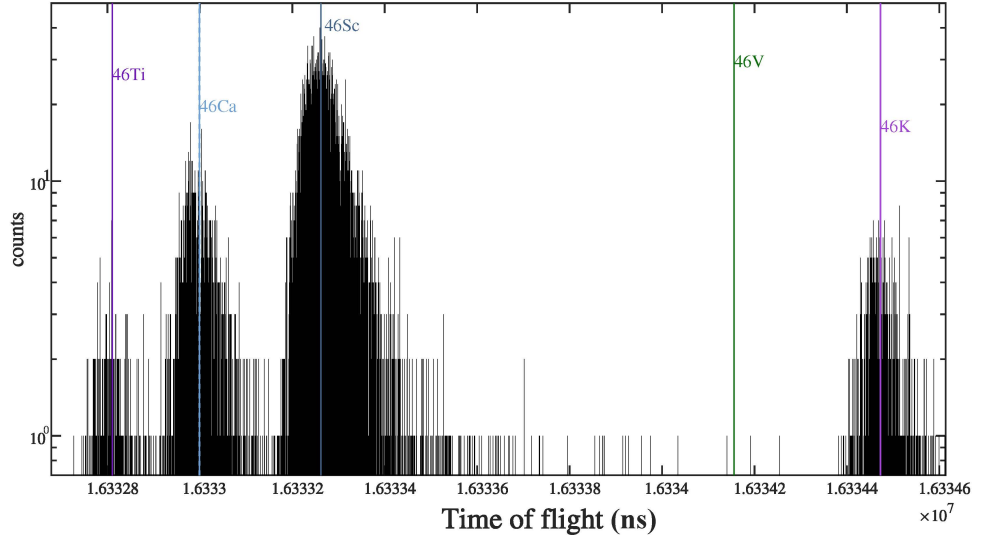


Figure 8.13: Time-of-flight spectrum of  $A = 46$  nuclides.

- settings were not changed during data acquisition, e.g. no buncher cooling scanning, laser on/off tests, etc.

Fig. 8.13 shows a TOF spectrum of  $A = 46$  nuclides that meets all the criteria. In Fig. 8.13,  $^{46}\text{Ca}$  was selected as the ion of interest,  $^{46}\text{Ti}$  and  $^{46}\text{K}$  were used as references. The most abundant peak of  $^{46}\text{Sc}$  can also be used as the ion of interest. However, its production strongly depends on the laser ion source: very few scandium isotopes could be seen if the laser was turned off. This was indeed the aim for the yield check measurement!

In the mass determination process, the ions with the smallest error on the TOF were selected as the ions of interest and other ions were used as references. In total, under such selected criteria, 47 measurements which include 15 cases of  $A = 46$ , two cases of  $A = 48$ , nine cases of  $A = 49$ , five cases of  $A = 50$ , three cases of  $A = 62$ , six cases of  $A = 74$ , and seven cases of  $A = 149$  were used.

Fig. 8.14 illustrates the deviations between the masses determined from experiments and that from AME2016. The normalized chi-square, which is defined as:

$$\chi_n = \sqrt{\frac{1}{N} \sum_i \frac{(M_{exp}^i - M_{AME}^i)^2}{\sigma_i^2}}, \quad (8.10)$$

is deduced to be 1.02 for all the 47 measurements under consideration, where  $\sigma_i$  is the statistical uncertainty of the  $i$ -th mass. The expected interval of  $\chi_n$  is  $1 \pm 1/\sqrt{(2 * 47)} = 1 \pm 0.10$ , which is overlapped by the experimental value. The systematic error derived from the on-line measurements is much smaller than the statistical uncertainties, i.e., no systematic error should be added to the final uncertainty.

The insert figure in Fig. 8.14 displays the distribution of  $v/s$ : 36 cases within  $1\sigma$ , seven cases between  $1\sigma$  and  $2\sigma$ , three cases between  $2\sigma$  and  $3\sigma$ , and one case slightly larger than  $3\sigma$ .

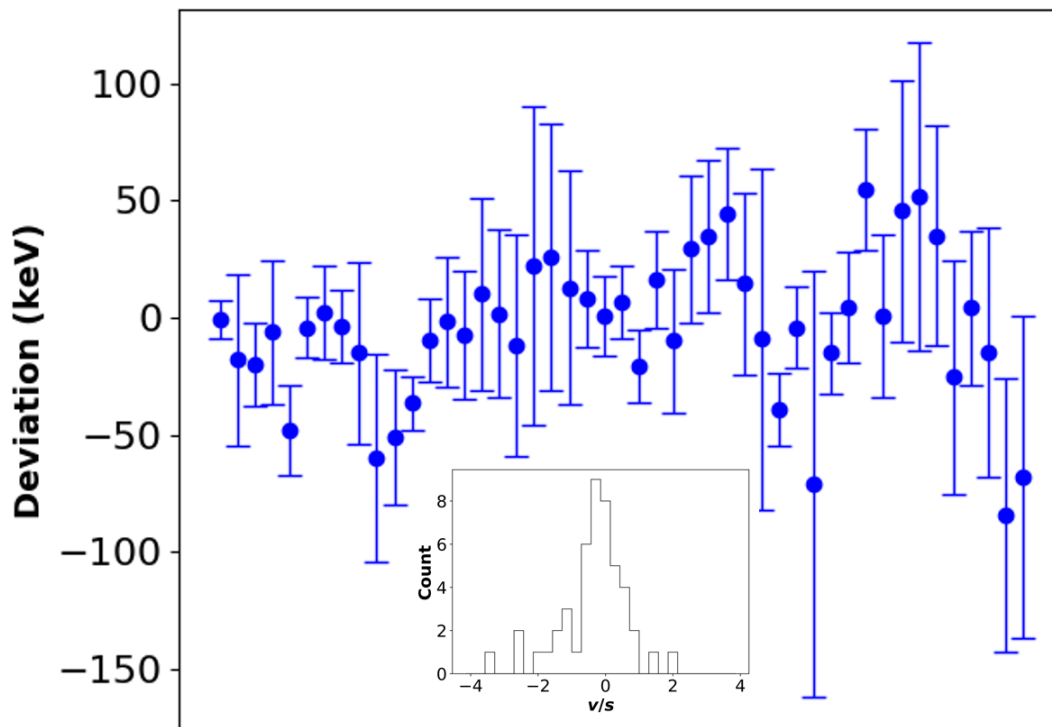


Figure 8.14: Mass deviations from AME2016 for 47 measurements. The insert figure displays the distribution of the deviation divided by the uncertainty for each measurement.

### The effect of $\beta$ in the mass calibration

For each of the 48 measurements, one could not always find two reference ions: the peak could be either contaminated by other component or weakly populated. In this case, only one reference peak was used in the mass calibration, meaning that the second parameter  $\beta$  in Eq. 8.2 was assumed to be zero.

Fig. 8.15 shows the  $\beta$  values when two references were used in the mass calibration. One would notice that its value, which was extracted from the on-line measurements, can be two orders of magnitude larger than that from off-line ion sources. However, considering the large uncertainty of each  $\beta$  value, we can assume that most of them are compatible with zero.

To examine the validity of using one reference ion in the mass calibration, one can do the following: compare the mass difference of the same nuclide determined by using one and two reference ions, respectively. The results are

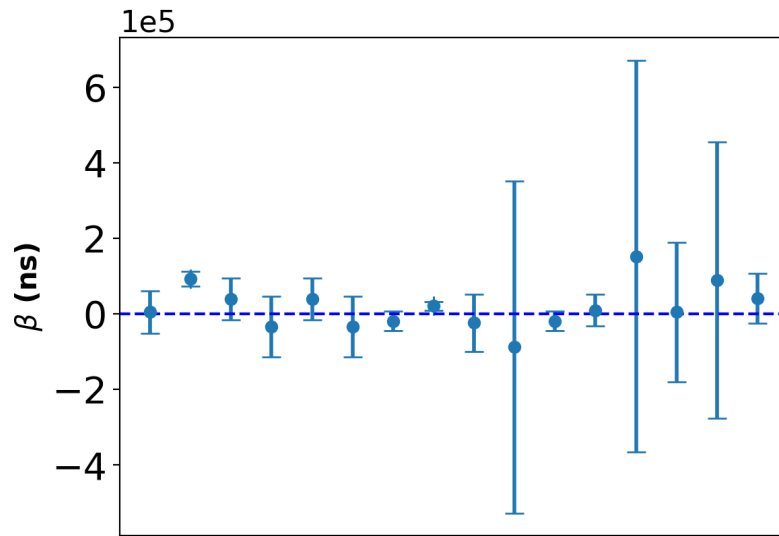


Figure 8.15: Parameter  $\beta$  in Eq. 8.2 for on-line measurements.

displayed in Fig. 8.16. From Fig. 8.16 one can note that the difference is negligible compared to the uncertainty. A linear fit to the data (including the large uncertainty in  $\beta$ ) presents a very small value for the slope. In the current study, the contribution of using one reference ion to the systematic error could be considered as negligible.

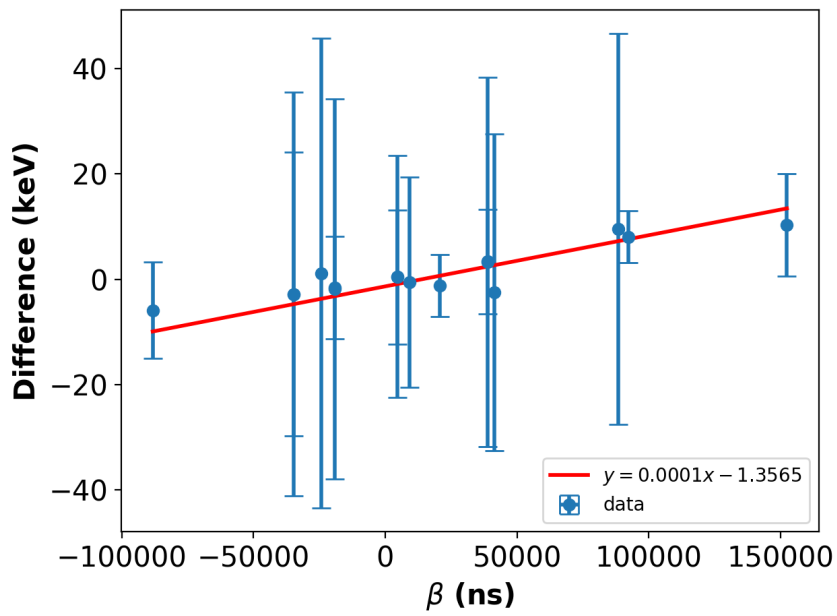


Figure 8.16: Difference of mass of the same nuclide determined by using one and two reference ions. The red curve is the linear fit to the data point.

# Conclusions and Outlook

In this thesis, the basic concept of Atomic Mass Evaluation (AME) is described. AME has been alive for more than 60 years and its main goal is to provide all the information related to atomic masses, by evaluating all *indirect* (reaction and decay) and *direct* (mass spectrometry) mass measurements. However, since the masses are overdetermined by the experimental connections, i.e., the number of measurements is much larger than that of masses, extracting the masses is not straightforward. Since all the input data is linear in mass, such an entangled system can be solved, without approximation, by the least-squares method, where the masses are considered as parameters. The use of the least-squares method on the overdetermined system is an ideal procedure in that it not only provides unbiased, reliable mass values derived from experimental data, but it also allows a check for the consistencies of all input data. One of the roles of AME is to reveal undiscovered systematic errors by comparing the input data with the adjusted values in a global prospect. Such task can only be performed under the AME framework. After obtaining the best value for each mass, we can calculate any combination of mass differences, such as decay and separation energies, based on the covariance matrix.

The developments for the latest mass table AME2016 are discussed. The first one is related to the careful treatment of the most accurate data. The most accurate mass data comes from Penning-trap mass spectrometry. Nowadays, as the precision from Penning traps can reach  $10^{-10}$  or even better, the molecular and electronic binding energies cannot be neglected. A method to calculate the molecular binding energy from the standard heat of formation is described and two detailed examples are given. We find that, by using the updated standard heat of formation, the recalculated values for some of the mass-spectrometric data can change significantly. In AME2016, all the precise data has been recalculated.

The second one is related to the corrections of decay energies. For  $\alpha$ - and proton-decay energies measured by implantation methods, the recoil energy of the decaying partner should be taken into account properly. We present a procedure to correct the published decay energies in case the recoiling nuclides were not considered in implantation experiments. A program has been developed based on Lindhard's integral theory, which predicts accurately the

energy deposition of heavy nuclides in matter. Three examples are given to illustrate the correction procedure.

The third one is about the consideration of relativistic effect and atomic effect in the formula of converting  $\alpha$ -particle energies to decay energies. The most precise  $\alpha$ -decay energies come from magnetic spectrograph. These  $\alpha$ -energy standards not only serve as calibration points for all  $\alpha$  spectra with high resolving power, but also provide precise input values to AME. In order to obtain correct decay energies from magnetic spectrograph, where only  $\alpha$  particles are detected, a relativistic formula considering also the helium electron binding energies is derived.

The mass models are the last resort to access to the most exotic nuclides that cannot be produced in the near future. These mass models, regardless of their intrinsic characters, could reproduce the experimentally known masses but predict different behavior when they extrapolate towards unknown regions. Based on this fact, the accuracy and predictive power of eight mass models of various types, i.e., Extended Thomas-Fermi plus Strutinsky Integral method (ETFSI-2), Finite Range Droplet Model (FRDM95) and its updated version with improved treatment of deformation (FRDM12), a recent Weizsäcker-Skyrme plus Radial Basic Function (WS4+RBF) model, two recent Hartree-Fock-Bogoliubov mass models HFB26 and HFB27, the Duflo and Zuker (DUZU) model, and the KTUY05 model, are studied. We find that the root-mean-square deviation ( $\delta_{\text{rms}}$ ) of all the mass models under consideration are well below 0.8 MeV compared to three mass tables AME2003, AME2012, and AME2016 for all nuclides ( $N, Z \geq 8$ ). The mass model WS4+RBF is the most accurate mass model which gives  $\delta_{\text{rms}}$  around 0.2 MeV. The microscopic mass model HFB27 also presents a good accuracy with  $\delta_{\text{rms}} \approx 0.5$  MeV. The mass model DUZU is still a robust mass model which gives  $\delta_{\text{rms}} \approx 0.4$  MeV.

The predictive power is the ability of a mass model to predict the unknown masses. To study the predictive power, we calculate the rms deviations for 61 newly measured masses ( $\delta_{\text{rms}}(\text{new})$ ) in AME2016. To compare the predictive power with the accuracy, the rms deviations for the known masses in AME2012 ( $\delta_{\text{rms}}(2012)$ ) are also calculated. In the Global region, the condition  $\text{rms}(\text{new}) \approx \text{rms}(2012)$  is only roughly fulfilled by the mass model ETFSI-2, while other mass models present a much large  $\text{rms}(\text{new})$  value than that of their  $\text{rms}(2012)$ . In the light region, ETFSI-2 has the best predictive power, while in other regions, the mass model WS4+RBF has the best predictive power. In the heavy region, all the mass models find their lowest  $\text{rms}(\text{new})$  value, and the predictive power is compatible with the accuracy.

The mass extrapolation of AME provides the best estimates for the unknown masses that are not too far (two or three mass unit) from the last known nuclides. This method is based on the smoothness of the mass surface and such a smooth feature should be preferred when we extrapolate the

masses towards the unknown region. The root-mean-square deviation for all estimated masses in AME2012 that are known in AME2016 is 0.396 MeV (55 cases in total), which is smaller than any of the the mass model discussed here.

Another part of this thesis is related to the mass measurements performed using the Penning-trap mass spectrometer ISOLTRAP at ISOLDE/CERN. The masses of eighteen nuclides from several experimental campaigns between 2011 and 2016 are analysed. The mass of  $^{168}\text{Lu}$  in its isomeric state has been measured and its value agrees with the recommended value in AME2012 but nine times more precise. The mass value of  $^{178}\text{Yb}$  obtained here differs from the previous reaction result by 31(13) keV but confirms extra binding of  $^{178}\text{Yb}$  by  $\sim 440$  keV. A sudden flattening in  $S_{2n}$  at  $^{178}\text{Yb}$  would indicate the existence of the phase transition in the region. However, more measurements are needed to clarify this issue. The masses of some rare-earth nuclides such as  $^{140}\text{Nd}$  and  $^{160}\text{Yb}$  are measured with higher precision compared to AME2016. The results of other nuclides also help improve the precision of the existing masses.

The systematic error of the multi-reflection time-of-flight mass spectrometer (MR-TOF MS) at ISOLTRAP is studied using off-line ion sources and on-line proton beams. In the off-line study, different settings on MR-TOF MS have been probed. Two of the most important conclusions are addressed. First, measurements performed at reflection number  $N = 100$  is not reliable. In order to minimize the deviation, reflection numbers higher than 100 should be used instead. secondly, if we use off-line ion sources for mass calibration, an uncertainty of 170 keV should be added to the final result.

Secondly, the deviation is probably not due to the drift of the electrode voltage. For the on-line study, 47 measurements are selected from the yield-check measurements. The reduced chi-square  $\chi_n$  is deduced to be 1.02, meaning that the systematic error is much smaller than the statistical uncertainties. No systematic error should be added to the final results. The effect of the second parameter  $\beta$  in the mass determination formula is also studied. The result shows that the use of only one reference ion will not affect for mass doublets the final determination of mass values and hence the conclusion of the systematic error.

AME serves as a reservoir which contains all the knowledge of atomic masses. Unlike other fields of physics, whose aim is to prove something, the intention of AME is to provide the physics community, by the best usage of the existing data, with the best, reliable mass values with improved precision. As a Ph.D student, I had the privilege to be one of the AME evaluators. I also feel responsible to keep AME in good shape, after the retirement of my supervisor Georges Audi. AME is a project which takes a lot of time. The inclusion of all experimental data is by no means a copy-paste task: it requires meticulous inspection and reconciles all the conflicting data. More importantly, evaluators

need to grasp the knowledge of all the experimental setup in order to have good judgement, which is also a long accumulation process. For the next two years, I will work at the Penning-trap mass spectrometer PENTATRAP installed at the Max-Planck Institute for Nuclear Physics (MPIK) under the supervision of Prof. Klaus Blaum. It will certainly offer a great opportunity for me to gain an overall knowledge of the Penning-trap technique and complement my present skills of mass evaluation. In the future, I will strongly collaborate with Prof. Meng Wang, the coordinator of the AME group at IMP, Lanzhou.

# Appendix A

## Relativistic formula of alpha decay

Lets consider that the parent nuclide of atomic mass  $M$  decays by the emission of an  $\alpha$  particle or proton, denoted here as  $s$ , that has a nuclear mass  $m_s$  and that the residual (daughter) nucleus has an atomic mass  $M'_d$  (it includes also two extract electrons for  $\alpha$ -decay and one for proton decay).

Since the emission of a particle  $s$  is a two body process, the conservation of momentum requires:

$$\vec{p}_p = \vec{p}_s + \vec{p}_d \quad (\text{A.1})$$

In the center-of-mass frame, the parent nuclide is at rest ( $\vec{p}_p=0$ ), so that  $\vec{p}_s = -\vec{p}_d$ , absolute value of both is  $p$ . The total energy of the emitted particle and the daughter nucleus can be expressed then as:

$$\begin{aligned} E_{total,s} &= \sqrt{m_s^2 + p^2} \\ E_{total,d} &= \sqrt{M_d'^2 + p^2} \end{aligned} \quad (\text{A.2})$$

where  $c = 1$ . The corresponding conservation of energy law requires that:

$$M = E_{total,s} + E_{total,d} = \sqrt{m_s^2 + p^2} + \sqrt{M_d'^2 + p^2} \quad (\text{A.3})$$

and after re-arranging Eq. (A.3) one can obtain:

$$\begin{aligned} M^2 &= m_s^2 + p^2 + M_d'^2 + p^2 + 2\sqrt{(m_s^2 + p^2) \cdot (M_d'^2 + p^2)} \\ (M^2 - m_s^2 - M_d'^2 - 2p^2)^2 &= 4(m_s^2 + p^2) \cdot (M_d'^2 + p^2) \\ M^4 - 2M^2 \cdot m_s^2 - 2M^2 \cdot M_d'^2 - 4M^2 \cdot p^2 + m_s^4 + 2m_s^2 \cdot M_d'^2 + 4m_s^2 \cdot p^2 + \\ &\quad + M_d'^4 + 4M_d'^2 \cdot p^2 + 4p^4 = 4(m_s^2 \cdot M_d'^2 + m_s^2 \cdot p^2 + M_d'^2 \cdot p^2 + p^4) \\ M^4 - 2M^2 \cdot (m_s^2 + M_d'^2) + (m_s^2 - M_d'^2)^2 &= 4M^2 \cdot p^2 \end{aligned} \quad (\text{A.4})$$

The momentum is then determined as:

$$p^2 = \frac{M^4 - 2M^2 \cdot (m_s^2 + M_d'^2) + (m_s^2 - M_d'^2)^2}{4M^2} \quad (\text{A.5})$$

By substituting Eq. (A.5) into (A.2), for the total energy of the emitted particle one can obtain:

$$\begin{aligned}
E_{total,s} &= \sqrt{\frac{4M^2 \cdot m_s^2 + M^4 - 2M^2 \cdot (m_s^2 + M_d'^2) + (m_s^2 - M_d'^2)^2}{4M^2}} \\
&= \sqrt{\frac{M^4 + 2M^2 \cdot (m_s^2 - M_d'^2) + (m_s^2 - M_d'^2)^2}{4M^2}} \\
&= \sqrt{\frac{(M^2 + m_s^2 - M_d'^2)^2}{4M^2}} \\
&= \frac{M^2 + m_s^2 - M_d'^2}{2M}
\end{aligned} \tag{A.6}$$

The kinetic energy of the emitted particle is then determined as:

$$E_s = E_{total,s} - m_s = \frac{M + m_s - M_d'^2}{2M} - m_s = \frac{(M - m_s)^2 - M_d'^2}{2M} \tag{A.7}$$

The decay  $Q$ -value is defined as:

$$\begin{aligned}
Q_s &= M - M_s - M_d \\
&= M - (m_s + n_s \cdot m_e - B_{e,s}) - (M_d' - n_s \cdot m_e) \\
&= M - m_s - M_d' - B_{e,s},
\end{aligned} \tag{A.8}$$

where  $n_s$  is electron number ( $n_s = 1$  for proton decay and  $n_s = 2$  for  $\alpha$ -decay) and  $m_e$  is the electron mass and  $B_{e,s}$  is the electron binding energy of the emitted nuclide.

By re-arranging Eq. (A.8), one can obtain:

$$\begin{aligned}
M_d' &= M - m_s - Q_s - B_{e,s} \\
&= M - m_s - Q_s'
\end{aligned} \tag{A.9}$$

where

$$Q_s' = Q_s - B_{e,s} \tag{A.10}$$

and hence Eq. (A.7) becomes:

$$\begin{aligned}
E_s &= \frac{(M^2 - m_s^2)^2 - (M - m_s - Q_s')^2}{2M} \\
&= \frac{2(M - m_s) \cdot Q_s' - Q_s'^2}{2M}
\end{aligned} \tag{A.11}$$

or

$$Q_s'^2 - 2(M - m_s) \cdot Q_s' - 2M \cdot E_s = 0 \tag{A.12}$$

By solving Eq. (A.12), one can obtain:

$$Q_s' = (M - m_s) \pm \sqrt{(M - m_s)^2 - 2M \cdot E_s} \tag{A.13}$$

Since, the solution with + sign before the square root does not have a physical meaning, one can write the expression for the Q value:

$$Q'_s = (M - m_s) - \sqrt{(M - m_s)^2 - 2M \cdot E_s} \quad (\text{A.14})$$

or alternatively:

$$\begin{aligned} Q'_s &= (M - m_s) - (M - m_s) \cdot \sqrt{1 - \frac{2M \cdot E_s}{(M - m_s)^2}} \\ &= (M - m_s) \cdot \left[ 1 - \sqrt{1 - \frac{2M \cdot E_s}{(M - m_s)^2}} \right] \end{aligned} \quad (\text{A.15})$$

Since  $\frac{2M \cdot E_s}{(M - m_s)^2} \approx \frac{2E_s}{M} \approx \frac{15 \text{ MeV}}{1 \text{ GeV}} \ll 1$ , one can use the Binomial theorem:

$$\sqrt{1 + x} = 1 + \frac{1}{2}x - \frac{1}{8}x^2 + \frac{1}{16}x^3 - \dots \quad (\text{A.16})$$

Thus, Eq. (A.15) can be rewritten as:

$$\begin{aligned} Q'_s &= (M - m_s) \cdot \left[ 1 - 1 + \frac{1}{2} \frac{2M \cdot E_s}{(M - m_s)^2} + \frac{1}{8} \frac{4M^2 \cdot E_s^2}{(M - m_s)^4} + \dots \right] \\ &= \frac{M}{(M - m_s)} \cdot E_s + \frac{1}{2} \frac{M^2}{(M - m_s)^3} \cdot E_s^2 + \dots \\ &\simeq \left[ 1 + \frac{m_s}{(M - m_s)} \right] \cdot E_s + \frac{1}{2} \frac{E_s^2}{M} \end{aligned} \quad (\text{A.17})$$

The first term in Eq. (A.17) is the non-relativistic part, while the second term is an estimate for the relativistic correction. Considering an  $\alpha$ -decay of  $A = 200$  and  $E_\alpha = 8 \text{ MeV}$ , the relativistic correction at the first order would be:

$$\frac{1}{2} \frac{E_\alpha}{M} E_\alpha \approx \frac{1}{2} \frac{8}{200 * 931.494} * 8 = 0.17 * 10^{-3} \text{ MeV}$$

or 0.17 keV.

Taking the electron binding energy into account, Eq. (A.14) can be rewritten as:

$$Q_s = (M - m_s) \pm \sqrt{(M - m_s)^2 - 2M \cdot E_s + B_{e,s}} \quad (\text{A.18})$$

When the decay takes place between the ground-state of the parent and excited state of the daughter nuclide, the decay Q-value should be revised to :

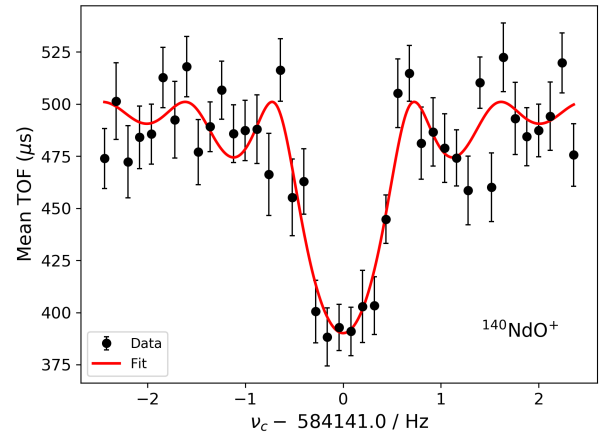
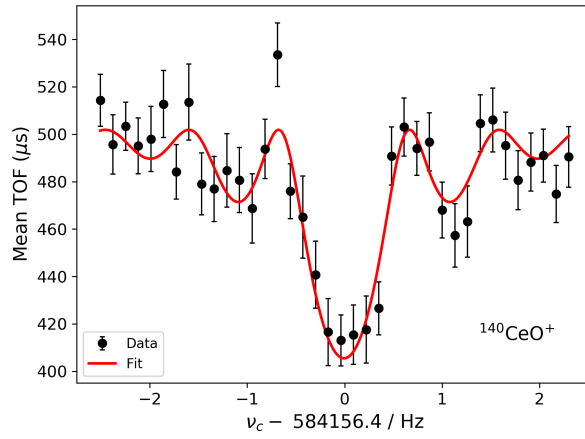
$$Q_s = Q_s^* - E_x \quad (\text{A.19})$$

where  $E_x$  is the excitation energy of the level.

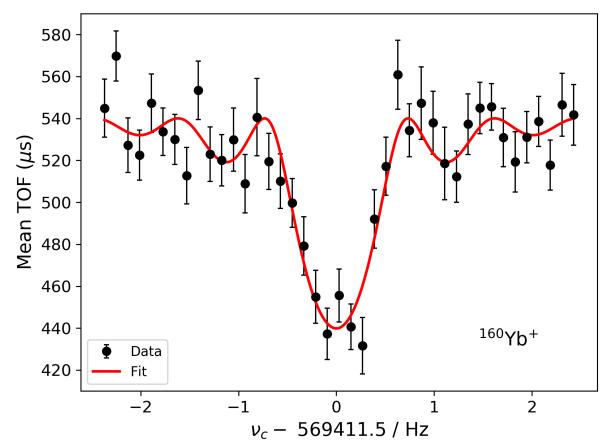
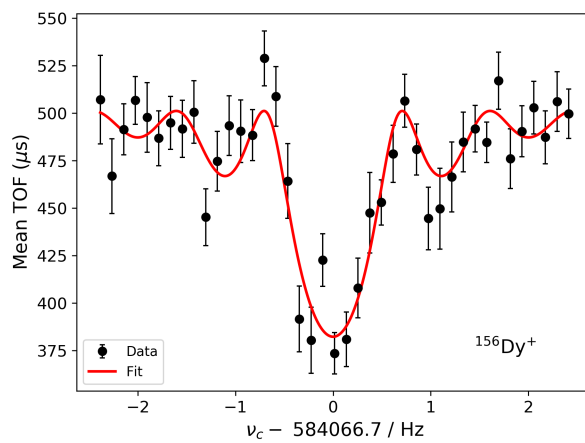


# Appendix B

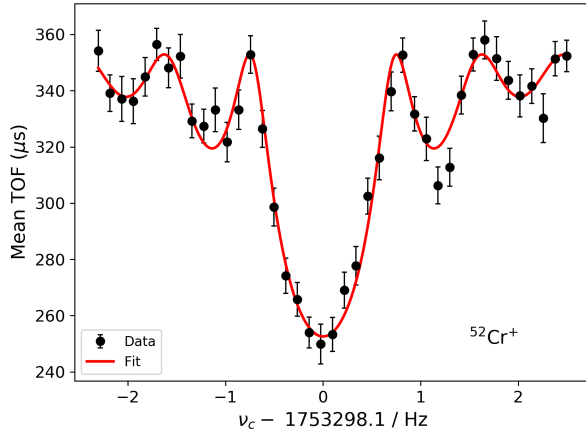
## TOF-ICR Spectra



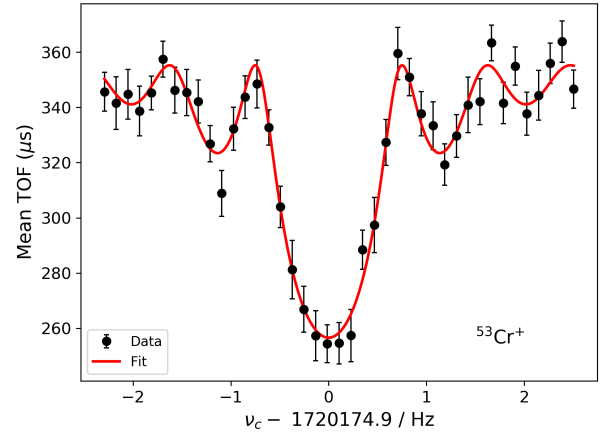
(a) TOF-ICR resonance of  $^{140}\text{CeO}^+$  at  $T_{rf} = 1200$  ms. (b) TOF-ICR resonance of  $^{140}\text{NdO}^+$  at  $T_{rf} = 1200$  ms.



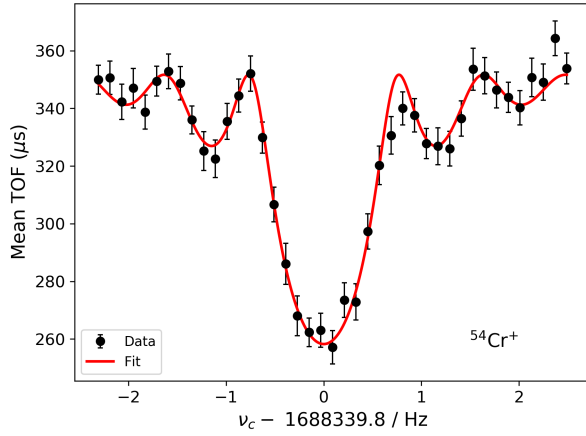
(c) TOF-ICR resonance of  $^{156}\text{Dy}^+$  at  $T_{rf} = 1200$  ms. (d) TOF-ICR resonance of  $^{160}\text{Yb}^+$  at  $T_{rf} = 1200$  ms.



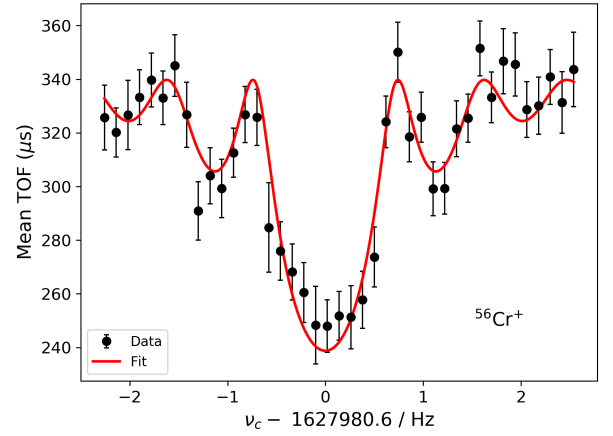
(e) TOF-ICR resonance of  $^{52}\text{Cr}^+$  at  $T_{rf} = 1200$  ms.



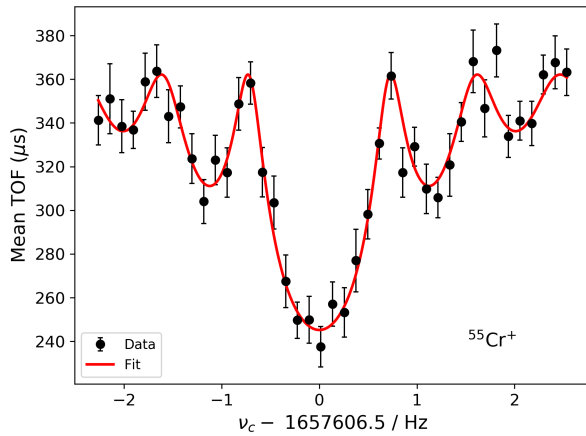
(f) TOF-ICR resonance of  $^{53}\text{Cr}^+$  at  $T_{rf} = 1200$  ms.



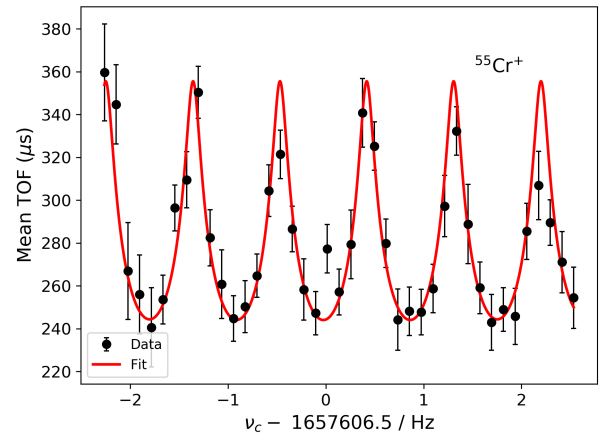
(g) TOF-ICR resonance of  $^{54}\text{Cr}^+$  at  $T_{rf} = 1200$  ms.



(h) TOF-ICR resonance of  $^{56}\text{Cr}^+$  at  $T_{rf} = 1200$  ms.

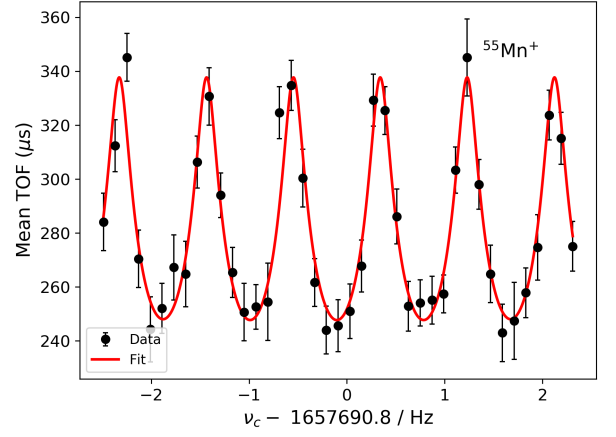
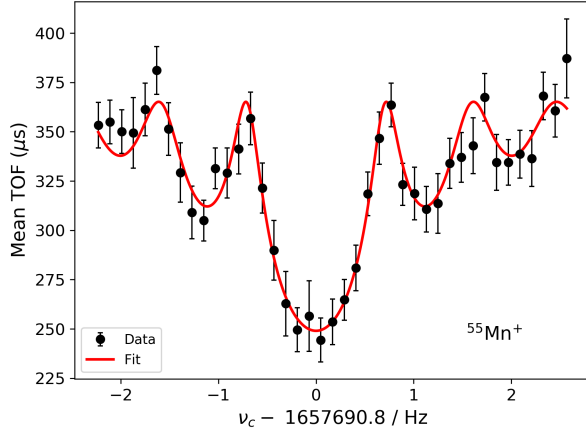


(i) TOF-ICR resonance of  $^{55}\text{Cr}^+$  at  $T_{rf} = 1200$  ms.

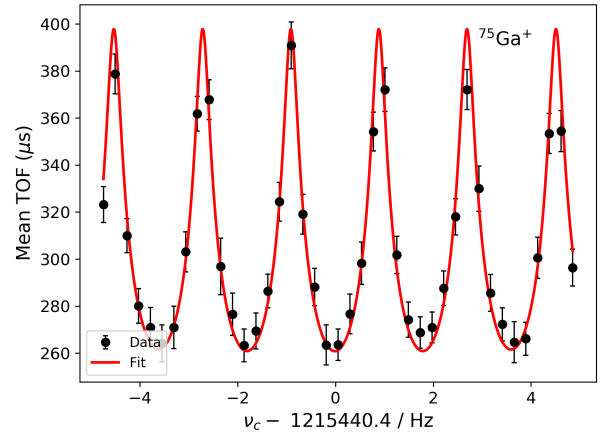
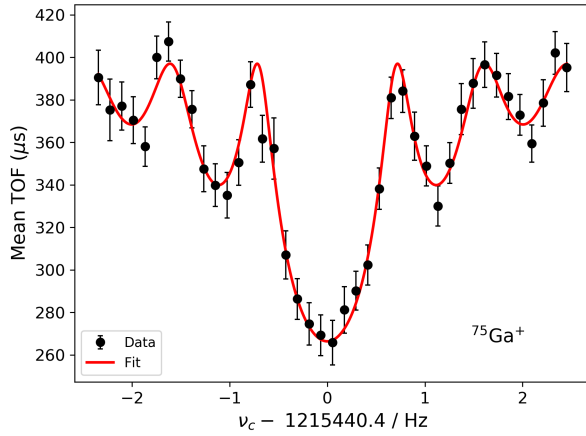


(j) Ramsey-type excitation TOF-ICR resonance of  $^{55}\text{Cr}^+$  at  $(100 - 1000 - 100)$  ms.

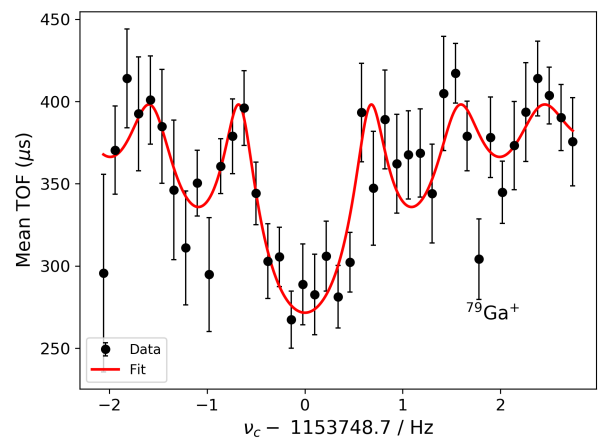
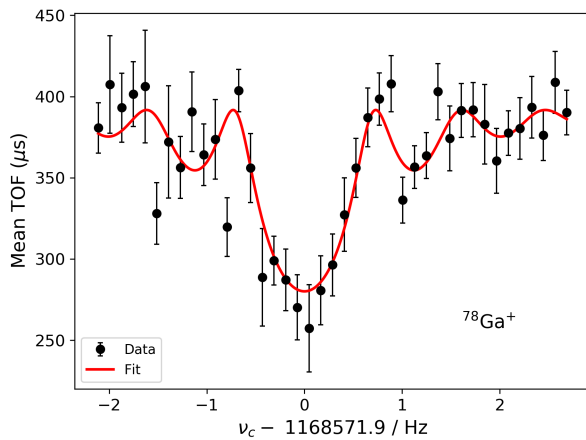
APPENDIX B. TOF-ICR SPECTRA



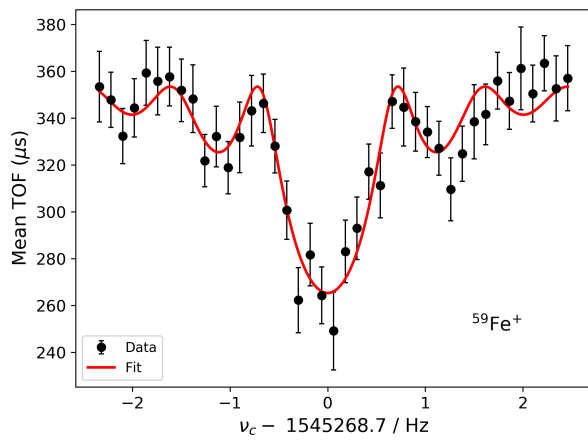
(k) TOF-ICR resonance of  $^{55}\text{Mn}^+$  at  $T_{rf} = 1200$  ms. (l) Ramsey-type excitation TOF-ICR resonance of  $^{55}\text{Mn}^+$  at  $(100 - 1000 - 100)$  ms.



(m) TOF-ICR resonance of  $^{75}\text{Ga}^+$  at  $T_{rf} = 1200$  ms. (n) Ramsey-type excitation TOF-ICR resonance of  $^{75}\text{Ga}^+$  at  $(100 - 1000 - 100)$  ms.



(o) TOF-ICR resonance of  $^{78}\text{Ga}^+$  at  $T_{rf} = 1200$  ms. (p) TOF-ICR resonance of  $^{79}\text{Ga}^+$  at  $T_{rf} = 1200$  ms.



(q) TOF-ICR resonance of  $^{59}\text{Fe}^+$  at  $T_{rf} = 1200$  ms.

Figure B.-2: TOF-ICR spectra.

# Bibliography

- [ABB<sup>+</sup>11] V. N. Aseev, A. I. Belesev, A. I. Berlev, E. V. Geraskin, A. A. Golubev, N. A. Likhovid, V. M. Lobashev, A. A. Nozik, V. S. Pantuev, V. I. Parfenov, A. K. Skasyrskaya, F. V. Tkachov, and S. V. Zadorozhny. Upper limit on the electron antineutrino mass from the troitsk experiment. *Phys. Rev. D*, 84:112003, Dec 2011.
- [ADLW86] G. Audi, W. G. Davies, and G. E. Lee-Whiting. A method of determining the relative importance of particular data on selected parameters in the least-squares analysis of experimental data. *Nuclear Instruments and Methods in Physics Research Section A: Accelerators, Spectrometers, Detectors and Associated Equipment*, 249(2):443–450, 1986.
- [AEH<sup>+</sup>10] A. N. Andreyev, J. Elseviers, M. Huyse, P. Van Duppen, S. Antalic, A. Barzakh, N. Bree, T. E. Cocolios, V. F. Comas, J. Diriken, D. Fedorov, V. Fedosseev, S. Franchoo, J. A. Heredia, O. Ivanov, U. Köster, B. A. Marsh, K. Nishio, R. D. Page, N. Patronis, M. Seliverstov, I. Tsekhanovich, P. Van den Bergh, J. Van De Walle, M. Venhart, S. Vermote, M. Veselsky, C. Wage-mans, T. Ichikawa, A. Iwamoto, P. Möller, and A.J. Sierk. New type of asymmetric fission in proton-rich nuclei. *Phys. Rev. Lett.*, 105:252502, Dec 2010.
- [AKM<sup>+</sup>17] G. Audi, F. G. Kondev, W. Meng, W. J. Huang, and S. Naimi. The NUBASE2016 evaluation of nuclear properties. *Chinese Physics C*, 41(3):030001, 2017.
- [Arn96] W. D. Arnett. *Supernovae and Nucleosynthesis : an Investigation of the History of Matter, from the Big Bang to the Present*. Princeton University Press, 1996.
- [Aud01] G. Audi. The evaluation of atomic masses. *Hyperfine Interactions*, 132(1):7–34, Jan 2001.
- [Aud06] G. Audi. The history of nuclidic masses and of their evaluation. *International Journal of Mass Spectrometry*, 251(2):85–94, 2006. ULTRA-ACCURATE MASS SPECTROMETRY AND RELATED TOPICS Dedicated to H.-J. Kluge on the occasion of his 65th birthday anniversary.

- [AW93] G. Audi and A. H. Wapstra. The 1993 atomic mass evaluation: (i) atomic mass table. *Nuclear Physics A*, 565(1):1 – 65, 1993.
- [AWT03] G. Audi, A. H. Wapstra, and C. Thibault. The Ame2003 atomic mass evaluation: (ii). tables, graphs and references. *Nuclear Physics A*, 729(1):337 – 676, 2003. The 2003 NUBASE and Atomic Mass Evaluations.
- [AWW<sup>+</sup>12] G. Audi, M. Wang, A. H. Wapstra, F.G. Kondev, M. MacCormick, X. Xu, and B. Pfeiffer. The Ame2012 atomic mass evaluation. *Chinese Physics C*, 36(12):1287, 2012.
- [BA93] C. Borcea and G. Audi. New methods for extrapolating masses far from stability. *Rev. Roum. Phys.*, 38:455, 1993.
- [BAA<sup>+</sup>00] D. Beck, F. Ames, G. Audi, G. Bollen, F. Herfurth, H. J. Kluge, A. Kohl, M. König, D. Lunney, I. Martel, R. B. Moore, H. Raimbault-Hartmann, E. Schark, S. Schwarz, M. de Saint Simon, and J. Szerypo. Accurate masses of unstable rare-earth isotopes by ISOLTRAP. *The European Physical Journal A*, 8(3):307–329, Sep 2000.
- [BAA<sup>+</sup>01] G. Bollen, F. Ames, G. Audi, D. Beck, J. Dilling, O. Engels, S. Henry, F. Herfurth, A. Kellerbauer, H.-J. Kluge, A. Kohl, E. Lamour, D. Lunney, R. B. Moore, M. Oinonen, C. Scheidenberger, S. Schwarz, G. Sikler, J. Szerypo, and C. Weber. Mass measurements on short-lived nuclides with ISOLTRAP. *Hyperfine Interactions*, 132(1):213–220, Jan 2001.
- [BAB<sup>+</sup>96] B. Blank, S. Andriamonje, F. Boué, S. Czajkowski, R. Del Moral, J. P. Dufour, A. Fleury, P. Pourre, M.S. Pravikoff, K.-H. Schmidt, E. Hanelt, and N. A. Orr. First spectroscopic study of <sup>22</sup>Si. *Phys. Rev. C*, 54:572–575, Aug 1996.
- [BATH97] V. Barci, G. Ardisson, D. Trubert, and M. Hussonnois. Excited states in the doubly odd <sup>168</sup>Lu nucleus fed by electron-capture decay of <sup>168</sup>Hf ( $T_{1/2} = 25.95$  min). *Phys. Rev. C*, 55:2279–2289, May 1997.
- [BB36] H. A. Bethe and R. F. Bacher. Nuclear physics a. stationary states of nuclei. *Rev. Mod. Phys.*, 8:82–229, Apr 1936.
- [BB08] B. Blank and M. J. G. Borge. Nuclear structure at the proton drip line: Advances with nuclear decay studies. *Progress in Particle and Nuclear Physics*, 60(2):403 – 483, 2008.
- [BBG<sup>+</sup>99] H. G. Bohlen, A. Blazević, B. Gebauer, W. Von Oertzen, S. Thummerer, R. Kalpakchieva, S. M. Grimes, and T. N. Massey. Spectroscopy of exotic nuclei with multi-nucleon transfer reactions. *Progress in Particle and Nuclear Physics*, 42(Supplement C):17 – 26, 1999. Heavy Ion Collisions from Nuclear to Quark Matter.

## BIBLIOGRAPHY

---

- [BBH<sup>+</sup>02] K. Blaum, G. Bollen, F. Herfurth, A. Kellerbauer, H.-J. Kluge, M. Kuckein, E. Sauvan, C. Scheidenberger, and L. Schweikhard. Carbon clusters for absolute mass measurements at ISOLTRAP. *The European Physical Journal A - Hadrons and Nuclei*, 15(1):245–248, Sep 2002.
- [BDN13] K. Blaum, J. Dilling, and W. Nörtershäuser. Precision atomic physics techniques for nuclear physics with radioactive beams. *Physica Scripta*, 2013(T152):014017, 2013.
- [BFG<sup>+</sup>89] L. Bianchi, B. Fernandez, J. Gastebois, A. Gillibert, W. Mittig, and J. Barrette. Spég: An energy loss spectrometer for ganil. *Nuclear Instruments and Methods in Physics Research Section A: Accelerators, Spectrometers, Detectors and Associated Equipment*, 276(3):509 – 520, 1989.
- [BG86] L. S. Brown and G. Gabrielse. Geonium theory: Physics of a single electron or ion in a Penning trap. *Rev. Mod. Phys.*, 58:233–311, Jan 1986.
- [BJP<sup>+</sup>91] V. Borrel, J. C. Jacmart, F. Pougheon, R. Anne, C. Detraz, D. Guillemaud-Mueller, A. C. Mueller, D. Bazin, R. Del Moral, J. P. Dufour, F. Hubert, M. S. Pravikoff, and E. Roeckl. <sup>31</sup>Ar and <sup>27</sup>S: Beta-delayed two-proton emission and mass excess. *Nuclear Physics A*, 531(2):353 – 369, 1991.
- [Bla06] K. Blaum. High-accuracy mass spectrometry with stored ions. *Physics Reports*, 425(1):1 – 78, 2006.
- [BMS<sup>+</sup>73] R. C. Barber, J. O. Meredith, F. C. G. Southon, P. Williams, J. W. Barnard, K. Sharma, and H. E. Duckworth. Spacing of nuclear ground-state levels in the region  $94 \leq n \leq 114$ . *Phys. Rev. Lett.*, 31:728–730, Sep 1973.
- [BMSS90] G. Bollen, R. B. Moore, G. Savard, and H. Stolzenberg. The accuracy of heavy-ion mass measurements using time of flight-ion cyclotron resonance in a Penning trap. *Journal of Applied Physics*, 68(9):4355–4374, 1990.
- [BND13] Y. Blumenfeld, T. Nilsson, and P. Van Duppen. Facilities and methods for radioactive ion beam production. *Physica Scripta*, 2013(T152):014023, 2013.
- [BNW10] K. Blaum, Yu. N. Novikov, and G. Werth. Penning traps as a versatile tool for precise experiments in fundamental physics. *Contemporary Physics*, 51(2):149–175, 2010.
- [Bol01] G. Bollen. Mass measurements of short-lived nuclides with ion traps. *Nuclear Physics A*, 693(1):3–18, 2001. Radioactive Nuclear Beams.
- [Bos77] K. Bos. Determination of atomic masses from experimental data. *PhD Thesis*, 1977.

- [BW72] K. Bos and A. H. Wapstra. *Mass Extrapolation and Mass Formulae*, pages 273–277. Springer US, Boston, MA, 1972.
- [Cas09] R. F. Casten. Quantum phase transitions and structural evolution in nuclei. *Progress in Particle and Nuclear Physics*, 62(1):183 – 209, 2009.
- [CCP+72] A. Charvet, R. Chéry, Do Huu Phuoc, R. Duffait, A. Emsallem, and G. Marguier. The decays of 5.5 min  $^{168g}\text{Lu}$  and 6.7 min  $^{168m}\text{Lu}$ . *Nuclear Physics A*, 197(2):490 – 496, 1972.
- [CS01] J. A. Cameron and B. Singh. Nuclear data sheets for  $A = 41$ . *Nuclear Data Sheets*, 94(3):429 – 603, 2001.
- [CSS+04] J. A. Clark, G. Savard, K. S. Sharma, J. Vaz, J. C. Wang, Z. Zhou, A. Heinz, B. Blank, F. Buchinger, J. E. Crawford, S. Gulick, J. K. P. Lee, A. F. Levand, D. Seweryniak, G. D. Sprouse, and W. Trimble. Precise mass measurement of  $^{68}\text{Se}$ , a waiting-point nuclide along the rp process. *Phys. Rev. Lett.*, 92:192501, May 2004.
- [CW83] E. R. Cohen and A. H. Wapstra. Recommended treatment of precision measurements related to nuclear energy levels and atomic masses. *Nuclear Instruments and Methods in Physics Research*, 211(1):153 – 157, 1983.
- [CWBG81] R. F. Casten, D. D. Warner, D. S. Brenner, and R. L. Gill. Relation between the  $Z = 64$  shell closure and the onset of deformation at  $N = 88 - 90$ . *Phys. Rev. Lett.*, 47:1433–1436, Nov 1981.
- [Dar70] B. D. Darwent. Bond dissociation energies in simple molecules. *NSRDS-NBS NO. 31, U. S. DEPT. COMMERCE, WASHINGTON, D. C. JAN. 1970, 48 P*, 1970.
- [DG80] J. Dechargé and D. Gogny. Hartree-fock-bogolyubov calculations with the  $d1$  effective interaction on spherical nuclei. *Phys. Rev. C*, 21:1568–1593, Apr 1980.
- [DMCD+03] P. De Marcillac, N. Coron, G. Dambier, J. Leblanc, and J. P. Moalic. Experimental detection of  $\alpha$ -particles from the radioactive decay of natural bismuth. *Nature*, 422(6934):876–878, 2003.
- [DNB+95] F. DiFilippo, V. Natarajan, M. Bradley, F. Palmer, and D. E. Pritchard. Accurate atomic mass measurements from Penning trap mass comparisons of individual ions. *Physica Scripta*, 1995(T59):144, 1995.
- [DNBP94] F. DiFilippo, V. Natarajan, K. R. Boyce, and D. E. Pritchard. Accurate atomic masses for fundamental metrology. *Phys. Rev. Lett.*, 73:1481–1484, Sep 1994.

## BIBLIOGRAPHY

---

- [DPB<sup>+</sup>15] T. Dickel, W. R. Plaß, A. Becker, U. Czok, H. Geissel, E. Haettner, C. Jesch, W. Kinsel, M. Petrick, C. Scheidenberger, A. Simon, and M. I. Yavor. A high-performance multiple-reflection time-of-flight mass spectrometer and isobar separator for the research with exotic nuclei. *Nuclear Instruments and Methods in Physics Research Section A: Accelerators, Spectrometers, Detectors and Associated Equipment*, 777:172 – 188, 2015.
- [DSI80] A. E. L. Dieperink, O. Scholten, and F. Iachello. Classical limit of the interacting-boson model. *Phys. Rev. Lett.*, 44:1747–1750, Jun 1980.
- [DZ95] J. Duffo and A. P. Zuker. Microscopic mass formulas. *Phys. Rev. C*, 52:R23–R27, Jul 1995.
- [DZ96] J. Duffo and A.P. Zuker. Private communication to G. Audi. February 1996.
- [EBB<sup>+</sup>13] S. Eliseev, K. Blaum, M. Block, C. Droese, M. Goncharov, E. Minaya Ramirez, D. A. Nesterenko, Yu. N. Novikov, and L. Schweikhard. Phase-imaging ion-cyclotron-resonance measurements for short-lived nuclides. *Phys. Rev. Lett.*, 110:082501, Feb 2013.
- [EBB<sup>+</sup>15] S. Eliseev, K. Blaum, M. Block, S. Chenmarev, H. Dorrer, Ch. E. Düllmann, C. Enss, P. E. Filianin, L. Gastaldo, M. Goncharov, U. Köster, F. Lautenschläger, Yu. N. Novikov, A. Rischka, R. X. Schüssler, L. Schweikhard, and A. Türler. Direct measurement of the mass difference of <sup>163</sup>Ho and <sup>163</sup>Dy solves the  $q$ -value puzzle for the neutrino mass determination. *Phys. Rev. Lett.*, 115:062501, Aug 2015.
- [EGB<sup>+</sup>11] S. Eliseev, M. Goncharov, K. Blaum, M. Block, C. Droese, F. Herfurth, E. Minaya Ramirez, Yu. N. Novikov, L. Schweikhard, V. M. Shabaev, I. I. Tupitsyn, K. Zuber, and N. A. Zubova. Multiple-resonance phenomenon in neutrinoless double-electron capture. *Phys. Rev. C*, 84:012501, Jul 2011.
- [EKMW60a] F. Everling, L. A. König, J. H. E. Mattauch, and A. H. Wapstra. Atomic masses of nuclides for  $A \leq 70$ . *Nuclear Physics*, 15:342 – 355, 1960.
- [EKMW60b] F. Everling, L.A. König, J. H. E. Mattauch, and A. H. Wapstra. Relative nuclidic masses. *Nuclear Physics*, 18:529 – 569, 1960.
- [EKMW61] F. Everling, L. A. König, J. H. E. Mattauch, and A. H. Wapstra. Adjustment of relative nuclidic masses (i)  $A \leq 70$ . *Nuclear Physics*, 25(Supplement C):177 – 215, 1961.

- [FGM08] B. Franzke, H. Geissel, and G. Münzenberg. Mass and lifetime measurements of exotic nuclei in storage rings. *Mass Spectrometry Reviews*, 27(5):428–469, 2008.
- [Fra87] B. Franzke. The heavy ion storage and cooler ring project esr at GSI. *Nuclear Instruments and Methods in Physics Research Section B: Beam Interactions with Materials and Atoms*, 24-25:18–25, 1987.
- [GAB<sup>+</sup>01] H. Geissel, F. Attallah, K. Beckert, F. Bosch, M. Falch, B. Franzke, M. Hausmann, Th. Kerscher, O. Klepper, H.-J. Kluge, C. Kozhuharov, Yu. Litvinov, K. E. G. Löbner, G. Münzenberg, N. Nankov, F. Nolden, Yu. Novikov, T. Ohtsubo, Z. Patyk, T. Radon, C. Scheidenberger, J. Stadlmann, M. Steck, K. Sümmerer, H. Weick, and H. Wollnik. Progress in mass measurements of stored exotic nuclei at relativistic energies. *Nuclear Physics A*, 685(1):115–126, 2001. Nucleus-Nucleus Collisions 2000.
- [GAB<sup>+</sup>05] C. Guénaut, G. Audi, D. Beck, K. Blaum, G. Bollen, P. Delahaye, F. Herfurth, A. Kellerbauer, H.-J. Kluge, D. Lunney, S. Schwarz, L. Schweikhard, and C. Yazidjian. Mass measurements of  $^{56-57}\text{Cr}$  and the question of shell reincarnation at  $N = 32$ . *Journal of Physics G: Nuclear and Particle Physics*, 31(10):S1765, 2005.
- [GAB<sup>+</sup>07] C. Guénaut, G. Audi, D. Beck, K. Blaum, G. Bollen, P. Delahaye, F. Herfurth, A. Kellerbauer, H.-J. Kluge, J. Libert, D. Lunney, S. Schwarz, L. Schweikhard, and C. Yazidjian. High-precision mass measurements of nickel, copper, and gallium isotopes and the purported shell closure at  $n = 40$ . *Phys. Rev. C*, 75:044303, Apr 2007.
- [GBB<sup>+</sup>07] S. George, S. Baruah, B. Blank, K. Blaum, M. Breitenfeldt, U. Hager, F. Herfurth, A. Herlert, A. Kellerbauer, H.-J. Kluge, M. Kretzschmar, D. Lunney, R. Savreux, S. Schwarz, L. Schweikhard, and C. Yazidjian. Ramsey method of separated oscillatory fields for high-precision Penning Trap Mass Spectrometry. *Phys. Rev. Lett.*, 98:162501, Apr 2007.
- [GCP13a] S. Goriely, N. Chamel, and J. M. Pearson. Further explorations of Skyrme-Hartree-Fock-Bogoliubov mass formulas. XIII. the 2012 atomic mass evaluation and the symmetry coefficient. *Phys. Rev. C*, 88:024308, Aug 2013.
- [GCP13b] S. Goriely, N. Chamel, and J. M. Pearson. Hartree-Fock-Bogoliubov nuclear mass model with 0.50 MeV accuracy based on standard forms of Skyrme and pairing functionals. *Phys. Rev. C*, 88:061302, Dec 2013.

## BIBLIOGRAPHY

---

- [GCP16] S. Goriely, N. Chamel, and J. M. Pearson. Latest results of Skyrme-Hartree-Fock-Bogoliubov mass formulas. *Journal of Physics: Conference Series*, 665(1):012038, 2016.
- [GKT80] G. Gräff, H. Kalinowsky, and J. Traut. A direct determination of the proton electron mass ratio. *Zeitschrift für Physik A Atoms and Nuclei*, 297(1):35–39, Mar 1980.
- [GMDN68] T. B. Grandy, W. J. McDonald, W. K. Dawson, and G. C. Neilson. The  $^{48}\text{Ca}(d,n)^{49}\text{Sc}$  reaction at  $E_d = 5.5$  and  $6.0$  MeV. *Nuclear Physics A*, 113(2):353 – 366, 1968.
- [GMO<sup>+</sup>12] L. Gaudefroy, W. Mittig, N. A. Orr, S. Varet, M. Chartier, P. Roussel-Chomaz, J. P. Ebran, B. Fernández-Domínguez, G. Frémont, P. Gangnant, A. Gillibert, S. Grévy, J. F. Libin, V. A. Maslov, S. Paschalis, B. Pietras, Yu.-E. Penionzhkevich, C. Spitaels, and A. C. C. Villari. Direct mass measurements of  $^{19}\text{B}$ ,  $^{22}\text{C}$ ,  $^{29}\text{F}$ ,  $^{31}\text{Ne}$ ,  $^{34}\text{Na}$  and other light exotic nuclei. *Phys. Rev. Lett.*, 109:202503, Nov 2012.
- [Gor00] S. Goriely. Nuclear inputs for astrophysics applications. *AIP Conference Proceedings*, 529(1):287–294, 2000.
- [GR71] B. Grennberg and A. Rytz. Absolute measurements of  $\alpha$ -ray energies. *Metrologia*, 7(2):65, 1971.
- [HA17] W. J. Huang and G. Audi. Corrections of alpha- and proton-decay energies in implantation experiments. *EPJ Web Conf.*, 146:10007, 2017.
- [HAW<sup>+</sup>17] W. J. Huang, G. Audi, Meng Wang, F. G. Kondev, S. Naimi, and Xing Xu. The ame2016 atomic mass evaluation (i). evaluation of input data; and adjustment procedures. *Chinese Physics C*, 41(3):030002, 2017.
- [HBGU<sup>+</sup>06] P. A. Hausladen, J. R. Beene, A. Galindo-Uribarri, Y. Larochelle, J. F. Liang, P. E. Mueller, D. Shapira, D. W. Stracener, J. Thomas, R. L. Varner, and H. Wollnik. Opportunistic mass measurements at the holifield radioactive ion beam facility. *International Journal of Mass Spectrometry*, 251(2):119 – 124, 2006. ULTRA-ACCURATE MASS SPECTROMETRY AND RELATED TOPICS Dedicated to H.-J. Kluge on the occasion of his 65th birthday anniversary.
- [HCJH77] J. C. Hardy, L. C. Carraz, B. Jonson, and P. G. Hansen. The essential decay of pandemonium: A demonstration of errors in complex beta-decay schemes. *Physics Letters B*, 71(2):307 – 310, 1977.
- [HHM<sup>+</sup>12] S. Hofmann, S. Heinz, R. Mann, J. Maurer, J. Khuyagbaatar, D. Ackermann, S. Antalic, W. Barth, M. Block, H. G. Burkhard,

- V. F. Comas, L. Dahl, K. Eberhardt, J. Gostic, R. A. Henderson, J. A. Heredia, F. P. Heßberger, J. M. Kenneally, B. Kindler, I. Kojouharov, J. V. Kratz, R. Lang, M. Leino, B. Lommel, K. J. Moody, G. Münzenberg, S. L. Nelson, K. Nishio, A. G. Popeko, J. Runke, S. Saro, D. A. Shaughnessy, M. A. Stoyer, P. Thörle-Pospiech, K. Tinschert, N. Trautmann, J. Uusitalo, P. A. Wilk, and A. V. Yeremin. The reaction  $^{48}\text{Ca} + ^{248}\text{Cm} \rightarrow ^{296}116^*$  studied at the gsi-ship. *Eur. Phys. J. A*, 48(5):62, 2012.
- [HKLR<sup>+</sup>17] F. Heiße, F. Köhler-Langes, S. Rau, J. Hou, S. Junck, A. Kracke, A. Mooser, W. Quint, S. Ulmer, G. Werth, K. Blaum, and S. Sturm. High-Precision Measurement of the Proton’s Atomic Mass. *Phys. Rev. Lett.*, 119:033001, Jul 2017.
- [HLMY<sup>+</sup>08] K. Hauschild, A. Lopez-Martens, A. V. Yeremin, O. Dorvaux, S. Antalic, A. V. Belozarov, Ch. Briançon, M. L. Chelnokov, V. I. Chepigin, D. Curien, B. Gall, A. Görgen, V. A. Gorshkov, M. Guttormsen, F. Hanappe, A. P. Kabachenko, F. Khalfallah, A. C. Larsen, O. N. Malyshev, A. Minkova, A. G. Popeko, M. Rousseau, N. Rowley, S. Saro, A. V. Shutov, S. Siem, L. Stuttgè, A. I. Svirikhin, N. U. H. Syed, Ch. Theisen, and M. Venhart. High- $k$ ,  $t_{1/2} = 1.4(1)$  ms, isomeric state in  $^{255}\text{Lr}$ . *Phys. Rev. C*, 78:021302, Aug 2008.
- [HMY<sup>+</sup>82] S. Hofmann, G. Münzenberg, K. Valli, F. Heßberger, J. R. H. Schneider, P. Armbruster, B. Thuma, and Y. Eyal. Stopping of alpha-recoil atoms in silicon. *GSI-Report*, page 241, 1982.
- [Hof89] C. Hofmeyr.  $^{53}\text{Cr}(n, \gamma)$ ; transition energies and levels excited in thermal neutron capture. *Nuclear Physics A*, 500(1):111 – 126, 1989.
- [HSFM17] S. Hamzeloui, J. A. Smith, D. J. Fink, and E. G. Myers. Precision mass ratio of  $^3\text{He}^+$  to  $\text{HD}^+$ . *Phys. Rev. A*, 96:060501, Dec 2017.
- [Hui54] J.R. Huizenga. Isotopic masses III.  $A > 201$ . *Physica*, 21(1):410 – 424, 1954.
- [IKKP80] M. A. Islam, T. J. Kennett, S. A. Kerr, and W. V. Prestwich. A self-consistent set of neutron separation energies. *Canadian Journal of Physics*, 58(2):168–173, 1980.
- [INT07] INTERNATIONAL ATOMIC ENERGY AGENCY. *Database of Prompt Gamma Rays from Slow Neutron Capture for Elemental Analysis*. INTERNATIONAL ATOMIC ENERGY AGENCY, Vienna, 2007.
- [ISW<sup>+</sup>13] Y. Ito, P. Schury, M. Wada, S. Naimi, T. Sonoda, H. Mita, F. Arai, A. Takamine, K. Okada, A. Ozawa, and H. Wollnik. Single-reference high-precision mass measurement with a

- multireflection time-of-flight mass spectrograph. *Phys. Rev. C*, 88:011306, Jul 2013.
- [IUP14] IUPAC. Compendium of chemical terminology, 2nd ed. (the “gold book”). by a.d. mc, 2014.
- [JAA<sup>+</sup>10] H. T. Johansson, Yu. Aksyutina, T. Aumann, K. Boretzky, M. J. G. Borge, A. Chatillon, L. V. Chulkov, D. Cortina-Gil, U. Datta Pramanik, H. Emling, C. Forssén, H.O.U. Fynbo, H. Geissel, G. Ickert, B. Jonson, R. Kulesa, C. Langer, M. Lantz, T. LeBlais, K. Mahata, M. Meister, G. Münzenberg, T. Nilsson, G. Nyman, R. Palit, S. Paschalis, W. Prokopowicz, R. Reifarth, A. Richter, K. Riisager, G. Schrieder, H. Simon, K. Sümmerer, O. Tengblad, H. Weick, and M. V. Zhukov. The unbound isotopes  $^9,^{10}\text{He}$ . *Nuclear Physics A*, 842(1):15 – 32, 2010.
- [JHJ84] A. S. Jensen, P. G. Hansen, and B. Jonson. New mass relations and two- and four-nucleon correlations. *Nuclear Physics A*, 431(3):393 – 418, 1984.
- [Jos62] B. D. Josephson. Possible new effects in superconductive tunnelling. *Physics Letters*, 1(7):251 – 253, 1962.
- [KAB<sup>+</sup>13] S. Kreim, D. Atanasov, D. Beck, K. Blaum, Ch. Böhm, Ch. Borgmann, M. Breitenfeldt, T.E. Cocolios, D. Fink, S. George, A. Herlert, A. Kellerbauer, U. Köster, M. Kowalska, D. Lunney, V. Manea, E. Minaya Ramirez, S. Naimi, D. Neidherr, T. Nicol, R. E. Rossel, M. Rosenbusch, L. Schweikhard, J. Stanja, F. Wienholtz, R. N. Wolf, and K. Zuber. Recent exploits of the ISOLTRAP mass spectrometer. *Nuclear Instruments and Methods in Physics Research Section B: Beam Interactions with Materials and Atoms*, 317:492 – 500, 2013. XVIth International Conference on ElectroMagnetic Isotope Separators and Techniques Related to their Applications, December 2-7, 2012 at Matsue, Japan.
- [Kar17] J. Karthein. Precision mass measurements using the Phase-Imaging Ion-Cyclotron-Resonance detection technique. *Master Thesis*, 2017.
- [KBB<sup>+</sup>03] A. Kellerbauer, K. Blaum, G. Bollen, F. Herfurth, H.-J. Kluge, M. Kuckein, E. Sauvan, C. Scheidenberger, and L. Schweikhard. From direct to absolute mass measurements: A study of the accuracy of ISOLTRAP. *Eur. Phys. J. D*, 22(1):53–64, 2003.
- [KBK<sup>+</sup>95] M. König, G. Bollen, H.-J. Kluge, T. Otto, and J. Szerypo. Quadrupole excitation of stored ion motion at the true cyclotron frequency. *International Journal of Mass Spectrometry and Ion Processes*, 142(1):95 – 116, 1995.

- [KCL80] J. Kopecky, R.E. Chrien, and H.I. Liou. Resonance neutron capture in  $^{52}\text{Cr}$ . *Nuclear Physics A*, 334(1):35 – 44, 1980.
- [KH88] K. S. Krane and D. Halliday. *Introductory nuclear physics*, volume 465. Wiley New York, 1988.
- [KLD<sup>+</sup>13] Z. Kohley, E. Lunderberg, P. A. DeYoung, A. Volya, T. Baumann, D. Bazin, G. Christian, N. L. Cooper, N. Frank, A. Gade, C. Hall, J. Hinnefeld, B. Luther, S. Mosby, W. A. Peters, J. K. Smith, J. Snyder, A. Spyrou, and M. Thoennessen. First observation of the  $^{13}\text{Li}$  ground state. *Phys. Rev. C*, 87:011304, Jan 2013.
- [KMW58] T. P. Kohman, J. H. E. Mattauch, and A. H. Wapstra. New Reference Nuclide. *Science*, 127(3312):1431–1432, 1958.
- [Kno12] G. F. Knoll. *Radiation detection and measurement 4th Edition*. John Wiley & Sons, 2012.
- [KNT<sup>+</sup>16] Y. Kondo, T. Nakamura, R. Tanaka, R. Minakata, S. Ogoshi, N. A. Orr, N. L. Achouri, T. Aumann, H. Baba, F. Delaunay, P. Doornenbal, N. Fukuda, J. Gibelin, J. W. Hwang, N. Inabe, T. Isobe, D. Kameda, D. Kanno, S. Kim, N. Kobayashi, T. Kobayashi, T. Kubo, S. Leblond, J. Lee, F. M. Marqués, T. Motobayashi, D. Murai, T. Murakami, K. Muto, T. Nakashima, N. Nakatsuka, A. Navin, S. Nishi, H. Otsu, H. Sato, Y. Satou, Y. Shimizu, H. Suzuki, K. Takahashi, H. Takeda, S. Takeuchi, Y. Togano, A. G. Tuff, M. Vandebrouck, and K. Yoneda. Nucleus  $^{26}\text{O}$ : A Barely Unbound System beyond the Drip Line. *Phys. Rev. Lett.*, 116:102503, Mar 2016.
- [Kön60] L. A. König. Mathematical Details of the Mass Computation. *Proc. Int. Conf. Nuclidic Masses*, pages 39–57, 1960.
- [Kre07] M. Kretschmar. The Ramsey method in high-precision mass spectrometry with Penning traps: Theoretical foundations. *International Journal of Mass Spectrometry*, 264(2):122 – 145, 2007.
- [KRR16] A. Kramida, Yu. Ralchenko, J. Reader, and NIST ASD Team (2015). *NIST Atomic Spectra Database (version 5.3)*, [Online]. Available: <http://physics.nist.gov/asd>. National Institute of Standards and Technology, Gaithersburg, MD., 2016.
- [KSB<sup>+</sup>12] Z. Kohley, J. Snyder, T. Baumann, G. Christian, P. A. DeYoung, J. E. Finck, R. A. Haring-Kaye, M. Jones, E. Lunderberg, B. Luther, S. Mosby, A. Simon, J. K. Smith, A. Spyrou, S. L. Stephenson, and M. Thoennessen. Unresolved Question of the  $^{10}\text{He}$  Ground State Resonance. *Phys. Rev. Lett.*, 109:232501, Dec 2012.

## BIBLIOGRAPHY

---

- [KTUY05] H. Koura, T. Tachibana, M. Uno, and M. Yamada. Nuclidic mass formula on a spherical basis with an improved even-odd term. *Progress of Theoretical Physics*, 113(2):305–325, 2005.
- [KUTY00] H. Koura, M. Uno, T. Tachibana, and M. Yamada. Nuclear mass formula with shell energies calculated by a new method. *Nuclear Physics A*, 674(1):47 – 76, 2000.
- [LGR<sup>+</sup>05] Yu. A. Litvinov, H. Geissel, T. Radon, F. Attallah, G. Audi, K. Beckert, F. Bosch, M. Falch, B. Franzke, M. Hausmann, and M. Hellstr. Mass measurement of cooled neutron-deficient bismuth projectile fragments with time-resolved schottky mass spectrometry at the frs-esr facility. *Nuclear Physics A*, 756(1):3 – 38, 2005.
- [LK12] Yu-Ran Luo and J. A. Kerr. Bond dissociation energies. *CRC Handbook of Chemistry and Physics*, 89, 2012.
- [LM16a] P. J. Linstrom and W. G. Mallard. *NIST Chemistry WebBook, NIST Standard Reference Database Number 69*. National Institute of Standards and Technology, Gaithersburg MD, 20899, <http://webbook.nist.gov>, 2016.
- [LM16b] A. Lopez-Martens. Private communication. April 2016.
- [LNST63] J. Lindhard, V. Nielsen, M. Scharff, and P.V. Thomsen. Integral equations governing radiation effects. *Mat. Fys. Medd. Vid. Selsk*, 33(10), 1963.
- [LPT03] D. Lunney, J. M. Pearson, and C. Thibault. Recent trends in the determination of nuclear masses. *Rev. Mod. Phys.*, 75:1021–1082, Aug 2003.
- [LS01] A. Lépine-Szily. Experimental overview of mass measurements. In David Lunney, Georges Audi, and H.-Jürgen Kluge, editors, *Atomic Physics at Accelerators: Mass Spectrometry*, pages 35–57, Dordrecht, 2001. Springer Netherlands.
- [LT72] G. D. Loper and G. E. Thomas. Gamma-ray intensity standards: The reactions  $^{14}\text{N}(n, \gamma)^{15}\text{N}$ ,  $^{35}\text{Cl}(n, \gamma)^{36}\text{Cl}$  and  $^{53}\text{Cr}(n, \gamma)^{54}\text{Cr}$ . *Nuclear Instruments and Methods*, 105(3):453 – 460, 1972.
- [MBC<sup>+</sup>13] A. G. Marshall, G. T. Blakney, T. Chen, N. K. Kaiser, A. M. McKenna, R. P. Rodgers, B. M. Ruddy, and F. Xian. Mass resolution and mass accuracy: How much is enough? *Mass Spectrometry*, 2, 2013.
- [Mei15] Z. Meisel. Private communication. October 2015.
- [MES<sup>+</sup>12] M. Matoš, A. Estradé, H. Schatz, D. Bazin, M. Famiano, A. Gade, S. George, W. G. Lynch, Z. Meisel, M. Portillo, A. Rogers, D. Shapira, A. Stolz, M. Wallace, and J. Yurkon. Time-of-flight mass measurements of exotic nuclei. *Nuclear*

- Instruments and Methods in Physics Research Section A: Accelerators, Spectrometers, Detectors and Associated Equipment*, 696:171 – 179, 2012.
- [MG13] Z. Meisel and S. George. Time-of-flight mass spectrometry of very exotic systems. *International Journal of Mass Spectrometry*, 349-350:145 – 150, 2013. 100 years of Mass Spectrometry.
- [MGA<sup>+</sup>15] Z. Meisel, S. George, S. Ahn, J. Browne, D. Bazin, B. A. Brown, J. F. Carpino, H. Chung, R. H. Cyburt, A. Estradé, M. Famiano, A. Gade, C. Langer, M. Matoš, W. Mittig, F. Montes, D. J. Morrissey, J. Pereira, H. Schatz, J. Schatz, M. Scott, D. Shapira, K. Smith, J. Stevens, W. Tan, O. Tarasov, S. Towers, K. Wimmer, J. R. Winkelbauer, J. Yurkon, and R. G. T. Zegers. Mass measurements demonstrate a strong  $N = 28$  Shell Gap in argon. *Phys. Rev. Lett.*, 114:022501, Jan 2015.
- [MLH<sup>+</sup>16] D. A. Matters, A. G. Lerch, A. M. Hurst, L. Szentmiklósi, J. J. Carroll, B. Detwiler, Zs. Révay, J. W. McClory, S. R. McHale, R. B. Firestone, B. W. Sleaford, M. Krtička, and T. Belgya. Investigation of  $^{186}\text{Re}$  via radiative thermal-neutron capture on  $^{185}\text{Re}$ . *Phys. Rev. C*, 93:054319, May 2016.
- [MN88] P. Möller and J. R. Nix. Nuclear masses from a unified macroscopic-microscopic model. *Atomic Data and Nuclear Data Tables*, 39(2):213 – 223, 1988.
- [MNMS95] P. Möller, J. R. Nix, W. D. Myers, and W. J. Swiatecki. Nuclear ground-state masses and deformations. *Atomic Data and Nuclear Data Tables*, 59(2):185 – 381, 1995.
- [MNT16a] P. J. Mohr, D. B. Newell, and B. N. Taylor. CODATA recommended values of the fundamental physical constants: 2014. *Journal of Physical and Chemical Reference Data*, 45(4):043102, 2016.
- [MNT16b] P. J. Mohr, D. B. Newell, and B. N. Taylor. CODATA recommended values of the fundamental physical constants: 2014. *Rev. Mod. Phys.*, 88:035009, Sep 2016.
- [MSIS16] P. Möller, A.J. Sierk, T. Ichikawa, and H. Sagawa. Nuclear ground-state masses and deformations: FRDM(2012). *Atomic Data and Nuclear Data Tables*, 109-110(Supplement C):1 – 204, 2016.
- [MSS<sup>+</sup>18] T. D. Morris, J. Simonis, S. R. Stroberg, C. Stumpf, G. Hagen, J. D. Holt, G. R. Jansen, T. Papenbrock, R. Roth, and A. Schwenk. Structure of the lightest tin isotopes. *Phys. Rev. Lett.*, 120:152503, Apr 2018.
- [MTW65] J. H. E. Mattauch, W. Thiele, and A. H. Wapstra. 1964 Atomic mass table. *Nuclear Physics*, 67(1):1 – 31, 1965.

## BIBLIOGRAPHY

---

- [MWKW15] E. G. Myers, A. Wagner, H. Kracke, and B. A. Wesson. Atomic masses of tritium and helium-3. *Phys. Rev. Lett.*, 114:013003, Jan 2015.
- [NBD<sup>+</sup>17] A. Negret, D. Balabanski, P. Dimitriou, Z. Elekes, T. J. Mertzimekis, S. Pascu, and J. Timar. Nuclear structure and decay data evaluation in europe. *EPJ Web Conf.*, 146:02042, 2017.
- [PBK<sup>+</sup>11] B. Pritychenko, E. Běták, M.A. Kellett, B. Singh, and J. Totans. The nuclear science references (NSR) database and web retrieval system. *Nuclear Instruments and Methods in Physics Research Section A: Accelerators, Spectrometers, Detectors and Associated Equipment*, 640(1):213 – 218, 2011.
- [Pea01] J. M. Pearson. The quest for a microscopic nuclear mass formula. *Hyperfine Interactions*, 132(1):59–74, Jan 2001.
- [Pen01] Yu. E. Penionzhkevich. *Mass Measurements in Nuclear Reactions*, pages 265–273. Springer Netherlands, Dordrecht, 2001.
- [Rat75] A. Ratkowski. Energy response of silicon surface-barrier particle detectors to slow heavy ions. *Nuclear Instruments and Methods*, 130(2):533 – 538, 1975.
- [rB96] Å. Björck. *Numerical Methods for Least Squares Problems*. Society for Industrial and Applied Mathematics, 1996.
- [RGG72] A. Rytz, B. Grennberg, and D. J. Gorman. *New Alpha Energy Standards*, pages 1–9. Springer US, Boston, MA, 1972.
- [RKA<sup>+</sup>04] D. Rodríguez, V. S. Kolhinen, G. Audi, J. Äystö, D. Beck, K. Blaum, G. Bollen, F. Herfurth, A. Jokinen, A. Kellerbauer, H. J. Kluge, M. Oinonen, H. Schatz, E. Sauvan, and S. Schwarz. Mass measurement on the *rp*-process waiting point <sup>72</sup>Kr. *Phys. Rev. Lett.*, 93:161104, Oct 2004.
- [Ros02] L. Rosta. Cold neutron research facility at the budapest neutron centre. *Applied Physics A*, 74(1):s52–s54, Dec 2002.
- [RTP04] S. Rainville, J. K. Thompson, and D. E. Pritchard. An ion balance for ultra-high-precision atomic mass measurements. *Science*, 303(5656):334–338, 2004.
- [RW84] A. Rytz and R. A. P. Wiltshire. Absolute determination of the energies of alpha particles emitted by <sup>236</sup>Pu. *Nuclear Instruments and Methods in Physics Research*, 223(2-3):325 – 328, 1984.
- [RWK86] A. Rytz, R. A. P. Wiltshire, and M. King. Absolute measurement of the energies of alpha-particles emitted by sources of <sup>252</sup>Cf and <sup>227</sup>Ac. *Nuclear Instruments and Methods in Physics Research Section A: Accelerators, Spectrometers, Detectors and Associated Equipment*, 253(1):47 – 50, 1986.

- [SBB<sup>+</sup>91] G. Savard, St. Becker, G. Bollen, H.-J. Kluge, R. B. Moore, Th. Otto, L. Schweikhard, H. Stolzenberg, and U. Wiess. A new cooling technique for heavy ions in a Penning trap. *Physics Letters A*, 158(5):247 – 252, 1991.
- [SBN<sup>+</sup>08] A. Solders, I. Bergström, Sz. Nagy, M. Suhonen, and R. Schuch. Determination of the proton mass from a measurement of the cyclotron frequencies of  $d^+$  and  $H_2^+$  in a Penning trap. *Phys. Rev. A*, 78:012514, Jul 2008.
- [Sch13] H. Schatz. Nuclear masses in astrophysics. *International Journal of Mass Spectrometry*, 349-350:181 – 186, 2013. 100 years of Mass Spectrometry.
- [SKB<sup>+</sup>12] A. Spyrou, Z. Kohley, T. Baumann, D. Bazin, B. A. Brown, G. Christian, P. A. DeYoung, J. E. Finck, N. Frank, E. Lunderberg, S. Mosby, W. A. Peters, A. Schiller, J. K. Smith, J. Snyder, M. J. Strongman, M. Thoennessen, and A. Volya. First Observation of Ground State Dineutron Decay:  $^{16}\text{Be}$ . *Phys. Rev. Lett.*, 108:102501, Mar 2012.
- [SKL<sup>+</sup>08] B. Sun, R. Knöbel, Yu.A. Litvinov, H. Geissel, J. Meng, K. Beckert, F. Bosch, D. Boutin, C. Brandau, L. Chen, I.J. Cullen, C. Dimopoulou, B. Fabian, M. Hausmann, C. Kozhuharov, S.A. Litvinov, M. Mazzocco, F. Montes, G. Münzenberg, A. Musumarra, S. Nakajima, C. Nociforo, F. Nolden, T. Ohtsubo, A. Ozawa, Z. Patyk, W.R. Plaß, C. Scheidenberger, M. Steck, T. Suzuki, P.M. Walker, H. Weick, N. Winckler, M. Winkler, and T. Yamaguchi. Nuclear structure studies of short-lived neutron-rich nuclei with the novel large-scale isochronous mass spectrometry at the FRS-ESR facility. *Nuclear Physics A*, 812(1):1 – 12, 2008.
- [SLP18] A. Sobiczewski, Yu.A. Litvinov, and M. Palczewski. Detailed illustration of the accuracy of currently used nuclear-mass models. *Atomic Data and Nuclear Data Tables*, 119(Supplement C):1 – 32, 2018.
- [SLS<sup>+</sup>15] Y. P. Shen, W. P. Liu, J. Su, N. T. Zhang, L. Jing, Z. H. Li, Y. B. Wang, B. Guo, S. Q. Yan, Y. J. Li, S. Zeng, G. Lian, X. C. Du, L. Gan, X. X. Bai, J.S. Wang, Y. H. Zhang, X.H. Zhou, X.D. Tang, J. J. He, Y. Y. Yang, S.L. Jin, P. Ma, J. B. Ma, M. R. Huang, Z. Bai, Y. J. Zhou, W. H. Ma, J. Hu, S. W. Xu, S. B. Ma, S.Z. Chen, L. Y. Zhang, B. Ding, and Z. H. Li. Measurement of the  $^{52}\text{Fe}$  mass via the precise proton-decay energy of  $^{53}\text{Co}^m$ . *Phys. Rev. C*, 91:047304, Apr 2015.
- [SMB<sup>+</sup>14] M. Del Santo, Z. Meisel, D. Bazin, A. Becerril, B. A. Brown, H. Crawford, R. Cyburt, S. George, G. F. Grinyer, G. Lorusso, P. F. Mantica, F. Montes, J. Pereira, H. Schatz, K. Smith, and

- M. Wiescher.  $\beta$ -delayed proton emission of  $^{69}\text{Kr}$  and the  $^{68}\text{Se}$  rp-process waiting point. *Physics Letters B*, 738:453 – 456, 2014.
- [SXZ<sup>+</sup>16] P. Shuai, X. Xu, Y. H. Zhang, H. S. Xu, Yu. A. Litvinov, M. Wang, X. L. Tu, K. Blaum, X. H. Zhou, Y. J. Yuan, X. L. Yan, X. C. Chen, R. J. Chen, C. Y. Fu, Z. Ge, W. J. Huang, Y. M. Xing, and Q. Zeng. An improvement of isochronous mass spectrometry: Velocity measurements using two time-of-flight detectors. *Nuclear Instruments and Methods in Physics Research Section B: Beam Interactions with Materials and Atoms*, 376:311 – 315, 2016. Proceedings of the XVIIth International Conference on Electromagnetic Isotope Separators and Related Topics (EMIS2015), Grand Rapids, MI, U.S.A., 11-15 May 2015.
- [Tay14] B. N. Taylor. Private communication. November 2014.
- [TBH<sup>+</sup>12] L. Trache, A. Banu, J.C. Hardy, V.E. Iacob, M. McCleskey, B.T. Roeder, E. Simmons, A. Spiridon, R.E. Tribble, A. Saastamoinen, A. Jokinen, J. Äystö, T. Davinson, G. Lotay, P.J. Woods, and E. Pollacco. Decay spectroscopy for nuclear astrophysics:  $\beta$  and  $\beta$ -delayed proton decay. *Journal of Physics: Conference Series*, 337(1):012058, 2012.
- [Tul96] J. K. Tuli. Evaluated nuclear structure data file. *Nuclear Instruments and Methods in Physics Research Section A: Accelerators, Spectrometers, Detectors and Associated Equipment*, 369(2):506 – 510, 1996.
- [TXW<sup>+</sup>11] X. L. Tu, H. S. Xu, M. Wang, Y. H. Zhang, Yu. A. Litvinov, Y. Sun, H. Schatz, X. H. Zhou, Y. J. Yuan, J. W. Xia, G. Audi, K. Blaum, C. M. Du, P. Geng, Z. G. Hu, W. X. Huang, S. L. Jin, L. X. Liu, Y. Liu, X. Ma, R. S. Mao, B. Mei, P. Shuai, Z. Y. Sun, H. Suzuki, S. W. Tang, J. S. Wang, S. T. Wang, G. Q. Xiao, X. Xu, T. Yamaguchi, Y. Yamaguchi, X. L. Yan, J. C. Yang, R. P. Ye, Y. D. Zang, H. W. Zhao, T. C. Zhao, X. Y. Zhang, and W. L. Zhan. Direct mass measurements of short-lived  $a = 2z - 1$  nuclides  $^{63}\text{Ge}$ ,  $^{65}\text{As}$ ,  $^{67}\text{Se}$ , and  $^{71}\text{Kr}$  and their impact on nucleosynthesis in the  $rp$  process. *Phys. Rev. Lett.*, 106:112501, Mar 2011.
- [VB72] D. Vautherin and D. M. Brink. Hartree-fock calculations with skyrme’s interaction. i. spherical nuclei. *Phys. Rev. C*, 5:626–647, Mar 1972.
- [VCB68] G. B. Vingiani, G. Chilosi, and W. Bruynesteyn. The  $^{49}\text{Ca}$  ground-state analogue. *Physics Letters B*, 26(5):285 – 287, 1968.
- [VDZS01] R. S. Van Dyck, S. L. Zafonte, and P. B. Schwinberg. Ultra-precise mass measurements using the uw-ptms. *Hyperfine Interactions*, 132(1):163–175, Jan 2001.

- [VWV<sup>+</sup>86] D. J. Vieira, J. M. Wouters, K. Vaziri, R. H. Kraus, H. Wollnik, G. W. Butler, F. K. Wohn, and A. H. Wapstra. Direct mass measurements of neutron-rich light nuclei near  $N=20$ . *Phys. Rev. Lett.*, 57:3253–3256, Dec 1986.
- [WA85] A. H. Wapstra and G. Audi. The 1983 atomic mass evaluation: (i). atomic mass table. *Nuclear Physics A*, 432(1):1 – 54, 1985.
- [WAA<sup>+</sup>17] A. Welker, N. A. S. Althubiti, D. Atanasov, K. Blaum, T. E. Cocolios, F. Herfurth, S. Kreim, D. Lunney, V. Manea, M. Mougeot, D. Neidherr, F. Nowacki, A. Poves, M. Rosenbusch, L. Schweikhard, F. Wienholtz, R. N. Wolf, and K. Zuber. Binding energy of  $^{79}\text{Cu}$ : Probing the structure of the doubly magic  $^{78}\text{Ni}$  from only one proton away. *Phys. Rev. Lett.*, 119:192502, Nov 2017.
- [WAH88] A. H. Wapstra, G. Audi, and R. Hoekstra. Atomic masses from (mainly) experimental data. *Atomic Data and Nuclear Data Tables*, 39(2):281 – 287, 1988.
- [WAK<sup>+</sup>17] M. Wang, G. Audi, F. G. Kondev, W. J. Huang, S. Naimi, and X. Xu. The ame2016 atomic mass evaluation (ii). tables, graphs and references. *Chinese Physics C*, 41(3):030003, 2017.
- [Wap54a] A. H. Wapstra. Isotopic masses I.  $A < 34$ . *Physica*, 21(1):367 – 384, 1954.
- [Wap54b] A. H. Wapstra. Isotopic masses II.  $33 < A < 202$ . *Physica*, 21(1):385 – 409, 1954.
- [Wap60] A. H. Wapstra. Treatment of input data for a least squares nuclidic mass adjustment. *Proc. Int. Conf. Nuclidic Mases*, pages 24–38, 1960.
- [Wap65] A. H. Wapstra. Two-proton and two-neutron binding-energy systematics and alpha-decay energies. *Nuclear Data Sheets. Section A*, 1:1 – 19, 1965.
- [WAW<sup>+</sup>12] M. Wang, G. Audi, A. H. Wapstra, F. G. Kondev, M. MacCormick, X. Xu, and B. Pfeiffer. The Ame2012 atomic mass evaluation. *Chinese Physics C*, 36(12):1603, 2012.
- [WBB<sup>+</sup>13a] F. Wienholtz, D. Beck, K. Blaum, Ch. Borgmann, M. Breitenfeldt, R. B. Cakirli, S. George, F. Herfurth, J. D. Holt, M. Kowalska, S. Kreim, D. Lunney, V. Manea, J. Menendez, D. Neidherr, M. Rosenbusch, L. Schweikhard, A. Schwenk, J. Simonis, J. Stanja, and K. Zuber. Masses of exotic calcium isotopes pin down nuclear forces. *Nature*, 498:346–349, 2013.
- [WBB<sup>+</sup>13b] R. N. Wolf, D. Beck, K. Blaum, Ch. Böhm, Ch. Borgmann, M. Breitenfeldt, N. Chamel, S. Goriely, F. Herfurth, M. Kowalska, S. Kreim, D. Lunney, V. Manea, E. Minaya Ramirez,

## BIBLIOGRAPHY

---

- S. Naimi, D. Neidherr, M. Rosenbusch, L. Schweikhard, J. Stanja, F. Wienholtz, and K. Zuber. Plumbing neutron stars to new depths with the binding energy of the exotic nuclide  $^{82}\text{Zn}$ . *Phys. Rev. Lett.*, 110:041101, Jan 2013.
- [Wei35] C. F. v. Weizsäcker. Zur theorie der kernmassen. *Zeitschrift für Physik*, 96(7):431–458, Jul 1935.
- [WG71] A. H. Wapstra and N. B. Gove. Part i. atomic mass table. *Atomic Data and Nuclear Data Tables*, 9(4):267 – 301, 1971.
- [WGB68] D. H. White, D. J. Groves, and R. E. Birkett. Precision measurements of gamma rays from  $^{60}\text{Co}$ ,  $^{41}\text{Ar}$  and  $^{53}\text{Cr}(n, \gamma)^{54}\text{Cr}$ . *Nuclear Instruments and Methods*, 66(1):70 – 76, 1968.
- [WKB77] A. H. Wapstra and K K. Bos. The 1977 atomic mass evaluation: in four parts. *Atomic Data and Nuclear Data Tables*, 20(1):1–125, 1977.
- [WL11] N. Wang and M. Liu. Nuclear mass predictions with a radial basis function approach. *Phys. Rev. C*, 84:051303, Nov 2011.
- [WLWM14] N. Wang, M. Liu, X. Wu, and J. Meng. Surface diffuseness correction in global mass formula. *Physics Letters B*, 734(Supplement C):215 – 219, 2014.
- [WMRS12] R. N. Wolf, G. Marx, M. Rosenbusch, and L. Schweikhard. Static-mirror ion capture and time focusing for electrostatic ion-beam traps and multi-reflection time-of-flight mass analyzers by use of an in-trap potential lift. *International Journal of Mass Spectrometry*, 313:8 – 14, 2012.
- [WP90] H. Wollnik and M. Przewloka. Time-of-flight mass spectrometers with multiply reflected ion trajectories. *International Journal of Mass Spectrometry and Ion Processes*, 96(3):267 – 274, 1990.
- [WWV<sup>+</sup>85] J. M. Wouters, D. J. Vieira, H. Wollnik, H. A. Enge, S. Kowalski, and K. L. Brown. Optical design of the tofi (time-of-flight isochronous) spectrometer for mass measurements of exotic nuclei. *Nuclear Instruments and Methods in Physics Research Section A: Accelerators, Spectrometers, Detectors and Associated Equipment*, 240(1):77 – 90, 1985.
- [WWA<sup>+</sup>13] R. N. Wolf, F. Wienholtz, D. Atanasov, D. Beck, K. Blaum, Ch. Borgmann, F. Herfurth, M. Kowalska, S. Kreim, Yu. A. Litvinov, D. Lunney, V. Manea, D. Neidherr, M. Rosenbusch, L. Schweikhard, J. Stanja, and K. Zuber. ISOLTRAP’s multi-reflection time-of-flight mass separator/spectrometer. *International Journal of Mass Spectrometry*, 349-350:123 – 133, 2013. 100 years of Mass Spectrometry.

- [XZW<sup>+</sup>02] J. W. Xia, W. L. Zhan, B. W. Wei, Y. J. Yuan, M. T. Song, W. Z. Zhang, X. D. Yang, P. Yuan, D. Q. Gao, H. W. Zhao, X. T. Yang, G. Q. Xiao, K. T. Man, J. R. Dang, X. H. Cai, Y. F. Wang, J. Y. Tang, W. M. Qiao, Y. N. Rao, Y. He, L. Z. Mao, and Z. Z. Zhou. The heavy ion cooler-storage-ring project (hirfl-csr) at lanzhou. *Nuclear Instruments and Methods in Physics Research Section A: Accelerators, Spectrometers, Detectors and Associated Equipment*, 488(1):11 – 25, 2002.
- [ZBM<sup>+</sup>82] J. D. Zumbro, C. P. Browne, J. F. Mateja, H. T. Fortune, and R. Middleton.  $^{176}\text{Yb}(t, p)^{178}\text{Yb}$  reaction. *Phys. Rev. C*, 26:965–968, Sep 1982.
- [ZJ15] S. L. Zafonte and R. S. Van Dyck Jr. Ultra-precise single-ion atomic mass measurements on deuterium and helium-3. *Metrologia*, 52(2):280, 2015.
- [ZXS<sup>+</sup>17] P. Zhang, X. Xu, P. Shuai, R. J. Chen, X. L. Yan, Y. H. Zhang, M. Wang, Yu. A. Litvinov, K. Blaum, H. S. Xu, T. Bao, X. C. Chen, H. Chen, C. Y. Fu, J. J. He, S. Kubono, Y. H. Lam, D. W. Liu, R. S. Mao, X. W. Ma, M. Z. Sun, X. L. Tu, Y. M. Xing, J. C. Yang, Y. J. Yuan, Q. Zeng, X. Zhou, X. H. Zhou, W. L. Zhan, S. Litvinov, G. Audi, T. Uesaka, Y. Yamaguchi, T. Yamaguchi, A. Ozawa, B. H. Sun, Y. Sun, and F. R. Xu. High-precision  $Q_{EC}$  values of superallowed  $0^+ \rightarrow 0^+ \beta^-$  emitters  $^{46}\text{Cr}$ ,  $^{50}\text{Fe}$  and  $^{54}\text{Ni}$ . *Physics Letters B*, 767:20–24, 2017.

# Synthèse

Les masses atomiques ont été largement utilisées en physique nucléaire, astrophysique et dans des applications avancées telles que l'énergie nucléaire et la gestion des déchets. La masse atomique est une empreinte digitale unique d'un noyau. En mesurant la masse atomique d'un noyau, nous pouvons en dériver l'énergie de liaison, qui reflète toutes les interactions (fortes, faibles et électromagnétiques) en action dans le noyau. L'évaluation des masses atomiques (AME), commencée dans les années 1950, vise à fournir l'information la plus fiable et la plus complète sur les masses atomiques. Jusqu'à présent, dix tables de masse ont été publiées sur la base de la méthode de Wapstra.

Les connaissances actuelles des masses atomiques peuvent être obtenues par quatre voies: a) les énergies de désintégration bêta, b) les énergies de désintégration dues aux émissions de particules légères, e.g.,  $\alpha$  et proton, c) les énergies libérées dans les réactions nucléaires, et d) les données de spectrométrie de masse. Les trois premières méthodes sont indirectes car elles mesurent l'énergie libérée, et la dernière est directe, car elle mesure la masse inertielle d'un atome dans un champ électromagnétique. Toutes ces mesures de masse sont relatives, ce qui signifie que chaque donnée expérimentale établit fondamentalement une relation entre deux masses, ou parfois plusieurs. En même temps, puisque le nombre de mesures est beaucoup plus grand que celui des masses, extraire les masses de ce système surdéterminé n'est pas simple. Sur la base de ces faits, l'évaluation des masses atomiques est soumise à un traitement spécial des données. Pour résoudre le problème de la surdétermination, nous pouvons recourir à la méthode des moindres carrés. Puisque toutes les données d'entrée sont linéaires en masse, nous pouvons considérer les masses comme des paramètres dans la méthode des moindres carrés. Un tel système intriqué peut ainsi être résolu, et les masses peuvent être dérivées sans approximation. L'utilisation de la méthode des moindres carrés sur le système surdéterminé est une procédure idéale dans la mesure où elle fournit non seulement des valeurs de masse non biaisées et fiables dérivées de données expérimentales, mais permet également de vérifier les consistances de toutes les données d'entrée. L'un des rôles de l'AME est de révéler des erreurs systématiques non découvertes, en comparant les données d'entrée avec les valeurs ajustées dans un ajustement global. Une telle tâche ne peut être effectuée que dans le cadre de l'AME. Après avoir obtenu la meilleure valeur pour chaque

---

masse, nous pouvons calculer toute combinaison de différences de masse, telles que les énergies de désintégration et de séparation, sur la base de la matrice de covariance. Pour trouver l'information qu'une équation apporte à chaque masse, on peut construire une matrice de flux d'information, découverte par G. Audi en 1986. Cette matrice permet de déterminer la contribution de chaque donnée d'entrée sur chaque masse.

Les développements pour la dernière table de masse AME2016 sont discutés. Le premier est lié au traitement soigneux des données les plus précises. Les données de masse les plus précises proviennent de la spectrométrie de masse à piège de Penning. De nos jours, comme la précision des pièges Penning peut atteindre  $10^{-10}$  ou même mieux, les énergies de liaison moléculaire et électronique doivent être prises en compte. Une méthode pour calculer l'énergie de liaison moléculaire à partir de la chaleur de formation standard est décrite et deux exemples détaillés sont donnés. Nous trouvons qu'en utilisant la chaleur de formation standard mise à jour, les valeurs recalculées pour certaines des données de spectrométrie de masse peuvent changer de manière significative. En AME2016, toutes les données précises ont été recalculées.

Le second est liée aux corrections des énergies de désintégration. Pour les énergies de décroissance  $\alpha$  et proton mesurées par des méthodes d'implantation, l'énergie de recul du partenaire de la décroissance doit être prise en compte correctement. Nous présentons une procédure pour corriger les énergies de désintégration publiées dans le cas où le recul du noyau n'est pas prise en compte dans les expériences d'implantation. Un programme a été développé basé sur la théorie intégrale de Lindhard, qui prédit avec précision le dépôt d'énergie des noyaux lourds dans la matière. Trois exemples sont donnés pour illustrer la procédure de correction.

Le troisième développement concerne la prise en compte de l'effet relativiste et de l'effet atomique dans la conversion des énergies des particules alpha en énergie de décroissance. Les énergies de décroissance  $\alpha$  les plus précises proviennent de la spectrographie magnétique. Ces étalons d'énergie  $\alpha$  servent non seulement de points d'étalonnage pour tous les spectres  $\alpha$  avec un pouvoir de résolution élevé, mais fournissent également des valeurs d'entrée précises à l'AME. Afin d'obtenir des énergies de décroissance correctes à partir de la spectrographie magnétique, où seules les particules  $\alpha$  sont détectées, une formule relativiste prenant en compte également les énergies de liaison des électrons de l'hélium est dérivée.

Les modèles de masse sont le dernier recours pour accéder aux nucléides les plus exotiques qui ne peuvent pas être produit actuellement, ni dans un proche avenir. Ces modèles de masse, indépendamment de leurs caractères intrinsèques, peuvent reproduire les masses connues expérimentalement mais prédire un comportement différent lorsqu'elles sont extrapolées vers des régions inconnues. Sur la base de ce fait, la précision et la puissance prédictive de huit masses des modèles de divers types, à savoir la méthode de Thomas-Fermi étendue plus l'intégrale de Strutinsky (ETFSI-2), le modèle de gouttelettes à

---

portée finie (FRDM95) et sa version mise à jour avec traitement amélioré de la déformation (FRDM12), un modèle récent Weizsäcker-Skyrme plus Radial Basic Function (WS4+RBF), deux modèles récents de masse Hartree-Fock-Bogoliubov HFB26 et HFB27, le modèle Duflo et Zuker (DUZU), le modèle KTUY05, sont étudiés. Nous trouvons que la déviation quadratique moyenne ( $\delta_{\text{rms}}$ ) de tous les modèles de masse considérés est bien inférieure à 0.8 MeV par rapport aux trois tables de masse AME2003, AME2012 et AME2016 pour tous les nucléides ( $N, Z \geq 8$ ). Le modèle de masse WS4+RBF est le modèle de masse le plus précis qui donne  $\delta_{\text{rms}}$  autour de 0.2 MeV. Le modèle de masse microscopique HFB27 présente également une bonne précision avec  $\delta_{\text{rms}} \approx 0.5$  MeV. Le modèle de masse DUZU est encore un modèle de masse robuste qui donne  $\delta_{\text{rms}} \approx 0.4$  MeV. Les écarts quadratiques très similaires pour chaque modèle de masse par rapport aux différentes tables de masse sont dus au fait que, dans AME2016, seules 17 masses ont changé de plus de 500 keV par rapport à AME2003.

L'extrapolation de masse d'AME est une autre façon d'obtenir des masses inconnues. La régularité est considérée comme une propriété fondamentale de la surface de masse et peut aider à dériver des masses inconnues à partir des masses mesurées. Les représentations directes des masses dans un espace tridimensionnel ne sont pas pratiques, car la surface de masse a une très grande extension le long de l'axe de la masse (nombre de masse allant de 1 u à environ 300 u). Dans le travail de [WAH88], l'extrapolation a été faite en examinant la surface de la masse en quatre projections. Wapstra *et al.* [WAH88] ont analysé les différences entre masses expérimentales et une expression obtenue par un examen approprié des effets d'appariement [JHJ84] plus une fonction lisse. Un tel traitement a permis d'examiner la surface de masse à peu près à la même échelle (plusieurs MeV) et remédier à certaines oscillations causées par l'appariement. Cependant, la procédure était plutôt complexe (voir Fig. 1 dans [WAH88]). Une alternative pour contourner ces difficultés est d'examiner les dérivées de la surface de la masse. Par dérivée, nous entendons une différence spécifique entre les masses de deux nucléides voisins. Les dérivés conservent le comportement lisse qui s'étend des masses connues aux inconnues d'une part, et amplifient la structure locale d'un autre côté. Le travail de pionnier de [Wap65] vise à estimer des masses inconnues sur la base des études de cinq dérivés: énergies de séparation à deux neutrons et à deux protons, énergies de désintégration  $\alpha$ , désintégration bêta et les énergies de désintégration double-bêta. L'intention première de l'extrapolation de masse était d'exploiter les énergies de réaction et de décroissance entre noyaux n'ayant aucun lien avec les noyaux de masses connues. Une masse suspecte qui perturbe les graphiques des dérivées peut également être repérée facilement.

Un modèle de masse peut également être utile dans l'extrapolation de masse. Nous soustrayons les masses prédites par un modèle de masse des masses expérimentales et étudions la tendance des écarts. Treize modèles de masse ont été étudiés [BA93] et le modèle de DUZU à base sphérique

---

(DZ10sph) [DZ96] a été choisi comme modèle préféré, car sa surface de masse peut être affichée beaucoup plus en douceur avec ce modèle. En supposant que la tendance des écarts est régulière et continue, nous pourrions étendre cette tendance des masses connues aux masses inconnues.

La combinaison de produits dérivés et l'utilisation de la différence entre les masses et les masses d'un modèle permet une extrapolation pratique. Comme chaque point dans les graphiques des dérivées implique deux masses et que l'on doit trouver lequel est le responsable du point de déraillement dans tout graphiques des dérivées. Si l'on travaille sur le graphique de la différence de masse, on peut manipuler chaque masse plus facilement. Le développement d'un outil graphique interactif dans les années 1990, qui est encore utilisé aujourd'hui, nous permet de vérifier quatre types différents de surface de masse en même temps. Tout changement d'une masse unique dans un graphique de la surface de masse spécifique mettra à jour l'information dans les autres graphiques. Et un tel changement devrait être cohérent dans les quatre graphiques. L'extrapolation de masse fournit les meilleures estimations pour les masses inconnues qui ne sont pas trop loin (deux ou trois unités de masse) des derniers nucléides connus. Cette méthode est basée sur la douceur de la surface de masse et une telle caractéristique lisse devrait être préférée lorsque nous extrapolons les masses vers la région inconnue. L'écart moyen-carré pour toutes les masses estimées dans l'AME2012 qui sont connues dans l'AME2016 est de 0.396 MeV (55 cas au total), ce qui est plus petit que tous les modèles de masse discutés ici.

Une autre partie de cette thèse est liée aux mesures de masse effectuées en utilisant le spectromètre de masse à piège de Penning ISOLTRAP à ISOLDE/CERN. Le confinement spatial complet exige un minimum de potentiel dans les trois dimensions. Une force de confinement souhaitable est celle qui dépend linéairement de la distance entre les ions stockés et le centre du piège. Cela entraîne un potentiel harmonique pour les ions confinés. Cependant, ni un champ magnétique pur ni un champ électrostatique ne peuvent confiner un ion en 3-dimensions. Une superposition d'un champ magnétique homogène fort, assurant un confinement radial, et un champ quadripolaire électrostatique faible, assurant un confinement axial, est utilisé pour atteindre le confinement tridimensionnel dans le piège de Penning. Les ions dans cette combinaisons de champs effectuent trois mouvements propres indépendants [BG86]: l'oscillation harmonique le long de l'axe du piège à la fréquence d'oscillation axiale  $\omega_z$ , le mouvement cyclotron modifié à la fréquence  $\omega_+$  et le magnétron à la fréquence  $\omega_-$ . Les deux derniers mouvements sont des mouvements radiaux et perpendiculaires à l'axe du piège. En raison des imperfections du vrai piège de Penning, tels que les trous d'ouverture pour l'injection et l'éjection d'ions, ou les électrodes ne s'étendant pas à l'infini, ce qui induirait un champ électrique multipolaire d'ordre supérieur, ce qui rend  $\omega_c = \omega_+ + \omega_-$  invalide. Basé sur ce fait, le refroidissement est important pour effectuer des mesures de haute précision, puisque les ions sondent moins les imperfections

---

des champs électriques et magnétiques. Pour les nucléides radioactifs, le refroidissement du gaz tampon est généralement utilisé. Puisque les gaz nobles ont un potentiel d'excitation élevé, ils constituent un choix idéal pour refroidir les ions. Par collisions avec des atomes de gaz rares, tels que l'hélium, les ions chauds perdent de l'énergie et leur mouvement peut être amorti. Cependant, la situation dans les pièges Penning devient plus complexe. Pendant le refroidissement, les amplitudes des mouvements cyclotron axial et modifié diminuent alors que l'amplitude du mouvement magnétron augmente. Finalement, les ions heurtent l'électrode annulaire et sont perdus. Pour contrer la diffusion radiale vers l'extérieur provoquée par le gaz tampon, on peut utiliser la technique de refroidissement par bandes latérales [SBB+ 91]. En appliquant une tension RF à l'électrode annulaire segmentée à la fréquence cyclotron  $\omega_c = \omega_+ + \omega_-$ , les mouvements radiaux se couplent, c'est-à-dire que la conversion du mouvement cyclotron modifié en mouvement magnétron aura lieu périodiquement. Puisque le mouvement cyclotron modifié est amorti plus rapidement que le mouvement magnétron, les ions peuvent être recentrés après un certain temps de refroidissement. Le refroidissement par bandes latérales est sélectif en masse et peut être utilisé pour recentrer les ions d'intérêt et éliminer les contaminations isobariques.

Une excitation quadripolaire à la somme des fréquences propres individuelles peut être utilisée pour coupler des mouvements propres et déterminer des fréquences. L'approche la plus directe pour la spectrométrie de masse est la mesure de la fréquence somme  $\omega_c = \omega_+ + \omega_-$ . Le couplage des deux mouvements radiaux peut être réalisé par un champ rf azimutal quadripolaire à la fréquence  $\omega_{rf}$  appliquée avec des déphasages de  $180^\circ$  sur des ensembles de segments d'électrodes annulaires perpendiculaires l'un à l'autre. En résonance,  $\omega_{rf} = \omega_c$ , on obtient une conversion périodique complète entre les deux mouvements. Dans les expériences, nous scannons la fréquence rf en rechargeant et en vidant le piège de Penning et en détectant le temps de vol d'un ion éjecté depuis le centre du piège. Le minimum dans le spectre de temps de vol nous donne la fréquence cyclotron de l'ion.

Les masses de dix-huit nucléides provenant de plusieurs campagnes expérimentales entre 2011 et 2016 sont analysées. La masse de  $^{168}\text{Lu}$  dans son état isomérique a été mesurée et sa valeur est conforme à la valeur recommandée dans AME2012 mais neuf fois plus précise. La valeur de masse de  $^{178}\text{Yb}$  obtenue ici diffère de 31 (13) keV du résultat d'une mesure par réaction antérieure, mais confirme la liaison supplémentaire de  $^{178}\text{Yb}$  de 440 keV. Un aplatissement soudain dans  $S_{2n}$  de  $^{178}\text{Yb}$  indiquerait l'existence d'une transition de phase dans la région. Cependant, plus de mesures sont nécessaires pour clarifier cette divergence. Les masses de certains nucléides de terres rares tels que  $^{140}\text{Nd}$  et  $^{160}\text{Yb}$  sont mesurées avec une plus grande précision par rapport à AME2016. Les résultats d'autres nucléides aident également à améliorer la précision des masses existantes.

Dans une autre étude, l'erreur systématique des mesures avec un spec-

---

tromètre de masse à multi-réflexion à temps de vol d'ISOLTRAP (MR-TOF MS) à ISOLTRAP a été étudiée en utilisant des sources d'ions hors ligne et avec faisceaux de protons. Dans l'étude hors ligne, différents paramètres sur MR-TOF MS ont été sondés. Deux des conclusions les plus importantes sont abordées. Premièrement, les mesures effectuées au nombre de réflexion  $N = 100$  n'est pas fiable. Afin de minimiser l'écart, les nombres de réflexion supérieurs à 100 doivent être utilisés à la place. Deuxièmement, si nous utilisons des sources d'ions hors ligne pour l'étalonnage de masse, une incertitude de 170 keV devrait être ajoutée au résultat final. Pour l'étude en ligne, 47 mesures sont sélectionnées à partir des mesures de contrôle de rendement. Le chi-carré réduit  $\chi_n$  est déduit à 1.02, ce qui signifie que l'erreur systématique est beaucoup plus petite que les incertitudes statistiques. L'effet du second paramètre  $\beta$  dans la formule de détermination de la masse est également étudié. Le résultat montre que l'utilisation d'un seul ion de référence n'affectera pas pour les doublets de masse la détermination finale des valeurs de masse et donc la conclusion ci-dessus en ce qui concerne l'erreur systématique.

**Titre :** Mesures Directes de Masses et Évaluation Globale des Masses Atomiques)

**Mots clés :** Évaluation des masses atomiques (AME), Masse atomique, Méthode des moindres carrés, Spectrométrie de masse

**Résumé :**

L'évaluation des masses atomiques (AME), commencée dans les années 1960, est la source la plus fiable d'informations complètes sur les masses atomiques. Elle fournit les meilleures valeurs pour les masses atomiques et les incertitudes associées en évaluant les données expérimentales de désintégration, de réactions et de la spectrométrie de masse.

Dans cette thèse, la philosophie et les caractéristiques les plus importantes de l'AME seront discutées en détail. Les développements les plus récents de l'évaluation, AME2016, tels que l'énergie de liaison moléculaire, la correction d'énergie des mesures par implantation, et la formule relativiste pour le proces-

sus de décroissance alpha, seront présentés.

Une autre partie de cette thèse concerne l'analyse des données du spectromètre à piège de Penning ISOLTRAP au ISOLDE/CERN. Les nouveaux résultats sont inclus dans l'ajustement global et leurs influences sur les masses existantes sont discutées. La dernière partie de cette thèse porte sur les études des erreurs systématiques du spectromètre de masse à multi-réflexion à temps de vol d'ISOLTRAP, utilisant une source d'ions hors ligne et le faisceau de protons en ligne. A partir de l'analyse des mesures sélectionnées, j'ai trouvé que l'erreur systématique est beaucoup plus faible que les incertitudes statistiques obtenues jusqu'à présent.

**Title :** Direct Mass Measurements and Global Evaluation of Atomic Masses

**Keywords :** Atomic Mass Evaluation (AME), Atomic Mass, Least-squares Method, Mass Spectrometry

**Abstract :** The Atomic Mass Evaluation (AME), started in the 1960s, is the most reliable source for comprehensive information related to atomic masses. It provides the best values for the atomic masses and their associated uncertainties by evaluating experimental data from decay, reactions, and mass spectrometry.

In this thesis, the philosophy and the most important features of the AME will be discussed in detail. The most recent developments of the latest mass table (AME2016), such as molecular binding energy, energy correction of the implantation measurements, and the relativistic formula for the alpha-decay pro-

cess, will be presented.

Another part of this thesis concerns the data analysis from the Penning-trap spectrometer ISOLTRAP at ISOLDE/CERN. The new results are included in the global adjustment and their influences on the existing masses are discussed.

The last part of this thesis is related to the systematic error studies of the ISOLTRAP multi-reflection time-of-flight mass spectrometer, using an off-line ion source and the on-line proton beam. From the analysis of the selected measurements, I found that the systematic error is much smaller than the statistical uncertainties obtained up to now.

